On nonconvex special relativistic hydrodynamics

Marina Berbel Palomeque

On nonconvex special relativistic hydrodynamics

Marina Berbel Palomeque

Advisor: Professor Susana Serna

PhD in Mathematics
Departament de Matemàtiques
Universitat Autònoma de Barcelona

2023

“ ‘Do you understand what’s going on?’
‘Not at all,’ he shouted back. ‘I can
almost prove this can’t be happening.
Do you know the Boyer-Lindquist
coordinates?’ ”

Contact,
Carl Sagan (1985)

Acknowledgements

I would like to express my gratitude and appreciation to the people and institutions who have played significant roles in the completion of my thesis:

First, I have to say a big thank you to my advisor, Professor Susana Serna, for her guidance and support throughout this journey. I am genuinely grateful for the hours we enjoyed discussing and eating chocolate bars.

I am thankful to the scientific community that attended the CoCoNUT meeting in 2023. Their interest in my research and the good questions that they proposed were inspiring. In particular, I would like to thank Professor Micaela Oertel for her valuable ideas and enlightening conversations.

I would like to mention my gratitude to Professor Antonio Marquina for the stimulating discussions and Professor Jose María Ibáñez for his feedback and enthusiasm.

On a more personal note, I would like to say thank you:

To the one that supported me at every small of step of this thesis, making me dinner and python plots. We are a team and I am grateful for all the times you listened to how a mixed curve is calculated.

To all the people met along the journey, bringing me a hug, a cup of coffee or a discussion about gravitational wave imprints at 2 a.m. You kept me sane when there were too many EoSs.

To all who believed in me during the process and tried to understand why I talked so much about this “Riemann guy”. I hope that my explanations of relativity for dummies were good enough.

Finally, and as a reminder to never give up, to my 16 years-old self: you reached for the stars, so we could touch them now (numerically).

Abstract

This thesis is dedicated to the complex wave structure arising in hydrodynamics of relativistic scenarios when considering realistic fluids with a rich thermodynamics. The equation of state is a constitutive relation encoding the thermodynamic properties of a fluid and, in compressible fluid dynamics, it is needed to close the evolution equations. A nonconvex equation of state is a candidate for inducing complex wave dynamics. With the purpose of studying nonconvex Special Relativistic Hydrodynamics (SRHD), the thesis is divided in two parts. The first one is devoted to the study of nonconvex SRHD from the point of view of the solution of the evolution equations, which consist of a nonlinear hyperbolic system of conservation laws. The second part put the stress on the modeling of realistic fluids taking into account the implications on the dynamics studied in the first part.

On the one hand, we present an exact Riemann solver for nonconvex SRHD, extending its applicability to the case of nonzero tangential velocities. The Riemann problem is an initial condition for the system, the fundamental test in hydrodynamics. Its solution contains all the elements present in more complicated scenarios and allows to understand the wave dynamics that may arise. By providing the exact solution, we enhance the understanding of the intricate dynamics at play in nonconvex relativistic systems. We particularize the solver for a phenomenological nonconvex equation of state and provide the exact solution for a series of standard problems including relativistic blast waves. We employ the exact solutions obtained to validate numerical methods used to solve SRHD equations initialized with complex initial conditions. We measure the accuracy of two of the most commonly used methods in the field and analyze their performance in the presence of complex wave structure.

We continue our analysis focusing on neutron stars as astrophysical objects composed by a fluid that undergo relativistic hydrodynamics evolution. Realistic models for this matter lead to tabulated equations of state, comprising detailed mycrophysical effects but representing a computationally inefficient option for numerical simulations. We concentrate on the modeling of this tabulated data with a simple analytic expression that gives special consideration to phase transitions, a phenomena of the matter with the potential to make the equation of state nonconvex. We analyze the implications of our model in the stellar properties of the neutron star and its hydrodynamic evolution, comparing the results with current analytic models employed in simulations.

Contents

List of Figures

List of Tables

Chapter 1

Introduction

1.1 Context and motivation

The theory of General Relativity, proposed by Albert Einstein in 1915, offered a new way of understanding the Universe. New discoveries and observations through the years have confirmed predictions of this theory of gravitation (for example [52, 123, 4]). The increasing sensibility of experimental instrumentation and the computational power achieved in supercomputers are opening an era where the subtle intricacies of General Relativity can be explored. In the case of the study of massive objects, Einstein field equations need to be coupled with the corresponding hydrodynamic equations [127]. The first system dictates the evolution of the spacetime metric. The second one governs the evolution of matter. The whole coupled system of equations has been extensively studied, as well as each set of equations on their own [92, 113, 48, 21, 65, 22, 120, 34, 35]. The differential equations that model relativistic hydrodynamics are genuinely nonlinear, in contrast to the Einstein field equations which can be formulated as a quasi-linear system of differential equations. From this observation it can be affirmed that the equations of relativistic hydrodynamics for high densities present an additional difficulty from the analytical and computational point of view. The wave dynamics arising from the hydrodynamic evolution alone remains an ongoing area of research. To focus on this issue without introducing the additional complexity of a dynamic metric, we study the evolution of matter under the framework of Special Relativity Hydrodynamics (SRHD).

Our interest relies on understanding the complex wave dynamics in SRHD in realistic scenarios.

Fluid dynamics is based on nonlinear hyperbolic systems of conservation laws (HSCL) closed with a constitutive relation represented by an equation of state (EoS) defining the equilibrium thermodynamics properties of the considered matter.

Let us consider a system of N conservation laws

$$\frac{\partial \mathbf{u}}{\partial t} + \frac{\partial \mathbf{f}(\mathbf{u})}{\partial x} = 0, \quad \mathbf{u}(x,t) \in \mathcal{U}, \quad t > 0, x \in \mathbb{R} \tag{1.1.1}$$

where $\mathcal{U} \subset \mathbb{R}^N$ is an open set, $\mathbf{f} : \mathcal{U} \to \mathbb{R}^N$ is a smooth function representing the flux of the system and $\mathbf{u}$ is the vector of conserved magnitudes. The Cauchy problem prescribes an initial condition $\mathbf{u}(x,0) = \mathbf{u}_0(x)$.

The system (1.1.1) is *strictly hyperbolic* if the Jacobian of the flux admits N distinct real eigenvalues $\lambda_k(\mathbf{u})$ with corresponding right $\mathbf{r}_k(\mathbf{u})$ and left $\mathbf{l}_k(\mathbf{u})$ eigenvectors. The pair $(\lambda_k, \mathbf{r}_k)$ defines the *k-characteristic field* of the system of equations.

The characteristic fields are classified [62] according to the sign of the *nonlinearity factor* η as *linearly degenerated* if

$$\eta \coloneqq \nabla\lambda_k(\mathbf{u}) \cdot \mathbf{r}_k(\mathbf{u}) = 0, \ \ \forall \mathbf{u} \in \mathcal{U}$$

and as *genuinely nonlinear* when

$$\eta \coloneqq \nabla\lambda_k(\mathbf{u}) \cdot \mathbf{r}_k(\mathbf{u}) \neq 0, \ \ \forall \mathbf{u} \in \mathcal{U}. \tag{1.1.2}$$

A field is *non-genuinely nonlinear* if it presents isolated zeros of the nonlinearity factor [62].

The solutions of system (1.1.1) can develop discontinuities in finite time. However, there are functions that satisfy the system (1.1.1) in the sense of distributions. A solution $\mathbf{u}$ is a *weak solution* of (1.1.1) with initial condition $\mathbf{u}_0$ if

$$\int\int (\mathbf{w}_t\mathbf{u} + \mathbf{w}_x\mathbf{f})\mathrm{d}x \ \mathrm{d}t + \int \mathbf{w}(0,x)\mathbf{u}_0(x)\mathrm{d}x = 0$$

holds for every test vector $\mathbf{w}$ with continuous first derivatives that vanishes outside a bounded region [62].

In the context of weak solutions, linearly degenerated fields develop *contact discontinuities*. These are transition waves that unite the dynamics of the other fields. Genuinely nonlinear fields induce elementary waves in the dynamic of the fluid, which are rarefactions and shocks. *Rarefaction waves* are viscid solutions that change smoothly. *Shock waves* are jump discontinuities across which the entropy of the solution increases. Non-genuinely nonlinear fields may result in complex dynamics with *composite waves* formed by more than one elementary wave.

A HSCL induces *convex* dynamics if all characteristic fields are either linearly degenerated or genuinely nonlinear. This is, if all fields maintain the sign of the nonlinearity factor for all states. The notion of convexity is inherited from the scalar case, where the the second derivative of the flux correspond in systems to the gradient of the eigenvalue multiplied by the right eigenvector. The system develops *nonconvex* dynamics if it presents non-genuinely nonlinear fields. This is, if the nonlinearity factor changes sign on any nonlinear field.

The material properties strongly influence the structure and dynamics of waves by means of the EoS [80]. The properties can be studied through thermodynamic quantities: the *sound speed*, the *adiabatic exponent* and the *fundamental derivative*.

The *sound speed* of a fluid is defined as

$$c_s^2 = \left.\frac{\partial P}{\partial \rho}\right|_s \tag{1.1.3}$$

where s stands for entropy, P for the pressure and ρ for the density.

The *adiabatic exponent* is expressed

$$\gamma = -\frac{V}{P}\left.\frac{\partial P}{\partial V}\right|_s = \frac{\rho}{P}\left.\frac{\partial P}{\partial \rho}\right|_s \tag{1.1.4}$$

with $V = 1/\rho$ the specific volume.

The *fundamental derivative* [124] is defined as

$$\mathcal{G} = -\frac{1}{2}V\frac{\left.\frac{\partial^2 P}{\partial V^2}\right|_s}{\left.\frac{\partial P}{\partial V}\right|_s}. \tag{1.1.5}$$

It measures the convexity of isentropic lines through the second derivative of the pressure.

For many materials the fundamental derivative is generally positive and therefore the isentropes (lines of constant entropy) are strictly convex. This render the name of *convex* EoS. If the fundamental derivative changes sign the EoS is *nonconvex*.

In the context of Newtonian hydrodynamics (Euler equations) the nonlinearity factor of the system, η, is proportional to $\mathcal{G}$ [124]. Most studies have been carried out using the ideal gas EoS [64, 129, 116]. The ideal gas EoS is convex ($\mathcal{G}(\mathbf{u}) > 0 \, \forall \mathbf{u}$) and induces convex dynamics in the system ($\eta(\mathbf{u}) \neq 0 \, \forall \mathbf{u}$), leading to expansive rarefactions and compressive shock waves [124]. Nonconvex dynamics in Euler equations ($\eta(\mathbf{u}) = 0$ for some $\mathbf{u}$) is developed when considering nonconvex EoSs ($\mathcal{G}(\mathbf{u}) = 0$ for some $\mathbf{u}$). In this case there are composite waves related to the change of sign of η and expansive shocks and compressive rarefactions in the regions of negative fundamental derivative [14, 39, 125, 106, 111].

In this research we focus on the HSCL representing Special Relativistic Hydrodynamics (SRHD). The system describes the movement of a test particle with a relativistic speed and/or relativistic energy in a background static metric of weak gravitational field. This situation applies to many astrophysical scenarios, such as the morphology and dynamics of astrophysical jets and the modeling of gamma-ray bursts [76]. Special relativistic flows are also involved in nuclear physics, where heavy-ion collision experiments of particle accelerators propel the particle beams to a large fraction of the speed of light [117]. Moreover, SRHD can be used to study the fundamental hydrodynamics phenomena that would take place in General Relativistic hydrodynamics under strong gravitational fields and a dynamic metric.

The system of SRHD has been subject of intensive research by mean of numerical simulations, which allow to confront theoretical models with observations and experimental results [34, 27, 76, 67, 77, 73, 98, 136, 137]. The design and validation of numerical schemes has been traditionally performed using the ideal gas EoS. The knowledge of realistic EoSs describing the thermodynamical properties of high density matter is an open issue in astrophysics [90, 42, 40, 17, 54].

In this thesis we aim to study the complex dynamics of SRHD when considering realistic EoSs. In the first part of the thesis we analyze the exact solution of the SRHD system of equations closed with a nonconvex EoS. In the second part we attempt the modeling of realistic EoSs for high density matter presenting phase transitions.

The first part is organized as follows. In Chapter 2 we present an exact Riemann solver for nonconvex SRHD. The *Riemann problem* [101] is the fundamental test problem in hydrodynamics. It is defined as an initial condition for the system where two constant states are separated by a jump discontinuity. Godunov's method [38], the base of modern high resolution numerical schemes, is based in the solution of Riemann problems. As a consequence, the exact solution of the Riemann problem is a key ingredient in the development of reliable numerical schemes. Besides its use in the construction of the schemes, validation against the exact solution tests the accuracy of the methods.

In Chapter 3 we extend the study to the exact solution of the Riemann problem in nonconvex SRHD with tangential velocities, which can be used to validate multidimensional schemes.

In Chapter 4 we employ the presented exact solutions to analyze the behavior of two well-known and widely used numerical schemes for SRHD in one and two spatial dimensions.

The second part of the thesis is devoted to the modeling of relativistic EoSs containing phase transitions.

The EoS establishes the degree of realism of the physical system. Over the years its

description in a relativistic context has become more complex, adding microphysical effects that shape the thermodynamics. The need of an accurate modeling of the matter has become explicit in many astrophysical scenarios such as stellar evolution [57, 94], treatment of interstellar medium [68, 118] or envelopes of young planets [104, 25]. Besides, the recent detection of gravitational waves (GWs) by the LIGO-Virgo-KAGRA collaboration has pushed the need of obtaining numerical simulations as realistic as possible.

GWs are ripples in spacetime due to the change in the quadrupolar momentum of compact objects [127]. The first direct detection [4], in 2015, was related to the merger of two black holes. Two years later, the GW from the coalescence of two neutron stars (NSs) [5] opened a new window to the study of high density matter. To identify the properties of the source of a GW detected by the laser interferometer, the signal is compared to a waveform catalog built from numerical simulations of different events. As a consequence, an appropriate description of NS matter is fundamental to the study of future detections.

The core of NSs reaches densities above nuclear saturation density. This regime cannot be replicated on Earth and the description of such matter is restricted to theory. The current more realistic EoSs for NS matter are provided in tables. The tabulated EoSs contain sparse values of pressure, density and internal energy of the fluid throughout the star.

These tabulated EoSs require interpolation and numerical derivatives to be used in hydrodynamics. Apart from computationally costly, this way of calculating quantities is not unique. Analytic, simple relations are used to fit the tabulated data and provide computationally efficient EoSs. One of the most used analytic fits is the piecewise polytropic EoS [95]. These fits have allowed the computation of challenging simulations in realistic scenarios (see for example [26, 113]). Still, significant thermodynamics effects that appear in the tables, such as phase transitions of matter, cannot be replicated with a broad purpose model. The aim for simplicity of the analytic models may provoke that relevant features of the tabulated EoSs are not properly captured.

We analyze this phenomenology in the second part of the thesis.

In Chapter 5 we design a strategy to locate phase transitions in tabulated EoSs. In this Chapter we also study the computation of the stellar properties that depend completely on the EoS.

In Chapter 6 we attempt to model phase transitions and present a new class of analytic EoS models which enables nonconvex dynamics.

1.2 Special relativistic hydrodynamics equations

The motion of a relativistic fluid is described by the conservation of rest-mass and energy momentum

$$(\rho u^\mu)_{;\mu} = 0 \tag{1.2.1}$$

$$T^{\mu\nu}_{\ \ ;\nu} = 0 \tag{1.2.2}$$

with Greek indices varying from 0 to 3, latin indices henceforward from 1 to 3 and using natural units where the light speed and the gravitational constant equal to one. Quantity ρ is the rest-mass density, u^μ the 4-velocity of the fluid and the semicolon denotes the covariant derivative. The stress-energy tensor $T^{\mu\nu}$ contains the matter information and its coupling to the background metric. We consider a perfect fluid, thus

$$T^{\mu\nu} = \rho h u^\mu u^\nu + P g^{\mu\nu},$$

with $g^{\mu\nu}$ Minkowski metric with sign convention $\{-,+,+,+\}$. The pressure P relates to the specific enthalpy h through the specific internal energy ε and the rest-mass density as

$$h = 1 + \varepsilon + \frac{P}{\rho}. \tag{1.2.3}$$

The equations (1.2.1)-(1.2.2) with the considerations above, written in conservation form [34] lead to

$$\frac{\partial \mathbf{u}}{\partial t} + \sum_i \frac{\partial \mathbf{F}^i(\mathbf{u})}{\partial x^i} = 0 \tag{1.2.4}$$

where $x^\mu = (t, x, y, z)$, $\mathbf{u}$ is the vector of *conserved quantities* and $\mathbf{F}^i(\mathbf{u})$ their corresponding fluxes. In this system the conserved quantities are the rest-mass, momentum and total energy densities measured in the laboratory frame $\mathbf{u} = (D, S^i, \tau)$. We can express these quantities in terms of the *primitive variables* measured in the local rest frame of the fluid (ρ, υ^i, P) as

$$\begin{aligned} D &= \rho w \\ S^i &= \rho h w^2 \upsilon^i \\ \tau &= \rho h w^2 - P - \rho w. \end{aligned}$$

Here $\upsilon^i = u^i/w$ is the i-component of the velocity of the fluid and w the *Lorentz factor*, $w = (1 - \upsilon^2)^{-1/2}$ with $\upsilon^2 = \delta_{ij}\upsilon^i\upsilon^j$. Then, the fluxes are

$$\mathbf{F}^i(\mathbf{u}) = \left(D\upsilon^i,\, S^i\upsilon^j + P\delta_{ij},\, S^i - D\upsilon^i \right).$$

The system of partial differential equations is closed with an EoS $P = P(\rho, \varepsilon)$. The *relativistic sound speed* is defined dividing the classic definition of the sound speed of the fluid (1.1.3) by the specific enthalpy (1.2.3)

$$c_s^2 = \frac{1}{h} \left.\frac{\partial P}{\partial \rho}\right|_s = \frac{1}{h} \left(\frac{\partial P}{\partial \rho} + \frac{P}{\rho^2} \frac{\partial P}{\partial \varepsilon} \right).$$

The HSCL (1.2.4) is hyperbolic when the EoS is causal ($c_s^2 < 1$) and thermodynamically consistent ($c_s^2 > 0$) [13].

For SRHD, the *nonlinearity factor* is defined by Ibáñez et al. in [53] as

$$\eta = \frac{c_s}{\rho} \left(\mathcal{G} - \frac{3}{2} c_s^2 \right), \tag{1.2.5}$$

being $\mathcal{G}$ the fundamental derivative.

Notice that a nonconvex EoS (an EoS where $\mathcal{G}$ changes sign) implies nonconvex SRHD. Moreover, a convex EoS could lead to nonconvex SRHD due to purely relativistic effects, according to the sign of the term $\mathcal{G} - 3c_s^2/2$.

Part I

Exact Riemann solver for nonconvex Special Relativistic Hydrodynamics

Chapter 2

The exact solution of the Riemann problem in nonconvex SRHD

The Riemann problem [101] is a classic test problem in computational fluid dynamics. Usually considered in one spatial dimension, it allows to study the solution of hyperbolic partial differential equations describing the evolution of a fluid. It is defined as an initial condition for system (1.1.1) consisting in two constant states separated by a jump discontinuity

$$\mathbf{u}(0,x) = \begin{cases} \mathbf{u}_L & \text{if } x < \zeta \\ \mathbf{u}_R & \text{if } x \geq \zeta \end{cases}$$

where $\mathbf{u}_L$ and $\mathbf{u}_R$ are states in the open set $\mathcal{U} \subset \mathbb{R}^N$ separated at an arbitrary point in space ζ.

The Riemann problem is the simplest yet non-trivial initial condition. Its solution contains the fundamental physical and mathematical character of the equations. Furthermore, every other initial condition can be seen as a nonlinear superposition of Riemann problems. Therefore, it is the building block for understanding the dynamics arising in more complex scenarios.

The solution of a Riemann problem is the weak entropy solution of the hyperbolic system. In compressible hydrodynamics, it consists of *rarefactions*, viscid waves where the solution changes smoothly, and *shock waves* that satisfy the Rankine-Hugoniot condition, jump discontinuities across which the entropy increases. The waves arise from the initial discontinuity and move towards the boundaries of the domain. They coincide at a third type of wave, the contact discontinuity, where two new constant states originate. Solving a Riemann problem involves finding the two intermediate states that arise and defining the waves which connect them to the initial states.

At the contact discontinuity, the pressure and velocity of the waves to the left and the right coincide in what is called the *equilibrium state* [60]. As a consequence, the solution of the Riemann problem is studied in a phase space defined as the velocity-pressure plane. In this space a curve unite each initial state to the equilibrium one. These curves are known as *wave curves*, since they are related to waves in the spatial domain. The Riemann problem is solved when the two wave curves are traced and their intersection is found, defining the equilibrium state.

The nonlinear wave structure depends on the convexity of the dynamics induced by the system. When the nonlinearity factor η (1.2.5) has the same sign over all the solution, there is *convex dynamics*. A single *elementary* wave develops for each characteristic field of the system. When $\eta > 0$ shock waves are compressive and rarefaction waves are expansive.

If $\eta < 0$ the nature of the waves is interchanged [124]. As η does not change sign, the behavior of the waves is the same for the whole solution. When the nonlinearity factor changes sign, the system presents *nonconvex dynamics*. Nonlinear fields may develop *composite* waves formed by more than one elementary wave and the nature of shocks and rarefactions can change along the solution.

In convex dynamics, the wave propagation speed is monotone along the wave curves. To solve the Riemann problem, the wave curves are selected depending on the initial states and the equilibrium is found equating velocity and pressure. Martí and Müller in [75] present the exact solution of the Riemann problem in SRHD closed with the ideal gas EoS. In this case the system is convex and the solution consists of two waves, both either shocks or rarefactions, traveling in opposite directions with a contact discontinuity in between.

In nonconvex dynamics the wave propagation speed might not be monotone along the wave curves. As we explain along this Chapter, the change of monotony may terminate the curves. In Newtonian hydrodynamics this phenomena is known to induce composite waves [134, 135, 100, 80]. Their occurrence in general system of conservation laws was studied by Liu [70], who introduced a new type of wave curve which allows the continuation of wave curves in phase space.

The *existence* of the solution of the Riemann problem depends on the asymptotic properties of the EoS modeling the fluid. In general, any EoS motivated by physics has these properties [80] and therefore there exist solutions to a given Riemann problem.

The *uniqueness* of the solution depends on the monotony of the wave curves in phase space. In Newtonian and relativistic hydrodynamics, it is straightforward to prove that the wave curves associated to the rarefaction waves are always monotonic (see [80] for the Newtonian case). However, this is not the case for the curves associated to shock waves.

In [70], Liu establishes main results to determine the uniqueness of the solution of the Riemann problem for general hyperbolic systems of conservation laws. The hypothesis of the theorems have to be proved for every particular problem. He shows an application to Newtonian hydrodynamics with differentially close initial states. The uniqueness of the solution of the Riemann problem for arbitrary initial conditions is an open problem, even in Newtonian hydrodynamics. In this work we assume that the wave curves are monotone and therefore the solution of the problem is unique. This is a common practice in literature [75, 84, 36, 129].

In this Chapter we present the exact solution of the Riemann problem for nonconvex SRHD. We aim to understand the complex phenomena arising in a nonconvex relativistic context and provide a tool to test numerical methods when composite waves are present.

First, we study the wave curves that may appear in phase space in nonconvex SRHD. Then, we analyze the way that the wave structure is built to solve the Riemann problem. We detail the expressions for a particular nonconvex EoS and describe the strategy used for the calculation of the presented curves.

2.1 Wave curves for nonconvex SRHD

The construction of wave curves in nonconvex Newtonian hydrodynamics was studied by Müller and Voss [84]. In this Chapter we delve in nonconvex SRHD following a similar approach, adequating their ideas for the relativistic case. We trail the formulation of the convex scenario in [75].

The three types of wave curves present in nonconvex dynamics are Hugoniot curves,

related to shock waves, integral curves, related to rarefaction waves and mixed curves, a subordinate Hugoniot curve introduced by Liu [70] for nonconvex dynamics.

2.1.1 Hugoniot curves

Hugoniot curves are wave curves in the velocity-pressure plane associated to shock waves. They are calculated using the relativistic Rankine-Hugoniot conditions [121] applied to the hyperbolic system (1.2.1)-(1.2.2) :

$$[\rho u^\mu] n_\mu = 0$$
$$[T^{\mu\nu}] n_\nu = 0,$$

where u_μ is the unit normal to the hypersurface across which there is the jump discontinuity. We have used the notation $[q] = q_a - q_b$ where a and b are the states ahead and behind the discontinuity.

If the shock is moving at velocity v_s along the x-axis then $u_\mu = w_s(-v_s, 1, 0, 0)$, with w_s the corresponding Lorentz factor. Let $\mathbf{f}$ be the fluxes of the SRHD system of equations (1.2.4) and $\mathbf{u}$ the conserved variables. Considering one spatial dimension the conditions can be summarized as

$$[\mathbf{f}] = v_s[\mathbf{u}]. \tag{2.1.1}$$

In order to calculate a Hugoniot curve from an origin state $\mathbf{u}_a$, a relation between the pressure and velocity of the fluid is needed for all states $\mathbf{u}_b$ behind the discontinuity. Given $\mathbf{u}_a = (D_a, S_a, \tau_a)$ with pressure value P_a the origin state of the shock we obtain an expression $v_b = v(P_b)$ for each $\mathbf{u}_b = (D_b, S_b, \tau_b)$ state with pressure P_b behind of the shock, jumping from $\mathbf{u}_a$ by imposing the Rankine-Hungoniot conditions (2.1.1) between both states,

$$D_b v_b - D_a v_a = v_s(D_b - D_a) \tag{2.1.2}$$
$$S_b v_b + P_b - S_a v_a - P_a = v_s(S_b - S_a) \tag{2.1.3}$$
$$S_b - D_b v_b - S_a + D_a v_a = v_s(\tau_b - \tau_a). \tag{2.1.4}$$

From (2.1.2) we obtain the (invariant) mass flux across the shock

$$j = w_s D_a(v_s - v_a) = w_s D_b(v_s - v_b). \tag{2.1.5}$$

In what follows, positive values of j determine waves traveling to the right, and negative values do for those traveling to the left, as in [121, 13, 75]. The shock speed then reads

$$v_s^\pm = \frac{\rho_a^2 w_a^2 v_a \pm j^2\sqrt{1 + (\rho_a/j)^2}}{\rho_a^2 w_a^2 + j^2} \tag{2.1.6}$$

with the same sign criteria.

Rewriting (2.1.2)-(2.1.4) using the mass flux invariant (2.1.5), we obtain

$$v_b - v_a = -\frac{j}{W_s}\left(\frac{1}{D_b} - \frac{1}{D_a}\right) \tag{2.1.7}$$
$$P_b - P_a = \frac{j}{W_s}\left(\frac{S_b}{D_b} - \frac{S_a}{D_a}\right) \tag{2.1.8}$$
$$v_b P_b - v_a P_a = \frac{j}{W_s}\left(\frac{\tau_b}{D_b} - \frac{\tau_a}{D_a}\right). \tag{2.1.9}$$

From relation $S = \upsilon(\tau + P + D)$ and plugging (2.1.7) and (2.1.9) into (2.1.8) we obtain the flow velocity at state b as a function of the pressure P_b and the invariant j [75]

$$\upsilon_b = \left[h_a W_a \upsilon_a + \frac{W_s(P_b - P_a)}{j}\right]\left[h_a W_a + (P_b - P_a)\left(\frac{W_s \upsilon_a}{j} + \frac{1}{\rho_a W_a}\right)\right]^{-1}. \tag{2.1.10}$$

Multiplying the conservation of the stress energy tensor by a unit normal n_μ [75], we get

$$j^2 = \frac{P_a - P_b}{\frac{h_b}{\rho_b} - \frac{h_a}{\rho_a}}, \tag{2.1.11}$$

which relates the pressure with the mass flux, rest-mass density and enthalpy of the fluid.

A relation for the enthalpy between the states ahead and behind the shock can be derived from the Taub adiabat [126]

$$h_b^2 - h_a^2 = \left(\frac{h_b}{\rho_b} + \frac{h_a}{\rho_a}\right)(P_b - P_a)$$

which is a parabola in h_b,

$$h_b^2 + h_b \frac{P_b - P_a}{\rho_b} - \left(h_a^2 + (P_b - P_a)\frac{h_a}{\rho_a}\right) = 0,$$

where the quadratic coefficient is positive. As density and enthalpy are strictly positive, the independent term is always negative: if $P_b > P_a$ then the two terms are positive and so is their sum, to which we change the sign. If $P_b < P_a$ then we can divide by h_a and check that

$$h_a > \frac{P_a - P_b}{\rho_a}, \text{ as } h_a = 1 + \varepsilon_a + \frac{P_a}{\rho_a}$$
$$\Rightarrow 1 + \varepsilon_a > -\frac{P_b}{\rho_a}.$$

Thus the parabola always have two roots and only one of them is positive, therefore with a physical meaning

$$h_b = \frac{\frac{P_b - P_a}{\rho_b} + \sqrt{\frac{(P_b - P_a)^2}{\rho_b^2} + 4\left(h_a^2 + \frac{h_a}{\rho_a}(P_b - P_a)\right)}}{2}. \tag{2.1.12}$$

In order to complete the relations to calculate the flow velocity (2.1.10) as a function of the post-shock pressure P_b, the density behind the shock is also needed. Once ρ_b is derived from the EoS, enthalpy is obtained from (2.1.12) and (2.1.11) can be evaluated. Selecting the sign of j by the direction of the wave then the flow velocity (2.1.10) is defined for every state in the Hugoniot curve.

Termination and continuation of Hugoniot curves

Hugoniot curves are admissible while *Liu entropy condition* is satisfied [70]. The condition states that the shock speed should be monotone along the Hugoniot curve.

Let $H(\mathbf{u}_a)$ be the Hugoniot curve with origin in $\mathbf{u}_a$. Therefore a shock uniting states $(\mathbf{u}_a, \mathbf{u}_b)$ with $\mathbf{u}_b \in H(\mathbf{u}_a)$ and speed $\upsilon_s(\mathbf{u}_a, \mathbf{u}_b)$ is admissible if $\upsilon_s(\mathbf{u}_a, \mathbf{u}_b) < \upsilon_s(\mathbf{u}_a, \mathbf{u})$ for waves going to the left, $\upsilon_s(\mathbf{u}_a, \mathbf{u}_b) > \upsilon_s(\mathbf{u}_a, \mathbf{u})$ for waves going to the right, for any $\mathbf{u} \in H(\mathbf{u}_a)$ between $\mathbf{u}_a$ and $\mathbf{u}_b$.

If the monotony of the shock speed changes then its derivative vanishes in between. Liu also states that $v_s' = 0 \Leftrightarrow v_s = \lambda_k$, with λ_k the characteristic speed of the corresponding characteristic field. The calculation of states of a Hugoniot curve is summarized in Algorithm 2.1.1, including a check for admissibility of every new state. We introduce the value P_* to reference the pressure value that the Hugoniot curve has to continue. This value will be referred to in later Sections.

When Liu condition is violated, the Hugoniot curve terminates to ensure admissibility of the corresponding shock wave. In phase space, the wave curves sequence is continued by an integral curve. The terminated wave is a *sonic shock*.

Algorithm 2.1.1 Calculation of a Hugoniot curve from initial known state a.

while not intersection with opposite wave curve **do**
  $P_b = P_* + \delta P$
  $\rho_b =$ obtain through EoS using P_b
  $h_b = h_b(P_b, \rho_b)$ eq(2.1.12)
  $j^2 = j^2(P_b, h_b, \rho_b)$ eq(2.1.11)
  if wave moving left **then**
    $j = -\sqrt{j^2}$
  else
    $j = \sqrt{j^2}$
  $v_b = v_b(P_b, j)$ eq(2.1.10)
  $v_s = v_s(j^2)$ eq(2.1.6)
  $\lambda_k = eigenvalue_k(\mathbf{u}_b)$
  if $v_s = \lambda_k$ **then**
    break
  $P_* = P_b$

2.1.2 Integral curves

Integral curves are wave curves associated to rarefaction waves, which are smooth and self-similar solutions of the hyperbolic system of conservation laws [64].

The self-similar solution of the form $\mathbf{u}(\xi)$, where $\xi = \frac{x}{t}$, of system (1.1.1) simplifies to a system of ordinary differential equations

$$-\xi \frac{\mathrm{d}\mathbf{u}}{\mathrm{d}\xi} + \mathbf{f}'(\mathbf{u}) \frac{\mathrm{d}\mathbf{u}}{\mathrm{d}\xi} = 0 \tag{2.1.13}$$

where $\mathbf{f}'$ is the Jacobian of the fluxes.

Following Taub's general analysis, we can derive a relation between the velocity and the pressure of the fluid from the equations of self-similar solutions of the SRHD system [122].

We consider system (1.2.4) written in terms of the derivatives with respect to the self-similar variable ξ using $\frac{\partial}{\partial x} = \frac{1}{t}\frac{\partial}{\partial \xi}$ and $\frac{\partial}{\partial t} = -\frac{\xi}{t}\frac{\partial}{\partial \xi}$

$$(v - \xi)\frac{\mathrm{d}\rho}{\mathrm{d}\xi} + \rho(w^2 v(v - \xi) + 1)\frac{\mathrm{d}v}{\mathrm{d}\xi} = 0 \tag{2.1.14}$$

$$v(v - \xi)\frac{\mathrm{d}}{\mathrm{d}\xi}(\rho h w^2) + (v - \xi)\rho h w^2 \frac{\mathrm{d}v}{\mathrm{d}\xi} + \rho h w^2 v \frac{\mathrm{d}v}{\mathrm{d}\xi} + \frac{\mathrm{d}P}{\mathrm{d}\xi} = 0 \tag{2.1.15}$$

$$\xi \frac{\mathrm{d}P}{\mathrm{d}v} + (v - \xi)\frac{\mathrm{d}}{\mathrm{d}\xi}(\rho h w^2) + \rho h w^2 \frac{\mathrm{d}v}{\mathrm{d}\xi} = 0. \tag{2.1.16}$$

Multiplying equation (2.1.16) by the flow velocity v and subtracting the result to equation (2.1.15) we can reduce it to

$$(1-v\xi)\frac{\mathrm{d}P}{\mathrm{d}\xi}+(v-\xi)\rho hw^2\frac{\mathrm{d}v}{\mathrm{d}\xi} = 0. \tag{2.1.17}$$

Following the principle of conservation of entropy along fluid lines and rewriting in terms of the self-similar variable we have that

$$c_s^2=\frac{1}{h}\left.\frac{\mathrm{d}P}{\mathrm{d}\rho}\right|_s=\frac{1}{h}\frac{\mathrm{d}P}{\mathrm{d}\rho} \;\Rightarrow\; \frac{\mathrm{d}P}{\mathrm{d}\xi}=hc_s^2\frac{\mathrm{d}\rho}{\mathrm{d}\xi}. \tag{2.1.18}$$

The system formed by equations (2.1.14), (2.1.17) and (2.1.18) is simplified to

$$(v-\xi)\frac{\mathrm{d}\rho}{\mathrm{d}\xi}+\rho(w^2v(v-\xi)+1)\frac{\mathrm{d}v}{\mathrm{d}\xi} = 0 \tag{2.1.19}$$

$$h(1-v\xi)c_s^2\frac{\mathrm{d}\rho}{\mathrm{d}\xi}+\rho hw^2(v-\xi)\frac{\mathrm{d}v}{\mathrm{d}\xi} = 0 \tag{2.1.20}$$

by substituting (2.1.18) in (2.1.17).

The new system (2.1.19)-(2.1.20) admits the trivial solution $(\mathrm{d}\rho/\mathrm{d}\xi=0,\mathrm{d}v/\mathrm{d}\xi=0)$. Non null solutions are obtained by imposing that the determinant of the matrix of the system vanishes

$$\rho hw^2((v-\xi)^2-c_s^2(1-v\xi)^2)=0,$$

where we have used that $w^2v(v-\xi)+1=w^2(1-v\xi)$. The equation is satisfied when

$$c_s=\pm\frac{v-\xi}{1-v\xi}, \tag{2.1.21}$$

having that the $+$ $(-)$ signs refer to rarefactions propagating to the left (right).

Substituting (2.1.21) in (2.1.20) we have

$$w^2\mathrm{d}v\pm\frac{c_s}{\rho}\mathrm{d}\rho=0.$$

Its primitive is the Riemann invariant

$$J_\pm=\frac{1}{2}\ln\left(\frac{1+v}{1-v}\right)\pm\int\frac{c_s}{\rho}\mathrm{d}\rho,$$

which is constant along integral curves [121]. Given two states a (ahead) and b (behind) of an integral curve, with i a state in between we have the identity

$$\frac{1}{2}\ln\left(\frac{1+v_a}{1-v_a}\right)\pm\int_{\rho_a}^{\rho_i}\frac{c_s}{\rho}\mathrm{d}\rho=\frac{1}{2}\ln\left(\frac{1+v_b}{1-v_b}\right)\pm\int_{\rho_b}^{\rho_i}\frac{c_s}{\rho}\mathrm{d}\rho$$

and then

$$\frac{1}{2}\left(\ln\left(\frac{1+v_a}{1-v_a}\right)-\ln\left(\frac{1+v_b}{1-v_b}\right)\right)=\pm\int_{\rho_b}^{\rho_i}\frac{c_s}{\rho}\mathrm{d}\rho\mp\int_{\rho_a}^{\rho_i}\frac{c_s}{\rho}\mathrm{d}\rho=\mp\int_{\rho_a}^{\rho_b}\frac{c_s}{\rho}\mathrm{d}\rho.$$

Let us denote the last term

$$\mp X_a^b=\mp\int_{\rho_a}^{\rho_b}\frac{c_s}{\rho}\mathrm{d}\rho. \tag{2.1.22}$$

When a state a is known then the flow velocity at a posterior state b is given by

$$\upsilon_b = \frac{\dfrac{1+\upsilon_a}{1-\upsilon_a}e^{\mp 2X_a^b} - 1}{\dfrac{1+\upsilon_a}{1-\upsilon_a}e^{\mp 2X_a^b} + 1}. \tag{2.1.23}$$

Quantity X_a^b (2.1.22) needs to be solved for a specific EoS determining the expression for the sound speed. Once solved, $\upsilon(P_b)$ is defined for every state in the integral curve.

Termination and continuation of integral curves

In order to determine the continuation and termination of integral curves we analyze their existence as self-similar solutions of system (1.1.1). The corresponding system, (2.1.13), can be written in matrix form as

$$(-\xi\mathbf{I} + \mathbf{f}'(\mathbf{u}))\frac{\mathrm{d}\mathbf{u}}{\mathrm{d}\xi} = 0.$$

If $\frac{\mathrm{d}\mathbf{u}}{\mathrm{d}\xi} \neq 0$, the system can be solved by means of the corresponding characteristic equation. Therefore there exists a characteristic field $k \in \{1, \cdots, N\}$ and a scalar factor $a(\xi) \in \mathbb{R}$ such that if $\mathbf{r}_k(\mathbf{u}(\xi))$ is the right eigenvector associated to field k and $\lambda_k(\mathbf{u}(\xi))$ the corresponding eigenvalue, then

$$\frac{\mathrm{d}\mathbf{u}}{\mathrm{d}\xi} = a(\xi)\mathbf{r}_k(\mathbf{u}(\xi)) \quad \text{and} \quad \xi = \lambda_k(\mathbf{u}(\xi)).$$

By calculating the derivative of the latest equation with respect to ξ we obtain

$$1 = a(\xi)\nabla\lambda_k(\mathbf{u}(\xi)) \cdot \mathbf{r}_k(\mathbf{u}(\xi)),$$

which allows to determine $a(\xi) = \frac{1}{\nabla\lambda_k(\mathbf{u}(\xi))\cdot\mathbf{r}_k(\mathbf{u}(\xi))}$ when $\nabla\lambda_k(\mathbf{u}(\xi)) \cdot \mathbf{r}_k(\mathbf{u}(\xi)) \neq 0$. The system becomes

$$\frac{\mathrm{d}\mathbf{u}}{\mathrm{d}\xi} = \frac{\mathbf{r}_k(\mathbf{u}(\xi))}{\nabla\lambda_k(\mathbf{u}(\xi)) \cdot \mathbf{r}_k(\mathbf{u}(\xi))}.$$

Therefore, an integral curve is a smooth solution $\mathbf{u}(\xi; \mathbf{u}_0)$ of the initial value problem

$$\frac{\mathrm{d}\mathbf{u}}{\mathrm{d}\xi} = \frac{\mathbf{r}_k(\mathbf{u}(\xi))}{\nabla\lambda_k(\mathbf{u}(\xi)) \cdot \mathbf{r}_k(\mathbf{u}(\xi))}, \ \mathbf{u}(\xi_0) = \mathbf{u}_0 \tag{2.1.24}$$

with $\nabla\lambda_k(\mathbf{u}_0) \cdot \mathbf{r}_k(\mathbf{u}_0) \neq 0$ and wave speed $\lambda_k(\mathbf{u}(\xi))$.

The term in the denominator is the nonlinearity factor η in equation (1.1.2), which determines the convexity of the system. Notice that (2.1.24) presents a singularity wherever the nonlinearity factor vanishes, $\eta(\mathbf{u}) = 0$. If this happens along an integral curve, it is terminated because is no longer defined.

In Algorithm 2.1.2 we summarize the calculation of states within an integral curve, which should take into account the termination at vanishing η.

In order to continue integral curves in phase space, which last state $\mathbf{u}$ comes from the limit $\eta(\mathbf{u}) \to 0$ over the curve, we use a particular type of a subordinate Hugoniot curve known as mixed curve.

Algorithm 2.1.2 Calculation of an integral curve from initial known state a.

while not intersection with opposite wave curve **do**
  $\rho_b = \rho_a + \delta\rho$
  calculate X_a^b eq(2.1.22) with EoS defining c_s
  $\upsilon_b = \upsilon_b(X_a^b)$ eq(2.1.23)
  if $\eta(\mathbf{u}_b) = 0$ **then**
    break
  $\rho_a = \rho_b$

2.1.3 Mixed curves

A third type of wave curve is introduced by Liu in [70] for nonconvex dynamics. Mixed curves are subordinate Hugoniot curves that continue integral curves when they are no longer defined at $\eta(\mathbf{u}) = 0$.

Following Liu's definition a mixed curve $\alpha^\Diamond$ associated to the integral curve α is the set of states $\mathbf{u}$ where, for any $\mathbf{u} \in \alpha^\Diamond$ there exists $\mathbf{u}^\Diamond \in \alpha$ such that $\mathbf{u}$ is in the Hugoniot curve with origin in $\mathbf{u}^\Diamond$ and with shock speed $\upsilon_s(\mathbf{u}^\Diamond, \mathbf{u}) = \lambda_k(\mathbf{u}^\Diamond)$.

Therefore a mixed curve is composed by the states $\mathbf{u}$ that solve the Rankine-Hugoniot conditions with origin state $\mathbf{u}^\Diamond$ and shock speed $\upsilon_s = \lambda_k(\mathbf{u}^\Diamond) = \lambda^\Diamond$

$$\lambda^\Diamond(\mathbf{u}^\Diamond - \mathbf{u}) = f(\mathbf{u}^\Diamond) - f(\mathbf{u}) \tag{2.1.25}$$

for different, consecutive points of the previous integral curve. The construction starts from the termination point of the integral curve and the states considered advance towards its origin.

Termination and continuation of mixed curves

Mixed curves are formed by states belonging to Hugoniot curves, hence they correspond to shock waves. As integral curves extend in regions where the sign of the convexity is constant, their speed, this is the corresponding eigenvalue, is monotone. Thus the shock speed in a mixed curve is also monotone, ensuring that this type of shocks are always admissible according to Liu entropy condition.

We terminate a mixed curve, however, if the shock speed is equal to the characteristic speed. We may not have the condition $\upsilon_s' = 0$ because of the artificial construction of the curve, although [70] establishes that both are equivalent. In this case, as in the termination of Hugoniot curves, the wave curves sequence in phase space is continued with an integral curve. The corresponding terminated wave is a sonic shock.

Algorithm 2.1.3 Calculation of a mixed curve from known previous integral curve

store integral curve from beginning $\mathbf{u}_0^\Diamond$ to $\mathbf{u}_N^\Diamond$, such that $\eta(\mathbf{u}_N^\Diamond) = 0$
while not intersection with opposite wave curve and $\mathbf{u}^\Diamond \neq \mathbf{u}_0^\Diamond$ **do**
  take next point $\mathbf{u}^\Diamond$ from the end of the integral curve
  solve system (2.1.25) to obtain $\mathbf{u}$
  $\lambda_k = eigenvalue_k(\mathbf{u})$
  if $\lambda_k = \lambda^\Diamond$ **then**
    break

Moreover, a mixed curve can end because of its own construction method. The states of the mixed curve are related to subsequently prior states of an integral curve. Thus if

its beginning is reached, the mixed curve ends. The jump discontinuity associated has to be prolonged through a Hugoniot or a mixed curve, depending of the origin of the wave. We summarize the calculation of states in a mixed curve in Algorithm 2.1.3, attending to both termination conditions.

2.2 Construction of sequence of wave curves

In the evolution of a Riemann problem, the waves are born from the initial discontinuity present in all characteristic fields (linear and nonlinear). The nonlinear waves start from the contact discontinuity and move towards the initial states at the domain boundaries, which are ahead of the waves, in opposite directions. New constant states are created at both sides of the contact discontinuity, where the nonlinear waves coincide in pressure and fluid velocity.

In convex dynamics a *single* wave curve connects every initial state to the equilibrium one, resulting in an elementary wave moving in each direction. In nonconvex dynamics, wave curves may terminate and be continued in phase space. From each initial state there is a *sequence* of wave curves connecting it to the equilibrium state. This can lead to composite waves moving in each direction.

In the following we describe the procedure for determining the sequence of wave curves in the phase space that lead to the solution of the Riemann problem. We start with the first wave curve and detail the criteria to continue each of the successive ones.

2.2.1 First wave

The wave curves are constructed from the initial states and develop through the phase space until their intersection at the intermediate state.

The first wave is determined by its compressible character and the convexity of the system [13]. When the nonlinearity factor is positive, $\eta > 0$, shocks are compressive (pressure increases across them) and rarefactions are expansive (pressure decreases). The nature of the waves is interchanged when $\eta < 0$. The first wave is selected by knowing if the pressure will decrease or increase from the initial state. Depending on the sign of the nonlinearity factor at the boundary state we can declare it a rarefaction or a shock. The selection criteria is gathered in table 2.1 referring to the curves in phase space.

	$P_a > P_b$	$P_a < P_b$
$\eta_a > 0$	Integral curve	Hugoniot curve
$\eta_a < 0$	Hugoniot curve	Integral curve

Table 2.1: Determination of the first wave type for nonconvex SRHD.

The procedure to follow in an arbitrary Riemann problem for which the expected behavior of the pressure is unknown is the following. We take into account that the two wave curves, one from each boundary state, have to intersect. Therefore, progressive states of a wave curve should get closer to the other wave curve. For the first wave, the left (right) wave curve is just the left (right) initial state. From initial left state (v_L, P_L) we set $P_b = P_L + \delta P$ with δP a differential increment of pressure. Then calculate $v_b = v(P_b)$ using the relation of a Hugoniot or an integral curve. Both are valid as their tangent is the same at the initial states [70]. If state (v_b, P_b) is closer to the initial right state (v_R, P_R)

than the left initial state, then the relation $P_b > P_L$ is the appropriate one and using table 2.1 we can declare the first wave curve a Hugoniot or an integral curve. If it is further, then we should have $P_b < P_L$ instead. To decide which wave goes to the right the process is analogous. The increasing or decreasing tendency of the pressure found for the first curve maintains for the rest of the wave curves sequence since it is assumed monotone in phase space.

2.2.2 Continuation of curves and origin state

The first wave curve from each side, either Hugoniot or integral curve, is calculated with origin in the corresponding initial state. It may terminate along its path in the phase space following the termination conditions described in the previous section, which are summarized in table 2.2.

	Termination condition	Next wave
Hugoniot curve ($\mathcal{H}$)	$\upsilon_s = \lambda$	$\mathcal{I}$
Integral curve ($\mathcal{I}$)	$\eta = 0$	$\mathcal{M}$
Mixed curve ($\mathcal{M}$)	$\upsilon_s = \lambda$	$\mathcal{I}$
	Start of $\mathcal{I}$ reached	$\mathcal{H}/\mathcal{M}$

Table 2.2: Termination conditions for the different wave curves and how to continue them.

The sequence of wave curves forms a continuous curve in phase space. Given a state (υ_i, P_i) belonging to a wave curve, it is continued by a new state $(\upsilon_{i+1}, P_{i+1})$, which is obtained following the relations of the type of wave curve it belongs to. For integral curves, P_{i+1} is obtained from $\rho_{i+1} = \rho_i + \delta\rho$ through the EoS. For Hugoniot curves we take $P_{i+1} = P_i + \delta P$.

However, it is necessary to clearly differentiate between the origin of the wave curve and the value that is continuing in phase space. For the integral curves, the latest state calculated, which the curve has to continue, is taken as origin. This is not the general case for Hugoniot and mixed curves.

In Hugoniot curves the origin state a remains fixed throughout the calculation of the curve. The pressure value P_* that is continued in phase space moves with every new calculated state.

When the calculation of a Hugoniot curve starts for the first time then $P_* = P_a$. Once a new state $P_b = P_* + \delta P$ (see Algorithm 2.1.1) is calculated, $P_* = P_b$ updates while P_a remains the same. A Hugoniot curve is terminated when it does not satisfy the entropy condition in order to ensure the admissibility of the corresponding shock wave, but the wave curve is defined beyond this state. If a subsequent wave reaches the speed of the shock where the curve was terminated then this is resumed in a new region of phase space where the entropy condition is again satisfied.

In this case, the origin of the Hugoniot curve is again state a, while the pressure value P_* that it continues is the latest in the wave curves sequence, where the shock speed was reached.

Mixed curves behave similarly, as they are a kind of Hugoniot curves. The first point calculated has P_1 continuing the pressure $P_N^{\diamondsuit}$ of the last state of the previous integral curve (the superscript $\diamondsuit$ here is compliant with notation in Section §2.1.3). For subsequent states, P_i continues from P_{i-1} rather than the pressure of the origin state, $P_{N-i}^{\diamondsuit}$.

In the case of a terminated mixed curve that last jumped from integral curve state $\mathbf{u}_M^{\Diamond}$, let us suppose that the shock speed is reached again at a wave curve state (v_i, P_i). Then the calculation is resumed with origin in the next state backwards of the integral curve, $\mathbf{u}_{M-1}^{\Diamond}$, continuing pressure P_i, not $P_{M-1}^{\Diamond}$.

If there are multiple terminated shocks along a wave curve sequence, the order of continuation can be seen as a stack, where the last broken wave is resumed first and then removed from the stack. This follows the concept presented in [84].

To settle this idea we use an example illustrated in figure 2.1. A Hugoniot curve starts at initial state $\mathbf{u}_0$, which is its origin. Therefore $P_a = P_0$ and the pressure to continue is $P_* = P_a$. The shock speed reaches a maximum and to ensure admissibility we terminate the wave curve. We push the shock speed at state $\mathbf{u}_1$ in the stack. The sequence of wave curves is continued by an integral curve. It terminates when $\eta(\mathbf{u}_2) = 0$ and it is followed by a mixed curve. The speed profiles are symmetric for these two curves because the shock speed during a mixed curve is the characteristic speed during the rarefaction. When the mixed curve reaches state $\mathbf{u}_3$, calculated from the first point of the rarefaction $\mathbf{u}_1$, the wave speed is equal to the shock speed stored in the stack. Therefore, the first Hugoniot curve is continued with origin still in $\mathbf{u}_0$, $P_a = P_0$, but using pressure values continuing $\mathbf{u}_3$, $P_* = P_3$.

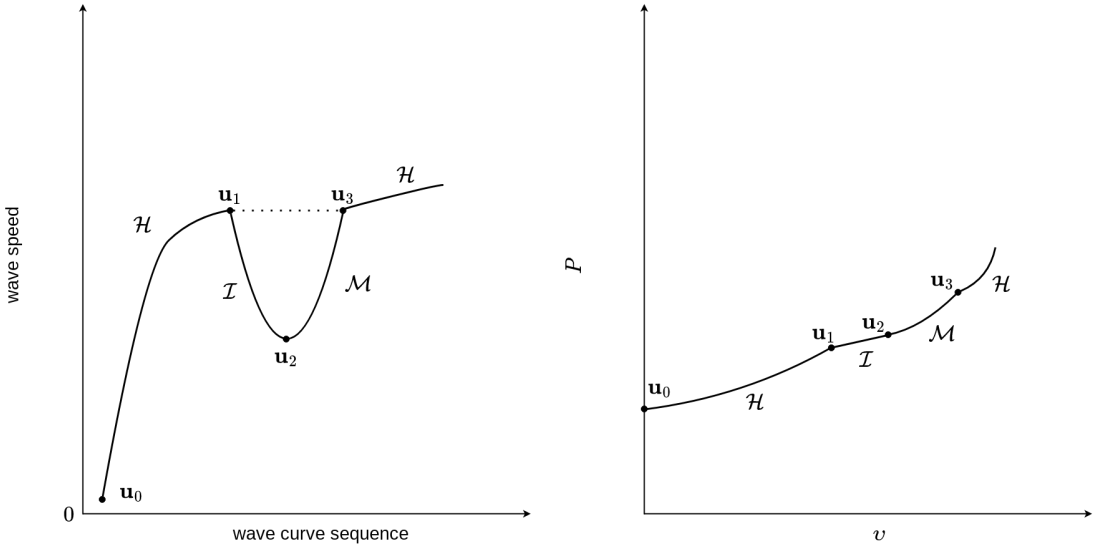

Figure 2.1: Schematic representation of a configuration of wave curves. At the left, behavior of the wave speed along the wave curves. At the right, their appearance in the phase space.

These instructions, an extension of those in the works of [70, 84], allow for the construction of wave curves yielding the solution of a Riemann problem for general systems of hyperbolic conservation laws. With the wave curves drawn in the velocity-pressure plane the equilibrium state can be found and the solution is complete. Once solved, it can be represented in the spatial domain.

2.2.3 From wave curves to waves in the spatial domain

The wave structure originates from the initial discontinuity of the Riemann problem at $x_{init.discont.}$ and therefore time t does not change the intermediate states, only the position

of the waves. Their location is determined by the wave speed v_w as

$$x_w = x_{init.discont.} + t \cdot v_w. \tag{2.2.1}$$

Hugoniot and mixed curves are shock waves, a jump discontinuity from the origin state of the wave curve until its final state, which determines the shock speed. Integral curve states are rarefaction states moving with characteristic speed.

The waves in each wave curves sequence are considered from the one starting at the initial condition until the last calculated, which reaches the equilibrium state. Due to its spatial location by (2.2.1), a wave may be at a position that a posterior wave overtakes. As a result, the criteria for determining whether a wave related to a wave curve is present in the spatial domain is if the wave curve is faster than the subsequent wave curves in the sequence. It is important to note that wave speeds for waves moving to the left are typically negative.

The overtaking of waves is inherent to integral curves that break and are continued with a mixed curve. By definition, the mixed curve has the same wave speed than its associated integral curve but in reverse order, and therefore every calculated state overtakes the origin state from the rarefaction. If all the points in the integral curve are used for calculating the mixed curve, then the rarefaction is completely overtaken and just the jump discontinuity appears in the spatial plane. If the mixed curve is terminated, the related integral curve shows until the last state used for the mixed curve, attached to a jump discontinuity thus appearing as a composite wave in the spatial plane. Due to the overtaking, it is usual to have more wave curves in the phase space that waves in the spatial domain. All wave curves are necessarily part of the wave structure.

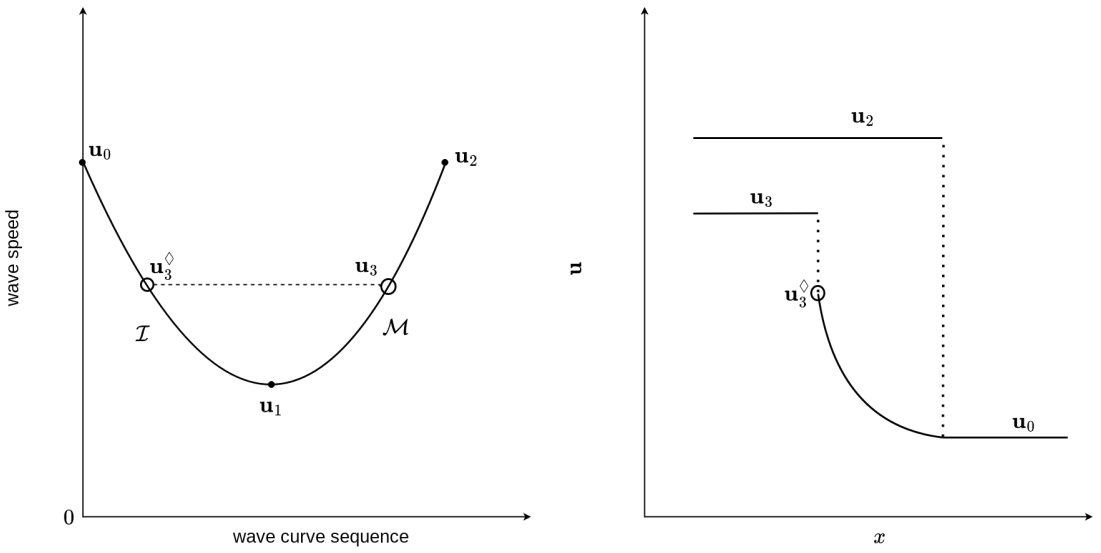

Figure 2.2: Schematic representation of a configuration of wave curves. At the left, behavior of the wave speed along the wave curves. At the right, their corresponding waves in the spatial domain.

We exemplify the overtaking of waves in the spatial domain in figure 2.2. Let $\mathbf{u}_0$ be the initial state of an integral curve which is terminated at $\mathbf{u}_1$ due to $\eta(\mathbf{u}_1) = 0$. Then, a mixed curve continues. Let us consider first the case where the mixed curve is calculated using all states of the integral curve until $\mathbf{u}_2$. As the mixed curve has the same speed

that the integral curve and the mixed curve is posterior in the wave curve sequence, it overtakes the whole integral curve and there is just a jump discontinuity from $\mathbf{u}_0$ to $\mathbf{u}_2$ in the spatial domain. On the other hand, let us consider that we stop calculating the mixed curve at state $\mathbf{u}_3$ if, for instance, it reaches the equilibrium state at this point. Then, the mixed curve is faster than the integral curve states from $\mathbf{u}_1$ to $\mathbf{u}_3^{\diamondsuit}$, but not the previous ones. Therefore, in the spatial domain we can find first the integral curve connecting the initial state $\mathbf{u}_0$ to $\mathbf{u}_3^{\diamondsuit}$, and a jump discontinuity from this origin state until the state $\mathbf{u}_3$ behind the shock.

2.3 Application to a nonconvex EoS

The solution of the Riemann problem requires the use of a specific EoS. In order to exhibit the challenges that may arise based on the specific shape of the EoS, we consider the phenomenological Mie-Grüneisen type EoS [54, 74], referred to as Gaussian Gamma Law ('GGL') EoS. It is defined as

$$P = (\gamma(\rho) - 1)\rho\varepsilon, \tag{2.3.1}$$

with

$$\gamma(\rho) = \gamma_0 + (\gamma_1 - \gamma_0)\mathrm{e}^{-(\rho-\rho_0)^2/\sigma_0^2}. \tag{2.3.2}$$

The parameters γ_0, γ_1 are such that $1 < \gamma_0 < \gamma_1 < 2$. The parameter σ has to be chosen so the EoS is causal and thermodynamically consistent [74] and ρ_0 is a scale factor for the density. This EoS is smooth and can exhibit nonconvex regions depending on the values of the parameters, therefore it is a suitable EoS for nonconvex SRHD.

The thermodynamic quantities needed for constructing the solution are the sound speed

$$c_s^2 = \frac{\varepsilon}{h}\left(\gamma(\rho)(\gamma(\rho) - 1) + \rho\gamma'(\rho)\right) \tag{2.3.3}$$

and the fundamental derivative

$$\mathcal{G} = \frac{1 + \gamma(\rho)}{2} + \frac{\rho}{2}\frac{2\gamma(\rho)\gamma'(\rho) + \rho\gamma''(\rho)}{\gamma(\rho)(\gamma(\rho) - 1) + \rho\gamma'(\rho)}.$$

Notice that along the wave curves the density related to a pressure value is sometimes needed. With the GGL EoS this inverse relation cannot be solved analytically and thus this example also allows to show techniques that may be used in these situations.

2.3.1 Hugoniot curves with GGL EoS

In the description of Hugoniot curves in Section §2.1.1 the EoS is needed to obtain a density ρ_b given a pressure value P_b for a new state. Due to the exponential fashion of the adiabatic index (2.3.2) on the density for the GGL EoS, the variable ρ cannot be isolated and should be obtained numerically.

From (2.3.1) and enthalpy definition $h = 1 + \varepsilon + \frac{P}{\rho}$ we have

$$P = \frac{(\gamma(\rho) - 1)\rho(h(\varepsilon, \rho) - 1)}{\gamma(\rho)}.$$

Considering the post-shock pressure P_b, having a known state a and using (2.1.12) as expression for the enthalpy, we obtain an implicit equation on ρ_b

$$P_b = \frac{(\gamma(\rho_b) - 1)\rho_b(h_b(P_b, \rho_b) - 1)}{\gamma(\rho_b)}. \tag{2.3.4}$$

An approximation of ρ_b can be obtained with the Newton method, considering as initial guess the latest density value in the wave curve. Once ρ_b is calculated, pressure, enthalpy and density are available to evaluate (2.1.11). By selecting the sign of j according to the direction of the wave, we can evaluate the shock speed (2.1.6) and flow velocity (2.1.10).

2.3.2 Integral curves with GGL EoS

Following the procedure to calculate integral curves in Section §2.1.2, the EoS is needed to particularize the expression of the sound speed that determines the integral X_a^b (2.1.22).

Expressing the sound speed (2.3.3) in terms of the density and the internal energy, we have that X_a^b reads

$$X_a^b = \int_{\rho_a}^{\rho_b} \frac{c_s}{\rho} \mathrm{d}\rho = \int_{\rho_a}^{\rho_b} \frac{1}{\rho} \sqrt{\frac{\varepsilon\left(\gamma(\rho)(\gamma(\rho)-1) + \rho\gamma'(\rho)\right)}{1+\varepsilon\rho}} \mathrm{d}\rho. \tag{2.3.5}$$

The internal energy is related to the density through the pressure in the EoS. We explicit their relation using that self similar solutions are isentropic. First law of thermodynamics with constant entropy states

$$\mathrm{d}\varepsilon = \frac{P}{\rho^2}\mathrm{d}\rho,$$

that for GGL EoS reads

$$\mathrm{d}\varepsilon = \frac{\gamma(\rho)-1}{\rho}\mathrm{d}\rho.$$

If we consider a known state a of the integral curve that is followed by a state b, we get

$$\varepsilon_b = \varepsilon_a \left(\frac{\rho_b}{\rho_a}\right)^{\gamma_0 - 1} e^{(\gamma_1 - \gamma_0)Y} \tag{2.3.6}$$

where Y is an integral that comes from the exponential term of the adiabatic index,

$$Y = \int_{\rho_a}^{\rho_b} \frac{e^{\frac{-(\rho-\rho_0)^2}{\sigma_0^2}}}{\rho} \mathrm{d}\rho. \tag{2.3.7}$$

The relation between density and internal energy is not analytic for this EoS due to the exponential term in the adiabatic index. Therefore, (2.3.5) does not count with a primitive expression and needs a numerical resolution for every new state in the integral curve. A process suggested for the integration of (2.3.5) is summarized in Algorithm 2.3.1.

Algorithm 2.3.1 Calculation of (2.1.22) for the GGL EoS from a known state a.

1: $\rho_b = \rho_a + \delta\rho$
2: select $\{\rho_j\}_{j=1}^{j=N}, \rho_a < \rho_1 < .. < \rho_N = \rho_b$
3: calculate $\{Y_j\}_{j=1}^{j=N}$ eq(2.3.7) from ρ_a to ρ_j
4: calculate $\{\varepsilon_j\}_{j=1}^{j=N}$ eq(2.3.6) using Y_j, ρ_j
5: calculate X_a^b eq(2.3.5) numerically using intermediate values $\{\rho_j\}_{j=1}^{j=N}, \{\varepsilon_j\}_{j=1}^{j=N}$

2.3.3 Mixed curves with GGL EoS

When calculating mixed curves defined in Section §2.1.3 the EoS is needed at applying the Rankine-Hugoniot conditions, as the pressure and the specific enthalpy appear in the equations. Expanding the system (2.1.25) in terms of the primitive variables we obtain

$$\upsilon\rho w - D^\Diamond \upsilon^\Diamond - \lambda(\rho w - D^\Diamond) = 0 \tag{2.3.8}$$

$$w^2\upsilon^2\rho(1+\varepsilon\gamma) + (\gamma-1)\rho\varepsilon - S^\Diamond\upsilon^\Diamond - P^\Diamond - \lambda(\rho\upsilon w^2(1+\varepsilon\gamma) - S^\Diamond) = 0 \tag{2.3.9}$$

$$w^2\upsilon\rho(1+\varepsilon\gamma) - w\upsilon\rho - S^\Diamond + D^\Diamond\upsilon^\Diamond - \lambda(\rho(1+\varepsilon\gamma)w^2 - (\gamma-1)\rho\varepsilon - \rho w - \tau^\Diamond) = 0 \tag{2.3.10}$$

where the superscript $\Diamond$ indicates that the quantity belongs to an integral curve. We have written $\lambda_k(\mathbf{u}^\Diamond) = \lambda$, $\gamma(\rho) = \gamma$ for readability. The unknowns of this system are the density, the internal energy and the velocity, $(\rho, \varepsilon, \upsilon)$. Recall that $\mathbf{u}^\Diamond$, integral curve state, is a trivial solution of the system.

From (2.3.8) we obtain a conservation equation

$$\rho w(\upsilon - \lambda) = D^\Diamond(\upsilon^\Diamond - \lambda). \tag{2.3.11}$$

Substituting this in (2.3.9) and (2.3.10) we respectively obtain

$$(\gamma-1)\rho\varepsilon + w(1+\gamma\varepsilon)\upsilon D^\Diamond(\upsilon^\Diamond - \lambda) = S^\Diamond(\upsilon^\Diamond - \lambda) + P^\Diamond \tag{2.3.12}$$

$$\lambda(\gamma-1)\rho\varepsilon + D^\Diamond(\upsilon^\Diamond - \lambda)(w(1+\gamma\varepsilon) - 1) = S^\Diamond - D^\Diamond\upsilon^\Diamond - \lambda\tau^\Diamond. \tag{2.3.13}$$

Some terms cancel out by subtracting λ(2.3.12) from (2.3.13)

$$w(1+\gamma\varepsilon)(1-\lambda\upsilon) = w^\Diamond h^\Diamond(1-\lambda\upsilon^\Diamond) \tag{2.3.14}$$

and υ(2.3.13) from (2.3.12)

$$\rho\varepsilon(\gamma-1)(1-\lambda\upsilon) = P^\Diamond(1-\lambda\upsilon) + D^\Diamond w^\Diamond h^\Diamond(\upsilon^\Diamond - \lambda)(\upsilon^\Diamond - \upsilon), \tag{2.3.15}$$

where we have made simplifications using the definition of the conserved variables. Now the system is formed by equations (2.3.11), (2.3.14) and (2.3.15).

From (2.3.11) we can obtain the velocity as a function of the density only

$$\upsilon(\rho) = \frac{\lambda + \frac{D^\Diamond(\upsilon^\Diamond-\lambda)}{\rho}\sqrt{1-\lambda^2 + \left(\frac{D^\Diamond(\upsilon^\Diamond-\lambda)}{\rho}\right)^2}}{1 + \left(\frac{D^\Diamond(\upsilon^\Diamond-\lambda)}{\rho}\right)^2}, \tag{2.3.16}$$

where the sign of the root has been selected with the criteria that $\upsilon(\rho^\Diamond) = \upsilon^\Diamond$ must hold. The two other equations are linear in the internal energy. We can rewrite them as

$$\varepsilon = \left(\frac{w^\Diamond h^\Diamond(1-\lambda\upsilon^\Diamond)}{w(1-\lambda\upsilon)} - 1\right)\frac{1}{\gamma} \tag{2.3.17}$$

$$\varepsilon = \frac{P^\Diamond(1-\lambda\upsilon) + D^\Diamond w^\Diamond h^\Diamond(\upsilon^\Diamond - \lambda)(\upsilon^\Diamond - \upsilon)}{\rho(\gamma-1)(1-\lambda\upsilon)}. \tag{2.3.18}$$

Equating expressions (2.3.17), (2.3.18) and using the equation (2.3.16) for the fluid velocity, we obtain an implicit equation in ρ whose zeros are density solutions of the system

$$g(\rho) = w(1-\lambda v)(\gamma P^{\diamondsuit} + (\gamma-1)\rho) + h^{\diamondsuit} w^{\diamondsuit} \left(\gamma w D^{\diamondsuit}(v^{\diamondsuit}-\lambda)(v^{\diamondsuit}-v) - (\gamma-1)\rho(1-\lambda v^{\diamondsuit})\right). \tag{2.3.19}$$

The equation $g(\rho)$ (2.3.19) has to be solved numerically and the Newton method is a viable option. However, as the density in the rarefaction $\rho^{\diamondsuit}$ is always a solution, it is necessary to fine-tune the initial guess in order to converge to a different root. Liu states in [70] that the correct value for the density that belongs to the mixed curve is the root that is closest to, yet different from, $\rho^{\diamondsuit}$. We have observed that when a mixed curve develops into a sonic shock, as we get closer to the final state of the curve several roots of the equation become increasingly close to each other. This invokes the need of high numerical accuracy in the resolution process and a criterion for distinguishing the appropriate root for convergence.

Once the density is known we can evaluate the internal energy through (2.3.17) or (2.3.18) and the velocity with (2.3.16).

2.4 A practical methodology to calculate wave curves

We have defined the three types of wave curves arising in nonconvex SRHD and specified the equations associated with these curves that depend on the EoS for the GGL model. In what follows we provide a comprehensive overview of our calculation strategy and the challenges encountered during the resolution process.

Recall that when a shock is terminated to ensure admissibility we store its wave speed and origin state in a stack. If the speed is reached again during a posterior wave curve, we say the curve has been *reached by stack* and it has to be terminated to continue the stacked wave. The curve that is continued is pushed out of the stack. This kind of structure ensures that the latest wave that was terminated is the first one that can be continued.

2.4.1 Practical calculation of a Hugoniot curve

To calculate a Hugoniot curve one should define first the origin state a, which is the start of the jump discontinuity. Following Algorithm 2.1.1 we also define the pressure value P_* that the curve has to continue in phase space. For calculating a new state in the curve we move the pressure value $P_b = P_* + \delta P$ and apply the Rankine-Hugoniot conditions to solve the rest of the quantities. In particular we use $\delta P = 0.0005$[1] to progress slowly along the curve. Once the pressure of the new state is defined, we find the related density through Newton iterations of equation (2.3.4). We use a tolerance of 10^{-12} for convergence. For the initial guess of the Newton method we use the density of the previous state in the sequence of wave curves.

Once the shock speed and the fluid velocity are calculated from the pressure and density values we check for termination conditions. First we need to check if the curve has been reached by stack and thus it should be terminated to continue a previous wave curve. We do this by monitoring the sign of the difference between the shock speed and the speed in the stack through iterations. If it changes sign, then the Hugoniot curve was reached by the wave in the stack.

[1] All tolerances and increments provided in this section are defined to work with an EoS that takes density values of $\mathcal{O}(1)$.

If the Hugoniot curve was not reached by stack while getting to this new state, we check if it violated the entropy condition. That would happen if there is a zero of the derivative of the shock speed from the previous state to the new one. In this case we look for changes of sign of the difference between the new shock speed and the previous one: $(v_s^{i)} - v_s^{i-1)}) \cdot (v_s^{i-1)} - v_s^{i-2)}) < 0$. If there is a change of sign, the curve terminates.

In both cases above, if a change of sign is detected we restore the previous state calculated and decrease δP by half. In this way we can get to the state where the Hugoniot curve ends more accurately. We consider we have the final state when we reach it using $\delta P < 10^{-12}$.

2.4.2 Practical calculation of an integral curve

In an integral curve the origin state a in the calculation of a new state b is always the latest calculated state. Following Algorithm 2.1.2 we set the new state density $\rho_b = \rho_a + \delta\rho$, where we use $\delta\rho = 0.0005$. To obtain a good accuracy in the calculation of integral curves with the GGL EoS it is important to select a small increment of the density, since the next step is to solve equation (2.3.5) numerically and the error increases with the distance between the integration limits.

We choose Simpson 3/8 rule to calculate integral (2.3.5). Denoting by $r(\rho, \varepsilon)$ the integrand and using $a = \rho_a$ and $b = \rho_b$ for readability, then the formula for the integral is

$$X_a^b \approx \frac{b-a}{8}\left(r(a,\varepsilon_a) + 3r\left(c = \frac{2a+b}{3}, \varepsilon_c\right) + 3r\left(d = \frac{a+2b}{3}, \varepsilon_d\right) + r(b,\varepsilon_b)\right).$$

Therefore, for this integration, we also need to calculate ε_b, ε_c and ε_d from (2.3.6). First we need to solve (2.3.7) from state a to b, c and d respectively. As the limit states are closer because they are subdivisions of the original interval of integration, we use the simpler Simpson 1/3 rule

$$Y_a^x \approx \frac{x-a}{6}\left(q(a) + 4q\left(\frac{a+x}{2}\right) + q(x)\right)$$

for $x \in \{b, c, d\}$ and being $q(x)$ the integrand of (2.3.7).

Using ρ_b and ε_b we can evaluate the nonlinearity factor η (1.2.5) at the new state. If $\eta_a \cdot \eta_b < 0$ then there is a zero of the nonlinearity factor between both states, marking the termination of the wave curve. Despite the fact that an integral curve is not defined at the zero of the nonlinearity factor, it can be calculated at both sides of it. Once we delimit where the zero takes place, we look for the termination state with a bisection method on the nonlinearity factor imposing a tolerance of 10^{-12}.

If $\eta_a \cdot \eta_b > 0$ the integral curve can continue. We calculate the fluid speed using X_a^b and the pressure from the EoS.

2.4.3 Practical calculation of a mixed curve

The states of a mixed curve solve the Rankine-Hugoniot conditions with origin in a state of a previous integral curve, which is known when calculating the mixed curve. Therefore we can store states along it to use in the calculations. In particular we use 1000 points equidistant in density.

Following Algorithm 2.1.3 we select the first point from the last of the integral curve that has not been used before as origin state for the mixed curve. Given this state we

can solve equation $g(\rho) = 0$, (2.3.19), to obtain the density of the state belonging to the mixed curve. The rest of quantities follow from analytic relations.

Equation $g(\rho)$ can be solved with the Newton method, which we use with a tolerance of 10^{-12}. However the selection of the initial guess can be challenging. The density value in the integral curve, $\rho^{\diamondsuit}$, is always a trivial solution of the equation but not the one belonging to the mixed curve. Therefore, the initial guess has to avoid the convergence basin of $\rho^{\diamondsuit}$.

When the equation has more than two solutions, Liu [70] specifies that the density value belonging to the mixed state is the closer one to $\rho^{\diamondsuit}$. Therefore we need to converge to that solution and identify the case if we have not.

In our study we have found that, in general, $g(\rho)$ takes the schematic shapes in figure 2.3 depending on the origin integral curve state. Therefore, as initial guess we take a perturbation of $\rho^{\diamondsuit}$ and increase the perturbation in case of convergence to the trivial solution.

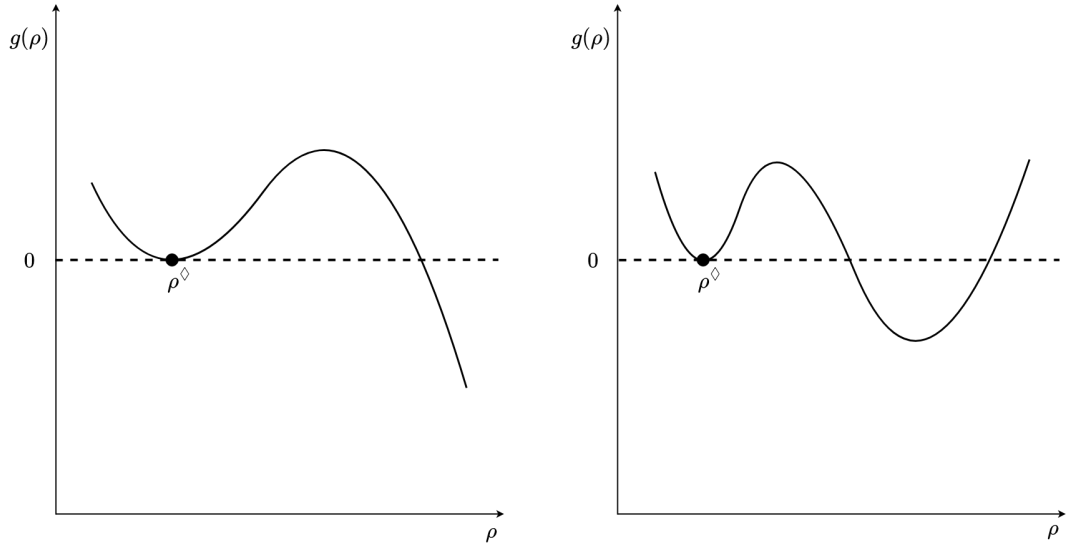

Figure 2.3: Schematic representation of the shape of function $g(\rho)$ (2.3.19).

However, if the mixed curve becomes a sonic shock, the shape of equation $g(\rho)$ changes resembling those in figure 2.4 some states before the final one. Two roots grow increasingly closer and the root-finder may jump to the second root. We identify the roots by the sign of the derivative of $g(\rho)$ in them. Therefore if we find the further one, we take it as initial point to start a bisection method moving towards $\rho^{\diamondsuit}$ and locate the root described by Liu. As we approach the final state of the mixed curve, the roots are closer and the local extreme between them takes a value that goes to zero.

Beyond the integral curve state that serves as origin to the final state of the mixed curve, the only solution of $g(\rho)$ is the trivial one. In this case, where we cannot find a different solution, we calculate new integral curve states between this latest state and the previous one that gave a non trivial solution. In this way we can refine the location of the last state of the sonic mixed curve. We locate the termination state with an accuracy of $|\lambda - \lambda^{\diamondsuit}| < 10^{-5}$ at least.

During the calculation of the mixed curve we also check if the curve has been reached by stack in a similar fashion as we do in the Hugoniot curves.

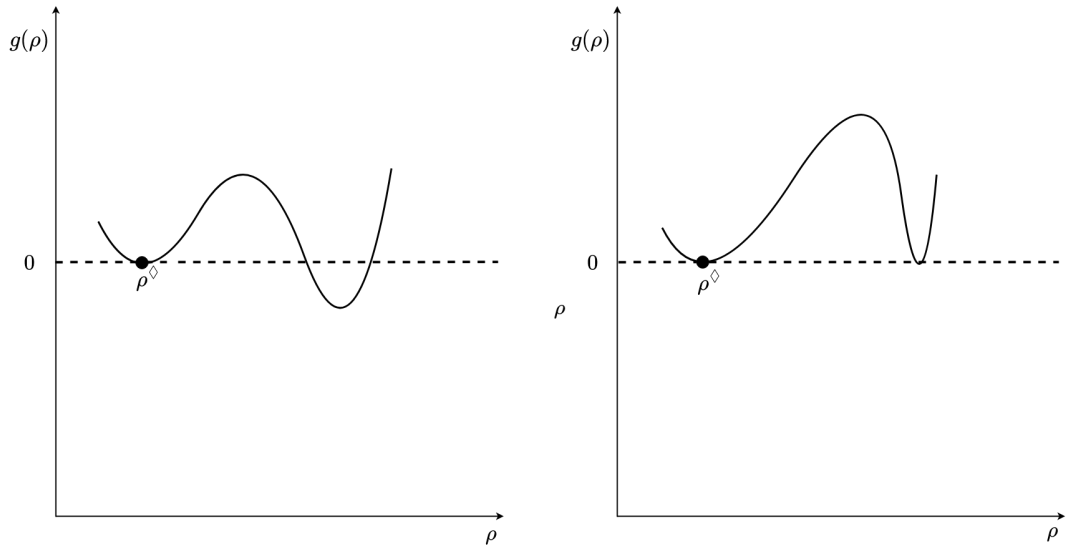

Figure 2.4: Schematic representation of the shape of function $g(\rho)$ (2.3.19) when the mixed curve is close to its final state as sonic shock.

2.4.4 Intersection of wave curves

In convex dynamics, the type of wave reaching the equilibrium state from each side can be determined from the initial states since it depends only on the behavior of the pressure. Therefore, to calculate the intersection, one needs to solve the equation that arises from making the fluid velocity of the two coincident curves equal [75].

In nonconvex dynamics, however, the two initial wave curves may terminate and be continued by a sequence of other wave curves, making it impossible to know a priori which type of wave curve will reach the equilibrium state from each side. In this case, the two sequences have to be calculated and checked for intersection as they progress in phase space.

One method for determining a potential interval of intersection is by tracking the difference in pressure $\Delta P_i = P_i^L - P_i^R$ and velocity $\Delta v_i = v_i^L - v_i^R$ along the curves. If the curves intersect, these differences will change sign with respect to their values at the initial condition. These differences are calculated at the termination point of each wave curve. If a wave curve is not broken by its termination condition, limits in the pressure and density are applied for the calculations. These limits are extended if the intersection does not occur.

Given a possible intersection interval $[a, b]$ (in fluid velocity if $P_L = P_R$, in pressure if $v_L = v_R$, either of them if the initial conditions are different in P and v), the equilibrium state is located using inverse parabolic interpolation. The process is outlined in Algorithm 2.4.1. The method involves defining a set of fixed, equally spaced abscissas $\{x_i\}_{i=0}^N$ and taking as their ordinate values the difference between the value of the two curves at each abscissa $\{\Delta y = y_L(x_i) - y_R(x_i)\}_{i=0}^N$. A change of sign in two consecutive Δy points indicates the presence of an intersection of the curves. A parabola is then used to interpolate the abscissa value at which the intersection occurs. The interpolation is called inverse as Δy is used as the abscissas and x as the ordinates. Evaluating at zero yields the original abscissa value where the curves coincide.

To evaluate the wave curves at a set of fixed abscissas, they are first calculated at con-

Algorithm 2.4.1 Finding the intersection between wave curve branches

Locate interval $[a, b]$ where curves may intersect
Subdivide interval and define equiespaced $\{x_i\}_{i=0}^{i=N}, x_0 = a, x_N = b$
Calculate corresponding left wave curve in the interval and get points in phase space (α_j^L, β_j^L)
Interpolate left wave curve $y^L = parabola(x = \alpha^L, y = \beta^L, eval = x)$
Calculate corresponding right wave curve in the interval and get points in phase space (α_j^R, β_j^R)
Interpolate right wave curve $y^R = parabola(x = \alpha^R, y = \beta^R, eval = x)$
Consider $\{(x_i, \Delta y_i = y_i^L - y_i^R)\}_{i=0}^{i=N}$
if Δy changes sign between index i and $i + 1$ **then**
    $x_{eq} = parabola(x = \Delta y, y = x, eval = 0)$
    return x_{eq}
if Δy keeps sign $\forall i$ **then**
    break, no intersection

venient values. Then, for every fixed abscissa, we perform a local parabolic reconstruction of the wave curve.

2.5 Examples

We calculate the exact solution of four Riemann problems proposed in [74], where the authors explore numerically the wave dynamics arising from the GGL EoS. They use two set of parameters gathered in table 2.3, yielding EoSs with different nonconvex regions. We label them GGL1 and GGL2, as they will be referred to henceforward. These values ensure that the EoSs are causal and thermodynamically consistent. Therefore, they represent physically valid fluids and the hydrodynamic system of equations is hyperbolic [13].

Model	γ_0	γ_1	ρ_0	σ_0
GGL1	4/3	5/3	1	0.6
GGL2	4/3	1.9	1	1.1

Table 2.3: GGL EoS parameters.

The Riemann problems proposed, see table 2.4, include strong blast wave problems and highly relativistic gas slabs [85].

	ρ_L	v_L	P_L	ρ_R	v_R	P_R
Blast Wave 1 GGL1 (`BW1-GGL1`)	1	0	1000	0.125	0	0.01
Blast Wave 2 GGL2 (`BW2-GGL2`)	5	0	1000	0.125	0	0.01
Expanding Slabs GGL1 (`ES-GGL1`)	1.8	-0.8	20	1.8	0.8	20
Colliding Slabs GGL2 (`CS-GGL2`)	0.05	0.999	0.05	0.05	-0.999	0.05

Table 2.4: Riemann problems solved using GGL1 and GGL2 EoSs, proposed in [74].

We consider the spatial domain $x \in [0, 1]$ with initial discontinuity located at $x = 0.5$. For each problem we present the wave curves obtained and detail their termination values for reference. The evolution of the wave speed along the different curves is shown to determine which waves appear in the spatial domain, where we draw the solution profiles for density, pressure, and velocity at $t = 0.4$.

2.5.1 Blast wave 1 GGL1

This blast wave problem features a jump of pressure of five order of magnitude in the initial conditions. According to the behavior of this type of Riemann problems, the arising waves should make the higher pressure decrease and the lower one increase. The first wave is therefore known for this scenario, but we exemplify the calculations to do for an unknown case. Following Section §2.2.1 we increase slightly the pressure from the initial conditions to get new points in phase space. For the new state $P_b = P_I + \delta P$ being $I \in \{L, R\}$, we take $\delta P = 0.0005$. We could calculate the corresponding velocity using an integral or a Hugoniot curve. We choose the latest as we can impose a final pressure easily. To know if the curves grow closer in phase space we use the Euclidean distance.

In this Riemann problem, from the initial left condition ($\upsilon = 0, P = 1000$) we get the state $(-2.449 \cdot 10^{-7}, 1000.0005)$. As it is further from the initial right condition $(0, 0.01)$, the pressure of the waves to the left must decrease. On the right side, the resulting state is $(0.0102, 0.0105)$, which is closer to the initial left state and, therefore, the wave to the right increase the pressure.

We evaluate the nonlinearity factor (1.2.5) at the initial conditions and obtain $\eta(\mathbf{u}_L) < 0$ and $\eta(\mathbf{u}_R) > 0$. According to the results obtained, following table 2.1 we have that a Hugoniot curve starts to the left as an expansive shock and another Hugoniot curve starts to the right as a compressive shock.

The process to dictaminate the first waves for the other Riemann problem examples is analogous. We indicate the behavior of the pressure and the sign of the nonlinearity factor.

Wave curves obtained

The wave curves calculated in phase space are shown in figure 2.5. We present separately the wave curves moving to the left and the right and an additional plot with the two sequences together focusing on the intersection. In the legend we denote for L (left) and R (right) the direction of the movement of the curve followed by the type of wave curve it represents (H for Hugoniot, I for integral and M for mixed curves).

	Origin state			Termination state			
w. curves	υ	P	ρ	υ	P	ρ	υ_ω
$\mathcal{H}$	0	1000	1.000	0.2085	627.5	0.7834	-0.8393
$\mathcal{I}$	0.2085	627.5	0.7834	0.9794	4.922	0.0378	0.9196

Table 2.5: Origin and termination states of the wave curves moving to the left in `BW1-GGL1`.

We gather the details about the origin and termination state of the left wave curves sequence in table 2.5, where the wave speed is denoted as υ_ω. The sequence starts with a Hugoniot curve with origin in the initial state. It is terminated as a sonic shock, located when $|\upsilon_s^{i)} - \upsilon_s^{i-1)}| \approx 5.13 \cdot 10^{-14}$ and, therefore, its speed is pushed to the stack. An

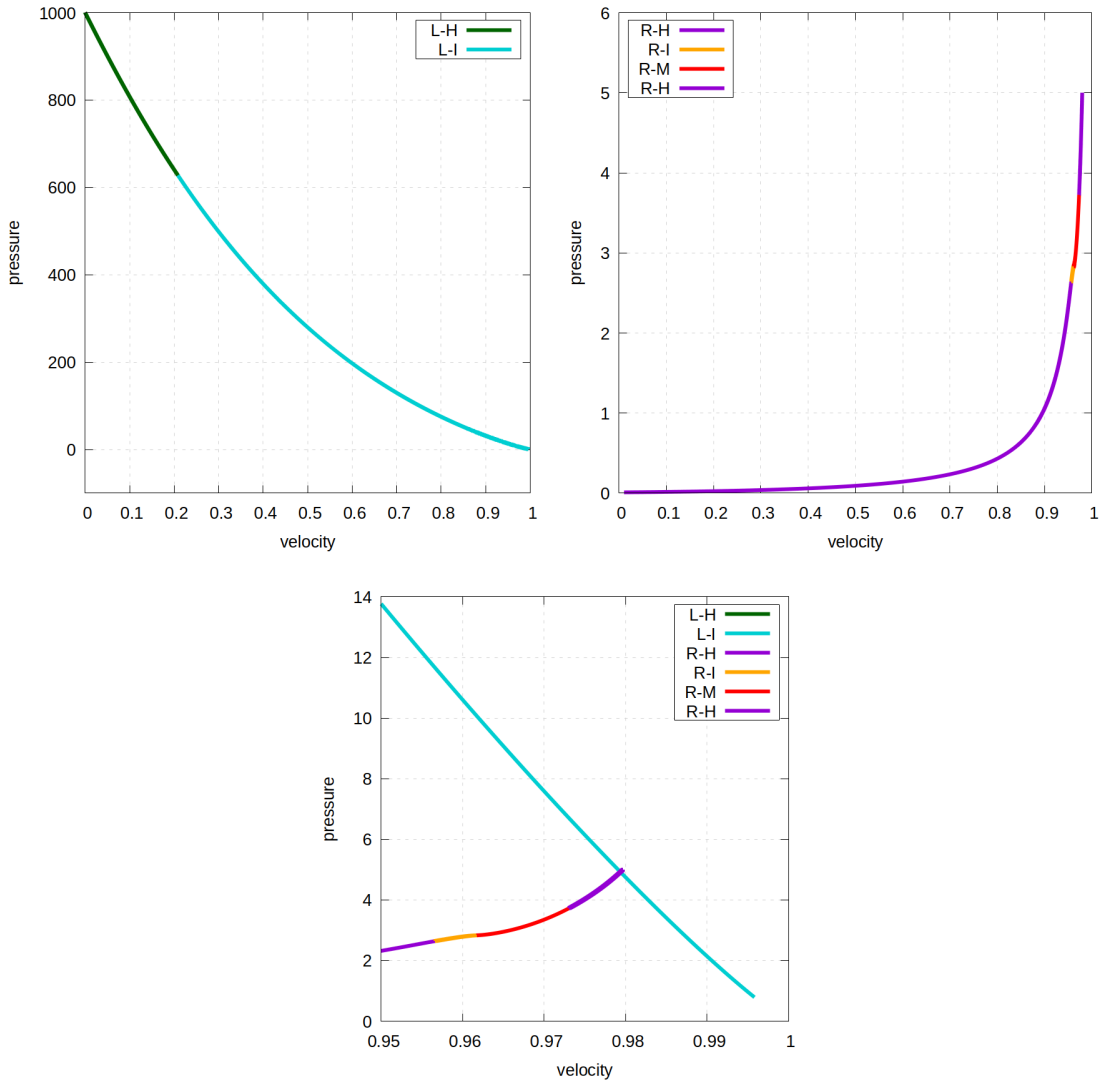

Figure 2.5: Wave curves for `BW1-GGL1` in phase space. Left picture depicts the sequence of wave curves moving to the left. Right picture shows the sequence of wave curves moving to right. Bottom picture displays the intersection of the wave curves, determining the equilibrium state.

integral curve continues. There are no more changes of convexity along the curve ($\eta \neq 0$) and the wave speed never reaches the speed in the stack. Thus, the integral curve is not terminated. This is a case where we make use of a limit in density to stop the calculations.

The details of origin and termination of the right wave curves sequence are displayed in table 2.6. It starts with a Hugoniot curve that becomes sonic. We locate the final state when $|v_s^{i)} - v_s^{i-1)}| \approx 3.23 \cdot 10^{-14}$ and push the shock speed to the stack. The wave curves sequence is continued by an integral curve that terminates at $\eta \approx 9.58 \cdot 10^{-13}$ and a mixed curve follows. This curve uses all the rarefaction states for the calculation and in the last one it reaches the shock speed of the first terminated Hugoniot curve. The first Hugoniot curve resumes and continues the sequence. It does not cross any other change of convexity hence we also make use of the practical limit in pressure to stop the calculations. In table

2.6 we label $\mathcal{H}_1$ the two Hugoniot curves appearing because they are the same curve.

	Origin state			Termination state			
w. curves	v	P	ρ	v	P	ρ	v_ω
$\mathcal{H}_1$	0	0.0100	0.1250	0.9566	2.642	1.272	0.9848
$\mathcal{I}$	0.9566	2.642	1.272	0.9617	2.833	1.613	0.9669
$\mathcal{M}$	-	-	-	0.9731	3.727	2.416	0.9848
$\mathcal{H}_1$	0	0.0100	0.1250	0.9794	4.922	2.733	0.9885

Table 2.6: Origin and termination states of the wave curves moving to the right in `BW1-GGL1`.

The equilibrium state is found as the intersection of the integral curve to the left and the resumed Hugoniot curve to the right. The fluid velocity is $v = 0.9794$ where both curves give a pressure of $P = 4.922$, with an error of $3.82 \cdot 10^{-10}$. We can observe the jump in density at the final state of the two curves.

Translation to spatial domain

Once the wave curves and their point of intersection have been calculated, we can identify the waves present in the spatial domain. In figure 2.6 we show the evolution of the wave speeds along the curves, although the wave speeds listed in tables 2.5, 2.6 are enough to deduce the waves appearing in the spatial domain.

The wave curves to the left begin with a Hugoniot curve. The speed of the associated shock is the wave speed at the final state. As there is no posterior faster wave to the left (notice that speeds moving to the left are negative), there will be a shock wave uniting the initial condition to the final state of the wave curve. The next curve, an integral curve, displays states with negative and positive velocities, indicating a rarefaction wave with a head moving to the left and a tail moving to the right. It unites the end of the shock wave with the new constant equilibrium state.

In the wave curves to the right, the fastest wave is the Hugoniot curve resumed after the mixed curve. This means that only a shock wave is observed connecting the initial state to the equilibrium state.

The exact solution can be drawn at any time of the evolution knowing the type of waves that appear, their boundaries and wave speeds, and the new constant states that emerge on both sides of the contact discontinuity. We plot density, pressure and velocity in figure 2.7. We use points to represent the key states calculated for the jumps discontinuities. We also use points in the rarefactions to highlight their curvature. All points are connected with lines for readability.

In the spatial domain, see figure 2.7, a composite wave displays moving to the left formed by a shock wave and a rarefaction fan. A single shock wave moves to the right. We remark that although we observe a single wave to the right, it is due to four wave curves in phase space.

Perturbation analysis of the initial condition

For this particular Riemann problem we show that in nonconvex dynamics, little perturbations of the initial conditions can lead to quite different wave structure in the spatial domain, although the sequence of wave curves in phase space is similar.

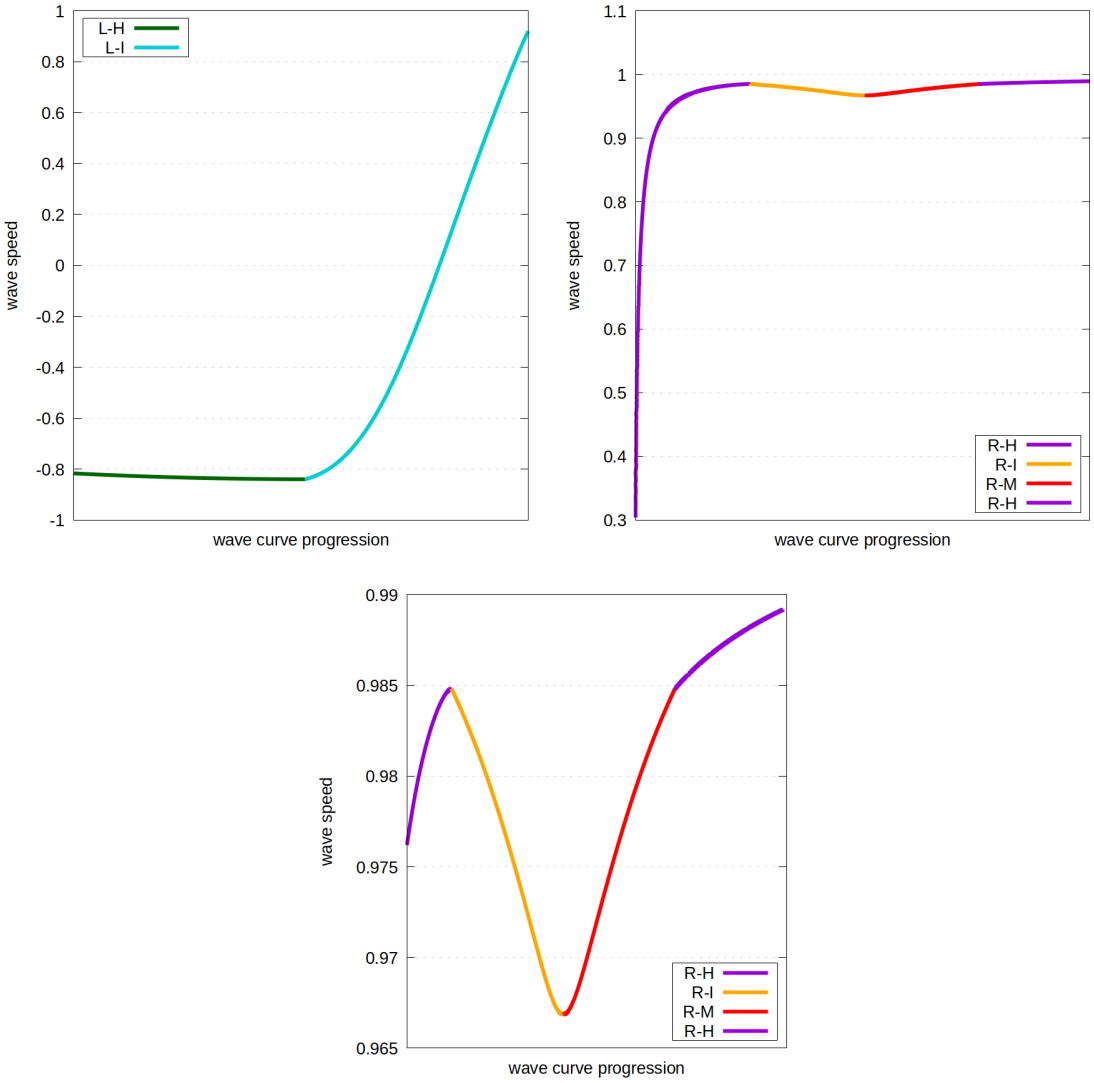

Figure 2.6: Wave speeds for the wave curves solution of `BW1-GGL1`. Left picture shows wave speed of the curves towards the left, right picture wave speed of the curves towards the right. Bottom picture displays an enlargement of the latest.

To perturb the initial data, we slightly modify the density of the initial right state as shown in table 2.7.

	ρ_L	v_L	P_L	ρ_R	v_R	P_R
`BW1-GGL1`	1	0	1000	0.125	0	0.01
Perturbation 1	1	0	1000	0.084	0	0.01
Perturbation 2	1	0	1000	0.090	0	0.01
Perturbation 3	1	0	1000	0.096	0	0.01

Table 2.7: Perturbations proposed for the right initial condition of `BW1-GGL1`.

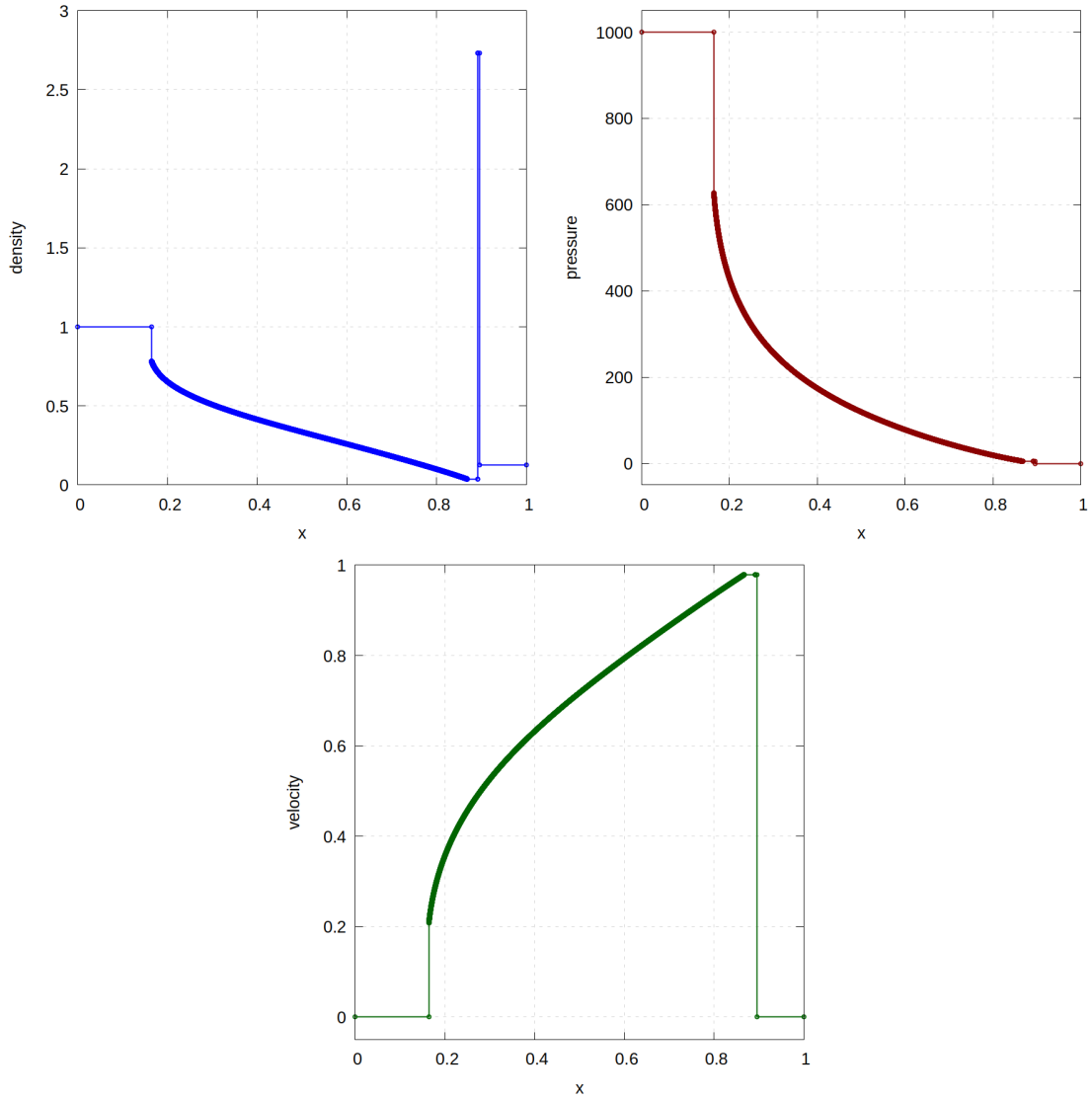

Figure 2.7: Solution profiles for density, pressure and velocity for `BW1-GGL1` at $t = 0.4$.

The sequence of wave curves to the left is the same for all perturbed Riemann problems, since the initial condition remains unchanged.

The right sequence exhibits the same types of wave curves as in the original problem: a Hugoniot curve that becomes sonic followed by an integral curve that terminates, a mixed curve and, finally, a continuation of the first Hugoniot curve.

However, modifying the initial density causes the first Hugoniot curve to terminate sooner or later in its progression through phase space. This leads to a different intersection point with the left sequence in each case. The wave curves corresponding to all perturbed problems can be seen in figure 2.8.

The density solution profile for the considered perturbations is shown in figure 2.9 focusing specifically on the density shell since the left wave remains the same.

In Perturbation 1, the first Hugoniot curve to the right reaches the middle state resulting in a shock wave in the spatial domain moving towards the right. In Perturbation 2, the first shock wave becomes sonic and is attached to a slower rarefaction fan producing

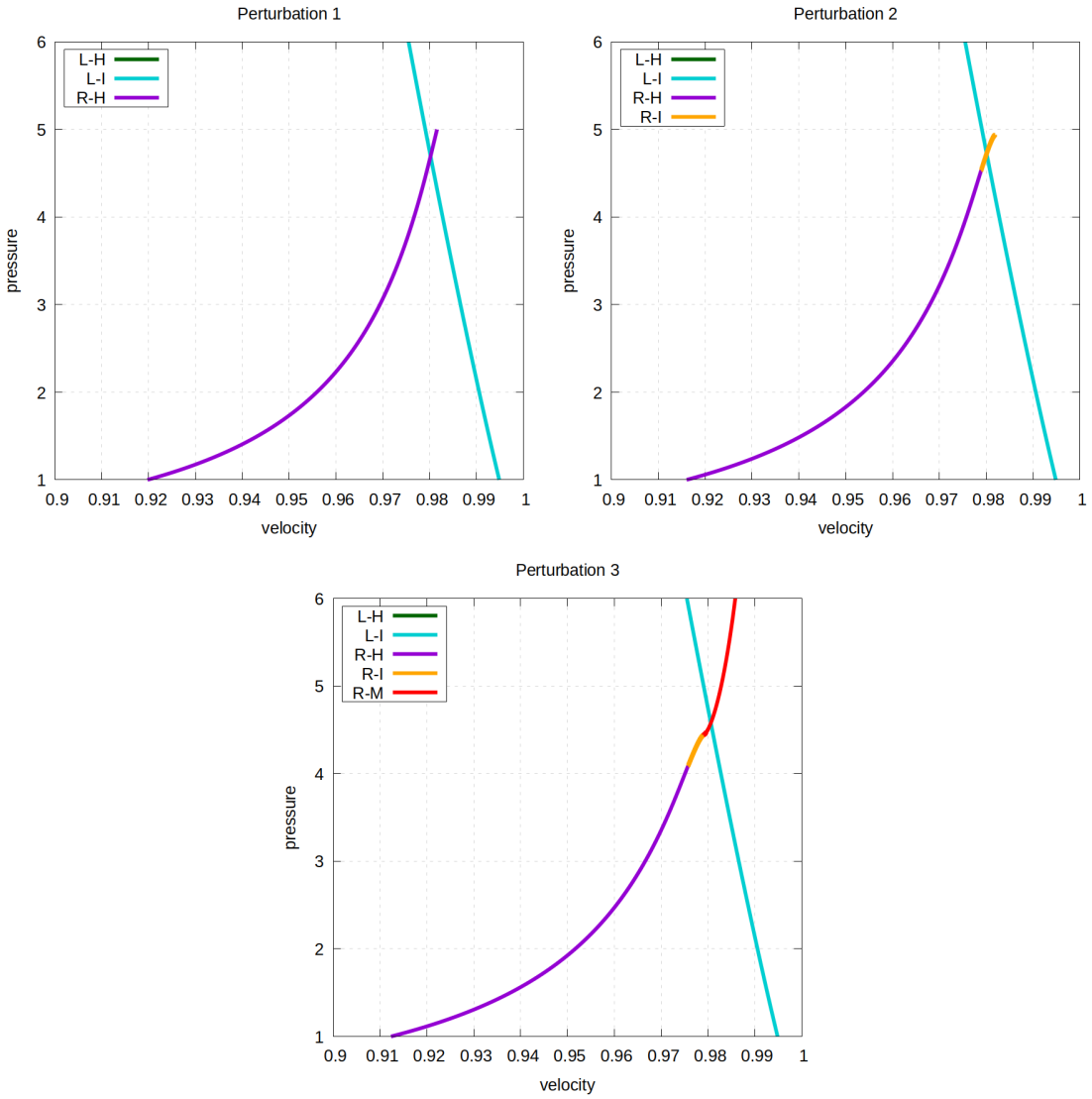

Figure 2.8: Wave curves for perturbations of `BW1-GGL1` focusing on the intersection.

a composite shell front in the spatial domain. In Perturbation 3, the integral curve terminates and is followed by a mixed curve which reaches the equilibrium state. The solution in the spatial domain is therefore comprised of the first shock wave from the Hugoniot curve, the states in the rarefaction that were not used in the calculation of the mixed curve and the shock wave from the mixed curve jumping to the equilibrium state.

Looking at the problem in phase space allows to see that all the perturbations indeed lead to similar solutions. The wave curves sequence constructed is the same, interrupted when intersecting the waves to the left at different states. However, the solution in the spatial domain depicts different wave structure.

Knowing how to construct the exact solution of the Riemann problem let us understand the underlying structure and the development of the waves.

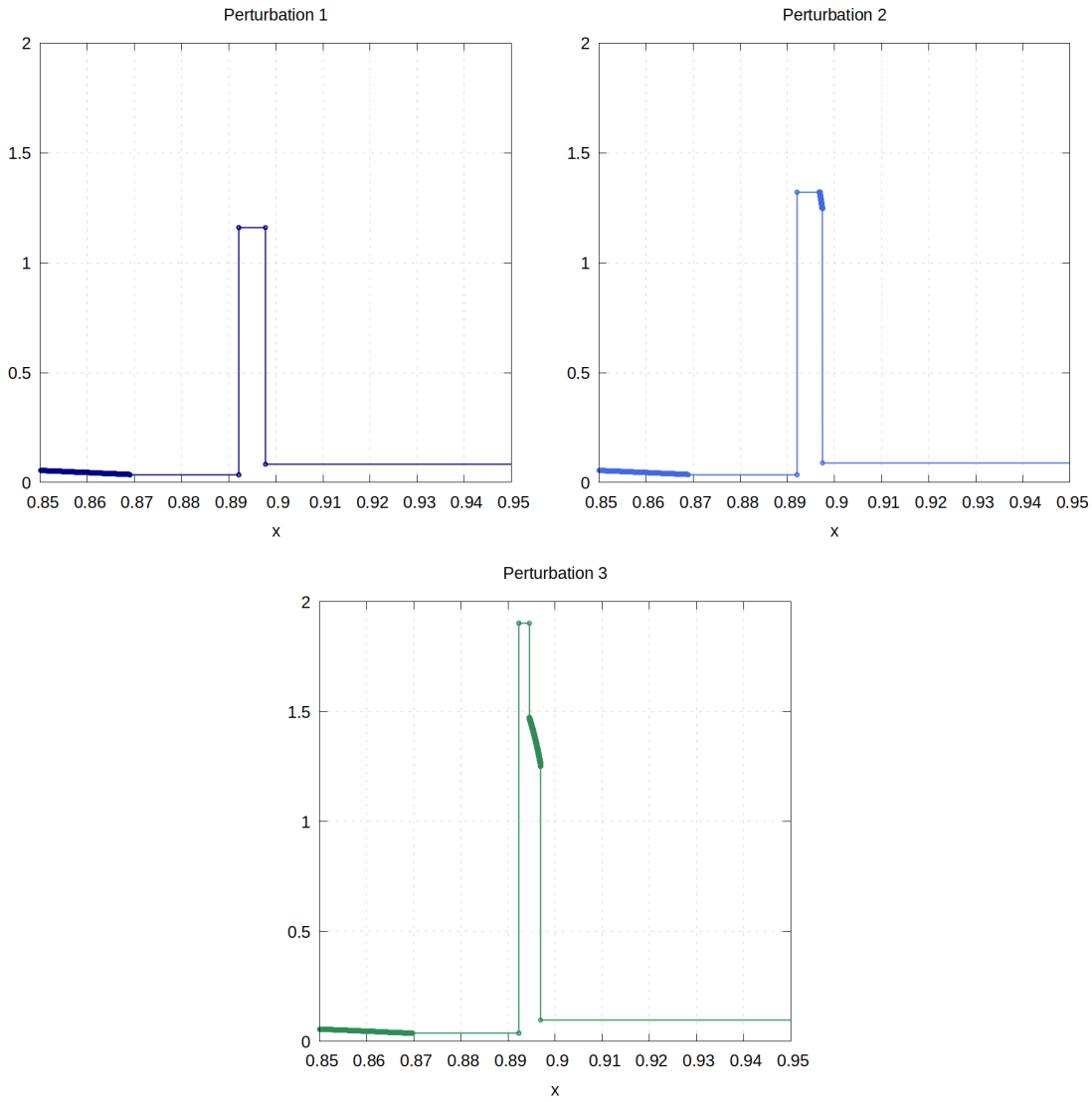

Figure 2.9: Density shells of perturbations of `BW1-GGL1`, depicting different wave structure at the front.

2.5.2 Blast wave 2 GGL2

This blast wave problem features a jump in pressure of five orders of magnitude as `BW1-GGL1` and also a higher density jump. Both initial conditions are situated in a convex region of the EoS, with $\eta(\mathbf{u}_L) > 0$ and $\eta(\mathbf{u}_R) > 0$. As a result, the first wave is consistent with a typical blast wave problem, with an expanding rarefaction moving to the left and a compressive shock moving to the right.

Wave curves obtained

The wave curves calculated in phase space for this problem are shown in figure 2.10. As in the previous example, we separate the plots for the curves moving to the left and to the right and then show the region of intersection.

The origin and termination of the wave curves of the left sequence are described in detail in table 2.8. The sequence begins with an integral curve that is calculated until it terminates, when $\eta \approx 8.15 \cdot 10^{-13}$. This is followed by a mixed curve that becomes sonic. The final state is located where $|\lambda^{\diamondsuit} - \lambda| \approx 9.49 \cdot 10^{-7}$. The final shock speed is pushed to the stack and the wave curves sequence continues. The following integral curve reaches the equilibrium state. Since this last curve does not encounter any changes in the convexity, the calculation is stopped by the density limit.

	Origin state			Termination state			
w. curves	v	P	ρ	v	P	ρ	v_ω
$\mathcal{I}_1$	0	1000	5.00	0.3394	494.3	2.266	0.2939
$\mathcal{M}$	-	-	-	0.9200	50.76	0.4424	-0.0861
$\mathcal{I}_2$	0.9200	50.76	0.4424	0.9863	7.438	0.1583	0.8635

Table 2.8: Origin and termination states of the wave curves moving to the left in `BW2-GGL2`.

The origin and termination states of the wave curves moving towards the right are presented in table 2.9. The sequence begins with a Hugoniot curve, which becomes sonic. The last state is located when $|v_s^{i)} - v_s^{i-1)}| \approx 7.33 \cdot 10^{-15}$. The shock speed is pushed to the stack and the sequence continues with an integral curve. This terminates at a zero of the nonlinearity factor, found as $\eta \approx 2.88 \cdot 10^{-13}$. A mixed curve follows and it is calculated using all states in the integral curve. After ending this curve we find that the intersection with the left sequence takes place along it and therefore no more curves are calculated.

	Origin state			Termination state			
w. curves	v	P	ρ	v	P	ρ	v_ω
$\mathcal{H}$	0	0.0100	0.1250	0.9780	5.635	1.457	0.9958
$\mathcal{I}$	0.9780	5.635	1.457	0.9843	6.992	2.266	0.9857
$\mathcal{M}$	-	-	-	0.9863	7.438	2.902	0.9907

Table 2.9: Origin and termination states of the wave curves moving to the right in `BW2-GGL2`.

The equilibrium state is found at $v = 0.9863$, where the intersecting integral curve moving to the left and mixed curve moving to the right present a pressure value of $P =$

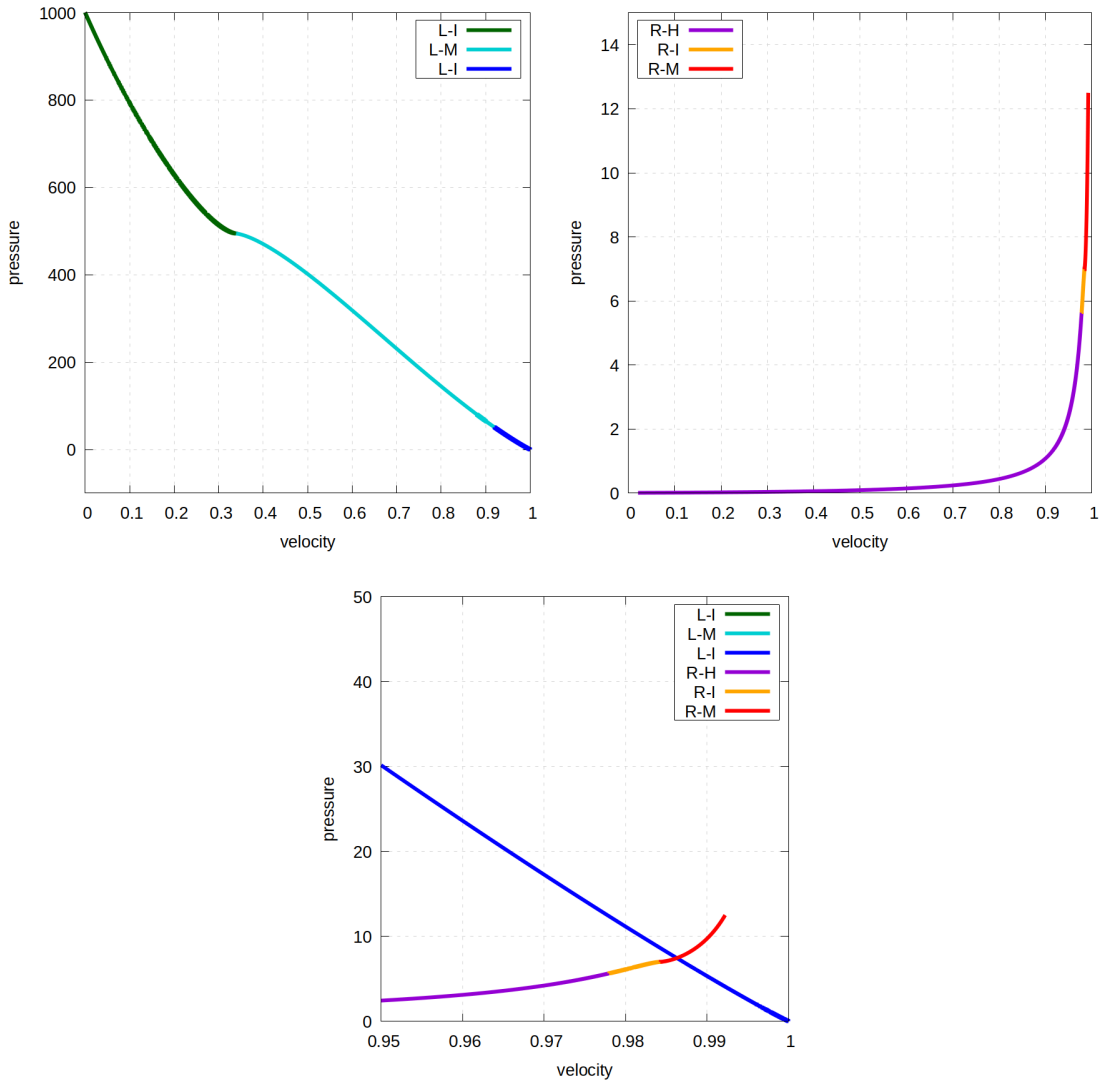

Figure 2.10: Wave curves for `BW2-GGL2` in phase space. Left picture depicts the sequence of wave curves moving to the left. Right picture shows the sequence of wave curves moving to right. Bottom picture displays the intersection of the wave curves determining the equilibrium state.

7.438, with error $4.53 \cdot 10^{-8}$. We also observe the jump in density between the left and right waves characterizing the density shell.

Translation to spatial domain

We show the wave speed along the wave curves in figure 2.11. This Riemann problem features the same number of waves in the spatial domain than wave curves in phase space.

The left branch of wave curves starts with an integral curve representing a rarefaction wave. This wave has a head that moves to the left with negative speed and a tail that moves to the right with positive speed. However, it is partially overtaken by the subsequent mixed curve, which becomes sonic and therefore does not overtake the whole rarefaction. As a result, the rarefaction shows until the state used as origin for the final state of the

mixed curve. The head and tail of the rarefaction both move to the left and are attached to a shock wave that stems from the mixed curve. The following integral curve starts behind the jump discontinuity. Its head moves to the left attached to the previous structure, while its tail moves to the right and reaches the equilibrium state.

The curves moving to the right start with a Hugoniot curve, which terminates as the fastest wave of the sequence. Although the subsequent integral curve is followed by a mixed curve, this one reaches the equilibrium state before using the whole integral curve for its calculation. As a result, a portion of the rarefaction wave appears in the spatial domain and is attached to a shock wave that reaches the equilibrium state.

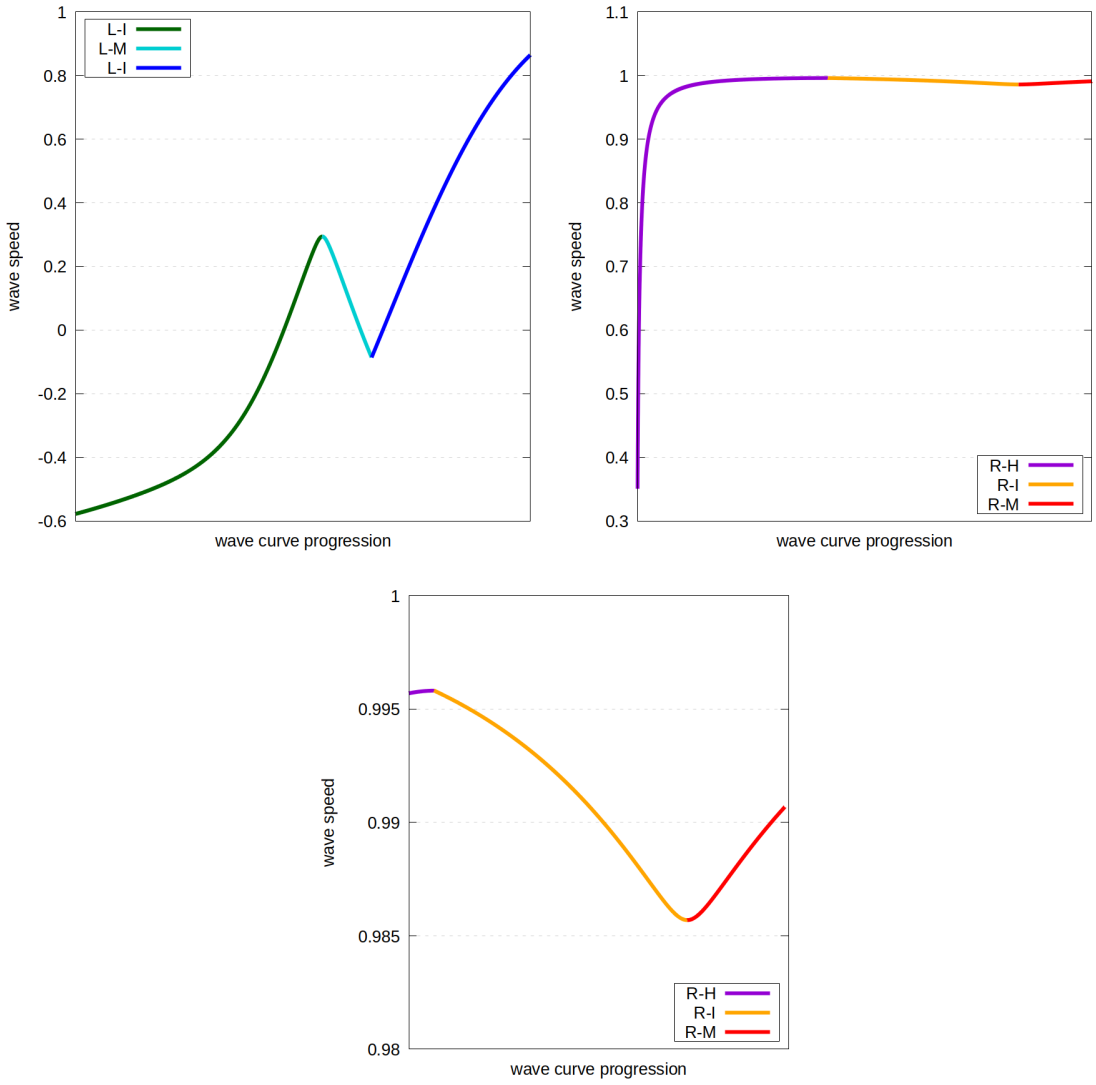

Figure 2.11: Wave speeds for the wave curves solution of `BW2-GGL2`. Left picture shows wave speed of the curves towards the left. Right picture wave speed of the curves towards the right. Bottom picture displays an enlargement of the latest.

The density, pressure and velocity profiles are depicted in the spatial domain in figure 2.12, and an enlargement of the contact discontinuity area is included to provide a clearer view of the composite wave moving towards the right.

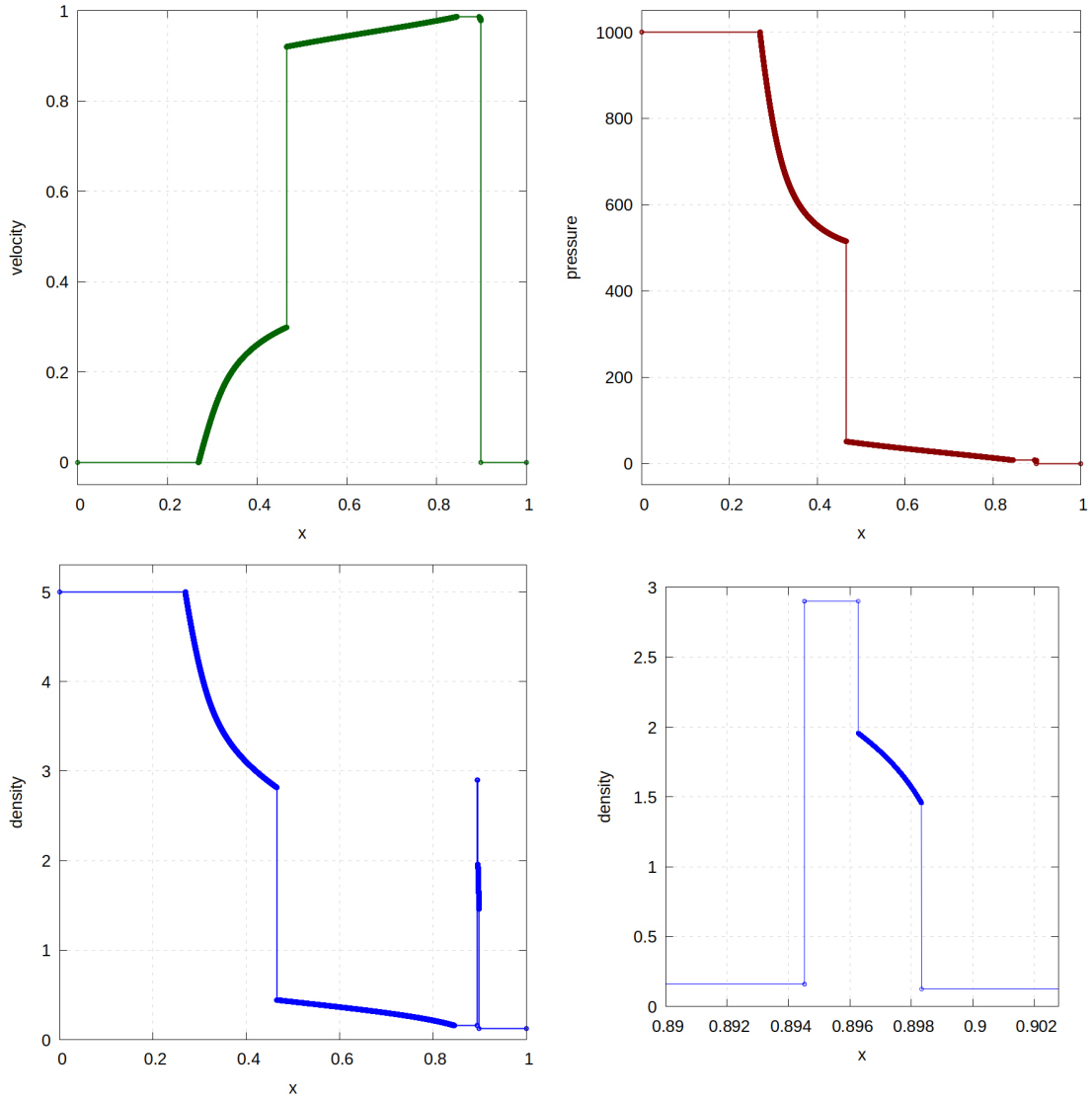

Figure 2.12: Solution profiles for density, pressure and velocity for `BW2-GGL2` at $t = 0.4$.

2.5.3 Expanding slabs GGL1

This problem features two gas slabs moving away from each other. This kind of initial condition can produce vacuum solutions between the moving gas slabs if their speed is high enough.

The solution to this Riemann problem is symmetric with respect to the vertical axis passing through the origin in phase space. The reason is that pressure and density are equal across the initial discontinuity while velocities are equal but with opposite signs. As a result, the solution is the same towards both sides and we only describe one.

The initial pressure and density lie in a convex region of the EoS and therefore the first wave is an expansive rarefaction.

Wave curves obtained

The wave curves moving to the left and the right are symmetrical, with equal values but opposite sign of the speeds. We present the curves in phase space in figure 2.13 and detail their origin and termination in tables 2.10 and 2.11.

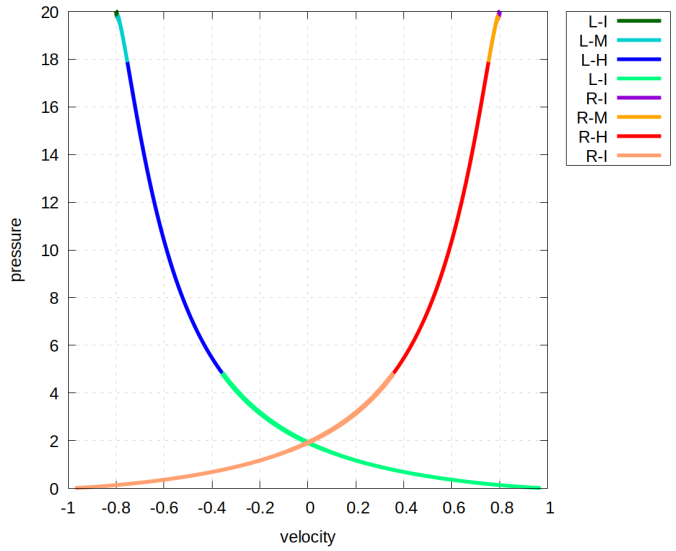

Figure 2.13: Wave curves for `ES-GGL1` in phase space. The problem is symmetrical with respect to a vertical axis that passes through $v = 0$.

The first integral curve terminates very close to the initial condition in phase space, when $\eta \approx 5.49 \cdot 10^{-14}$. A mixed curve follows. The integral curve that serves as origin is short and the mixed curve ends at the state that jumps from the start of the integral curve. Therefore the jump discontinuity has to be prolonged with the same origin. A Hugoniot curve follows with origin in the initial state. After traversing a change of the convexity, it becomes sonic and the last state is found when $|v_s^{i)} - v_s^{i-1)}| \approx 1.00 \cdot 10^{-10}$. The shock speed is pushed to the stack. An integral curve follows and we make use of the limit in density to stop its calculation. The intersection of the wave curves sequences takes place during this last integral curve.

	Origin state			Termination state			
w. curves	v	P	ρ	v	P	ρ	v_ω
$\mathcal{I}$	-0.8000	20.00	1.800	-0.7940	19.80	1.613	-0.8212
$\mathcal{M}$	-	-	-	-0.7529	17.88	1.217	-0.8756
$\mathcal{H}$	-0.8000	20.00	1.800	-0.3562	4.817	0.5713	-0.9136
$\mathcal{I}$	-0.3562	4.817	0.5713	0.0000	1.917	0.3508	-0.7071

Table 2.10: Origin and termination states of the wave curves moving to the left in `ES-GGL1`.

The equilibrium state is found at $P = 1.917$, where the integral curves yield a velocity of $v = 0$, with error $5.97 \cdot 10^{-9}$.

	Origin state			Termination state			
w. curves	v	P	ρ	v	P	ρ	v_ω
$\mathcal{I}$	0.8000	20.00	1.800	0.7940	19.80	1.613	0.8212
$\mathcal{M}$	-	-	-	0.7529	17.88	1.217	0.8756
$\mathcal{H}$	0.8000	20.00	1.800	0.3562	4.817	0.5713	0.9136
$\mathcal{I}$	0.3562	4.817	0.5713	0.0000	1.917	0.3508	0.7071

Table 2.11: Origin and termination states of the wave curves moving to the right in `ES-GGL1`.

Translation to spatial domain

The wave speed along the wave curves is shown in figure 2.14. The speeds are equal but of opposite sign, as the waves move in opposite directions.

The first integral curve is completely overtaken by the subsequent mixed curve. Its related jump discontinuity does not show in the spatial domain, since it is prolonged by the next Hugoniot curve. The shock related to this wave curve is the fastest wave and appears in the spatial domain, originating from the initial condition. Attached to this shock wave is a rarefaction, which arises due to the subsequent integral curve reaching the equilibrium state.

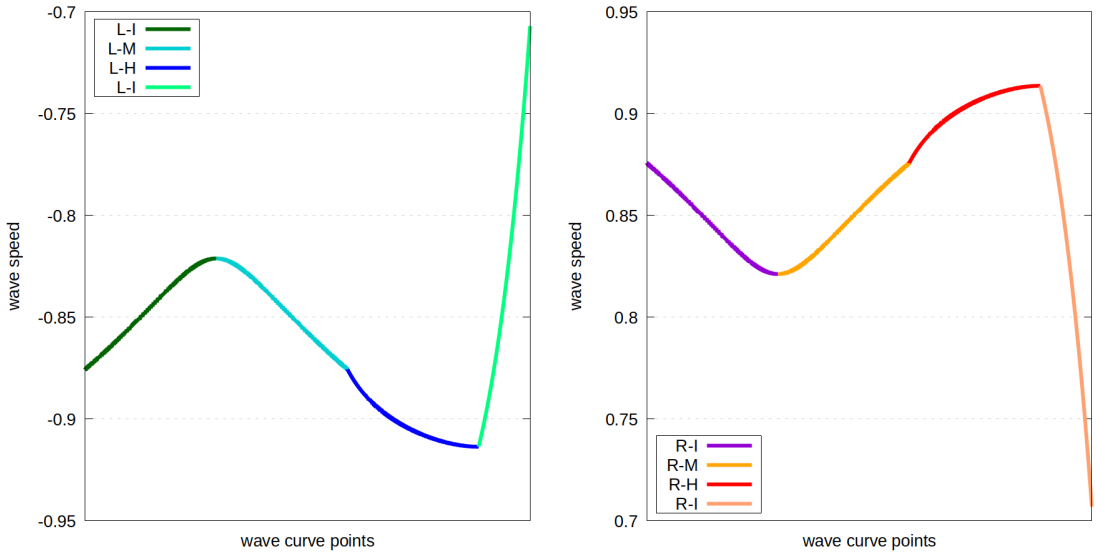

Figure 2.14: Wave speeds for the wave curves solution of `ES-GGL1`. Left (right) picture shows wave speed of the curves towards the left (right).

We plot the density, pressure and velocity profiles in the spatial domain in figure 2.15. We can see the symmetric composite wave and the point locating the contact discontinuity at the position of the initial discontinuity of the problem, as it has speed zero and therefore it does not move.

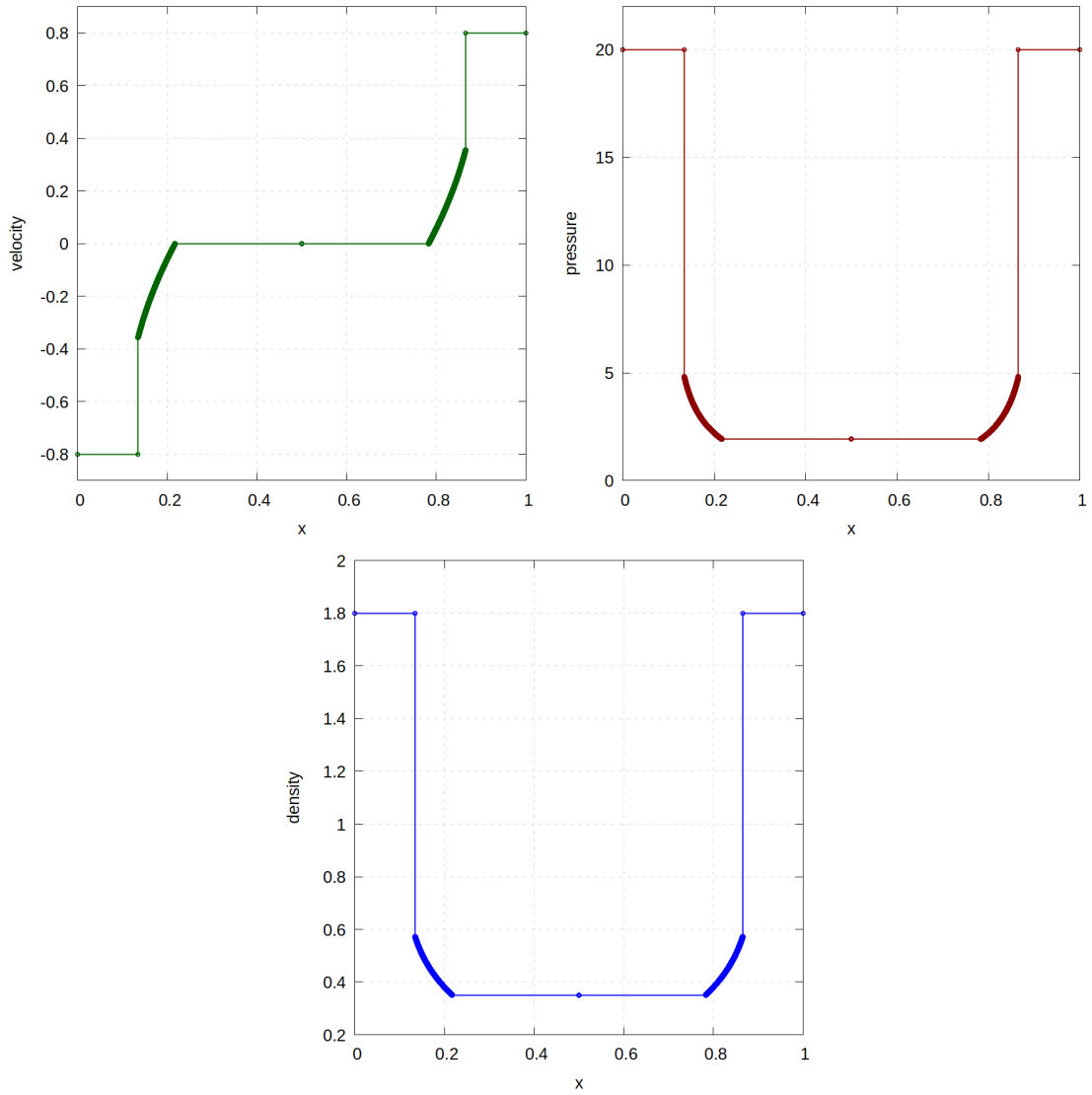

Figure 2.15: Solution profiles for density, pressure and velocity for `ES-GGL1` at $t = 0.4$.

2.5.4 Colliding slabs GGL2

This Riemann problem involves a fluid with low pressure and density that collides against the initial discontinuity at a very high velocity with Lorentz factor of 22.37. This collision results in the formation of waves that propagate towards both left and right. At the center of the collision there is a high pressure and high density region that remains at rest. The initial conditions are in a convex region of the EoS and therefore the pressure increases with a compressive shock wave. The solution of this problem is also symmetric thus we detail only one side.

Wave curves obtained

We present the symmetric wave curves in phase space in figure 2.16, and detail their origin and termination in tables 2.12 and 2.13. The values are equal, except for the velocities that have opposite sign.

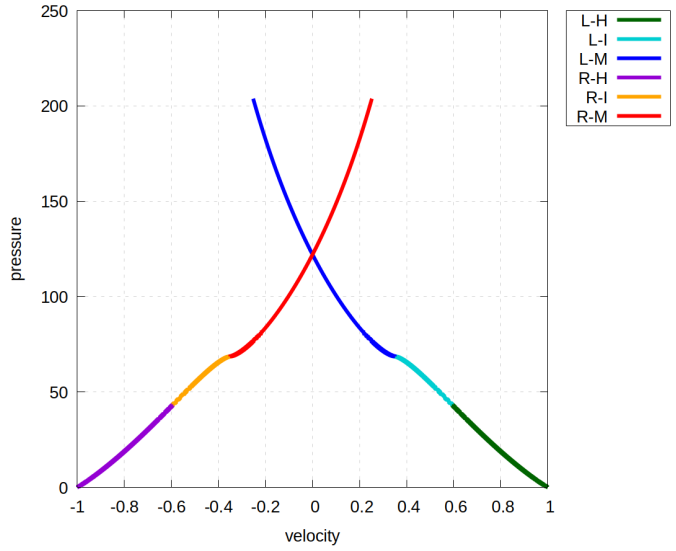

Figure 2.16: Wave curves for `CS-GGL2` in phase space. The problem is symmetrical with respect to a vertical axis that passes through $v = 0$.

The first Hugoniot curve becomes sonic. We locate its final state where $|v_s^{i)} - v_s^{i-1)}| \approx 1.43 \cdot 10^{-13}$ and its speed is pushed to the stack. It is continued by an integral curves that breaks when $\eta \approx 4.05 \cdot 10^{-14}$. A mixed curve follows and intersects the opposite sequence of curves.

	Origin state			Termination state			
w. curves	v	P	ρ	v	P	ρ	v_ω
$\mathcal{H}$	0.999	0.050	0.050	0.5920	43.49	1.226	-0.5378
$\mathcal{I}$	0.5920	43.49	1.226	0.3508	68.62	2.266	0.3060
$\mathcal{M}$	-	-	-	0.0000	122.0	4.308	-0.3162

Table 2.12: Origin and termination states of the wave curves moving to the left in `CS-GGL2`.

	Origin state			Termination state			
w. curves	v	P	ρ	v	P	ρ	v_ω
$\mathcal{H}$	-0.999	0.050	0.050	-0.5920	43.49	1.226	0.5378
$\mathcal{I}$	-0.5920	43.49	1.226	-0.3508	68.62	2.266	-0.3060
$\mathcal{M}$	-	-	-	0.0000	122.0	4.308	0.3162

Table 2.13: Origin and termination states of the wave curves moving to the right in `CS-GGL2`.

The equilibrium state is found at $P = 122.0$, where both mixed curves have a velocity $v = 0$, with error $3.78 \cdot 10^{-9}$.

Translation to spatial domain

We present the wave speed along the wave curves in figure 2.17. Notice that both sequences have the same speed with opposite sign.

The Hugoniot curve is the fastest curve, so its associated shock wave appears in the spatial domain. The following integral curve is partially overtaken by the subsequent mixed curve, although not completely because the latest reaches the equilibrium state before going over the whole integral curve. Therefore, the wave structure is a composite wave of a shock originating at the initial condition attached to a small rarefaction wave that is continued by another shock reaching the equilibrium state.

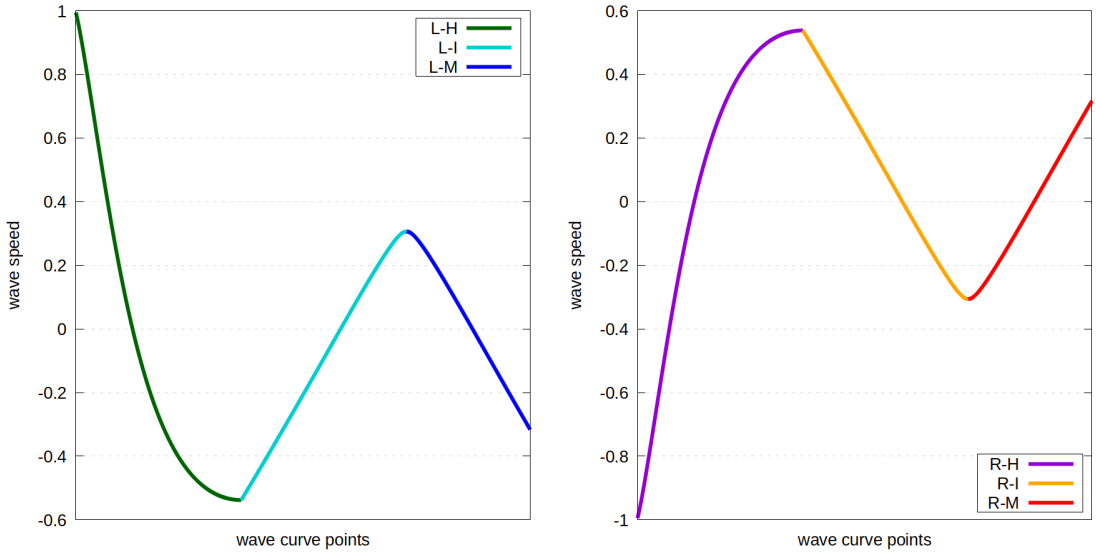

Figure 2.17: Wave speeds for the wave curves solution of `CS-GGL2`. At the left (right), the waves moving to the left (right).

The density, pressure and velocity profiles in figure 2.18 show this wave structure. The symmetric waves move towards the boundaries of the domain leaving the fluid at rest in between.

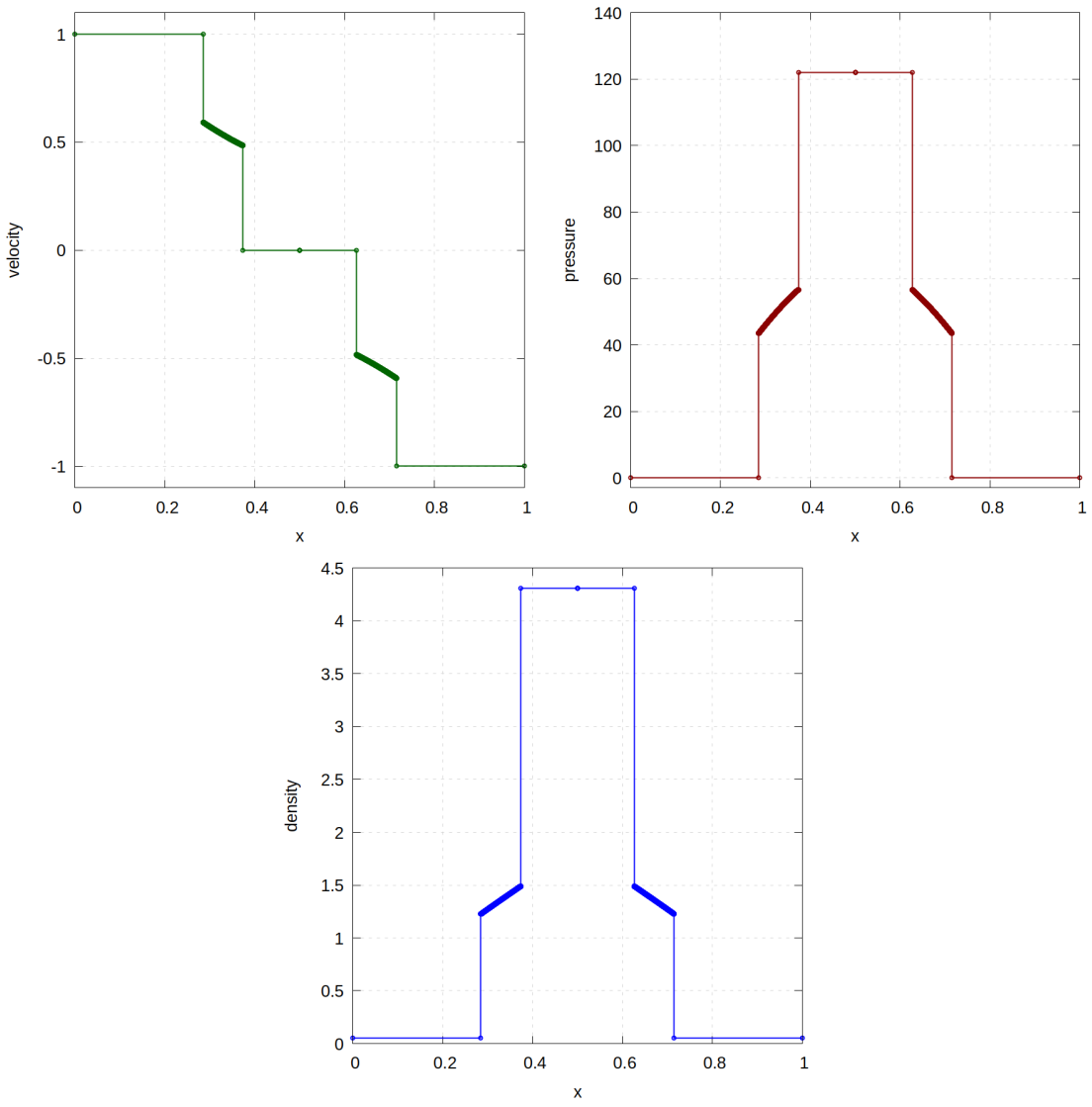

Figure 2.18: Solution profiles for density, pressure and velocity for `CS-GGL2` at $t = 0.4$.

Chapter 3

The exact solution of the Riemann problem in nonconvex SRHD with nonzero tangential velocities

Realistic astrophysics scenarios involve three spatial dimensions (3D). In the context of SRHD, 3D not only accounts for highly relativistic fluids. The presence of tangential velocities make the equations tightly coupled through the Lorentz factor w and the specific enthalpy h. As a result, the limit to classical dynamics, when $w \approx 1$, does not coincide with the Newtonian hydrodynamic formulation [91]. Thus, even for slow fluids, if the thermodynamics is relativistic ($h > 1$), SRHD must be used in more than one spatial dimension.

A Riemann problem in 3D can be simplified considering the reference frame such that the initial hypersurface of discontinuity is normal to the x-axis. The decay of the discontinuity takes place in this axis and while the hydrodynamics equations have components in the three dimensions, the resolution of the Riemann problem is analogous to the 1D case. The wave curves solving the Riemann problem coincide at the equilibrium state in the $v^x - P$ plane.

The exact solution of a Riemann problem is an important tool for studying the wave phenomena arising in a given hydrodynamic context and testing numerical methods that will be used to solve more complex initial conditions. Although 1D validations are a necessary first step, realistic simulations require 3D space, making multidimensional codes essential for more complex scenarios. As a consequence, exact solutions can be particularly useful for checking the accuracy in multiple dimensions. To this end, in [91, 99] the authors extended the solution for convex SRHD developed in [75] to include tangential velocities. Analogously, in this second Chapter we extend the exact solution for nonconvex SRHD with nonzero tangential velocities.

Firstly, we present the wave curves that arise in 3D nonconvex SRHD, namely Hugoniot, integral and mixed curves. However, the relationships between pressure and velocity differ from those already presented. Then we particularize the expressions for a nonconvex phenomenological EoS, the GGL EoS [54] and detail how we perform the calculations that are different from the 1D case. Finally, we provide examples of the exact solution for the blast wave problems presented in the previous Chapter with the addition of tangential velocities. We demonstrate how the wave curves and solutions in the spatial domain change in the presence of tangential speeds.

3.1 Wave curves for nonconvex SRHD in 3D

While the definition of the wave curves presented in the previous Chapter is general, the SRHD equations change with the number of spatial dimensions. In what follows we revisit the three types of wave curves and detail the differences that arise in 3D nonconvex SRHD as compared to the 1D case.

3.1.1 Hugoniot curves

Hugoniot curves are calculated through the relativistic Rankine-Hugoniot conditions, derived first by Taub in [121]. Let n_μ be the unit vector normal to the hypersurface across which there is the discontinuity. Since we select this to be the x-axis, then $n_\mu = w_s(\upsilon_s, 1, 0, 0)$. The conditions read

$$[\rho u^\mu] n_\mu = 0 \tag{3.1.1}$$

$$[T^{\mu\nu}] n_\nu = 0. \tag{3.1.2}$$

The Greek indices run from 0 to 3.

From equation (3.1.1) we can define the invariant mass flux, analogous to the one in 1D. It contains the x-component of the velocity instead of the modulus:

$$j = w_s D_a(\upsilon_s - \upsilon_a^x) = w_s D_b(\upsilon_s - \upsilon_b^x).$$

We still consider $j > 0$ ($j < 0$) for waves traveling to the right (left).

Expanding (3.1.2) and writing the equations in terms of the invariant j, one can get ([91])

$$[\upsilon^x] = \frac{-j}{w_s}\left[\frac{1}{D}\right] \tag{3.1.3}$$

$$[P] = \frac{j}{w_s}\left[\frac{S^x}{D}\right] \tag{3.1.4}$$

$$\left[\frac{S^y}{D}\right] = 0 \tag{3.1.5}$$

$$\left[\frac{S^z}{D}\right] = 0 \tag{3.1.6}$$

$$[\upsilon^x P] = \frac{j}{w_s}\left[\frac{\tau}{D}\right]. \tag{3.1.7}$$

From the mass flux invariant one can deduce the shock speed

$$\upsilon_s^\pm = \frac{\rho_a^2 W_a^2 \upsilon_a^x \pm |j|\sqrt{j^2 + \rho_a^2 w_a^2 (1 - (\upsilon_a^x)^2)}}{\rho_a^2 w_a^2 + j^2} \tag{3.1.8}$$

and from equations (3.1.3), (3.1.4) and (3.1.7), analogously to the 1D case, we can isolate the x-velocity of the fluid after the shock

$$\upsilon_b^x = \left[h_a w_a \upsilon_a^x + \frac{w_s(P_b - P_a)}{j}\right]\left[h_a w_a + (P_b - P_a)\left(\frac{w_s \upsilon_a^x}{j} + \frac{1}{\rho_a w_a}\right)\right]^{-1}. \tag{3.1.9}$$

We can use (2.1.11), derived for 1D, to relate the mass flux invariant, pressure and enthalpy, given that the hypersurface of discontinuity is normal to the x-axis. Additionally,

since thermodynamic quantities are independent of spatial dimensions, we can employ the Taub adiabat to obtain the expression for enthalpy (2.1.12).

Equations (3.1.5)-(3.1.6) determine the tangential speed behind the shock. Assuming state a is known, and once v_b^x has been calculated, from (3.1.5) we have

$$h_a w_a v_a^y = \frac{h_b v_b^y}{\sqrt{1-(v_b^x)^2-(v_b^y)^2-(v_b^z)^2}}.$$

Isolating the y-velocity we get

$$(v_b^y)^2 = \frac{h_a^2 w_a^2 (v_a^y)^2 (1-(v_b^x)^2-(v_b^z)^2)}{h_b^2 + h_a^2 w_a^2 (v_a^y)^2}. \tag{3.1.10}$$

and analogously for the z-velocity, from (3.1.6) we get

$$(v_b^z)^2 = \frac{h_a^2 w_a^2 (v_a^z)^2 (1-(v_b^x)^2-(v_b^y)^2)}{h_b^2 + h_a^2 w_a^2 (v_a^z)^2}. \tag{3.1.11}$$

We introduce notation $(v^t)^2 = (v^y)^2 + (v^z)^2$. Then, inserting (3.1.11) into (3.1.10) for the y component and viceversa for the z component, after some algebra we have

$$(v_b^{y,z})^2 = \frac{h_a^2 w_a^2 (v_a^{y,z})^2 (1-(v_b^x)^2)}{h_b^2 + h_a^2 w_a^2 (v_a^t)^2}.$$

The tangential speed after the shock is

$$(v_b^t)^2 = \frac{h_a^2 w_a^2 (v_a^t)^2 (1-(v_b^x)^2)}{h_b^2 + h_a^2 w_a^2 (v_a^t)^2}. \tag{3.1.12}$$

The termination and continuation of Hugoniot curves remain unchanged with spatial dimensions. Therefore, to calculate Hugoniot curves with nonzero tangential speed, one could follow Algorithm 2.1.1 using (3.1.8) to evaluate the shock speed, (3.1.9) to obtain v_b^x and include the calculation of the tangential speed behind the shock v_b^t using equation (3.1.12).

3.1.2 Integral curves

We choose the discontinuity of the Riemann problem to be normal to the x-axis. Therefore, the integral curves correspond to self-similar solutions of the hyperbolic system with respect to the variable $\xi = \frac{x}{t}$. Upon changing the variables of the system $\mathbf{u}_t + \mathbf{f}(\mathbf{u})_x = 0$ to ξ, we can eliminate the derivatives in y and z and obtain the following equations

$$-\xi \frac{\partial(\rho w)}{\partial \xi} + \frac{\partial(\rho w v^x)}{\partial \xi} = 0 \tag{3.1.13}$$

$$-\xi \frac{\partial(h\rho w^2 v^x)}{\partial \xi} + \frac{\partial(h\rho w^2 (v^x)^2 + P)}{\partial \xi} = 0 \tag{3.1.14}$$

$$-\xi \frac{\partial(h\rho w^2 v^y)}{\partial \xi} + \frac{\partial(h\rho w^2 v^x v^y)}{\partial \xi} = 0 \tag{3.1.15}$$

$$-\xi \frac{\partial(h\rho w^2 v^z)}{\partial \xi} + \frac{\partial(h\rho w^2 v^x v^z)}{\partial \xi} = 0 \tag{3.1.16}$$

$$-\xi \frac{\partial(h\rho w^2 - \rho w - P)}{\partial \xi} + \frac{\partial(h\rho w^2 v^x - \rho w v^x)}{\partial \xi} = 0. \tag{3.1.17}$$

Using $\partial w/\partial v^i = v^i w^3 \partial v^i/\partial\xi$, equation (3.1.13) can be written as

$$\frac{\partial\rho}{\partial\xi}(v^x-\xi)+\frac{\partial v^x}{\partial\xi}\Big(\rho+\rho w^2 v^x(v^x-\xi)\Big)+\frac{\partial v^y}{\partial\xi}\Big(\rho w^2 v^y(v^x-\xi)\Big)+\frac{\partial v^z}{\partial\xi}\Big(\rho w^2 v^z(v^x-\xi)\Big)=0. \tag{3.1.18}$$

The other four equations, (3.1.14)-(3.1.17), can be reduced to three. Introducing (3.1.13) into (3.1.17) we get

$$\xi\frac{\partial P}{\partial\xi}+\frac{\partial(\rho h w^2)}{\partial\xi}(v^x-\xi)+\frac{\partial v^x}{\partial\xi}\rho h w^2=0, \tag{3.1.19}$$

and then subtracting (3.1.14)-v^x(3.1.19), (3.1.15)-v^y(3.1.19) and (3.1.16)-v^z(3.1.19) we have

$$\rho h w^2(v^x-\xi)\frac{\partial v^x}{\partial\xi}+(1-v^x\xi)\frac{\partial P}{\partial\xi}=0 \tag{3.1.20}$$

$$\rho h w^2(v^x-\xi)\frac{\partial v^y}{\partial\xi}-v^y\xi\frac{\partial P}{\partial\xi}=0 \tag{3.1.21}$$

$$\rho h w^2(v^x-\xi)\frac{\partial v^x}{\partial\xi}-v^z\xi\frac{\partial P}{\partial\xi}=0. \tag{3.1.22}$$

Finally for the last equation of the system we consider the conservation of entropy along fluid lines. At constant entropy it holds that $\partial P/\partial\rho = hc_s^2$ and therefore

$$\frac{\partial P}{\partial\xi}=hc_s^2\frac{\partial\rho}{\partial\xi}. \tag{3.1.23}$$

Equations (3.1.18), (3.1.20)-(3.1.23) are the system of ordinary differential equations describing integral curves. It admits non trivial solutions only if the determinant is zero, which leads to condition

$$\xi=\frac{v^x(1-c_s^2)\pm\sqrt{(1-v^2)[1-v^2c_s^2-(v^x)^2(1-c_s^2)]}}{1-v^2c_s^2}$$

where $+$ $(-)$ signs refer to integral curves propagating to the left (right).

After some algebra, the system of five equations reduces to

$$\rho h w^2(v^x-\xi)\mathrm{d}v^x+(1-v^x\xi)\mathrm{d}P=0 \tag{3.1.24}$$

$$hwv^y=constant \tag{3.1.25}$$

$$hwv^z=constant. \tag{3.1.26}$$

Following [99], conditions (3.1.25)-(3.1.26) state that between two states a and b in the integral curve we have $h_a w_a v_a^y = h_b w_b v_b^y$ and $h_a w_a v_a^z = h_b w_b v_b^z$. Summing both expressions squared we obtain a quantity A that remains constant along integral curves

$$A=hwv^t. \tag{3.1.27}$$

It is then straightforward to see that

$$(v^t)^2=\frac{A^2(1-(v^x)^2)}{h^2+A^2} \tag{3.1.28}$$

and

$$w^2=\frac{h^2+A^2}{h^2(1-(v^x)^2)}. \tag{3.1.29}$$

Equation (3.1.24) needs to be solved imposing the conservation of A (3.1.27). To do so, we rewrite the equation as

$$\frac{\mathrm{d}v^x}{\mathrm{d}P} = \frac{1}{\rho h w^2}\frac{(1-\xi v^x)}{(\xi - v^x)}. \tag{3.1.30}$$

The right hand side can be written in terms of A.

First we rewrite ξ by expanding the terms in the square root and substituting every tangential velocity by (3.1.28)

$$\xi = \frac{v^x(1-c_s^2)(h^2+A^2) \pm c_s h(1-(v^x)^2)\sqrt{h^2+A^2(1-c_s^2)}}{A^2(1-c_s^2)+h^2(1-c_s^2(v^x)^2)}.$$

Then

$$1-\xi v^x = \frac{A^2(1-(v^x)^2)(1-c_s^2)+h^2(1-(v^x)^2) \mp c_s h v^x(1-(v^x)^2)\sqrt{h^2+A^2(1-c_s^2)}}{A^2(1-c_s^2)+h^2(1-c_s^2(v^x)^2)}$$

and

$$\xi - v^x = \frac{-h^2c_s^2v^x(1-(v^x)^2) \pm c_s h(1-(v^x)^2)\sqrt{h^2+A^2(1-c_s^2)}}{A^2(1-c_s^2)+h^2(1-c_s^2(v^x)^2)}.$$

All together we obtain

$$\frac{\mathrm{d}v^x}{1-(v^x)^2} = \pm\frac{\sqrt{h^2+A^2(1-c_s^2)}}{h^2+A^2}\frac{\mathrm{d}P}{\rho c_s}.$$

The left hand side can be solved analytically ([99])

$$\int \frac{\mathrm{d}v^x}{1-(v^x)^2} = \frac{1}{2}\log\left(\frac{1+v^x}{1-v^x}\right) = \tanh^{-1}(v^x).$$

Denoting by

$$X = \int_{P_a}^{P_b} \frac{\sqrt{h^2+A^2(1-c_s^2)}}{h^2+A^2}\frac{\mathrm{d}P}{\rho c_s} \tag{3.1.31}$$

the integral yet to solve depending only on the EoS, we obtain that the x-velocity in the new state of the integral curve is

$$v_b^x = \tanh\left(\frac{1}{2}\log\left(\frac{1+v_a^x}{1-v_a^x}\right) \pm X\right) \tag{3.1.32}$$

using the + (-) sign for waves traveling to the right (left).

To calculate an integral curve with non-zero tangential speed, we can follow a procedure similar to Algorithm 2.1.2 for the 1D case. The modifications include the calculation of the constant expression A (3.1.27) from the known state a, solving integral (3.1.31) for the new state and evaluating v_b^x using (3.1.32).

Although the self-similar solution leads to a different expression for the x-component of the velocity behind the wave than in the 1D case, the system can still be written as equation (2.1.2). Therefore, integral curves terminate when they traverse a zero of the nonlinearity factor and are continued with a mixed curve.

3.1.3 Mixed curves

Mixed curves are Hugoniot curves that continue a terminated integral curve by using the states in the integral curve as the origin for the Rankine-Hugoniot conditions.

In 3D nonconvex SRHD, the jump conditions for mixed curves involve a larger number of equations than in 1D, tightly coupled through the Lorentz factor because of the presence of tangential velocity. However, the termination and continuation of mixed curves follow the same procedure as in 1D.

To calculate a mixed curve with non-zero tangential speed, one can follow Algorithm 2.1.3 and solve the system of Rankine-Hugoniot conditions with three velocity components.

3.2 Application to a nonconvex EoS

We detail the equations for the GGL phenomenological model [54]

$$P = (\gamma(\rho) - 1)\rho\varepsilon,$$

with

$$\gamma(\rho) = \gamma_0 + (\gamma_1 - \gamma_0)\mathrm{e}^{-(\rho-\rho_0)^2/\sigma_0^2}.$$

For more details about its parameters and related thermodynamic quantities, refer to its previous definition in Section §2.3.

3.2.1 Hugoniot curves with GGL EoS

In order to build the Hugoniot curves we need to provide ρ_b given a pressure value P_b for the GGL EoS. Since the EoS is independent of the spatial domain, we can apply the Newton method described for the 1D case to solve the implicit equation (2.3.4).

3.2.2 Integral curves with GGL EoS

The integral curves can be solved when particularizing integral (3.1.31) for an EoS. The integration is indicated with respect to pressure although the integrand contains density and internal energy terms. However, the exponential shape of the GGL EoS does not allow to isolate density in terms of pressure, requiring a change of variable in the integral. For the sake of readability, we use $\gamma(\rho) = \gamma$.

For the GGL EoS, first law of thermodynamics with constant entropy reads

$$\mathrm{d}\varepsilon = \frac{\gamma - 1}{\rho}\mathrm{d}\rho.$$

Deriving the pressure and applying this equality we get

$$\mathrm{d}P = \varepsilon(\gamma + \rho\gamma' - 1)\mathrm{d}\rho + (\gamma - 1)\rho\mathrm{d}\varepsilon = \varepsilon(\gamma'\rho + \gamma(\gamma - 1))\mathrm{d}\rho,$$

where the apostrophe means derivative with respect to density.

Changing the integration variable for the density, expanding $h = 1 + \varepsilon\gamma$ and using the expression of the relativistic sound speed (2.3.3), the integral becomes

$$X = \int_{\rho_a}^{\rho_b} \frac{\sqrt{(1+\varepsilon\gamma)^3 + A^2(1 + \varepsilon(2\gamma - \gamma^2 - \rho\gamma'))}}{(A^2 + (1+\varepsilon\gamma)^2)\rho\sqrt{\varepsilon(\gamma(\gamma-1) + \rho\gamma')}}\varepsilon(\gamma'\rho + \gamma(\gamma-1))\mathrm{d}\rho. \tag{3.2.1}$$

The integral has to be solved numerically. From a state a we can approximate (3.2.1) to a state ρ_b, using at any intermediate point the value of the internal energy given by (2.3.6). Once calculated we obtain the flow velocity using (3.1.32). The pressure is given by the EoS using the internal energy and the density.

3.2.3 Mixed curves with GGL EoS

To calculate states on a mixed curve, we use the Rankine-Hugoniot conditions (3.1.3)-(3.1.7) and jump from a known state in a previous integral curve, which we mark with the subscript $\Diamond$. The shock speed is equal to the characteristic speed at the integral curve state $v_s = \lambda_\Diamond = \lambda$. We omit the $\Diamond$ here for readability.

From (3.1.3) we have

$$\underbrace{D_\Diamond(v^x_\Diamond - \lambda)}_{M} = \rho w(v^x - \lambda),$$

where we label as M the known term. From (3.1.5) and (3.1.6) the quantity $A = hwv^t$ is conserved. Expanding the Lorentz factor and using A to replace the tangential speed by (3.1.28), we get

$$(v^x_b)^2\left(1 + \left(\frac{M}{\rho}\right)^2 \frac{h^2}{A^2 + h^2}\right) - 2\lambda v^x_b + \lambda^2 - \left(\frac{M}{\rho}\right)^2\left(1 - \frac{A^2}{A^2 + h^2}\right) = 0.$$

Solving for the x-velocity, we obtain

$$v^x_b(\rho, \varepsilon) = \frac{\lambda + \sqrt{K}\sqrt{1 - \lambda^2 + K}}{1 + K} \tag{3.2.2}$$

with

$$K = \left(\frac{M}{\rho}\right)^2 \frac{(1 + \varepsilon\gamma)^2}{(1 + \varepsilon\gamma)^2 + A^2}, \tag{3.2.3}$$

where the sign of the square root is taken such that $v^x(\rho_\Diamond, \varepsilon_\Diamond) = v^x_\Diamond$. In the 1D case the velocity depended just on the density. Here the internal energy appears coupled through the specific enthalpy.

Using the definition of the invariant mass flux, (3.1.4) recasts as

$$P_\Diamond - P = S^x_\Diamond(\lambda - v^x_\Diamond) - S^x(\lambda - v^x).$$

Introducing (3.1.3), the EoS and substituting $h = 1 + \varepsilon\gamma$ we get

$$\rho\varepsilon(\gamma - 1) + (1 + \varepsilon\gamma)wv^x_b D_\Diamond(v^x_\Diamond - \lambda) = S^x_\Diamond(v^x_\Diamond - \lambda) + P_\Diamond. \tag{3.2.4}$$

Similarly, from (3.1.7) we can get to

$$D_\Diamond(v^x_\Diamond - \lambda)((1 + \varepsilon\gamma)w - 1) + \varepsilon\rho(\gamma - 1)\lambda = -\lambda\tau_\Diamond + S^x_\Diamond - D_\Diamond v^x_\Diamond. \tag{3.2.5}$$

The equations can be simplified further by substracting λ(3.2.4)$-$(3.2.5) and v^x(3.2.5) $-$ (3.2.4). The result is a system of two equations with two unknowns, the density ρ and the specific internal energy ε:

$$f \equiv (1 + \varepsilon\gamma)(1 - v^x\lambda)w - h_\Diamond w_\Diamond(1 - v^x_\Diamond\lambda) = 0, \tag{3.2.6}$$

$$g \equiv \rho\varepsilon(\gamma - 1)(1 - \lambda v^x) - P_\Diamond(1 - \lambda v^x) - D_\Diamond w_\Diamond h_\Diamond(v^x_\Diamond - v^x)(v^x_\Diamond - \lambda) = 0, \tag{3.2.7}$$

where v^x is to be replaced by expression (3.2.2).

Calculating a state of a mixed curve involves solving the nonlinear system (3.2.6)-(3.2.7) to get ρ and ε, then evaluating (3.2.2) to obtain v^x and finally getting the tangential speed through (3.1.28).

3.3 A practical methodology to calculate wave curves

The wave curves are computed using the same methodology as in the 1D case, employing the formulas derived for tangential velocities. The calculation procedure, the termination criteria and the tolerances for root finding are those detailed in Chapter 2.

However, in the case of mixed curves, there is a significant difference. In 1D, finding the density of a new state belonging to a mixed curve involves solving an implicit equation. The addition of tangential velocities results in a nonlinear system of equations (3.2.6)-(3.2.7). This system can be expressed in the form of a matrix equation

$$\mathbf{G}(\mathbf{x}) = 0 \quad \text{where } \mathbf{x} = \begin{pmatrix} \rho \\ \varepsilon \end{pmatrix}, \quad \mathbf{G} = \begin{pmatrix} f \\ g \end{pmatrix}.$$

The trivial solution $(\rho_\diamondsuit, \varepsilon_\diamondsuit)$ always satisfies the system. Liu [70] establishes that the density in the mixed curve is the nontrivial solution of the system with density closest to $\rho_\diamondsuit$. In the 1D case, the presence of a single equation allowed us to distinguish between roots by examining the sign of the derivative. However, with a system of equations, this approach is not viable. Instead of using the Newton method with quadratic convergence, which might miss the first nontrivial root, we solve the system using a fixed point iterative method. Although the linear convergence of this method makes it slower, it guarantees monotonicity and therefore convergence to the desired root.

The method reads

$$\begin{aligned} &\mathbf{x}^{k+1)} = \mathbf{x}^{k)} - \alpha \cdot \mathbf{m} \cdot \mathbf{G}(\mathbf{x}^{k)}) \\ &\text{where } \mathbf{m} = \mathbf{J}^{-1}(\mathbf{x}^{0)}) \text{ and initially } \alpha = 1. \end{aligned}$$

The parameter $0 < \alpha \leq 1$ controls the step of the method. The matrix $\mathbf{J}$ is the Jacobian of the system,

$$\mathbf{J} = \begin{pmatrix} a_{11} = \dfrac{\partial f}{\partial \rho} & a_{12} = \dfrac{\partial f}{\partial \varepsilon} \\ a_{21} = \dfrac{\partial g}{\partial \rho} & a_{22} = \dfrac{\partial g}{\partial \varepsilon} \end{pmatrix},$$

whose components are

$$\begin{aligned} \frac{\partial f}{\partial \rho} &= (1 - \upsilon^x \lambda) \left((1 + \varepsilon\gamma) \frac{\partial w}{\partial \rho} + w\varepsilon\gamma' \right) - w(1 + \varepsilon\gamma)\lambda \frac{\partial \upsilon^x}{\partial \rho} \\ \frac{\partial f}{\partial \varepsilon} &= (1 - \upsilon^x \lambda) \left((1 + \varepsilon\gamma) \frac{\partial w}{\partial \varepsilon} + w\gamma \right) - w(1 + \varepsilon\gamma)\lambda \frac{\partial \upsilon^x}{\partial \varepsilon} \\ \frac{\partial g}{\partial \rho} &= (1 - \lambda\upsilon^x)(\varepsilon(\gamma - 1) + \rho\varepsilon\gamma') + \frac{\partial \upsilon^x}{\partial \rho} \left(D_\diamondsuit w_\diamondsuit h_\diamondsuit (\upsilon^x_\diamondsuit - \lambda) + \lambda P_\diamondsuit - \lambda\rho\varepsilon(\gamma - 1) \right) \\ \frac{\partial g}{\partial \varepsilon} &= (1 - \lambda\upsilon^x)(\gamma - 1)\rho + \frac{\partial \upsilon^x}{\partial \varepsilon} \left(D_\diamondsuit w_\diamondsuit h_\diamondsuit (\upsilon^x_\diamondsuit - \lambda) + \lambda P_\diamondsuit - \lambda\rho\varepsilon(\gamma - 1) \right). \end{aligned}$$

Using the definition (3.1.29) for the Lorentz factor its derivatives read

$$\begin{aligned} \frac{\partial w}{\partial \rho} &= \frac{-A^2(1 - (\upsilon^x)^2\varepsilon\gamma' + (1 + \varepsilon\gamma)\upsilon^x((1 + \varepsilon\gamma)^2 + A^2)\frac{\partial \upsilon^x}{\partial \rho}}{(1 + \varepsilon\gamma)^3(1 - (\upsilon^x)^2)^2} \\ \frac{\partial w}{\partial \varepsilon} &= \frac{-A^2(1 - (\upsilon^x)^2\gamma + (1 + \varepsilon\gamma)\upsilon^x((1 + \varepsilon\gamma)^2 + A^2)\frac{\partial \upsilon^x}{\partial \varepsilon}}{(1 + \varepsilon\gamma)^3(1 - (\upsilon^x)^2)^2}. \end{aligned}$$

We derive v^x from expression (3.2.2) by the factor K (3.2.3) to obtain its derivatives using the chain rule

$$\frac{\partial v^x}{\partial K} = \frac{-2\lambda\sqrt{K(1-\lambda^2+K)}+1+\lambda^2(K-1)+K}{2(1+K)^2\sqrt{K(1-\lambda^2+K)}}$$
$$\frac{\partial K}{\partial \rho} = \frac{2D_\Diamond^2(v_\Diamond^x-\lambda)^2}{\rho^2}\frac{1+\varepsilon\gamma}{A^2+(1+\varepsilon\gamma)^2}\left(\frac{A^2\varepsilon\gamma'}{A^2+(1+\varepsilon\gamma)^2}-\frac{1+\varepsilon\gamma}{\rho}\right)$$
$$\frac{\partial K}{\partial \varepsilon} = \frac{2D_\Diamond^2(v_\Diamond^x-\lambda)^2}{\rho^2}\frac{2(1+\varepsilon\rho)\gamma A^2}{(A^2+(1+\varepsilon\gamma)^2)^2}.$$

The Jacobian is evaluated at the initial guess of the method. This is selected as a perturbation of the solution of the last system solved, or a perturbation of the integral curve state for the first point of the mixed curve. Fixing the evaluation point of the Jacobian ensures that the solution is searched in a fixed direction that points towards the first root. Inverting the matrix analytically we can write explicitly the method

$$\begin{pmatrix}\rho\\ \varepsilon\end{pmatrix}^{k+1)} = \begin{pmatrix}\rho\\ \varepsilon\end{pmatrix}^{k)} - \frac{\alpha}{a_{11}a_{22}-a_{12}a_{21}}\cdot\begin{pmatrix}a_{22}\cdot f(\mathbf{x}^{0)})-a_{12}\cdot g(\mathbf{x}^{0)})\\ -a_{21}\cdot f(\mathbf{x}^{0)})+a_{11}\cdot g(\mathbf{x}^{0)})\end{pmatrix}.$$

When solving the state where the mixed curve becomes sonic, the derivatives in the Jacobian become very steep in the last steps and two nontrivial solutions are very close (analogous to the 1D case shown in figure 2.4), making the root finder unstable. In some cases, the solution may blow up after a few iterations since $\mathbf{G}(\mathbf{x})$ increases drastically far from the solution, or the method may converge to the second root because both are very close. To overcome this issue, we decrease α for a smaller step that can converge to the desired root.

3.4 Examples

The methodology for constructing the solution of the Riemann problem described in Section §2.2 can be applied in any number of spatial dimensions, since the solution is determined in a phase space. The same rules for pushing terminated shocks to the stack that can be continued later in the sequence apply in all dimensions. The only difference is that, when solving for a new state b of a curve, its corresponding tangential velocity must also be calculated.

Therefore, we can proceed to present examples using EoSs GGL1 and GGL2 to solve the blast wave problems `BW1-GGL1` and `BW2-GGL2` presented in Section §2.5. In this Section, we prescribe three different initial tangential speeds at both sides, i.e., 0, 0.9, and 0.99, in the same fashion as [91]. We provide the exact solution of the Riemann problems and analyze the effects of additional velocity components.

The different combinations of initial tangential speeds considered are gathered in table 3.1 and henceforth, we use the labeling in this table for the different cases.

The presence of tangential velocity in the fluid reduces the velocity component normal to the initial discontinuity, resulting in a modified intersection of the wave curves in phase space. This change affects not only the equilibrium state but also the development of wave curves. The left and right sequences of wave curves depend solely on the left and right initial conditions, respectively, which means that fixing an initial condition also fixes the corresponding wave curves sequence. However, changes in one sequence may cause it

Case	v_L^t	v_R^t
C1	0	0
C2	0.9	0
C3	0.99	0
C4	0	0.9
C5	0	0.99
C6	0.9	0.9
C7	0.9	0.99
C8	0.99	0.9
C9	0.99	0.99

Table 3.1: Labeling of the different initial conditions for the tangential speed prescribed to blast wave Riemann problems.

to intersect the opposite wave curves sequence earlier, thereby altering the overall wave structure.

We present the wave curves in phase space, demonstrating how they advance less in the x-velocity as we prescribe more tangential velocity. We also provide tables detailing the origin and termination of waves for reference and depict the profiles for density, velocity and pressure in the spatial domain.

3.4.1 Blast wave 1 GGL1 with tangential speed

This blast wave problem in 1D shows a composite wave moving to the left, formed by a shock and a rarefaction. To the right, it presents a shock wave, although the wave curves were four: a Hugoniot curve, an integral curve, a mixed curve and the Hugoniot curve resumed which reaches the equilibrium state.

Since the nonlinearity factor only depends on the EoS, $\eta(\mathbf{u}_L) < 0$ and $\eta(\mathbf{u}_R) < 0$ as in the 1D problem for all initial tangential speed configurations. Therefore, the first wave curve is a Hugoniot curve both to the left and the right.

Wave curves obtained

The wave curves calculated in phase space are shown in figure 3.1. From left to right, the tangential speed in the right initial condition changes from 0, to 0.9 and 0.99 respectively. From top to bottom, we do the same for the tangential speed of the left initial condition. We can see major changes in the wave structure when the left initial state presents tangential speed.

The details of the origin and termination states of the wave curves are gathered in table 3.2 for the waves to the left and table 3.3 for the waves to the right.

In the wave curves sequence moving to the left, there is always a Hugoniot curve followed by an integral curve. The pressure and density at which the Hugoniot curve terminates remain the same, as they depend on the nonlinearity factor. The shock speed at this point, as well as the x-velocity of the fluid, decrease as the tangential speed increases. The variation in v_R^t displaces the equilibrium state along the integral curve since it modifies the right sequence of wave curves and, consequently, the intersection point.

The wave curves sequence moving to the right presents four wave curves when $v_L^t = 0$, and just the first Hugoniot curve otherwise. This is because the left sequence of curves is

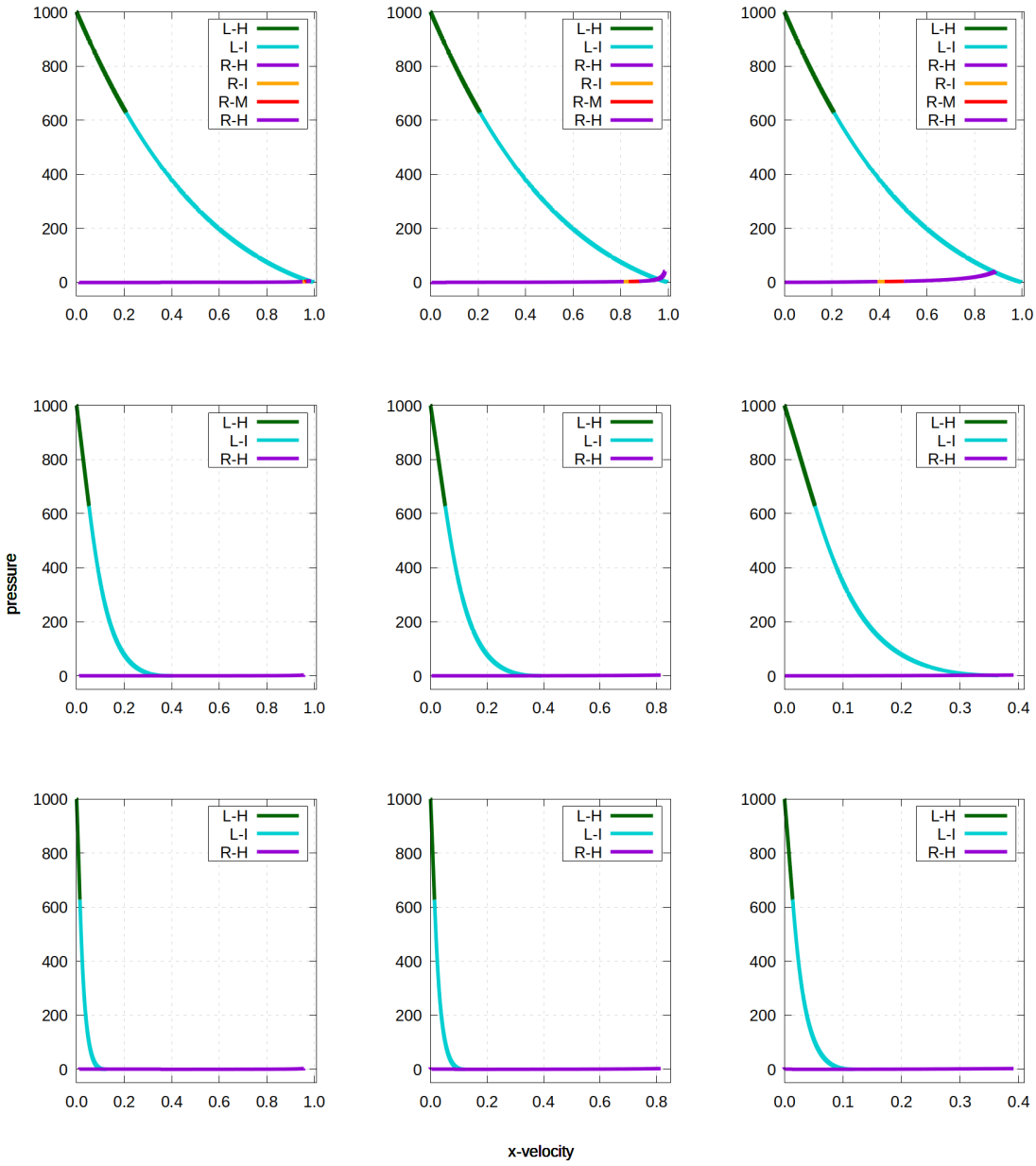

Figure 3.1: Wave curves for `BW1-GGL1` with tangential speed in phase space. From left to right $v_R^t = 0, 0.9, 0.99$. Top to bottom $v_L^t = 0, 0.9, 0.99$.

slower in phase space and intersects the first Hugoniot curve to the right before it becomes sonic. We could find the value of v_L^t such that the curves intersect in each of the wave curves of the right sequence, similarly to what we did in the perturbation analysis in Section §2.5.1 for the 1D case.

Translation to spatial domain

In all cases presented, the wave moving to the left is composed by a shock moving to the left attached to a rarefaction whose tail is moving to the right (see wave speed column in table 3.2). The wave moving to the right is always a shock. This is either because

Case	w. curves	Origin state			Termination state				
		v^x	P	ρ	v^x	P	ρ	v^t	v_ω
C1	$\mathcal{H}$	0	1000	1.000	0.2085	627.5	0.7834	0	-0.8393
	$\mathcal{I}$	0.2085	627.5	0.7834	0.9794	4.922	0.0378	0	0.9196
C2	$\mathcal{H}$	0	1000	1.000	0.0522	627.5	0.7834	0.9262	-0.5583
	$\mathcal{I}$	0.0522	627.5	0.7834	0.3990	0.0597	0.0015	0.9165	0.3801
C3	$\mathcal{H}$	0	1000	1.000	0.0140	627.5	0.7834	0.9929	-0.2128
	$\mathcal{I}$	0.0140	627.5	0.7834	0.1240	0.0179	0.0006	0.9926	0.1193
C4	$\mathcal{H}$	0	1000	1.000	0.2085	627.5	0.7834	0	-0.8393
	$\mathcal{I}$	0.2085	627.5	0.7834	0.9560	11.85	0.0714	0	0.8304
C5	$\mathcal{H}$	0	1000	1.000	0.2085	627.5	0.7834	0	-0.8393
	$\mathcal{I}$	0.2085	627.5	0.7834	0.8826	38.25	0.1624	0	0.5606
C6	$\mathcal{H}$	0	1000	1.000	0.0522	627.5	0.7834	0.9262	-0.5583
	$\mathcal{I}$	0.0522	627.5	0.7834	0.3840	0.2376	0.0041	0.9225	0.3565
C7	$\mathcal{H}$	0	1000	1.000	0.0522	627.5	0.7834	0.9262	-0.5583
	$\mathcal{I}$	0.0522	627.5	0.7834	0.3452	2.110	0.0204	0.9358	0.2941
C8	$\mathcal{H}$	0	1000	1.000	0.0140	627.5	0.7834	0.9929	-0.2128
	$\mathcal{I}$	0.0140	627.5	0.7834	0.1223	0.0356	0.0010	0.9925	0.1167
C9	$\mathcal{H}$	0	1000	1.000	0.0140	627.5	0.7834	0.9929	-0.2128
	$\mathcal{I}$	0.0140	627.5	0.7834	0.1167	0.1890	0.0034	0.9931	0.1079

Table 3.2: Origin and termination states of the wave curves moving to the left in BW1-GGL1 with tangential speed.

a Hugoniot curve is the only wave curve in the sequence originating at the right initial condition, or because the latest Hugoniot curve is the fastest wave of the sequence (see wave speed column in table 3.3).

We present the profiles of density, pressure and x-velocity in the spatial plane in figure 3.2. When fixing the initial tangential speed at the left, the pressure and density of the equilibrium state increase with v_R^t, due to the higher inertia of the fluid moving to the right. Alternatively, when fixing v_R^t and increasing v_L^t, the equilibrium is reached at smaller pressure and density values as the rarefaction wave stretches.

Case	w. curves	Origin state			Termination state				
		v^x	P	ρ	v^x	P	ρ	v^t	v_ω
C1	$\mathcal{H}_1$	0	0.0100	0.1250	0.9566	2.642	1.272	0	0.9848
	$\mathcal{I}$	0.9566	2.642	1.272	0.9617	2.833	1.613	0	0.9669
	$\mathcal{M}$	-	-	-	0.9731	3.727	2.416	0	0.9848
	$\mathcal{H}_1$	0	0.0100	0.1250	0.9794	4.922	2.733	0	0.9885
C3	$\mathcal{H}$	0	0.0100	0.1250	0.3990	0.0597	0.3552	0	0.5891
C3	$\mathcal{H}$	0	0.0100	0.1250	0.1240	0.0179	0.1852	0	0.3757
C4	$\mathcal{H}_1$	0	0.0100	0.1250	0.8150	2.642	1.272	0.2200	0.9271
	$\mathcal{I}$	0.8150	2.642	1.272	0.8339	2.833	1.613	0.2058	0.8534
	$\mathcal{M}$	-	-	-	0.8777	3.727	2.416	0.1677	0.9271
	$\mathcal{H}_1$	0	0.0100	0.1250	0.9560	11.8515	4.0495	0.0604	0.9758
C5	$\mathcal{H}_1$	0	0.0100	0.1250	0.3914	2.642	1.272	0.7479	0.6248
	$\mathcal{I}$	0.3914	2.642	1.272	0.4216	2.833	1.613	0.7316	0.4565
	$\mathcal{M}$	-	-	-	0.5022	3.727	2.416	0.6794	0.6248
	$\mathcal{H}_1$	0	0.0100	0.1250	0.8826	38.25	6.999	0.1736	0.9343
C6	$\mathcal{H}$	0	0.0100	0.1250	0.3840	0.2377	0.5625	0.7102	0.5493
C7	$\mathcal{H}$	0	0.0100	0.1250	0.3452	2.110	1.081	0.7868	0.5947
C8	$\mathcal{H}$	0	0.0100	0.1250	0.1223	0.0356	0.2774	0.8738	0.2383
C9	$\mathcal{H}$	0	0.0100	0.1250	0.1167	0.1890	0.5280	0.9687	0.1846

Table 3.3: Origin and termination states of the wave curves moving to the right in BW1-GGL1 with tangential speed.

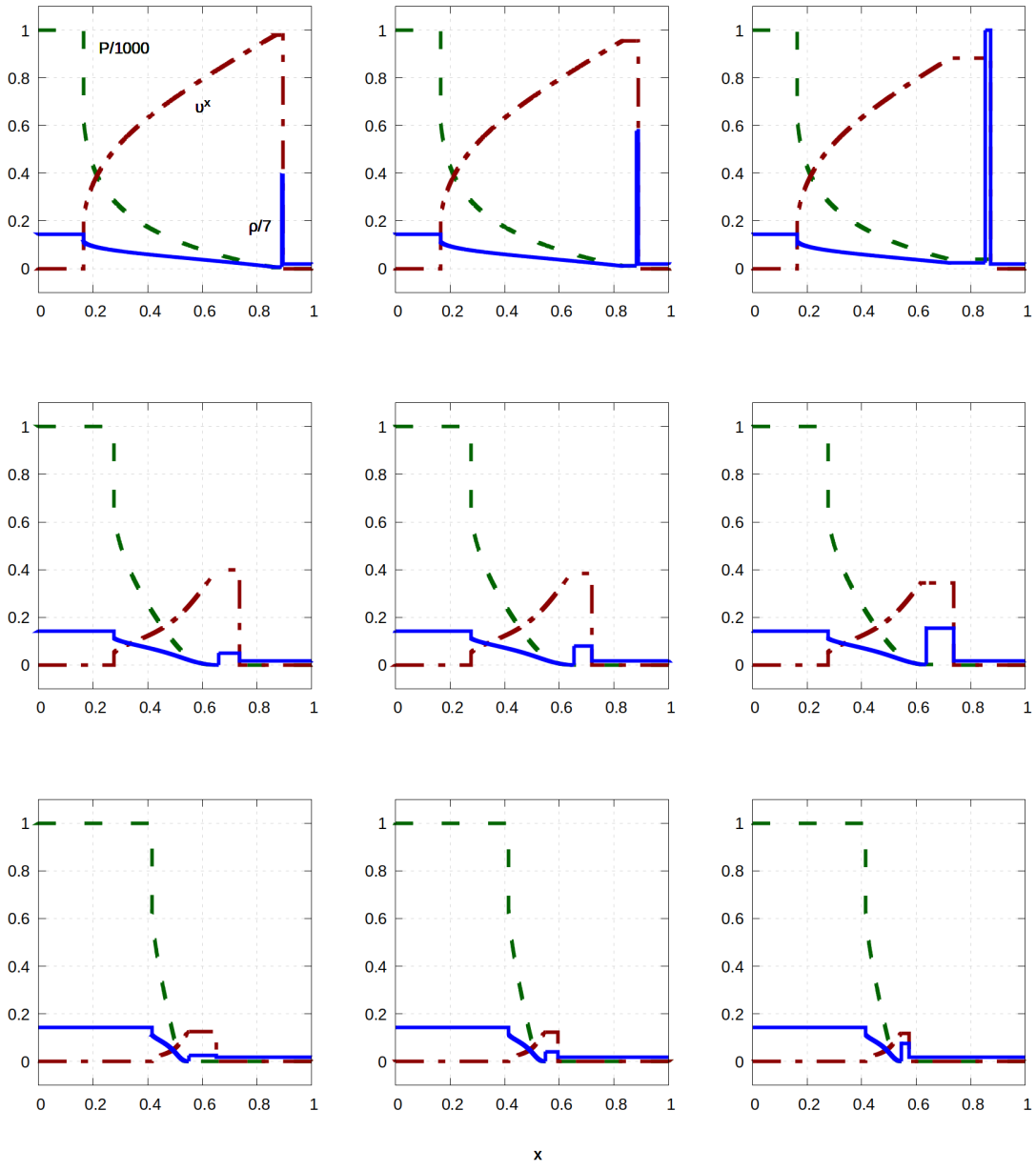

Figure 3.2: Solution profiles for density, pressure and velocity for `BW1-GGL1` considering tangential speed, at $t = 0.4$. From left to right $v_R^t = 0, 0.9, 0.99$. Top to bottom $v_L^t = 0, 0.9, 0.99$. Pressure in green dashed line, x-velocity in red dashdotted line, and density in blue solid line.

3.4.2 Blast wave 2 GGL2 with tangential speed

This blast wave problem presents composite waves moving to the left and the right in 1D. When adding tangential speed, we find that some waves are no longer in the solution, as it happened in the previous example. We find two cases where new wave curves develop.

As in 1D, $\eta(\mathbf{u}_L) > 0$ and $\eta(\mathbf{u}_R) > 0$. Therefore, an integral curve starts to the left decreasing the pressure and a Hugoniot curve starts to the right, increasing it.

Wave curves obtained

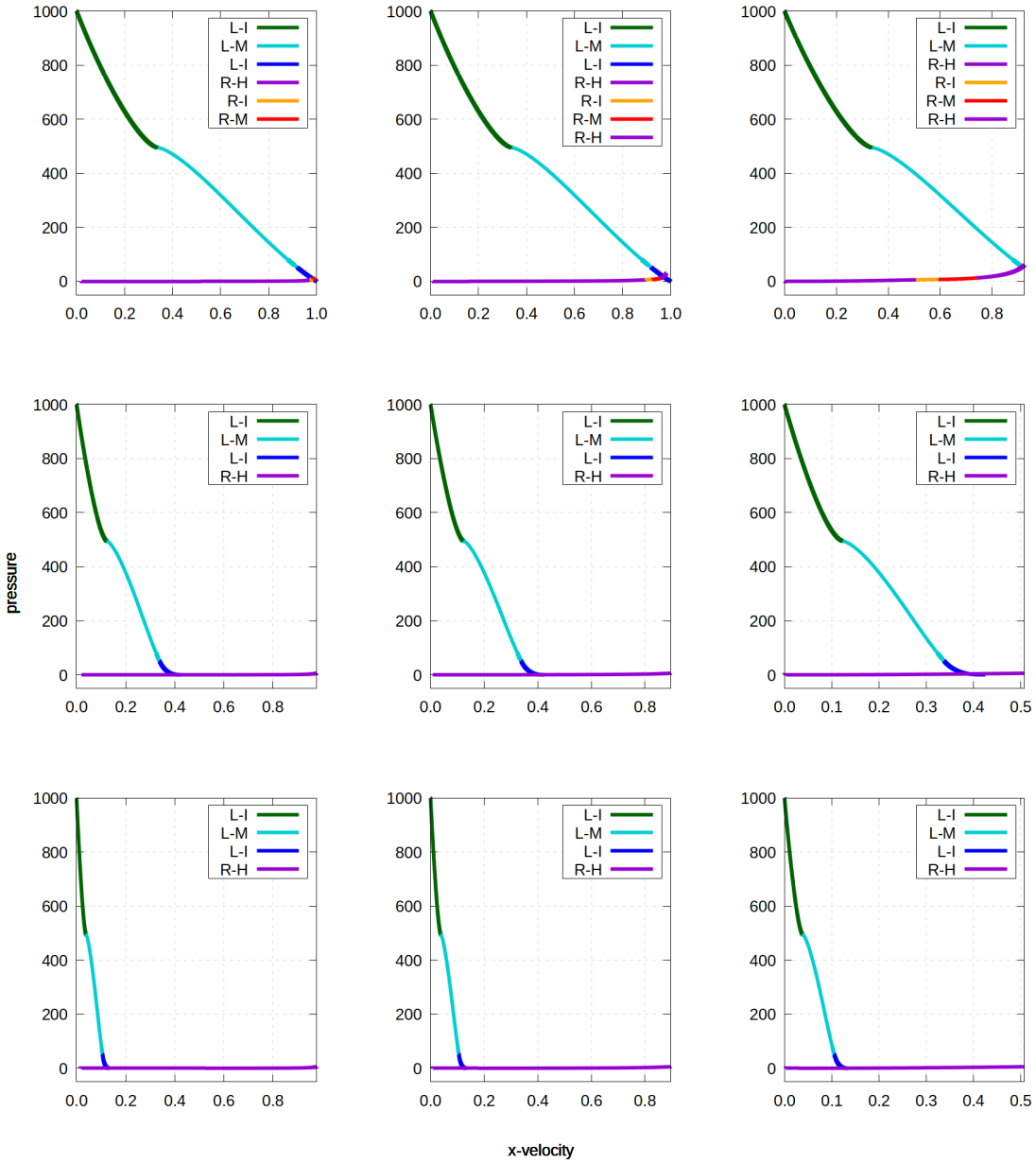

Figure 3.3: Wave curves for `BW2-GGL2` with tangential speed in phase space. From left to right $v_R^t = 0, 0.9, 0.99$. Top to bottom $v_L^t = 0, 0.9, 0.99$.

We show the wave curves in phase space in figure 3.3. From left to right, the tangential speed in the right initial condition changes from 0, to 0.9 and 0.99 respectively. From top to bottom, we do the same for the tangential speed of the left initial condition. The number of waves in the structure depends mostly on v_L^t being zero or not, and in that case then v_R^t plays a role.

We gather the origin and termination state of wave curves in table 3.4 for the left branch, and table 3.5 for the right one.

Case	w. curves	Origin state			Termination state				
		v^x	P	ρ	v^x	P	ρ	v^t	v_ω
C1	$\mathcal{I}_1$	0	1000	5.000	0.3394	494.3	2.266	0	0.2939
	$\mathcal{M}$	-	-	-	0.9200	50.76	0.4424	0	-0.0861
	$\mathcal{I}_2$	0.9200	50.76	0.4424	0.9863	7.438	0.1583	0	0.8635
C2	$\mathcal{I}_1$	0	1000	5.000	0.1242	494.3	2.266	0.9197	0.1055
	$\mathcal{M}$	-	-	-	0.3381	50.76	0.4424	0.9293	-0.0445
	$\mathcal{I}_2$	0.3381	50.76	0.4424	0.4184	0.0669	0.0089	0.9082	0.4063
C3	$\mathcal{I}_1$	0	1000	5.000	0.0387	494.3	2.266	0.9922	0.0327
	$\mathcal{M}$	-	-	-	0.1056	50.76	0.4424	0.9933	-0.0149
	$\mathcal{I}_2$	0.1056	50.76	0.4424	0.1337	0.0192	0.0041	0.9910	0.1310
C4	$\mathcal{I}_1$	0	1000	5.000	0.3394	494.3	2.266	0	0.2939
	$\mathcal{M}$	-	-	-	0.92003	50.76	0.4424	0	-0.0861
	$\mathcal{I}_2$	0.92003	50.76	0.4424	0.9706	16.91	0.2499	0	0.6557
C5	$\mathcal{I}$	0	1000	5.000	0.3394	494.3	2.266	0	0.2939
	$\mathcal{M}$	-	-	-	0.9134	50.76	0.4424	0	-0.0861
C6	$\mathcal{I}_1$	0	1000	5.000	0.1242	494.3	2.266	0.9197	0.1055
	$\mathcal{M}$	-	-	-	0.3381	50.76	0.4424	0.9293	-0.0445
	$\mathcal{I}_2$	0.3381	50.76	0.4424	0.4118	0.2998	0.0229	0.9110	0.3902
C7	$\mathcal{I}_1$	0	1000	5.000	0.1242	494.3	2.266	0.9197	0.1055
	$\mathcal{M}$	-	-	-	0.3381	50.76	0.4424	0.9293	-0.0445
	$\mathcal{I}_2$	0.3381	50.76	0.4424	0.3906	3.354	0.0997	0.9192	0.3283
C8	$\mathcal{I}_1$	0	1000	5.000	0.0387	494.3	2.266	0.9922	0.0327
	$\mathcal{M}$	-	-	-	0.1055	50.76	0.4424	0.9933	-0.0149
	$\mathcal{I}_2$	0.1055	50.76	0.4424	0.1330	0.0411	0.0066	0.9911	0.1295
C9	$\mathcal{I}_1$	0	1000	5.000	0.0387	494.3	2.266	0.9922	0.0327
	$\mathcal{M}$	-	-	-	0.1055	50.76	0.4424	0.9933	-0.0149
	$\mathcal{I}_2$	0.1055	50.76	0.4424	0.1304	0.2644	0.0211	0.9914	0.1233

Table 3.4: Origin and termination states of the wave curves moving to the left in BW2-GGL2 with tangential speed.

When $v_L^t = 0$, the left branch of wave curves is the same that the one described for the 1D case: an integral curve that terminates followed by a mixed curve that becomes sonic and is continued by a new integral curve. This curve reaches the equilibrium state.

As v_R^t increases, the right branch of wave curves is slower in phase space. Therefore, although the curves terminate at the same density and pressure values because the non-linearity factor depends on the EoS, they do it at smaller x-velocities. Consequently, the curves extend further in phase space.

In the case $v_R^t = 0.9$ the mixed curve to the right terminates when reaching the origin

of the previous integral curve and is followed by a Hugoniot curve. This is the first wave curve of the sequence, resumed as the wave speed of the mixed curve is reached by stack. In the case $v_R^t = 0.99$ this Hugoniot curve is resumed earlier in phase space and its pressure grows enough to intersect the left sequence at the mixed curve before it becomes sonic.

In the cases $v_L^t \neq 0$ the wave curves to the left slow down in phase space and therefore intersect the right sequence of curves at much lower x-velocity, before the first Hugoniot curve to the right becomes sonic.

Case	w. curves	Origin state			Termination state				
		v^x	P	ρ	v^x	P	ρ	v^t	v_ω
C1	$\mathcal{H}$	0	0.0100	0.1250	0.9780	5.635	1.457	0	0.9958
	$\mathcal{I}$	0.9780	5.635	1.457	0.9843	6.992	2.266	0	0.9857
	$\mathcal{M}$	-	-	-	0.9863	7.438	2.902	0	0.9907
C2	$\mathcal{H}$	0	0.0100	0.1250	0.4184	0.0669	0.3146	0	0.6546
C3	$\mathcal{H}$	0	0.0100	0.1250	0.1337	0.0192	0.1801	0	0.4282
C4	$\mathcal{H}_1$	0	0.0100	0.1250	0.8956	5.6345	1.4570	0.1113	0.9785
	$\mathcal{I}$	0.8956	5.6345	1.4570	0.9235	6.9924	2.266	0.0888	0.9301
	$\mathcal{M}$	-	-	-	0.9609	12.50	4.315	0.0538	0.9785
	$\mathcal{H}_1$	0	0.0100	0.1250	0.9706	16.91	4.957	0.0404	0.9841
C5	$\mathcal{H}$	0	0.0100	0.1250	0.5083	5.635	1.4570	0.5682	0.8382
	$\mathcal{I}$	0.5083	5.635	1.4570	0.5935	6.992	2.266	0.5062	0.6172
	$\mathcal{M}$	-	-	-	0.7425	12.50	4.315	0.3738	0.8382
	$\mathcal{H}_1$	0	0.0100	0.1250	0.9134	50.76	8.314	0.1286	0.9526
C6	$\mathcal{H}$	0	0.0100	0.1250	0.4118	0.2998	0.4929	0.6592	0.6496
C7	$\mathcal{H}$	0	0.0100	0.1250	0.3906	3.3542	1.0825	0.6868	0.7840
C8	$\mathcal{H}$	0	0.0100	0.1250	0.1330	0.0411	0.2601	0.8660	0.2838
C9	$\mathcal{H}$	0	0.0100	0.1250	0.1304	0.2644	0.4763	0.9578	0.2490

Table 3.5: Origin and termination states of the wave curves moving to the right in BW2-GGL2 with tangential speed.

Translation to spatial domain

We present the profiles of density, pressure and x-velocity in the spatial plane in figure 3.4.

From the study of the wave curves, we know there is always a composite wave moving to the left formed by two rarefactions separated by a shock. The shock is located very close to the initial discontinuity. The wave to the right is a shock due to a single Hugoniot curve except for the cases with $v_L^t = 0$. In these cases, the wave to the right is a shock because the final Hugoniot curve is the fastest wave and overtakes the previous ones.

The composite front of the shell appearing in the $v_L^t = v_R^t = 0$ case does not occur with the other tangential speed configurations.

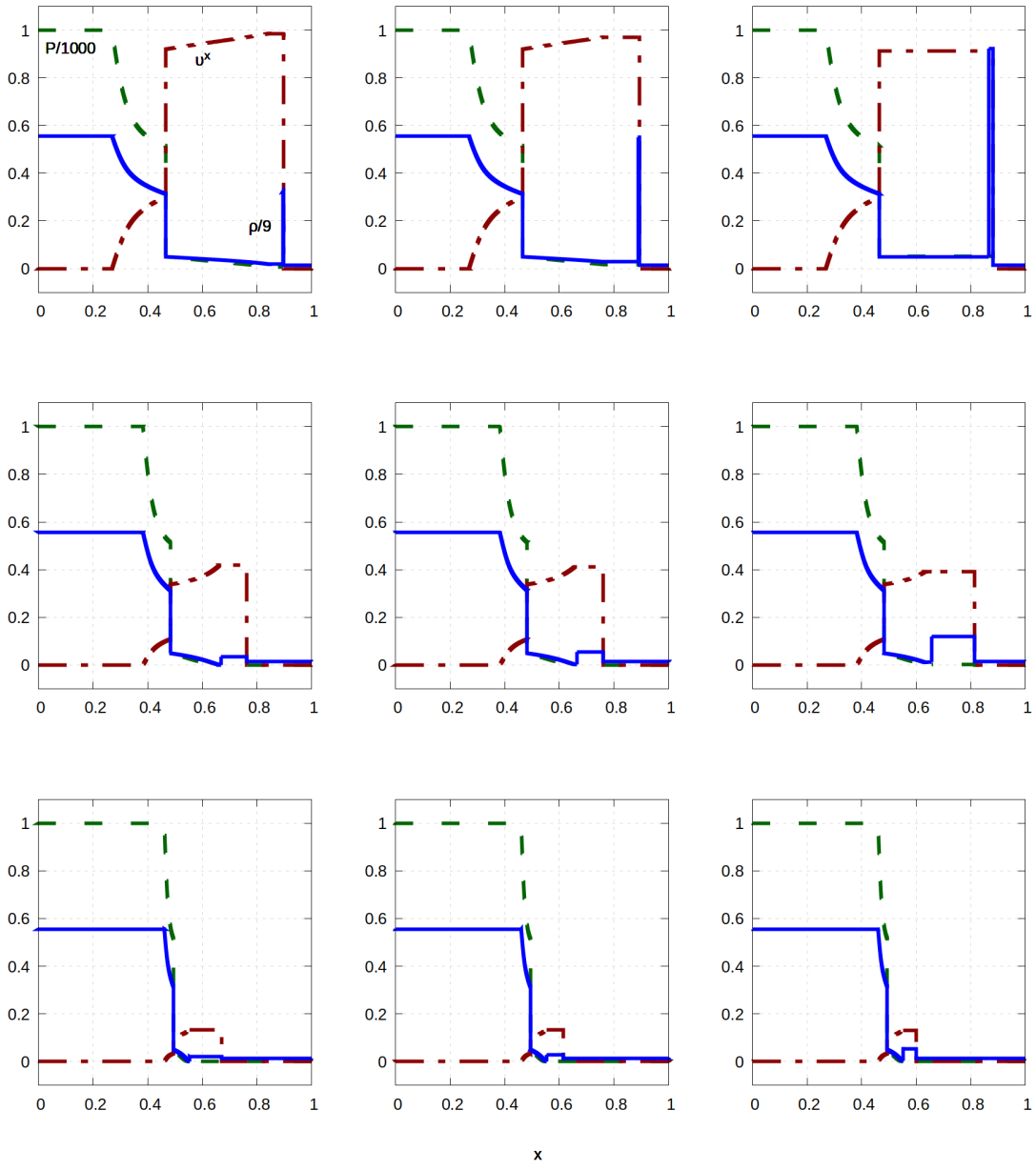

Figure 3.4: Solution profiles for density, pressure and velocity for `BW2-GGL2` considering tangential speed, at $t = 0.4$. From left to right $v_R^t = 0, 0.9, 0.99$. Top to bottom $v_L^t = 0, 0.9, 0.99$. Pressure in green dashed line, x-velocity in red dashdotted line, and density in blue solid line.

Chapter 4

Numerical approximation of nonconvex SRHD

The evolution of a fluid in relativistic hydrodynamics (RH) is governed by several highly nonlinear coupled partial differential equations, which cannot be solved analytically for complex astrophysical systems. As a result, numerical simulations have become an essential tool for the study of RH.

However, the reliability of the simulations hinge on the trustworthiness of the numerical methods used to solve the equations. Therefore, validating numerical methods is a critical step in ensuring the accuracy of simulations of astrophysical phenomena. Achieving accurate numerical simulations of RH necessitates the use of high-resolution schemes capable of capturing the complex dynamics that arise in these scenarios.

In this Chapter, we focus on *high-resolution shock-capturing* (HRSC) schemes, based on the conservation form of the evolution equations. We present the validation of two widely used numerical schemes, the *Marquina flux formula* (MFF) and the *Harten-Lax-van Leer* (HLL) scheme.

MFF [27] is known for its compressible character and for providing enough dissipation to avoid the carbuncle phenomenon [93]. It has been employed in several astrophysical scenarios, such as relativistic jets [78, 79], ultrarelativistic flow in 1D and 2D dimensions [79], and have been implemented in 3D General Relativity hydrodynamic codes [11, 35, 2, 71, 82]. The scheme is versatile and it has been used in other contexts such as granular gases [109, 108] and Newtonian magnetohydrodynamics [110, 111, 106].

HLL [46] is a simple, fast scheme widely used for its computational efficiency. It has been utilized in many astrophysical complex scenarios, such as multidimensional hydrodynamics along neutrino transport in the context of supernovae and neutron star mergers [12, 56] and 3D General Relativity magnetohydrodynamic codes including neutrinos [58, 2, 71, 82].

We focus on two different *reconstruction* techniques that enable the numerical schemes to achieve third-order accuracy.

Using the exact solution of the Riemann problem for nonconvex SRHD described in Chapters 2 and 3 we validate both methods, MFF and HLL, and measure their accuracy on scenarios including composite waves. Through our analysis of these schemes we aim to provide insights into their strengths and limitations and contribute to the development of more accurate and efficient numerical methods for RH simulations.

4.1 Numerical fluxes

Solving nonlinear hyperbolic systems of conservation laws numerically presents many challenges including instabilities triggered by nonlinear terms and convergence towards an unphysical solution (see e.g. [66]). To overcome these difficulties various numerical methods have been developed, each of them with its own advantages and disadvantages. In this work, we focus on HRSC methods, which are formulated in conservation form.

Lax-Wendroff theorem [63] states that if a scheme in conservation form converges, the solution obtained is guaranteed to be a weak solution of the conservation law.

To simplify our analysis, let us consider a scalar hyperbolic conservation law in one spatial dimension, given by the equation

$$\frac{\partial u}{\partial t} + \frac{\partial f(u)}{\partial x} = 0, \tag{4.1.1}$$

where u is the unknown quantity and f is a known flux function. To obtain a numerical solution, we introduce a discretization of time step Δt and cell width Δx, such that the solution is evaluated at the points $(t_n, x_j) = (t_0 + n\Delta t, x_0 + j\Delta x)$.

A numerical method is said to be in *conservation form* if the solution at a given spatial position is advanced in time in the form

$$U_j^{n+1} = U_j^n - \frac{\Delta t}{\Delta x}\left[F\left(U_{j-p}^n, U_{j-p+1}^n, \cdots, U_{j+q}^n\right) - F\left(U_{j-p-1}^n, U_{j-p}^n, \cdots, U_{j+q-1}^n\right)\right] \tag{4.1.2}$$

where U_j^n is the numerical approximation of u at the point (t_n, x_j), and F is a function of $p+q+1$ arguments, known as the *numerical flux*. This function should be consistent with the flux in (4.1.1) ($F(u, \cdots, u) = f(u)$).

If we consider U_j^n to be the numerical approximation of the *cell average*

$$\bar{u}_j^n \equiv \frac{1}{\Delta x}\int_{x_{j-1/2}}^{x_{j+1/2}} u(x, t_n)\mathrm{d}x,$$

and we take $p = 0, q = 1$ to simplify notation, one can see that $F(U_j, U_{j+1})$ plays the role of an average flux through the cell interface $x_{j+1/2}$ over the time interval $[t_n, t_{n+1}]$:

$$F(U_j, U_{j+1}) \approx \frac{1}{\Delta t}\int_{t_n}^{t_{n+1}} f(u(x_{j+1/2}, t))\mathrm{d}t.$$

The convergence of the scheme depends on its total variation stability [66]. It is considered stable if its total variation is bounded for any initial data. Schemes in conservation form are constructed to ensure that this condition is satisfied and therefore are named *total variation diminishing* schemes [45]. Additionally, to obtain physically consistent solutions, the weak solution must also satisfy the entropy condition, which corresponds to the limit of vanishing viscosity. This condition is guaranteed if the numerical flux is monotone [66].

HRSC schemes are based on Godunov's method [38]. This paradigm uses the information about the characteristics of the hyperbolic equation to advance the solution in time. At every cell interface, the approximated solution u describes a Riemann problem. Its exact solution provides information on the propagation of the characteristics. The solution u can be advanced to the next time step by averaging the solution of the Riemann problem over the cell space. This process leads to a scheme in conservation form (4.1.2), as the solutions of the Riemann problem are solutions to the conservation law and hence conservative solutions.

To prevent the information of a Riemann problem from influencing a non-neighboring cell, the Courant-Friedrichs-Lewy (CFL) condition relates the time step and cell width to the maximum speed of propagation of the information in the problem.

In practice, solving the Riemann problem exactly at every cell interface is computationally very expensive. Moreover, the fine structure is lost in the spatial averaging. Therefore it is more common to use an approximate Riemann solver.

The specific calculation of the fluxes in (4.1.2) may vary for different hyperbolic systems. Schemes used for Newtonian hydrodynamics have been adapted to relativistic fluids. In this work we focus on MFF [28] and HLL [46, 31] methods, extended to RH in [27] and [105] respectively.

Another commonly used method for RH is the Roe solver [103]. This method linearizes the problem by considering the Jacobian of the flux evaluated at an average state. Roe averages have been calculated for Newtonian dynamics [103] and SRHD [33]. However it is known [32] that Roe linearization can lead to unstable schemes for highly energetic fluids by predicting non-physical states. In particular we found that the method is not stable for nonconvex dynamics. Therefore, in this work we do not use Roe method.

In HRSC methods, numerical fluxes are used to advance the conserved quantities in time. Typically, the physical variables required to compute these fluxes must be obtained from the updated conserved quantities at each new time step. However, in RH, the relation between conserved and physical variables is nonlinear, requiring an iterative numerical method to obtain the physical variables from the conserved quantities. We use the combined fixed point and Newton iterations strategy proposed in [74].

HRSC methods can be extended to higher spatial dimensions using a dimension-by-dimension approach [27], where the one-dimensional method is applied separately to each dimension before combining the results. For example, in a two-dimensional grid with an additional spatial interval Δy, the conservative scheme can be written as:

$$\begin{aligned} U_{j,l}^{n+1} = U_j^n &- \frac{\Delta t}{\Delta x}\left[F\left(U_{j-p,l}^n, U_{j-p+1,l}^n, \cdots, U_{j+q,l}^n\right) - F\left(U_{j-p-1,l}^n, U_{j-p,l}^n, \cdots, U_{j+q-1,l}^n\right)\right] \\ &- \frac{\Delta t}{\Delta y}\left[F\left(U_{j,l-p}^n, U_{j,l-p+1}^n, \cdots, U_{j,l+q}^n\right) - F\left(U_{j,l-p-1}^n, U_{j,l-p}^n, \cdots, U_{j,l+q-1}^n\right)\right]. \end{aligned}$$

4.1.1 Marquina Flux Formula scheme

The fundamental idea of this method is to solve the fluxes appearing in the scheme in conservation form (4.1.2) along the *characteristic fields* of the system.

Let us consider once again a general hyperbolic system of conservation laws

$$\frac{\partial \mathbf{u}}{\partial t} + \frac{\partial \mathbf{f}(\mathbf{u})}{\partial x} = \mathbf{u}_t + \mathbf{A}(\mathbf{u})\mathbf{u}_x = 0 \tag{4.1.3}$$

where $\mathbf{A}(\mathbf{u})$ is the Jacobian of the fluxes. Because the system is hyperbolic $\mathbf{A}(\mathbf{u})$ is diagonalizable, with a complete set of linearly independent eigenvectors. The right and left eigenvectors can be written as matrices, $\mathbf{R}(\mathbf{u})$ and $\mathbf{L}(\mathbf{u})$ respectively. And so

$$\mathbf{L}(\mathbf{u}) \cdot \mathbf{A}(\mathbf{u}) \cdot \mathbf{R}(\mathbf{u}) = \mathbf{\Lambda}(\mathbf{u}),$$

where $\mathbf{\Lambda}(\mathbf{u})$ is the diagonal matrix of eigenvalues. The eigenvectors are chosen such that $\mathbf{r}_i\mathbf{l}_j = \delta_{ij}$, and so $\mathbf{L}(\mathbf{u}) = \mathbf{R}^{-1}(\mathbf{u})$.

Each eigenvalue is a characteristic speed of the system. We can define the *characteristic variables* by $\mathbf{v} = \mathbf{L}(\mathbf{u}) \cdot \mathbf{u}$. Multiplying equation (4.1.3) by $\mathbf{L}(\mathbf{u})$ we obtain the decoupled

system

$$\mathbf{v}_t + \mathbf{\Lambda}(\mathbf{u})\mathbf{v}_x = 0. \tag{4.1.4}$$

The equations in (4.1.4) are linearly independent scalar conservation laws. Once the solution for the characteristic variables is obtained, the original conserved quantities are recovered multiplying by the corresponding right eigenvector [66].

The MFF *flux splitting* strategy [27] consist in performing this decomposition locally at every cell interface, to its left and right. Therefore the MFF computes two different linearizations of the system for every interface.

The resolution of the decoupled scalar hyperbolic equations is done with the *entropy-fix* numerical flux introduced in [115]. An entropy-fix scheme uses an *upwind* flux, with better resolution of discontinuities, if the characteristics move the information in a single direction. This happens if the characteristic velocity, λ_k for the decoupled characteristic field, maintains its sign during the computational cells considered. If this is not the case the interface is called *sonic* and an upwind flux would not be monotone, hence not ensuring that the numerical solution satisfies the entropy condition. In sonic interfaces the *Lax-Friedrichs* flux is applied, which results in a bigger smearing of discontinuities although it is always monotone.

The numerical flux for scalar conservation laws can be applied to the characteristic variables. Defining the scalar quantities

$$\omega_L^p = \mathbf{l}^p(\mathbf{u}_L)\cdot\mathbf{u}_L \qquad \omega_R^p = \mathbf{l}^p(\mathbf{u}_R)\cdot\mathbf{u}_R \tag{4.1.5}$$

$$\phi_L^p = \mathbf{l}^p(\mathbf{u}_L)\cdot\mathbf{F}(\mathbf{u}_L) \qquad \phi_R^p = \mathbf{l}^p(\mathbf{u}_R)\cdot\mathbf{F}(\mathbf{u}_R) \tag{4.1.6}$$

with $p = 1..N$ the dimension of the system, the problem is translated to the characteristic space.

For every characteristic field, the *characteristic numerical fluxes* $\psi_\pm^p$ are defined for the left and right interface of a computational cell. If the characteristic speeds maintain their sign across the cell boundary, an upwind flux can be used and the fluxes are equal to $\phi_{L,R}^p$ defined above. If the interface is sonic, the Lax-Friedrichs flux is used to preserve monotonicity and the numerical fluxes read $\psi_\pm^p = 0.5(\phi_{L,R}^p \pm \alpha\omega_{L,R}^p)$. The viscosity α is taken as the maximum absolute value of the characteristic speeds across the considered cells.

The numerical flux has to be consistent with the coupled system of conservation laws. By multiplying the characteristic numerical flux with the right eigenvectors we can recover the conserved quantities, obtaining Marquina flux formula [28]:

$$\mathbf{F}^{\texttt{MFF}}(\mathbf{u}_L,\mathbf{u}_R) = \sum_{p=1}^{m}\left(\psi_+^p\mathbf{r}^p(\mathbf{u}_L) + \psi_-^p\mathbf{r}^p(\mathbf{u}_R)\right). \tag{4.1.7}$$

To handle changes of convexity in the system across a cell interface, the numerical flux is modified according to [74]. In these cases, the Lax-Friedrichs flux is used with increased viscosity to stabilize the method against large gradients in the solution. The viscosity is taken as the mean in L_2 norm between the maximum absolute value of the characteristic speeds and one, which is the maximum possible speed (since the speed of light is normalized). This approach allows the MFF to handle the complex dynamics that may arise in the solution.

In Algorithm 4.1.1 we present the procedure for the calculation of MFF in SRHD given the conserved variables u and v of two adjacent computational cells, with additional viscosity prescribed for nonconvex interfaces.

Algorithm 4.1.1 Calculation of first order MFF for nonconvex SRHD in 1D taken from [74]

function MFF(u,v)
  for $p = 1, p \leq 3$ **do**
    $\omega_L^p = \mathbf{l}^p(u) \cdot u$
    $\omega_R^p = \mathbf{l}^p(v) \cdot v$
    $\phi_L^p = \mathbf{l}^p(u) \cdot \mathbf{F}(u)$
    $\phi_R^p = \mathbf{l}^p(v) \cdot \mathbf{F}(v)$
    if $\eta(u) \cdot \eta(v) \leq 0$ **then** ▷ Non-convex interface
      $\alpha^p = \max(|\lambda_p(u)|, |\lambda_p(v)|)$
      $\alpha^p = \sqrt{1 + (\alpha^p)^2}/2$
      $\psi_+^p = \frac{1}{2}(\phi_L^p + \alpha^p \omega_L^p)$
      $\psi_-^p = \frac{1}{2}(\phi_R^p - \alpha^p \omega_R^p)$
    else if $\lambda_p(u) \cdot \lambda_p(v) \leq 0$ **then** ▷ Sonic interface
      $\alpha^p = \max(|\lambda_p(u)|, |\lambda_p(v)|)$
      $\psi_+^p = \frac{1}{2}(\phi_L^p + \alpha^p \omega_L^p)$
      $\psi_-^p = \frac{1}{2}(\phi_R^p - \alpha^p \omega_R^p)$
    else ▷ Upwind
      if $\lambda_p(u) > 0$ **then**
        $\psi_+^p = \phi_L^p$
        $\psi_-^p = 0$
      else
        $\psi_+^p = 0$
        $\psi_-^p = \phi_R^p$
  return $\sum_{p=1}^{m} \left(\psi_+^p \mathbf{r}_p(u) + \psi_-^p \mathbf{r}_p(v)\right)$

This numerical flux requires explicit expressions of the eigenvalues and eigenvectors of the Jacobian of the flux. We write here the full decomposition for the 1D case, while the expressions for the 3D case can be found in [27].

The eigenvalues read

$$\lambda_1 = \frac{\upsilon - c_s}{1 - \upsilon c_s} \qquad \lambda_2 = \upsilon \qquad \lambda_3 = \frac{\upsilon + c_s}{1 + \upsilon c_s},$$

and can be seen as the Lorentz addition of the flow and sound speeds.

In order to write the eigenvectors in a compact form we define the Grüneisen coefficient $\Gamma = P_\varepsilon/\rho$, with the subindex denoting partial derivative, and the parameter $\mathcal{K} = \Gamma/(\Gamma - c_s^2)$. Then the right eigenvectors are:

$$\mathbf{r}_1(\mathbf{u}) = \begin{pmatrix} 1 \\ hw(\upsilon - c_s) \\ hw(1 - \upsilon c_s) - 1 \end{pmatrix} \quad \mathbf{r}_2(\mathbf{u}) = \begin{pmatrix} \mathcal{K}/hw \\ \upsilon \\ 1 - \mathcal{K}/hw \end{pmatrix} \quad \mathbf{r}_3(\mathbf{u}) = \begin{pmatrix} 1 \\ hw(\upsilon + c_s) \\ hw(1 + \upsilon c_s) - 1 \end{pmatrix},$$

and the biorthonormal set of left eigenvectors with $\Delta = h^3 w(\mathcal{K} - 1)(1 - \upsilon^2)2c_s$ read :

$$\mathbf{l}_1(\mathbf{u}) = \frac{h^2}{\Delta}\Big(\mathcal{K}(\upsilon + c_s) - \upsilon - hwc_s(1 - \upsilon^2) \quad 1 - \mathcal{K}(1 + \upsilon c_s) \quad \mathcal{K}(\upsilon + c_s) - \upsilon\Big)$$
$$\mathbf{l}_2(\mathbf{u}) = \frac{w}{\mathcal{K} - 1}\left(h - w \quad w\upsilon \quad -w\right)$$
$$\mathbf{l}_3(\mathbf{u}) = -\frac{h^2}{\Delta}\Big(\mathcal{K}(\upsilon - c_s) - \upsilon + hwc_s(1 - \upsilon^2) \quad 1 - \mathcal{K}(1 - \upsilon c_s) \quad \mathcal{K}(\upsilon - c_s) - \upsilon\Big).$$

The advantages of this numerical flux are its compressive nature, that allows to capture very thin structure, and its generality for any type of dynamics.

The main disadvantage is the need of explicit expressions for the eigenvectors of the Jacobian of the flux. Their evaluation and the change to characteristic variable for the calculations make the method computationally costly. Also as the interfaces are treated very locally, the method is very sensitive to the type of high order reconstruction, blowing up if the reconstruction is not very smooth and stable.

4.1.2 Harten-Lax-van Leer scheme

The HLL method constructs the solution of the Riemann problem at every cell interface. Therefore it needs an *estimate* of the characteristic velocities to propagate the solution. The scheme is usually named HLLE, as Einfeldt in [31] proposed the estimates for Newtonian dynamics. This method is not based on characteristic decomposition hence it does not use the eigenvectors of the Jacobian of the fluxes.

The solution of the Riemann problem is composed of four constant states, namely the two initial and the two middle constant states separated by a jump discontinuity. The original HLL solver of [46] considers only three:

$$U(x,t;U_L,U_R) = \begin{cases} U_L & \text{for } x < \xi_- t \\ U_{LR} & \text{for } \xi_- t \le x \le \xi_+ t \\ U_R & \text{for } x > \xi_+ t \end{cases} \tag{4.1.8}$$

where ξ_+ and ξ_- are estimates of the characteristic velocities to the left and the right arising during the problem.

This formulation, although simple and entropy satisfying, disregards the contact discontinuity, causing the smearing of the solution around it. To address this issue, the HLLC solver proposed in [130, 81], where the C stands for contact, introduces a fourth state. Nevertheless the construction of the new state requires further information for the system and in this work we use the simpler HLL instead.

The intermediate state U_{LR} in (4.1.8) is obtained as a solution consistent with the integral conservation equations over the computational cell

$$U_{LR} = \frac{\xi_+ U_R - \xi_- U_L - f(U_R) + f(U_L)}{\xi_+ - \xi_-}.$$

This leads to the HLL flux [46]:

$$\mathbf{F}^{\mathtt{HLL}}(\mathbf{u}_L,\mathbf{u}_R) = \frac{\xi_+ \mathbf{f}(\mathbf{u}_L) - \xi_- \mathbf{f}(\mathbf{u}_R) + \xi_+\xi_-(\mathbf{u}_R - \mathbf{u}_L)}{\xi_+ - \xi_-}. \tag{4.1.9}$$

The velocity estimates ξ_+ and ξ_- play a crucial role in the HLL method providing the viscosity of the scheme. If they are chosen to be excessively high, the method is stable but also becomes too diffusive smearing out discontinuities. On the other hand, if they are chosen to be below the actual characteristic speeds, the scheme becomes unstable and can introduce entropy-violating shocks. Therefore, an appropriate choice of the velocity estimates is necessary for the HLL method to achieve both accuracy and stability.

For the relativistic case, the authors in [105] propose to use

$$\begin{aligned} \xi_+ &= \max(0, \lambda_+(\mathbf{u}_R), \bar{\lambda}_+) \\ \xi_- &= \min(0, \lambda_-(\mathbf{u}_L), \bar{\lambda}_-) \end{aligned} \tag{4.1.10}$$

where $\lambda_\pm$ refers to the fast and slow characteristic fields of the system. The estimate $\bar{\lambda}_\pm$ is the characteristic speed calculated at an average state between the two computational cells. In the non-relativistic case, Einfeldt [31] proposed to use the eigenvalues of the linearized Roe matrix as average estimates for the characteristic speeds. In RH, the average of conserved quantities can result in an unphysical state. To overcome this issue the authors of [105] propose a different approach where an intermediate fluid velocity value $\bar{v} = (v_L + v_R)/2$ and intermediate sound speed $\bar{c_s} = (c_{sL} + c_{sR})/2$ are calculated and then employed to calculate a characteristic speed estimate $\bar{\lambda}_\pm$.

While the HLL method described works satisfactorily for convex SRHD problems, it is unestable when using the GGL EoS near sonic and nonconvex interfaces. When the estimated speeds are set to their maximum possible values $\xi_+ = 1, \xi_- = -1$, this is, estimating that characteristics move at light speed, the scheme becomes stable. This suggests that estimates (4.1.10) may not accurately capture the characteristic speeds when they do not behave monotonically.

We propose new velocity estimates that can handle nonconvex dynamics. Instead of using an intermediate eigenvalue, in (4.1.10) we consider the eigenvalues at the left and right states, allowing for better capture of the behavior of the characteristic fields even when their monotonicity is inverted. Additionally, we consider all characteristic fields to obtain the larger estimate of the speed.

Once the initial estimate of the characteristic speeds is selected, we follow the approach of MFF in Subsection §4.1.1 and increase the numerical viscosity when the interface is either sonic or nonconvex to allow for the formation of complex dynamics. In the case of nonconvex interfaces, the new estimate is obtained as the square root of the mean of the estimate with the maximum possible value (i.e., the speed of light). This average is greater than the usual when the value of the estimate is below one, providing additional viscosity for composite waves. Sonic interfaces are detected when the eigenvalues change sign, resulting in one of the estimates being zero according to (4.1.10). To increase the viscosity in these cases, we can either follow the same strategy as in MFF nonconvex interfaces and select the mean in L_2 norm of the estimate with the light speed ($\sqrt{1+0}/2 = 0.5$), or we can impose the same value as the other estimate, which is different from zero.

After conducting several numerical tests, we found that both of the proposed approaches were effective in handling nonconvex SRHD, although each of them tended to smear out different types of discontinuities. Thus, we adopted a hybrid approach in which we take the minimum of the two estimates since both approaches provide sufficient viscosity. This new hybrid approach results in sharper discontinuities compared to either of the individual estimates.

In algorithm 4.1.2 we present the procedure for the calculation of HLL in nonconvex SRHD given the conserved variables u and v of two adjacent computational cells, already considering our own velocity estimates for nonconvex dynamics.

The advantages of this numerical flux include its simplicity, that leads to very fast calculations. An appropriate selection of the estimates reduces its viscosity and ensures stability even for higher order versions. Additionally, it does not require eigenvectors of the Jacobian of the flux.

However, there are some drawbacks to this method. Numerical experiments have shown that it smears contact discontinuities and does not resolve highly nonlinear phenomena sharply.

Algorithm 4.1.2 Calculation of first order HLL for nonconvex SRHD in 1D

function HLL(u,v)
  $\xi_+ = \max(0, \lambda_p(u), \lambda_p(v))$ for $p = 1, 2, 3$
  $\xi_- = \min(0, \lambda_p(u), \lambda_p(v))$ for $p = 1, 2, 3$
  if $\eta(u) \cdot \eta(v) \leq 0$ **then** ▷ Non-convex interface
    $\xi_+ = \sqrt{(1 + \xi_+)/2}$
    $\xi_- = -\sqrt{(1 + |\xi_-|)/2}$
  else if $\xi_+ = 0$ **then** ▷ Sonic right interface
    $\xi_+ = \min(0.5, |\xi_-|)$
  else if $\xi_- = 0$ **then** ▷ Sonic left interface
    $\xi_- = -\min(0.5, \xi_+)$
  return $\dfrac{\xi_+ f(u) - \xi_- f(v) + \xi_+ \xi_- (v - u)}{\xi_+ - \xi_-}$

4.2 High order reconstructions

Schemes in conservation form (4.1.2) provide first order accurate solutions. To achieve the sharp solutions characteristic of HRSC schemes, the solution at every time step must be updated with a high-order numerical flux. This is accomplished by interpolating the constant states in the cells to reconstruct a more accurate value of the solution at cell interfaces.

Total variation diminishing (TVD) methods [88] use reconstruction procedures up to the desired order of accuracy without introducing local extrema in the data [47, 114, 115, 55, 107]. According to [115], if there exists a reconstruction function $g(x)$ such that

$$f(u(x)) = \frac{1}{\Delta x} \int_{x_{j-1/2}}^{x_{j+1/2}} g(y) \mathrm{d}y$$

for the exact solution $u(x)$, then the derivative of the flux of the hyperbolic equation is

$$\frac{\partial f(u(x))}{\partial x} = \frac{g(x_{j+1/2}) - g(x_{j-1/2})}{\Delta x}.$$

Therefore, a high order reconstruction $g(x)$ provides a numerical flux of the same order of accuracy.

To achieve high-order accuracy in HRSC schemes, the variables used for the evaluation of the numerical flux are reconstructed at high order from the cell averages. When considering a cell interface, the reconstructed values at both sides are used instead of the cell averages. For instance, instead of computing $F(u_{j-1}, u_j)$ and $F(u_j, u_{j+1})$ to advance the value u_j in time, the reconstructed values at the two interfaces are used: $F(u^-_{j-1/2}, u^+_{j-1/2})$ and $F(u^-_{j+1/2}, u^+_{j+1/2})$.

In RH, it is very important to reconstruct the primitive variables, not the conserved ones, when evaluating the numerical flux at high order. Reconstructed conserved variables do not necessarily correspond to physically valid states with existing primitive variables. Instead, the physical variables are reconstructed and the conserved ones can be computed at high order from them if they are needed in the flux.

The evolution in time also needs to be done at a high order of accuracy. For this, we use the Shu-Osher third-order TVD Runge-Kutta method [115]. If $\mathcal{L}(u)$ denotes the time

iteration of a conservative scheme, where $\mathcal{L}(u) = u - \Delta t/\Delta x(F_{j+1/2} - F_{j-1/2})$, then to advance the solution in high order in time

$$
\begin{aligned}
u^{1)} &= \mathcal{L}(u^n) \\
u^{2)} &= \frac{3}{4}u^n + \frac{1}{4}\mathcal{L}(u^{1)}) \\
u^{n+1} &= \frac{1}{3}u^n + \frac{2}{3}\mathcal{L}(u^{2)}).
\end{aligned}
$$

In this work we discuss two different interpolation techniques, both of which are third-order accurate. The first technique is the ENO parabolas [114, 115], which use second-order polynomials to interpolate values at interfaces. The second technique is the piecewise hyperbolic method (PHM) [72], which uses hyperbolas. Both reconstruction methods have adaptive stencils that extract information from smooth regions of the solution while avoiding high gradients whenever possible [88].

In order to use high-order MFF (4.1.7), the left and right eigenvectors are evaluated at reconstructed primitive variables. However, the first-order version of the these quantities, i.e., the constant value in each cell, is used whenever a primitive variable is needed inside the flux. In addition, the quantities ω (4.1.5) and ϕ (4.1.6) are not evaluated at a single position j on the grid. To make the method more robust, these quantities are evaluated at several stencil points. Then they are used to reconstruct a higher order version of the characteristic numerical flux at the cell interfaces. While this approach makes the MFF method highly compressive and sharp at discontinuities, it also increases its computational cost.

For HLL numerical flux (4.1.9), the reconstructed primitive variables are used to evaluate the flux of the system and compute the right and left states of the conserved variables. Still, the evaluation of the eigenvalues that lead to the speed estimates is done using the first order primitive variables instead. This approach yields a more general value of the characteristic speed over the cell and can better capture the movement of the solution. High-order estimates can lead to numerical instability and spurious oscillations, especially in the presence of strong gradients.

While a comprehensive discussion of these techniques can be found in the existing literature, our focus is on presenting a practical review for their implementation.

4.2.1 Essentially non oscillatory parabolic method

The ENO method with parabolic reconstruction uses a second-order polynomial to interpolate the value of a given quantity at a cell interface.

To interpolate the value at the interfaces from the cell average u_j, a total of five consecutive data points are needed. All possible numerical first and second order derivatives involving u_j are calculated, hence the extensive numerical stencil. The *minmod* slope limiter [132] is used to select the smaller first derivative in absolute value, and then the related smaller second derivative. The derivatives and u_j determine a parabola that ensures the least variation, avoiding when possible the introduction of local extrema. In the presence of discontinuities, the method decays to a first order approximation.

4.2.2 Piecewise hyperbolic method

The PHM method employs hyperbolas to interpolate data and achieve third-order accuracy. However, since hyperbolas are monotonic functions, the reconstruction may degrade

to second-order accuracy if the derivative of the solution changes sign across a cell interface.

From [72] we consider the reconstruction that is local total variation bounded, which ensures stability for nonlinear fluxes. To interpolate values at the interfaces of the cell of u_j it uses a compact stencil of three points. The method considers first derivatives to both sides of u_j and chooses the smaller one in absolute value. In nonsmooth regions, this reconstruction reduces the derivative by using the harmonic mean of the derivatives at both sides of the cell.

The compact stencil makes PHM a more local reconstruction than ENO parabolas. This can help to the overall method stability in regions of steep gradients.

4.3 Comparison with exact solution

In this Section, we evaluate the performance of MFF and HLL numerical fluxes using third-order ENO and PHM reconstruction procedures solving a set of Riemann problems for nonconvex SRHD. The exact solution of the Riemann problems computed in Chapters 2 and 3 allows to quantify the error of the approximation obtained with these numerical methods. Notice that we code our own implementation of the methods from scratch.

For the one dimensional case we use the blast wave problems in Chapter 2. The blast wave Riemann problem, first proposed by Norman and Winkler [85], is a well-known test problem for numerical schemes due to the thin, high-density shell that arises because of relativistic effects.

In addition, we test the numerical schemes using the colliding and expanding slabs problems in the same Chapter to evaluate their stability for high Lorentz factors and oscillations at rest states.

To test the accuracy of the methods in higher dimensions, we implement both schemes in 2D. We solve the blast wave problems with different initial tangential speed prescriptions presented in Chapter 3 and compare the error with the exact solution along a transverse cut of the numerical solution.

4.3.1 One dimensional examples

We solve the Riemann problems `BW1-GGL1`, `BW2-GGL2`, `CS-GGL2` and `ES-GGL1` gathered in table 2.4. The spatial domain is $x \in [0, 1]$ with initial discontinuity at $x = 0.5$. We integrate until a final time of $t_f = 0.4$.

We evaluate the accuracy of the numerical solutions by computing the mean L1-norm error of the physical variables. The spatial grid for the blast wave problems consists of 6000 points, while for the colliding and expanding slabs it consists of 3000 points. The corresponding error values for `BW1-GGL1`, `BW2-GGL2`, `CS-GGL2` and `ES-GGL1` problems are presented in tables 4.1, 4.2, 4.3 and 4.4, respectively.

The numerical error is consistent across all problems, methods and reconstructions. The pressure exhibits higher errors due to its larger values except for `ES-GGL1`, where the pressure decreases and so does the error. However, HLL flux with ENO reconstruction fails when attempting to solve the `CS-GGL2` problem. A fluid speed greater than the speed of light is reconstructed during integration, preventing from obtaining a numerical physically consistent solution. Nonetheless, other authors [51] have reported similar superluminal speeds with high-order reconstructions and have reverted to lower-order reconstructions in such cases.

Scheme	Reconstruction	$\|\|E(P)\|\|_1$	$\|\|E(v)\|\|_1$	$\|\|E(\rho)\|\|_1$
MFF	ENO3	3.2379e-01	1.6444e-03	4.1033e-03
MFF	PHM	1.5965e-01	2.0915e-03	4.8524e-03
HLL	ENO3	6.0884e-01	3.5536e-03	8.2299e-03
HLL	PHM	1.4913e-01	2.9541e-03	7.6074e-03

Table 4.1: L1-norm mean error in the physical quantities for `BW1-GGL1`, with a spatial resolution of 6000 points.

Scheme	Reconstruction	$\|\|E(P)\|\|_1$	$\|\|E(v)\|\|_1$	$\|\|E(\rho)\|\|_1$
MFF	ENO3	2.5594e-01	2.4546e-03	6.7945e-03
MFF	PHM	1.8216e-01	2.2937e-03	6.3260e-03
HLL	ENO3	2.3389e-01	3.0792e-03	7.7297e-03
HLL	PHM	1.5512e-01	2.7678e-03	7.3208e-03

Table 4.2: L1-norm mean error in the physical quantities for `BW2-GGL2`, with a spatial resolution of 6000 points.

Scheme	Reconstruction	$\|\|E(P)\|\|_1$	$\|\|E(v)\|\|_1$	$\|\|E(\rho)\|\|_1$
MFF	ENO3	1.9497e-01	1.5326e-03	6.3286e-03
MFF	PHM	1.2267e-01	8.8395e-04	3.9880e-03
HLL	ENO3	-	-	-
HLL	PHM	2.3500e-01	1.9759e-03	6.4581e-03

Table 4.3: L1-norm mean error in the physical quantities for `CS-GGL2`, with a spatial resolution of 3000 points.

Scheme	Reconstruction	$\|\|E(P)\|\|_1$	$\|\|E(v)\|\|_1$	$\|\|E(\rho)\|\|_1$
MFF	ENO3	6.3559e-02	3.1787e-03	5.6769e-03
MFF	PHM	5.2727e-02	2.1986e-03	4.5485e-03
HLL	ENO3	7.4699e-02	4.2147e-03	6.8602e-03
HLL	PHM	5.0680e-02	2.0261e-03	4.4956e-03

Table 4.4: L1-norm mean error in the physical quantities for `ES-GGL1`, with a spatial resolution of 3000 points.

Since the main challenge for the numerical approximation is the density shell of the blast wave problems we perform a deeper analysis of these regions. According to [76], the analysis of a blast wave problem can be reduced to the accuracy of the density shell. The main three features that the numerical scheme has to capture are the compression of the fluid that happens at the contact discontinuity, the width of the shell and the maximum density that is reached in it.

The *compression ratio* σ is defined as the ratio of the densities before and after the contact discontinuity C

$$\sigma = \frac{\rho_{\text{after C}}}{\rho_{\text{before C}}}.$$

For the exact solution, $\rho_{\text{after C}}$ and $\rho_{\text{before C}}$ correspond to the density values in the

equilibrium state from each side. In the numerical solution, we take $\rho_{\text{before C}}$ as the density from where the density starts increasing to form the shell. For $\rho_{\text{after C}}$, we take the maximum value that is achieved along it. We compute the percentage error in the compression ratio as $(1 - \sigma_{\text{num}}/\sigma_{\text{exact}})100$. A positive value indicates that the numerical compression was lower than in the exact solution.

Scheme	Δx	error σ %	width (times exact)	undershoot %
MFF-PHM	$\frac{1}{6000}$	0.99	2.76	7.85
	$\frac{1}{18000}$	-0.72	1.62	-0.44
	$\frac{1}{32000}$	-2.84	1.58	-2.30
MFF-ENO	$\frac{1}{6000}$	1.43	3.38	1.34
	$\frac{1}{18000}$	-0.37	2.06	-0.20
	$\frac{1}{32000}$	-0.31	1.66	-0.13
HLL-PHM	$\frac{1}{6000}$	6.69	5.09	9.55
	$\frac{1}{18000}$	-3.36	1.83	-4.08
	$\frac{1}{32000}$	-2.63	1.54	-2.78
HLL-ENO	$\frac{1}{6000}$	14.26	3.87	15.87
	$\frac{1}{18000}$	-3.86	2.10	-4.03
	$\frac{1}{32000}$	-2.29	1.77	-2.15

Table 4.5: Error of parameters of density shell `BW1-GGL1` with scheme and resolution.

The *width of the density shell* at time t is calculated as $(v_{\text{front}} - v_{\text{contact}})t$. If the front of the shell is composed of several waves, we use the wave speed of the fastest one to calculate the front speed, which determines the maximum width of the shell. To obtain the fraction of the integration domain occupied by the shell, we divide the width of the shell by the length of the spatial domain.

To calculate the width of the shell in the numerical approximation, we take the position of $\rho_{\text{before C}}$ as the beginning of the shell. We select as the end of the shell the first position after the contact discontinuity not affected by the evolution. This interval indicates the number of points used to solve the shell. Dividing this number by the total number of points in the grid gives us the fraction of the numerical domain that the shell occupies. We present the quantity $w_{\text{num}}/w_{\text{exact}}$, which shows how many times the numerical width is greater than the exact width of the shell.

Finally we calculate the difference of the higher density of the shell, $\rho_{\text{after C}}$. The high order reconstructions may introduce spurious oscillations yielding local extrema near the high gradient of the contact discontinuity. This effect can introduce both an overshoot or an undershoot of the density in the shell. Following [76] we measure the relative difference

percentage as $(1 - \rho_{num}^{max}/\rho_{\text{after C}})100$ and name the quantity *undershoot*. Notice that a negative value means that there is an overshoot.

Scheme	Δx	error σ %	width (times exact)	undershoot %
MFF-PHM	$\frac{1}{6000}$	33.67	2.85	31.98
	$\frac{1}{18000}$	4.18	1.84	4.19
	$\frac{1}{32000}$	0.80	1.54	0.81
MFF-ENO	$\frac{1}{6000}$	30.85	3.29	29.22
	$\frac{1}{18000}$	4.27	2.08	3.80
	$\frac{1}{32000}$	2.28	1.74	1.82
HLL-PHM	$\frac{1}{6000}$	39.99	3.25	37.60
	$\frac{1}{18000}$	14.85	2.05	14.06
	$\frac{1}{32000}$	1.97	1.68	1.72
HLL-ENO	$\frac{1}{6000}$	43.86	3.73	41.13
	$\frac{1}{18000}$	22.23	2.25	20.89
	$\frac{1}{32000}$	6.75	1.82	6.62

Table 4.6: Error of parameters of density shell `BW2-GGL2` with scheme and resolution.

We perform the analysis for consequently thinner grids to observe the convergence of the numerical solution to the exact one as the spatial discretization reduces. The results for the described quantities related to the density shells in problems `BW1-GGL1` and `BW2-GGL2` are in tables 4.5 and 4.6 respectively. The density shell of `BW2-GGL2`, due to its composite front wave, is a difficult test for both numerical fluxes and reconstructions.

For the shell in `BW1-GGL1`, see table 4.5 , the error in the compression σ decreases in absolute value with increasing resolution for all methods. The increased error of MFF-PHM with the higher resolution is due to an oscillation at the top of the shell. The width error also decreases with the resolution, and the undershoot of the maximum density drops fast. Notice that for thin discretizations the undershoot becomes negative, meaning that there are oscillations causing overshooting. For small spatial interval, all fluxes and reconstructions lead to similar error values in all measured quantities. Among the methods, MFF-ENO achieves better compression and maximum density value, while HLL-PHM provides a thinner shell.

The composite shell in `BW2-GGL2`, errors in table 4.6, yields larger errors for the sparser discretization. These erros reduce when increasing the resolution. In this table, there are

no negative values, indicating that the methods could not reach the high compression and maximum density. For this problem, where the thin shell has a complex structure (a composite wave), MFF-PHM outperforms the other alternatives. The more local character of the PHM reconstruction, together with the efficient local treatment of the flux at the cell interface of the MFF, provides a much more accurate approximation. In the case of the HLL flux, PHM reconstruction leads to significantly better results than ENO in terms of compression and undershoot of the density. At steep gradients like those presented in this shell, the more local reconstruction (PHM) can reduce the smearing.

Finally we display the plots of the physical variables for the four Riemann problems solved. For the blast waves we select the numerical solution of 18000 points. We exhibit the profiles using PHM reconstruction since it has shown to provide less smeared solutions. They are displayed in figures 4.1 and 4.2.

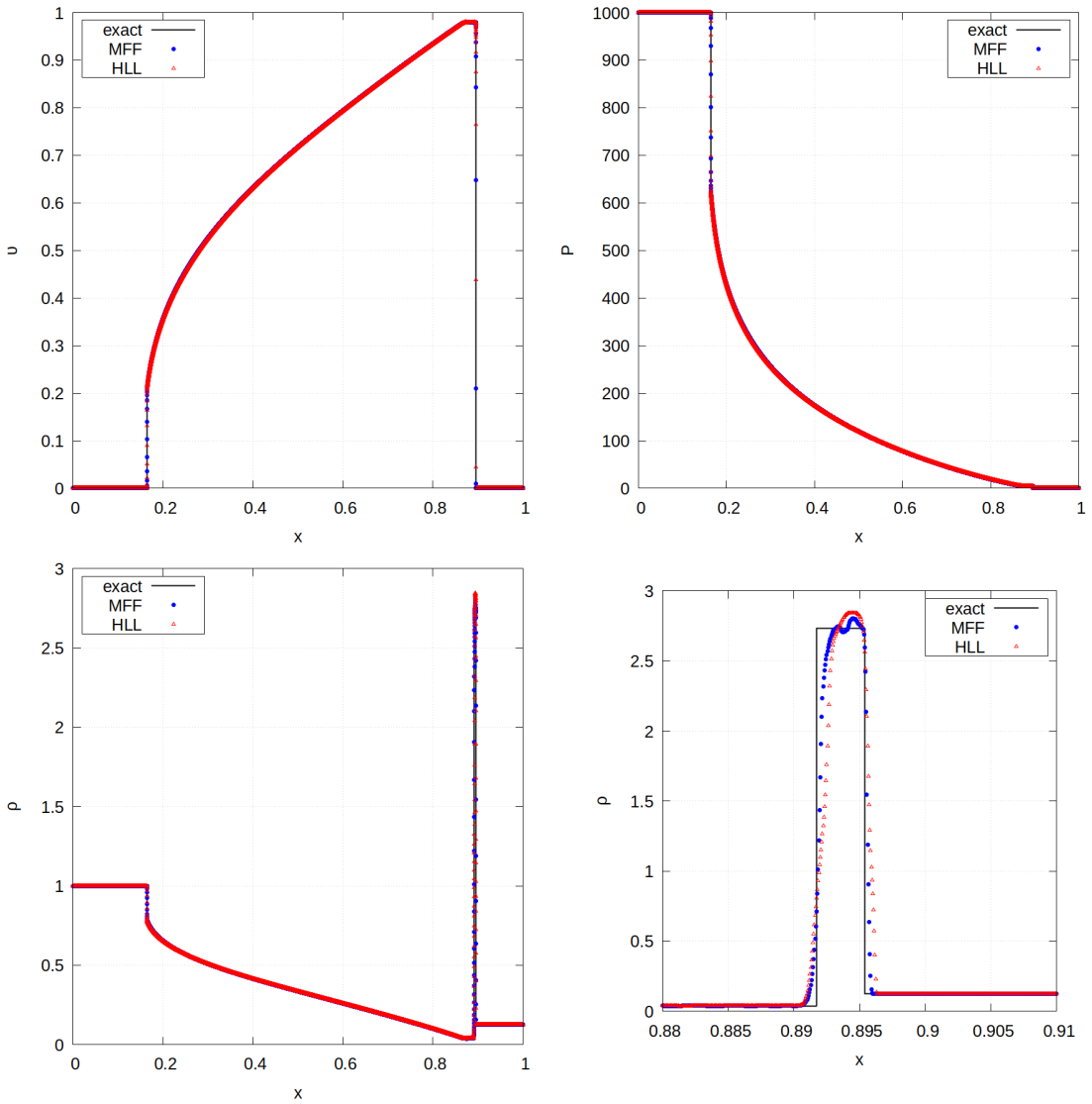

Figure 4.1: Velocity, pressure and density profiles for `BW1-GGL1` using 18000 points in the spatial domain. Comparison of MFF and HLL numerical fluxes with PHM reconstruction. Bottom right, a zoom of the density shell.

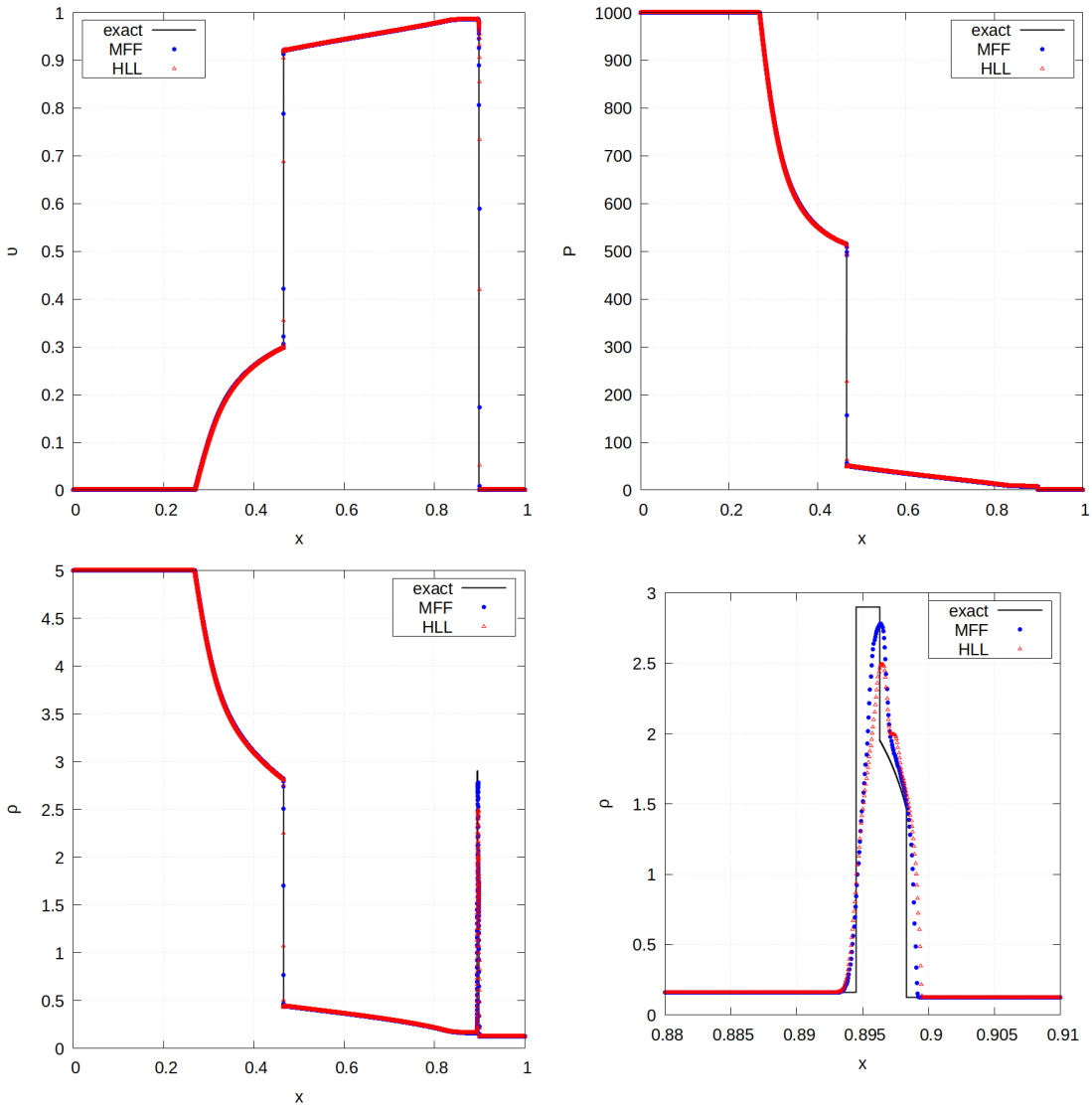

Figure 4.2: Velocity, pressure and density profiles for `BW2-GGL2` using 18000 points in the spatial domain. Comparison of MFF and HLL numerical fluxes with PHM reconstruction. Bottom right, a zoom of the density shell.

Figures 4.3 and 4.4 display the solution for the expanding and the colliding slabs, respectively. We also compare the fluxes using PHM reconstruction. In the expanding slabs, the typical density oscillation at the center of the domain (a known numerical issue of this type of Riemann problem, see it for example in [93]) has a bigger amplitude with the HLL flux. Otherwise both solutions are very similar. On the other hand, in the colliding slabs problem, MFF present a density oscillation at the center of the domain, that is not present with HLL. But HLL oscillates after the shocks of the composite waves, while MFF remains more stable.

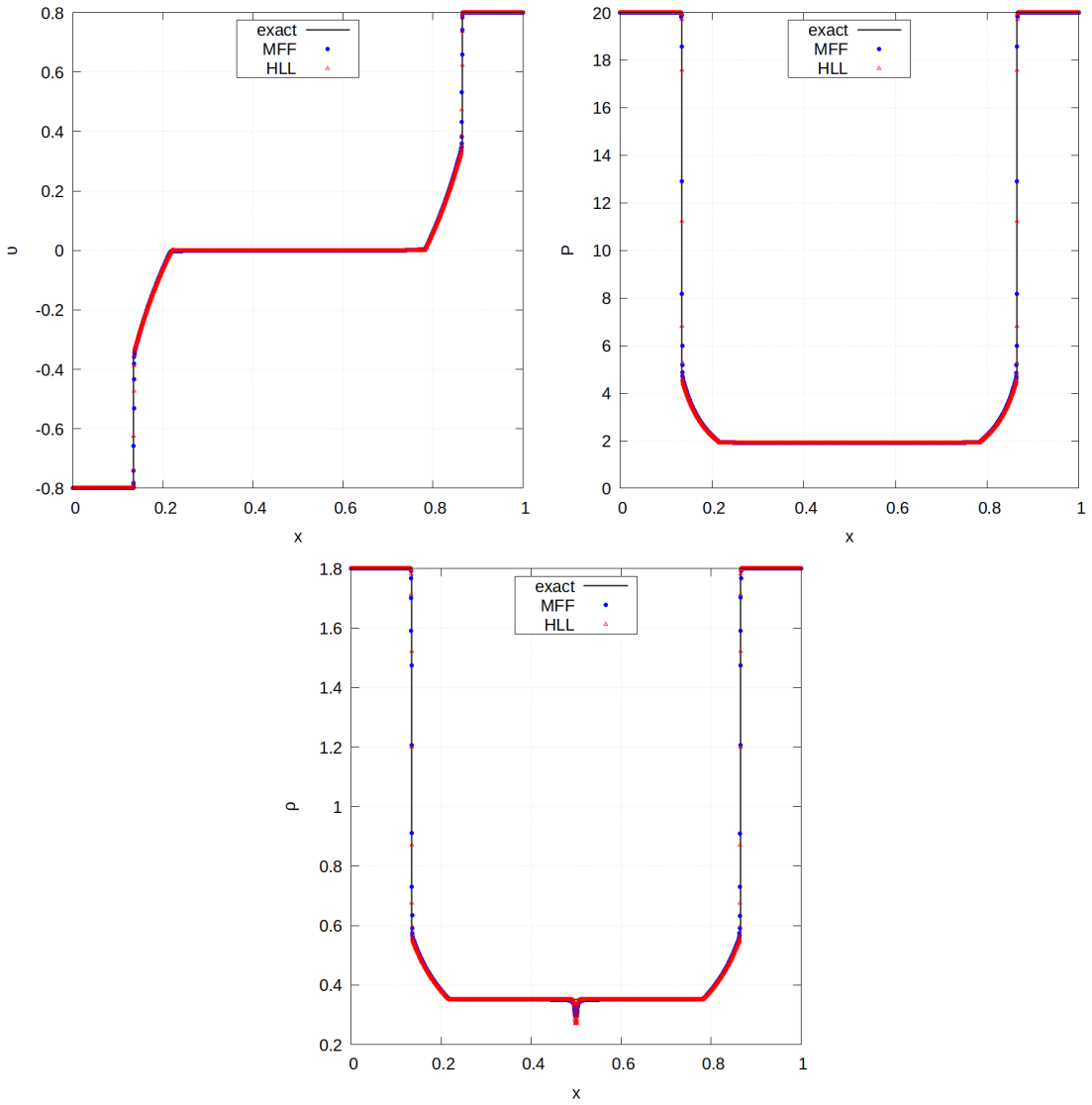

Figure 4.3: Velocity, pressure and density profiles for `ES-GGL1` using 3000 points in the spatial domain. Comparison of MFF and HLL numerical fluxes with PHM reconstruction.

4.3.2 Examples with tangential speed

In our analysis of the Riemann problem with tangential velocities we choose two test cases. For these problems, we compute the numerical approximation using a 2D numerical scheme with 6000 points in the direction of the evolution of the Riemann problem and 600 points in the perpendicular axis in the spatial domain $[0, 1] \times [0, 0.1]$.

Our first test case is `BW1-GGL1`, where we prescribe an initial tangential speed of $v_L^t = v_R^t = 0.9$. In the wave curves of the exact solution displayed in figure 3.1, we can see that this initial tangential speed is a representative example of the case where the highly relativistic tangential flow prevents the formation of complex wave structure in the perpendicular direction.

We compute the L1-norm mean error of the numerical approximation for the physical variables, including the tangential speed. We present the results in table 4.7. The errors remain similar for different fluxes and reconstructions and overall present the same order

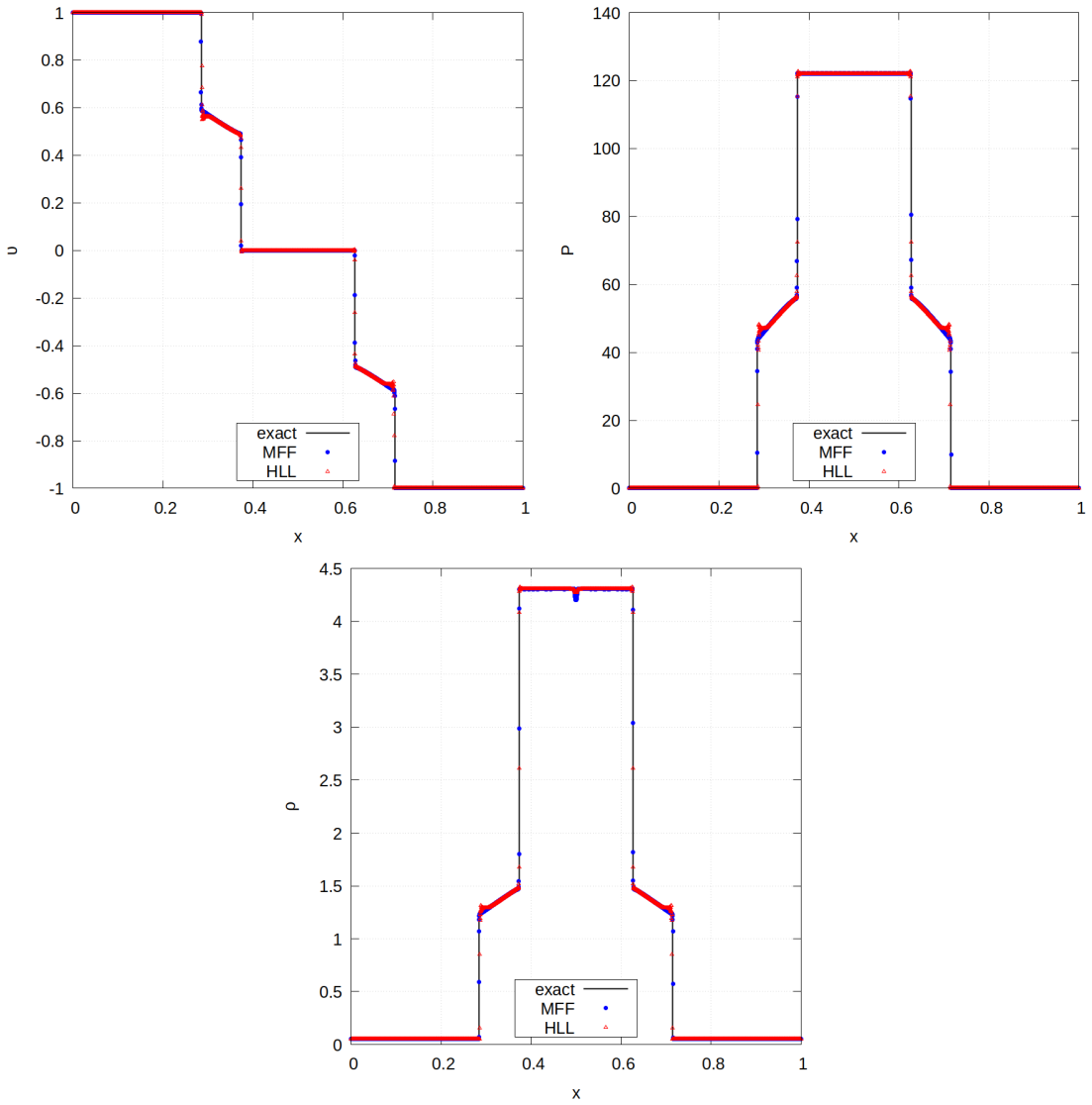

Figure 4.4: Velocity, pressure and density profiles for `CS-GGL2` using 3000 points in the spatial domain. Comparison of MFF and HLL numerical fluxes with PHM reconstruction.

of magnitude that in the 1D test case.

Scheme	Reconstruction	$\|\|E(P)\|\|_1$	$\|\|E(v^x)\|\|_1$	$\|\|E(v^t)\|\|_1$	$\|\|E(\rho)\|\|_1$
MFF	ENO3	2.8712e-01	1.0765e-02	9.0563e-03	2.1059e-02
MFF	PHM	1.6624e-01	8.5090e-03	7.1542e-03	1.6867e-02
HLL	ENO3	3.9425e-01	8.6085e-03	7.2561e-03	1.7580e-02
HLL	PHM	1.5439e-01	7.8592e-03	6.4327e-03	1.5956e-02

Table 4.7: L1-norm mean error in the physical quantities for 2D `BW1-GGL1`, for a spatial resolution of 6000×600 points.

In figure 4.5 we display the numerical solution for the two different fluxes considering PHM reconstruction. Both solutions agree in the overall structure and represent sharply

the shock waves.

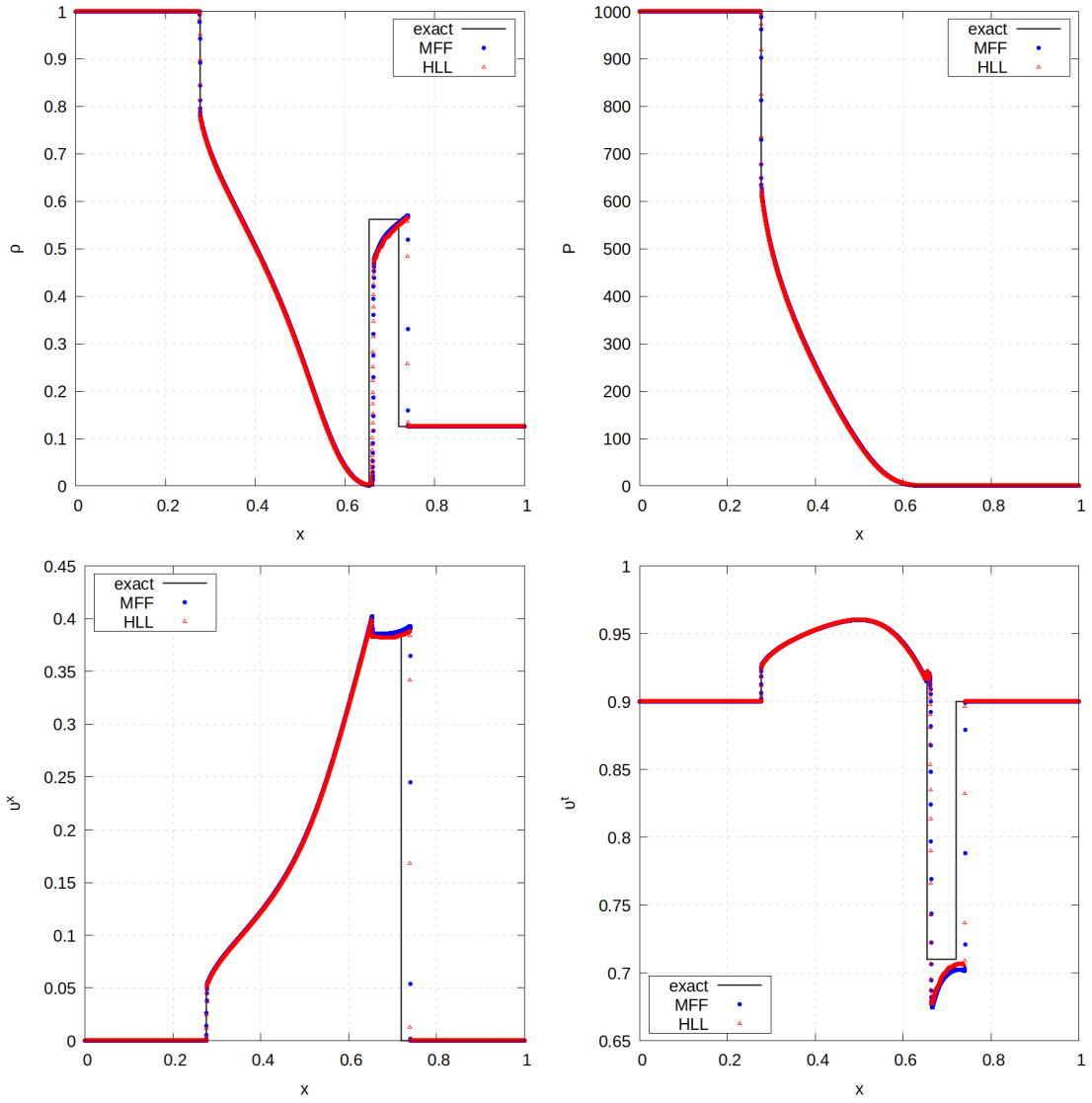

Figure 4.5: Density, pressure, x-velocity and tangential velocity profiles for 2D `BW1-GGL1` using a grid of 6000×600 points. Comparison of MFF and HLL numerical fluxes with PHM reconstruction.

We notice that the location of the shell is slightly shifted. Aiming to discard that both methods, MFF-PHM and HLL-PHM, are capturing an entropy-violating shock, we compute the solution for finer grid resolutions. The result is presented in figure 4.6. We observe that the numerical solution converges to the right position of the density shell as the numerical resolution increases. This finding highlights the difficulty of RH when there are more than one spatial dimensions.

We test the `BW2-GGL2` problem prescribing initial tangential speed $v_L^t = 0$, $v_R^t = 0.99$. The wave curves of the exact solution analyzed in figure 3.3 show that this is a good example of how the tangential speed can affect the wave structure of one side even if it is prescribed just on the other side.

We gather the error of the solution in table 4.8. Although the error in pressure for

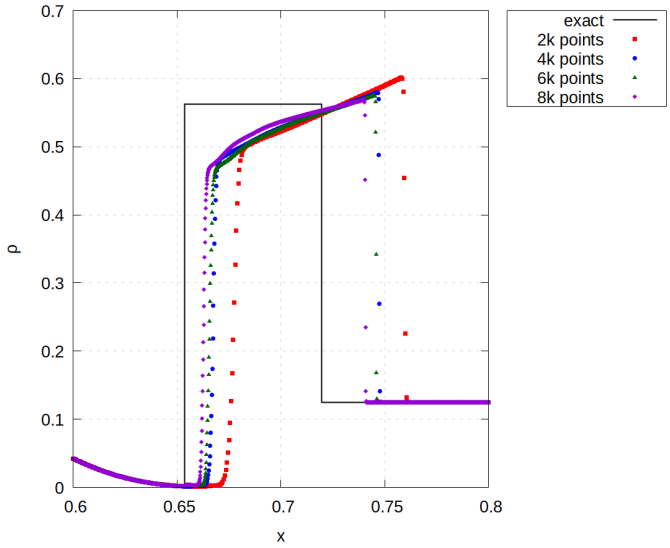

Figure 4.6: Convergence to the right position of the density shell for 2D `BW1-GGL1` problem for increasing spatial resolution.

this problem is larger, the results still resemble those of the 1D case. In this scenario MFF-ENO3 encounters the same unphysical reconstructions that we face in the 1D case with HLL-ENO3 for `CS-GGL2` and therefore we do not obtain a numerical approximation of the solution.

Scheme	Reconstruction	$\|\|E(P)\|\|_1$	$\|\|E(v^x)\|\|_1$	$\|\|E(v^t)\|\|_1$	$\|\|E(\rho)\|\|_1$
MFF	ENO3	-	-	-	-
MFF	PHM	1.0804e+00	2.9285e-03	1.2757e-03	2.3151e-02
HLL	ENO3	1.1976e+00	3.2007e-03	1.5273e-03	2.6973e-02
HLL	PHM	1.1446e+00	2.9257e-03	1.3993e-03	2.6759e-02

Table 4.8: L1-norm mean error in the physical quantities for 2D `BW2-GGL2` Riemann problem, for a spatial resolution of 6000×600 points.

We display the solution profiles in figure 4.7. The density shell location is more accurate for this problem. We can observe some oscillation of the solution after the shock of the composite wave to the left for HLL flux, and oscillations of the pressure at the contact discontinuity position for MFF.

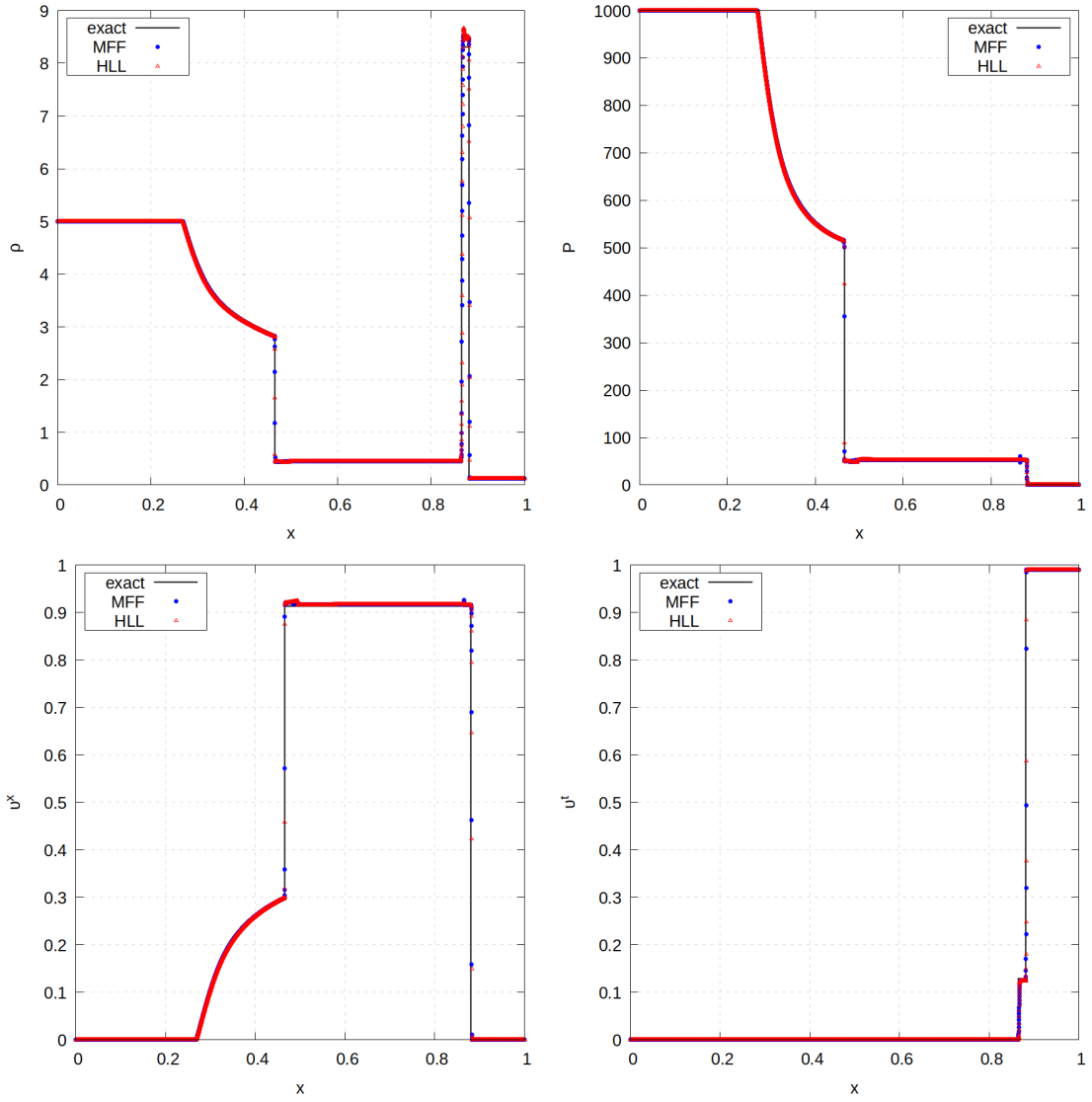

Figure 4.7: Density, pressure, x-velocity and tangential velocity profiles for 2D `BW2-GGL2` using a grid of 6000×600 points. Comparison of MFF and HLL numerical fluxes with PHM reconstruction.

Part II

Modeling of equations of state for high density matter

Chapter 5

Equation of state for high density matter

Our study of Special Relativistic Hydrodynamics (SRHD) is focused on the understanding and correct resolution of the wave structure that a test fluid with relativistic speed can develop. The fluid is taken as the matter that compose astrophysical objects aiming to replicate realistic scenarios that could be of interest in General Relativistic Hydrodynamics (GRHD) simulations. In particular, in this research we focus on neutron stars (NSs).

The properties of the fluid are encoded in the equation of state (EoS), which is needed to close the hydrodynamic system of equations. Nevertheless, the information about the insides of NSs is limited to astrophysics theory. The EoS is constructed using physical principles (thermodynamics, nuclear and particle physics) for the higher density regions, while the lower density parts can benefit also from experimental data.

A NS can be divided into a thin atmosphere and an interior. The latest is made up of a crust and a core, where each of these regions is composed of an inner and an outer layer [43]. We describe the star from the outside and advance towards its center. For the purposes of this analysis the atmosphere is neglected since the properties of the NS are determined by the denser regions.

The *outer crust*, which extends up to densities of around $4 \cdot 10^{11}$ g/cm^3 , is composed of ions and electrons. As the density increases the energy of the electron gas also raises, leading to the neutron enrichment of the nuclei. When the particles can no longer be held they begin to drip, forming a neutron gas. The *inner crust* begins after the neutron drip and extends up to densities of around 10^{14} g/cm^3 . As density augments, the neutrons become closer together and the repulsive force between them provide support to the interior of the star against gravity. The nuclei begin to deform until they disappear at the interface with the core.

The *outer core* extends to densities of around $5 \cdot 10^{14}$ g/cm^3 and consists of a liquid mixture of neutrons, protons, electrons and muons that are in a state of electric neutrality and β-equilibrium (a state of balance between the decay and creation of neutrons). In massive NSs, an *inner core* may also be present, reaching up to densities of $4 \cdot 10^{15}$ g/cm^3 at the center. Matter at such high densities is unknown since it cannot be replicated on Earth. The components are theoretical.

The EoS of the NSs is constructed from the modeling of the matter inside each region. Then all parts are put together to form a physically consistent model.

The behavior of the outer crust can be deduced from the known properties of nuclei and is commonly constructed using shells of different elements. It is then connected to

an EoS for the inner crust which is computed using effective neutron-neutron interactions and where the deformation of nuclei is model dependent. In the outer core, the EoS of the plasma is calculated using microscopic models of many-body theory for strongly interacting particles, although the accuracy of these models decreases with increasing density. For the inner core, the EoS is determined using a theory for matter at densities above nuclear density and typically depends on many unknown parameters. The global EoS reflects the change of properties of the fluid along the NS interior, with a softer EoS at the neutron drip (more compressible) that stiffens towards the core.

In a NS in equilibrium the thermal effects can be neglected. Therefore, the EoS is considered to be cold and is formulated as a relation between pressure and density, $P(\rho)$. This simplification is applied in the thermodynamic modeling of each part of the structure and the resulting equations are solved numerically to obtain a sparse set of pressure values for densities throughout the star.

The EoS of a NS is typically presented as a *table* of density, pressure, and internal energy per baryon values at a temperature of zero and in β-equilibrium. The EoS model may concentrate on the outer or inner core, selecting an approach to describe the interactions and properties of the components. There are many different tables, depending on the focus of the model and the techniques and parameters used for the resolution of the thermodynamics. For example, the EoS of matter in the outer core can be calculated using the ground-state energy of nucleons, which can be determined using various methods such as the Brueckner-Bethe-Goldstone theory, Green's function technique, the variational method or relativistic mean field theory [43].

Tabulated EoS are currently the best approximation to the behavior of the interior of NSs. However, for numerical relativity (NR) simulations, the EoS and its derivatives have to be evaluated at arbitrary values of density. Using tabulated data for the EoS has several disadvantages, including the need for interpolation and the lack of derivatives, both of which are affected by the sparsity of the data points.

Interpolation of a set of points is not unique and the results depend on the selected technique. It can also introduce thermodynamically inconsistent behavior, such as local extrema. While there is not a one-size-fits-all solution for this issue, it is common to use the interpolation method proposed in [119], which preserves a correct thermodynamic behavior and is implemented in many numerical codes. Furthermore, it can be challenging to accurately calculate the derivatives of the EoS due to the sparsity and the varying density of points in different regions, which can introduce a non-negligible and variable error.

Given these issues and the computational cost of working with tabulated data, *analytic models* are generally preferred for simulations. These models should be expressed as simple equations that can be easily derived and evaluated while accurately reproducing the tabulated data and maintaining consistent thermodynamics without introducing any artificial effects.

In this Chapter, we describe some of the current sources of tabulated EoS for NSs and how to interpret their data. Among their features we focus on phase transitions (PTs), as they can strongly influence the hydrodynamics. We present some continuous models that are currently used in numerical simulations and compare them with their tabulated counterparts by computing the stellar properties that they induce. We also discuss the effects of PTs in these properties.

5.1 Tabulated equations of state

We consider tables of cold EoSs from two different catalogs: CompOSE [1, 131, 86] and Arizona University Neutron Star EoS catalog [3]. Both provide pressure and density values at β-equilibrium and can include other thermodynamic quantities.

The CompOSE project [1] comprises both hot and cold EoSs from nuclear physics. These EoS tables provide sparse points of baryon number density (n_b) and corresponding pressure values. From this catalog, we attain the EoSs used in the analysis of gravitational waves (GWs) from NSs made by the LIGO-Virgo-KAGRA collaboration in [7]. In particular, we obtain the tables at the n_b points listed for each of these EoS and included the pressure P and scaled internal specific energy ε[1]. We convert the baryon number density to rest-mass density and change the units of the pressure to work with the quantities described in previous Chapters and in *cgs* units (centimeters-grams-seconds).

The other database is Arizona University Neutron Star EoS catalog [3] (cited as Arizona henceforward). A set of tabulated cold EoSs for NSs is provided with three columns already in *cgs* units: density, pressure and energy density ϵ. We transform the latest into dimensionless internal energy.

The rest of this Chapter uses the information of pressure P and density ρ in g/cm^3 and the dimensionless internal energy ε from the tables described above[2].

5.1.1 Phase transitions

As density and pressure grow within a NS, matter undergoes a series of transformations to increasingly unknown states. These alterations may be smooth or they may involve a sudden change in the properties of the matter. The change from one state of matter to another, such as from solid to liquid or from gas to plasma, is referred to as a *phase transition* (PT). PTs are characterized by an abrupt change in the thermodynamic properties of matter and involve the coexistence of two or more pure phases in a mixed phase that has the properties of neither.

At fixed temperature, pressure is constant with density within a PT . Therefore, quantities defined by the change of pressure with density $\partial P/\partial\rho$ undergo a large change in their behavior. These are the sound speed c_s^2 (1.1.3), the adiabatic exponent γ (1.1.4) and the fundamental derivative $\mathcal{G}$ (1.1.5). In pure phases, $\mathcal{G} > 1$ and γ is a smooth function that increases slowly, implying that the sound speed is monotone. Along a PT, the adiabatic exponent experiments a kink (discontinuity of first derivative) and the fundamental derivative may become negative. In this scenario, the sound speed is no longer monotonic and its value is smaller than in pure phases [80].

When constructing a cold tabulated EoS that includes a PT, there are two main approaches that can be considered [43]. The first approach, known as the *Maxwell construction*, imposes local electric neutrality of the matter and allows for a jump in density at constant pressure. By definition, the adiabatic exponent and sound speed are zero in this region and the fundamental derivative is not defined. These zero values for main thermodynamic quantities can introduce errors in the calculation other physical magnitudes.

[1] The quantities included in the EoSs for the analysis correspond to magnitudes 1 and 7 of Table 7.1 in the CompOSE manual v2.

[2] A NS EoS is often the result of combining a well-established crust model with a new approach for the core matter. This stitching together of two parts of the EoS may lead to unphysical values at the transition, such as decreasing pressure with density and negative internal energy. We find this phenomena in some of the studied tables. To address these issues, before using the tables we use linear interpolation to correct the pressure values and recalculate the internal energy using the first law of thermodynamics.

Therefore, this approach is generally not preferred.

The second approach, the *Gibbs construction*, imposes global electric neutrality on the matter resulting in a decrease of the slope of pressure with density. Therefore, the sound speed decreases although it does not reach zero. This smoother construction is most commonly used in the tables we study although it can mitigate other thermodynamic implications of the PT.

Given that the fundamental derivative determines the convexity of the EoS and therefore affect the hydrodynamics [80], we study how many PTs are present in realistic tabulated EoS and how strong they are.

5.1.2 Locating phase transitions on a tabulated equation of state

When matter undergoes a PT, more than one phase coexist and the thermodynamic properties deviate from their usual behavior along pure phases. As mentioned previously, the sound speed decreases reaching smaller values than in a pure phase, the fundamental derivative is below one and the adiabatic exponent is no longer smooth. If the table was constructed using the Maxwell approach the pressure would be constant with density. To identify a PT in a tabulated EoS we look for these changes in the thermodynamic quantities.

Getting the thermodynamic quantities

The magnitudes affected by a PT are related to derivatives of the pressure. We use definition (1.1.3) for c_s^2 and (1.1.4) for γ. The fundamental derivative (1.1.5) is rewritten in terms of the sound speed as

$$\mathcal{G} = 1 + \frac{\partial \ln c_s}{\partial \ln \rho},$$

in order to calculate it from the values of c_s^2. We tackle the first disadvantage of using a tabulated EoS since we need to perform numerical derivatives to study its properties.

We use the derivative of a three-point Lagrangian interpolation, as it allows for unevenly spaced data. Given consecutive abscissa points $[x_0, x_1, x_2]$ with corresponding $[y_0, y_1, y_2]$ ordinate values then

$$\frac{\partial y}{\partial x} \approx y_0 \frac{(2x - x_1 - x_2)}{(x_0 - x_1)(x_0 - x_2)} - y_1 \frac{2x - x_0 - x_2}{(x_0 - x_1)(x_1 - x_2)} + y_2 \frac{2x - x_0 - x_1}{(x_0 - x_2)(x_1 - x_2)}.$$

To calculate the derivative at $x = x_1$ the previous and next points in the table are needed. For the first point in the table, the derivative is evaluated at $x = x_0$ instead and for the last point it is evaluated at $x = x_2$. This allows us to extend the tabulated EoS to also include the values of c_s^2, γ and $\mathcal{G}$ for the tabulated densities.

One of the features used to identify a PT in a tabulated EoS is the presence of a *kink* in the adiabatic exponent. While it is possible to determine the discontinuities in the derivative of this parameter if it is described by a known equation, it can be more challenging to do so using discrete values. Deciding when a change in value represents a kink rather than a result of discretization requires an ad-hoc, case-dependent threshold value. Additionally, it is important to bear in mind that the points in a tabulated EoS are calculated numerically and therefore contain an intrinsic error. This can lead to oscillations in one or more quantities that need to be distinguished from actual properties of the fluid. We have observed this particular issue in the tables obtained from CompOSE [1].

Identifying phase transitions using discrete values

To summarize, the main features that can be used to identify a PT in a tabulated EoS include: at the start of the PT, the sound speed no longer increases leading to a kink in the adiabatic exponent; at the end of the PT, the sound speed starts to increase smoothly again. At the beginning of the mixed phase the fundamental derivative is smaller than one, which is a consequence of the decreasing sound speed.

The challenges come from detecting a kink in the discrete adiabatic exponent and determining that the sound speed is varying smoothly after the PT. For this purpose we introduce the use of the *total variation* (TV).

The TV is a measure of oscillatory behavior. For a set of discrete values $\{u_i\}_{i=0}^{m}$ it is defined as

$$TV(u) = \sum_{i=0}^{m-1} |u_{i+1} - u_i|.$$

A strategy to detect kinks, used in [72], is to define the *local total variation* (LTV) of n points at the value of index j as

$$TV_j^n(u) = \sum_{i=j}^{j+n} |u_{i+1} - u_i|. \tag{5.1.1}$$

This quantity measures how much the magnitude u is changing around the point of index j. If the magnitude varies smoothly the value of $TV_j^n(u)$ is similar for consecutive j and fixed n. If there is an abrupt change like a kink in the magnitude then the LTV increases.

In order to detect a kink in the adiabatic exponent we compute $TV_j^3(\gamma)$ for every point in the table except for the last two (we safely assume that there is no PT at the extremes of the EoS). The selection $n = 3$ is made to keep the study very local, as PTs extend for small regions of density and including more points can mix them with pure phases covering up their effects. A kink introduces a local maximum in the sequence of LTVs.

For a tabulated EoS including the sound speed and adiabatic exponent, which can be calculated from the pressure and density values as specified above, we propose the following *criteria* to identify a PT.

PT extreme	Criteria
Starts at ρ_j	c_{sj}^2 local maximum $c_{sj}^2 > c_{sj+1}^2 > c_{sj+2}^2$ $TV_p^3(\gamma)$ local maximum, $p \in \{j-1, j, j+1\}$
Ends at ρ_q	$c_{sq}^2 \geq c_{sj}^2$ $TV_q^3(c_s^2) \leq TV_j^3(c_s^2)$

Table 5.1: Criteria used to identify a PT in a tabulated EoS.

A PT starts at ρ_j if the corresponding value of the sound speed is a local maximum. To avoid misclassifying oscillations, we require that the sound speed decreases for at least two consecutive data points. In addition, the start of the PT must induce a kink in the adiabatic exponent, which implies a local maximum in its LTV. This maximum can occur at index $j-1$, j or $j+1$. The position of the kink may be shifted depending on how the numerical derivatives were calculated during the construction of the table hence we allow for three possible positions of the maximum.

A PT finishes at ρ_q if the sound speed is greater or equal than the value it had at the beginning of the PT, since the sound speed is always larger in pure phases than in mixed phases. Also, c_s^2 should increase monotonically and smoothly. We require $TV_q^3(c_s^2)$ to be less or equal than $TV_j^3(c_s^2)$, implying that the sound speed is smoother than when it suddenly changed at the start of the PT. The criteria is summarized in table 5.1.

Dealing with oscillations

Imposing the coincidence of a kink in the adiabatic index with a local maximum of the sound speed is a useful strategy to prevent identifying small and irrelevant oscillations in the data as PTs. However, this tactic may not always be effective, particularly when the data is highly oscillatory. In such cases, the approach can result in multiple short and closely spaced PTs being detected which are not genuine PTs of the fluid.

To address this issue, we have implemented a filter for oscillatory data in our analysis. When a PT is identified with the criteria presented above, we examine the data surrounding it. For the results presented below, we have selected 10 points in each direction. If a change in the monotony of the adiabatic index is observed within these points, the data is deemed to be oscillatory and the identification of the PT is discarded.

While this approach may result in the removal of some actual PTs that occur in regions where the data is slightly oscillatory, we consider it to be a worthwhile trade-off in order to avoid the introduction of ad-hoc threshold values for the oscillation amplitude and to maintain the generality of the method.

When applying the oscillation filter to the Arizona tables [3], it removes some thin PTs identified at the crust of the stars. Conversely, when applied to the more oscillatory Compose tables [1] the filter discards PTs as noise throughout the whole star.

Example of application

We apply the method described to locate PTs in tabulated EoS to the tables taken from Arizona [3]. Once the oscillation filter is applied, the EoSs that present at least one PT are: PS [89], GS1-GS2 [37], BGN1H1 [16], H4-H7 [59] and ALF1-2 [10]. The left and right extremes of the PTs are gathered in table 5.2.

	PT1		PT2		PT3		PT4	
EoS	ρ_L	ρ_R	ρ_L	ρ_R	ρ_L	ρ_R	ρ_L	ρ_R
PS	3.6453	7.4578						
GS1	4.3160	9.5566						
GS2	4.6480	8.5872						
BGN1H1	6.1420	11.620						
H4	5.0132	6.1088	6.8392	7.3704	11.388	12.018	14.475	17.297
H5	5.5112	7.0716	7.9348	8.6320	15.836	16.567		
H6	4.8472	6.3412	6.7728	7.6028	10.790	12.284		
H7	5.7768	7.2044	8.3664	8.8976	16.135	16.567		
ALF1	3.7350	7.0906						
ALF2	4.2097	6.3504						

Table 5.2: Density values of the extremes of the PTs located in EoS tables from Arizona [3]. Density is presented in 10^{14}g/cm^3.

The PTs located lie at the transition between the crust and the core of the NS, representing the change from solid to liquid matter. The EoS models H4-H7 present additional PTs deep into the core related to the progressive addition of hyperon species.

When used with the tables from CompOSE [1] mentioned in [7], our method finds at least a PT in models KDE0V [8], KDE0V1 [8], SK255 [9], SKI2-6 [97], SKMP [20], SKOP [96], SLY2 [23], SLY230A [24] and SLY9 [23]. We present the extremes in table 5.3.

These PTs are found at the crust of the star and are thinner than those located in the Arizona tables. The PTs are related to the different elements shells appearing in the crust and the deformation of the nuclei at increasing densities. These EoSs do not present a PT to the core of the NS.

	PT1		PT2	
EoS	ρ_L	ρ_R	ρ_L	ρ_R
KDE0V	5.201255	5.297953		
KDE0V1	6.856589	8.557214		
SK255	6.167484	6.698859		
SKI2	5.835903	6.210098		
SKI3	6.224552	6.843252		
SKI4	5.944400	7.014561		
SKI5	5.889902	6.208720		
SKI6	6.253283	7.189042		
SKMP	5.971838	6.520224		
SKOP	3.909381	4.000442	6.110941	6.690441
SLY2	6.920032	8.759473		
SLY230A	7.380880	9.632543		
SLY9	6.369540	7.784298		

Table 5.3: Density values of the extremes of the PTs located in EoS tables from CompOSE [1]. Density is presented in 10^{13}g/cm^3.

5.2 Equations of state for simulations

The main analytic models of EoS for NSs [15] are the spectral parametrization [69] and the piecewise polytropic (PP) [95]. These models are employed to fit tabulated data with continuous functions using as few parameters as possible while minimizing the error. A key requirement is that they accurately reproduce the stellar properties that depend on the EoS (such as mass and radius) obtained from the tabulated version.

The spectral parametrization described in [69] expresses the logarithm of the adiabatic index as a polynomial of pressure. The coefficients of the polynomial serve as free parameters of the model. By optimizing the polynomial to closely reproduce the mass and radius of several stars obtained from a tabulated EoS, this method can accurately approximate the EoS with just 2-3 parameters. The spectral parametrization allows for the use of observed stellar configurations to reconstruct an EoS that accurately reproduces real NSs. However, it cannot replicate abrupt changes along the EoS, such as PTs, which cannot be inferred from a few mass and radius points. There are also open questions regarding the need for a better optimization method to determine the parameters given the observed stars and how the construction may be affected by the uncertainty and dispersion

of observational data.

The PP model proposed by [95] utilizes polytropes to relate pressure values with density. In order to capture the changing behavior of the fluid throughout the star, different polytropes are employed for different regions while ensuring the continuity of the overall EoS. In the next Subsection we delve into the details of this analytic EoS.

To the extent of our knowledge, EoSs constructed using spectral parametrization have not yet been used in gravitational waves simulations. The first numerical simulation of a binary neutron star (BNS) merger used polytropes instead [113]. The current reference catalog of waveforms from BNS mergers is the CoRe database [26], which uses different EoSs to explore and demonstrate the influence of the matter model on the signal. The catalog includes two polytropes, nine PP models with an additional thermal term for the evolution, and five tabulated hot EoSs. Since PP EoSs have already been used to simulate mergers and are implemented in many NR codes we focus on this type of modeling.

5.2.1 Piecewise polytropic model

The PP approach developed in [95] fits the relation between pressure and density in the tabulated data with polytropes. A polytropic EoS has the form

$$P(\rho) = \kappa \rho^{\Gamma} \tag{5.2.1}$$

with κ and Γ free parameters, the latest representing the adiabatic index. The authors divide the star interior in density intervals and fit a different polytrope for each of them. As the crust of a NS barely influences the stellar properties, they fix four polytropes for the lower densities to reduce the number of free parameters of the whole model. These replicate the tabulated SLy EoS [29], commonly accepted as an appropriate EoS for the crust.

The high density region is fitted with three polytropes which mimic different tabulated data. Since the pressure function has to be continuous, the values κ of each piece are used to equal the polytropes at their common extremes. Therefore each EoS model has four free parameters: the adiabatic indices of the three high density polytropes and the pressure value where the first of them meets the low density fit. The authors analyze the parameter space for the adiabatic indices that keep the EoS causal and the derived stellar properties within observational constraints.

In [95] the authors provide the parameters that model 34 of the tabulated EoS from Arizona [3]. In the previous Section we identified PTs in several of these EoSs. In what follows we analyze how the PP models behave in these regions.

From the pressure expression of a polytrope (5.2.1) we can obtain the adiabatic exponent, sound speed and fundamental derivative:

$$\gamma = \Gamma, \qquad c_s^2 = \Gamma \kappa \rho^{\Gamma - 1}, \qquad \mathcal{G} = \frac{\Gamma + 1}{2}.$$

Along each polytrope, the sound speed is always increasing for $\Gamma > 1$. The adiabatic exponent and fundamental derivative are constant. Therefore, the features of a PT are not possible to replicate using this model.

However, the shape of the PP model introduces artificial PTs that do not represent actual properties of the fluid. When the model changes the polytrope parameters at selected densities there is a jump in Γ. This induces a jump discontinuity in the thermodynamics quantities above. While the fundamental derivative always remains positive, the sound

speed can decrease and its local maximum coincides with a kink in the adiabatic exponent. This artificial PT is a known issue of the PP model [95].

The strengths of a PP EoS are its simple expression, the reduced number of free parameter and the great accuracy far from joint densities between polytropes. On the other hand, it introduces artificial PTs not present in the fluid while not allowing for the real ones. Since they have been used for simulations, we analyze next how well the PP EoSs represent the stars arising from the corresponding tabulated models.

5.3 Stellar properties

When constructing an EoS for NSs, one must consider a theory for matter beyond nuclear density, a method to solve the thermodynamics and values for the parameters in the equations. The resulting EoS describes the properties of the star's matter, which should be consistent with observations. A stiff EoS corresponds to less compressible matter allowing the star to have a larger mass without collapsing under its own gravity. On the other hand, a soft EoS corresponds to more compressible matter, which leads to less massive stars.

One of the most commonly used parameters for evaluating an EoS against observations is the maximum mass it can support, since the observation of a more massive star than this would contradict the EoS. Previously, estimates of the *masses* and *radii* of NSs based on electromagnetic radiation from pulsars were compared with theoretical EoSs. The detection of GWs has also provided an additional parameter that depends on the EoS: the *tidal deformability*, that quantifies the ease with which the star deforms under the influence of gravitational forces. We state the mass of NSs in solar masses ($M_\odot$), the radius in kilometres *km* and the tidal deformability as a dimensionless quantity.

Nowadays the requirements imposed to an EoS to be in agreement with observations [5, 6] are that the maximum mass supported is bigger than $1.97M_\odot$ but does not exceed $2.2M_\odot$ ($2.3M_\odot$ for a conservative approach [112]) and that the tidal deformability for a $1.4M_\odot$ star is between 290 and 580. The high density region of the EoS will be constrained further by future measurements of NSs above $2M_\odot$ while lower densities can be constrained by observations of 1.7-$1.85M_\odot$ NSs [133].

If the stars built from an EoS obey the constraints obtained through observations, then the EoS is a suitable candidate for NSs interior. In this Section we recap how the observationally constrained parameters (mass, radius and tidal deformability) are calculated for a given EoS. The motivation is to compare the differences in the properties of NSs obtained from tabulated EoSs and PP models. The latest should not generate NS configurations that are inconsistent with those obtained from the tabulated EoSs, nor should it discard valid configurations. We focus on static, spherically symmetric stars. In this scenario we can develop our own numerical code, which gives us flexibility on the type of EoS that is used.

We devote the rest of this Chapter to present the equations that describe the mass, radius and tidal deformability of NSs. We solve them with the PP models proposed in [95] and with their corresponding tabulated EoSs, finding the effects related to PTs and stability described in [138, 139].

5.3.1 Mass-radius curve

Mass and radius are stellar properties that can be calculated from theory which depend completely on the EoS. From a theoretical point of view, a star is a solution of the Einstein

field equations corresponding to an equilibrium distribution of a perfect fluid.

Using the stress energy tensor of a perfect fluid and the conservation of baryonic number to obtain an equation for the pressure, one can obtain the Tolman-Oppenheimer-Volkoff (TOV) equations [128, 87]

$$\frac{\mathrm{d}P}{\mathrm{d}r} = -G\left(\rho(1+\varepsilon) + \frac{P}{c^2}\right)\frac{m + 4\pi r^3 P/c^2}{r(r - 2Gm/c^2)} \tag{5.3.1}$$

$$\frac{\mathrm{d}m}{\mathrm{d}r} = 4\pi r^2 \rho(1+\varepsilon), \tag{5.3.2}$$

that describe the change of mass and pressure inside the star given an EoS. Both magnitudes depend only on the radius because we consider spherically symmetric stars.

We denote by $m = m(r)$ the gravitational mass [61] comprised inside a sphere with radial coordinate r. The equations also involve pressure P, density ρ and internal specific energy ε, all of them related through the EoS. We write the gravitational constant G and the light speed in vacuum c explicitly to change the units of the equations. This will be particularly useful when using tabulated EoSs.

Note that we preset two of the three TOV equations. We omit the one that is needed to solve the metric inside the star but does not affect the mass and radius since we are only interested in these magnitudes. This is a common practice in literature when computing stellar properties [43].

Numerical solver

The TOV system (5.3.1)-(5.3.2) is formed by two coupled ordinary differential equations (ODEs) that depend on the radius. For the numerical solution an ODE solver is required. We use a *fourth order Runge-Kutta* (RK4), with $\Delta r = 1cm$. Given that the star radius is often expressed in kilometres this step keeps the error negligible. A reasonable level of numerical accuracy like this is typically sufficient to obtain the properties of a star within acceptable margins of error. However, higher precision may be necessary when solving the TOV equations in order to obtain the initial conditions for a system to be evolved numerically. In particular, the temporal component of the metric and the total baryon number of the star must satisfy a constraint equation exactly in order for the star to be stable. We verify that this condition is satisfied within the error described in literature [43].

Along the integration process, the solution value of pressure is known at each evaluation of the equations. The corresponding density is also required. When using a tabulated EoS, the density is interpolated from the table. A simple interpolation is sufficient for obtaining mass and radius [43], although thermodynamically consistent interpolations [119] are recommended for higher accuracy. For an analytic EoS, the function must be inverted. The method for obtaining density values for different types of EoSs is discussed in detail at the end of this Subsection.

Stopping criteria and initialization

The integration is performed from the center of the star ($r = 0$) until its surface ($r = R$). Since there is no matter beyond the surface, $P(r \geq R) = 0$ and $\rho(r \geq R) = 0$, making $m(r \geq R) = M$ the total gravitational mass of the star. Therefore, a natural stopping criteria is reaching $P = 0$. However, to achieve this numerically using a tabulated EoS is unfeasible because the tables are defined up to a certain low density and pressure, but not zero. Then extrapolation outside the defined region is needed.

The common approach to this problem is to select an arbitrary nonzero value to be the surface pressure of the star. This is a valid consideration as long as the value is much smaller than the central pressure of the NS. However, we have found that the solution for the radius of the star depends strongly on the pressure value selected.

On the other hand, when the matter outside the radius causing the surface pressure is negligible, the mass value saturates. We define our stopping criteria based in this phenomena. The matter that may remain outside the total radius can be considered as an atmosphere and the pressure values at the surface of the star typically remain within the ranges of the tabulated EoSs. The specific *stopping criteria* used in this study is $(m(r+\Delta r) - m(r))/m(r) < 10^{-12}$, where $m(r)$ is in grams along the integration.

The *initial conditions* are set at the center of the star with a radius of $r = 0$ and mass $m = 0$, since there is no mass contained within a radius of zero. It is worth noting that the equation for pressure (5.3.1) has a singularity at this initial state and therefore it is enforced to zero. This value is settled from the series expansion around the singular point. A central density is also prescribed, which corresponds to a central pressure through the EoS. This density determines a specific star and solving the TOV equations for a range of central densities determines the stars sequence that can be described by a particular EoS.

Calculating density from pressure values

Solving the TOV equations requires calculating the density associated to a pressure value obtained as solution for every integration step.

In the case of a tabulated EoS, the density has to be interpolated. We are not aiming to produce initial conditions for evolution, therefore a simple interpolation should suffice [43]. We compare two different methods calculating their accuracy for a known function.

The first proposal is *linear interpolation*. Given a set of data points $\{(x_i, y_i)\}_{i=0}^{N}$, and a value $x \in [x_0, x_N]$ where we want to interpolate, $x \in (x_i, x_{i+1})$ for some $i \in \{0, .., N-1\}$, then

$$y(x) = \frac{y_{i+1} - y_i}{x_{i+1} - x_i}(x - x_i).$$

Following [43] we also consider *logarithmic interpolation*. With the same assumptions that before, in this case

$$\begin{aligned} m &= \frac{\log(y_{i+1}) - \log(y_i)}{\log(x_{i+1}) - \log(x_i)}(\log(x) - \log(x_i)), \\ y(x) &= 10^m. \end{aligned} \tag{5.3.3}$$

To evaluate the effectiveness of both interpolation methods in a scenario similar to their intended application, we define a two-piece polytrope as the known function,

$$f(x) = a_j x^{b_j}, \tag{5.3.4}$$

where $j = \{0, 1\}$ and we change piece at some value x_p. We use $a_0 = 0.5$, $b_0 = 1.3$, and $b_1 = 1.8$. We calculate a_1 such that the function is continuous at x_p.

To sample the space in the same fashion that a tabulated EoS we take 40 consecutive points from BGN1H1 at high densities and normalize them by the first value. We obtain points in $x \in [1, 17.35]$. The corresponding y values for the data points are obtained applying our function (5.3.4). We select $x_p = 12.84$ and therefore $a_1 \approx 0.1395$. Then we produce 100 evenly spaced points in x between the extremes of the interval and obtain the corresponding y values with the two interpolation methods presented.

We calculate the error of an interpolation method as the 2-norm of the difference in value with respect to the exact solution. With the linear interpolation we obtain an error of $4.7 \cdot 10^{-2}$ while the logarithmic interpolation yields an error of $4.1 \cdot 10^{-14}$.

Logarithmic interpolation (5.3.3) shows to be more accurate when fitting a relation similar to that of density with pressure. This result is justified due to the wide span of the variables density and pressure across multiple orders of magnitude. As such, a logarithmic representation is better suited to accurately capture the underlying behavior as opposed to a linear fit. Therefore, for our solver we use logarithmic interpolation every time a quantity from the table is needed.

In the case of using a polytrope as the EoS model for the NS, the relation between pressure and density (5.2.1) can be inverted

$$\rho = (P/\kappa)^{1/\Gamma} \tag{5.3.5}$$

and we can obtain the density for any given value of the pressure.

When using a PP EoS we first have to find the polytropic piece to invert. As the pressure increases monotonically with density, the dividing densities also imply dividing pressures that we can use to locate in which polytrope is the pressure we want the density from.

5.3.2 Tidal deformability

The EoS determines the *tidal deformability* λ, which relates the quadrupole moment that a star induces to an external tidal field to linear order through the radius of the star and the k_2 Love number [49]

$$\lambda = \frac{2}{3G} k_2 R^5.$$

Henceforward we work instead with the dimensionless tidal deformability Λ [6]

$$\Lambda = \frac{2}{3} k_2 \left(\frac{Rc^2}{MG}\right)^5 = G\lambda \left(\frac{c^2}{MG}\right)^5 = \frac{2}{3} k_2 C^{-5}, \tag{5.3.6}$$

which also involves the mass of the star. It can be written in terms of the dimensionless compactness of the star C, where

$$C = \frac{MG}{Rc^2}.$$

Notice that $C = 1/2$ for an spherical compact object having the Schwarzschild radius.

The Love number k_2 can be obtained [50] as

$$\begin{aligned} k_2 = \frac{8C^5}{5}(1-2C)^2(2+2C(y-1)-y)\cdot[2C\left(6-3y+3C(5y-8)\right)+ \\ +4C^3\left(13-11y+C(3y-2)+2C^2(1+y)\right)+ \\ +3(1-2C)^2\left(2-y+2C(y-1)\right)\ln(1-2C)\Big]^{-1} \end{aligned}$$

where y

$$y = \frac{R\beta(R)}{H(R)} - \frac{4\pi R^3 \varepsilon(R)}{m},$$

is the result of evaluating two additional functions $H(r)$ and $\beta(r)$.

These functions are defined by two coupled ODEs in the star radius that are solved along the TOV system

$$\frac{\mathrm{d}H}{\mathrm{d}r} = \beta \tag{5.3.7}$$

$$\begin{aligned}\frac{\mathrm{d}\beta}{\mathrm{d}r} =& 2\left(1-\frac{2mG}{c^2 r}\right)^{-1} H\left[-\frac{2\pi G}{c^2}\left(5\epsilon + 9\frac{P}{c^2} + \frac{\mathrm{d}\epsilon}{\mathrm{d}P}c^2(\epsilon+\frac{P}{c^2})\right) + \frac{3}{r^2} + \right.\\ &\left. +2\left(1-\frac{2mG}{c^2 r}\right)^{-1}\left(\frac{mG}{r^2c^2} + 4\pi r\frac{P}{c^2}\frac{G}{c^2}\right)^2\right] + \\ &+\frac{2\beta}{r}\left(1-2\frac{mG}{rc^2}\right)^{-1}\left[-1+\frac{mG}{rc^2}+2\pi r^2\frac{G}{c^2}\left(\epsilon-\frac{P}{c^2}\right)\right],\end{aligned} \tag{5.3.8}$$

where $\epsilon = \rho(1+\varepsilon)$ is the total energy density. The integration starts right outside the center, where the approximations $H(r) = a_0 r^2$ and $\beta(r) = 2a_0 r$ are valid. The constant a_0 cancels out in the expression for the Love number. We choose $a_0 = 1$ and start the integration at $r = \Delta r$ considering that the density is still equal to the chosen central density.

Note the derivative $\mathrm{d}\epsilon/\mathrm{d}P$ in equation (5.3.8). When using a tabulated EoS, to calculate this derivative at a pressure $P \in (P_i, P_{i+1})$, where P_i is in the table, we obtain the discrete derivatives at P_i and P_{i+1} as

$$\left.\frac{\mathrm{d}\epsilon}{\mathrm{d}P}\right|_{P=P_i} \approx \frac{\epsilon_{i+1}-\epsilon_i}{P_{i+1}-P_i}.$$

We use logarithmic interpolation (5.3.3) to obtain the value of the derivative at the desired pressure P by interpolating between the two previously computed derivative values.

When using an analytic EoS in terms of the density and internal energy, we can recast the derivative as

$$\begin{aligned}\frac{\mathrm{d}\epsilon}{\mathrm{d}P} &= \left(\frac{\mathrm{d}P}{\mathrm{d}\epsilon}\right)^{-1} = \left(\frac{\mathrm{d}P}{\mathrm{d}\rho}\frac{\mathrm{d}\rho}{\mathrm{d}\epsilon}\right)^{-1} = \left(\frac{\mathrm{d}P}{\mathrm{d}\rho}\left(\frac{\mathrm{d}\epsilon}{\mathrm{d}\rho}\right)^{-1}\right)^{-1} = \\ &= \left(\frac{\mathrm{d}P}{\mathrm{d}\rho}\right)^{-1}\left(1+\varepsilon+\rho\frac{\mathrm{d}\varepsilon}{\mathrm{d}\rho}\right).\end{aligned}$$

In particular, for a polytrope we have

$$\frac{\mathrm{d}\epsilon}{\mathrm{d}P} = \frac{1+\varepsilon+\kappa\rho^{\Gamma-1}}{\kappa\Gamma\rho^{\Gamma-1}}.$$

5.3.3 Stability

The solutions of the TOV equations represent stellar configurations in static equilibrium. Still, they can be unstable and decay over time. A star is stable if the outwards force of the pressure of the fluid balance the gravitational pull inwards. Broadly, a massive NS, with mass above the maximum mass supported by the EoS, would collapse to form a black hole.

The quantity that determines the mass and radius of a NS for a given EoS is the central density. It is chosen from the estimated density range of the NS core, broadly from $10^{14}\mathrm{g/cm}^3$ to $4\cdot 10^{15}\mathrm{g/cm}^3$. The density range yielding stable configuration depends also on the EoS.

The stability is studied adding perturbations in the fluid elements of the star [43]. The whole analysis can be reformulated in the so called *static stability criterion*, which requires that the mass of the star increases with increasing central density [140, 44]. This condition is necessary but not sufficient. While solutions of decreasing mass with density are certainly unstable, the full criteria for stability involves considering the behavior of the radius with the central density [44].

Only stable solutions can be considered to study NSs. Therefore the stellar parameters are calculated for a wide range of central densities and then the branches of decreasing mass with density are discarded. The extremes are the minimum and maximum stellar masses supported by the EoS and the values in between conform the mass-radius curve of stable stars. In particular, we calculate the central densities that lead to the maximum mass up to a precision of $10^{12}\mathrm{g/cm}^3$.

Nevertheless, PTs in the EoSs can introduce unstable branches along the main curve due to the jump in density produced in the region of constant pressure [43]. This phenomena can also arise in the artificial PTs introduced by the jump in the adiabatic index in PP models [95].

5.3.4 Comparison of piecewise polytropic and tabulated EoS properties

We integrate the augmented system of the TOV equations (5.3.1)-(5.3.2), (5.3.7)-(5.3.8) to obtain mass, radius and tidal deformability (through (5.3.6)) of sequences of NSs. Tabulated EoSs and their corresponding PP fit provided in [95] are used.

Although the central density of the NS is taken in the core region, during the integration of the TOV equations the EoS has to be used until the star surface. The tables for EoSs MS2 [83], GS1-GS2 and H4-H7 provide information only for the core of the star, thus it is necessary to add a description of the crust before the integration.

For MS2, GS1 and GS2 we can add the SLy EoS, conveniently as in the PP model the crust is designed to always fit this table. On the other hand, the type of calculations for EoSs H4-H7 do not allow to consider a SLy crust since there would be a region of decreasing pressure at the matching densities. Therefore, we propose to use another crust, the HP EoS [42]. In this reference the EoS is constructed from the stitching of smaller tables. Following their procedure, we take BPS EoS [19] for densities below 10^8 $\mathrm{g/cm}^3$ and match it with the crust until the neutron drip with the original HP EoS table [41].

	Mean RPD	Max RPD	Min RPD
Mass	2.17	8.78 (ALF2)	0.26 (SLy)
Radius	1.50	3.69 (MS2)	0.29 (GNH3)
Tidal def.	21.22	44.33 (ALF2)	6.06 (H4)

Table 5.4: Summary of the relative percent difference (RPD) in mass, radius and tidal deformability calculated from tabulated EoS and its respective PP model. Stellar configurations are calculated for central densities varying from the one that gives the maximum mass to the one that surpasses a radius of 16km (whatever model reaches it first). In parenthesis, the name of the EoS that gives the presented difference.

We find that the difference of the maximum mass between the tabulated and the PP model of the EoSs is consistent with the results presented in [95]. In order to further compare the stellar configurations, we compute the star sequence from the minimum to the maximum mass for each tabulated EoS. We observe that the radius of the NS increases

rapidly and differently for smaller central densities. According to literature (see for example [102, 30]), the maximum possible radius of a NS is $16km$ and therefore we restrict the comparison to this value.

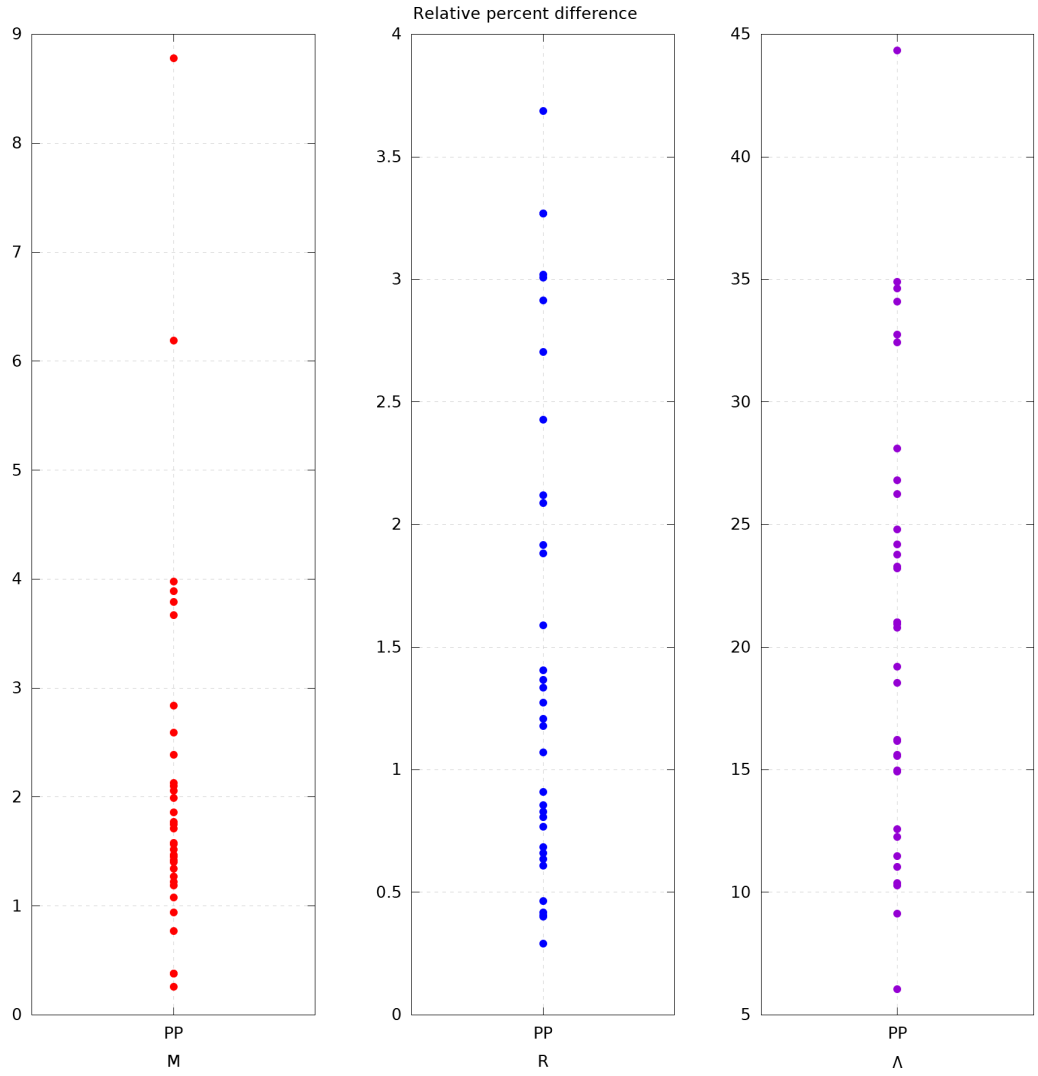

Figure 5.1: RPD of mass, radius and tidal deformability when comparing the PP model with its corresponding tabulated EoS. Notice the different scale of the y axis for each quantity.

The mean, maximum and minimum *relative percent differences* (RPDs) along the sequence, $(\text{average}|X_{PP}/X_{tab} - 1|)100$, for the three calculated quantities are summarized in table 5.4. It is noteworthy that the PP model leads to significantly different results for the tidal deformability as previously anticipated by [50].

In figure 5.1 we represent the RPD of the mass, radius and tidal deformability for all PP EoSs. The different scale of the graphic for every quantity indicates that each of them present a different magnitude of the error. The mass reaches an outlier error of around 9% but the error clusters around 2% RPD. This indicates that overall the mass curve is well approximated although there can be some significant deviations. In general, the radius is quite well approximated, with a maximum error below 4% and an average error around

the 1%. This quantity is the best approximated by the PP model. The tidal deformability, on the other hand, presents quite a poor representation. The error average is around 20% and all EoSs presents a significant deviation.

We explore the *influence of PTs* in the stellar properties and in their approximation by the PP model by displaying the mass, radius and tidal deformability against the central density. We show the graphics for SLy and BGN1H1 EoSs. The first one is an example of an EoS without PTs very well approximated by its PP model. The second one represents the EoSs with quite a wide PT in the transition from the crust to the core of the NS.

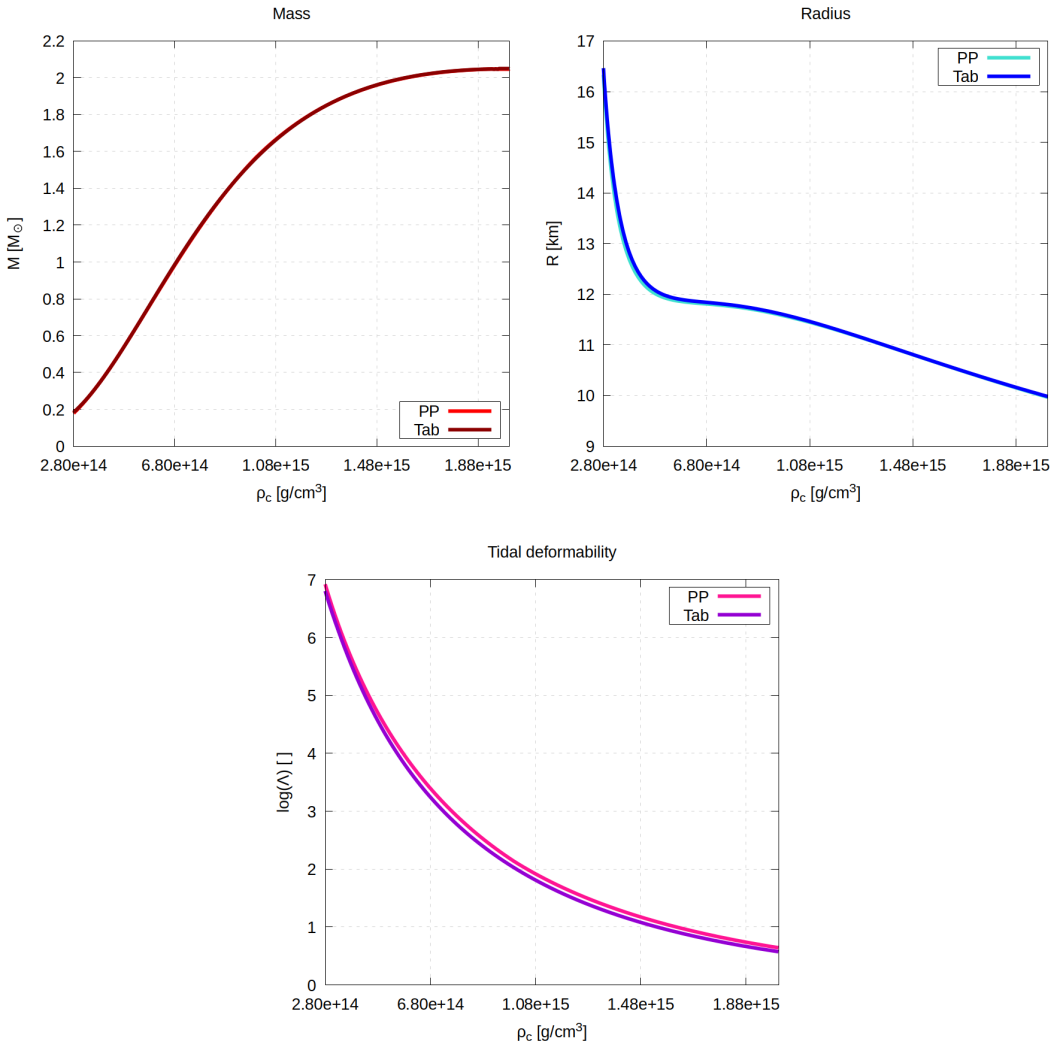

Figure 5.2: Mass, radius and tidal deformability for SLy EoS using the tabulated and the PP model.

The results for SLy EoS are presented in figure 5.2. While this EoS exhibits the least deviation in the mass curve between the tabulated and the PP model, we can observe that radius and tidal deformability are also very consistent between the two models.

In figure 5.3 we show the results for BGN1H1. We shadow the PT region found in Section §5.1.2. We can see that the curves coming from the tabulated and the PP EoS grow apart along the PT in the mass and tidal deformability graphics. Matter behaves differently in this region and the PP model, not being able to capture the different ther-

modynamics, departs from the tabulated result. At least in this example, the PT does not appear to have a major influence in the radius of the star.

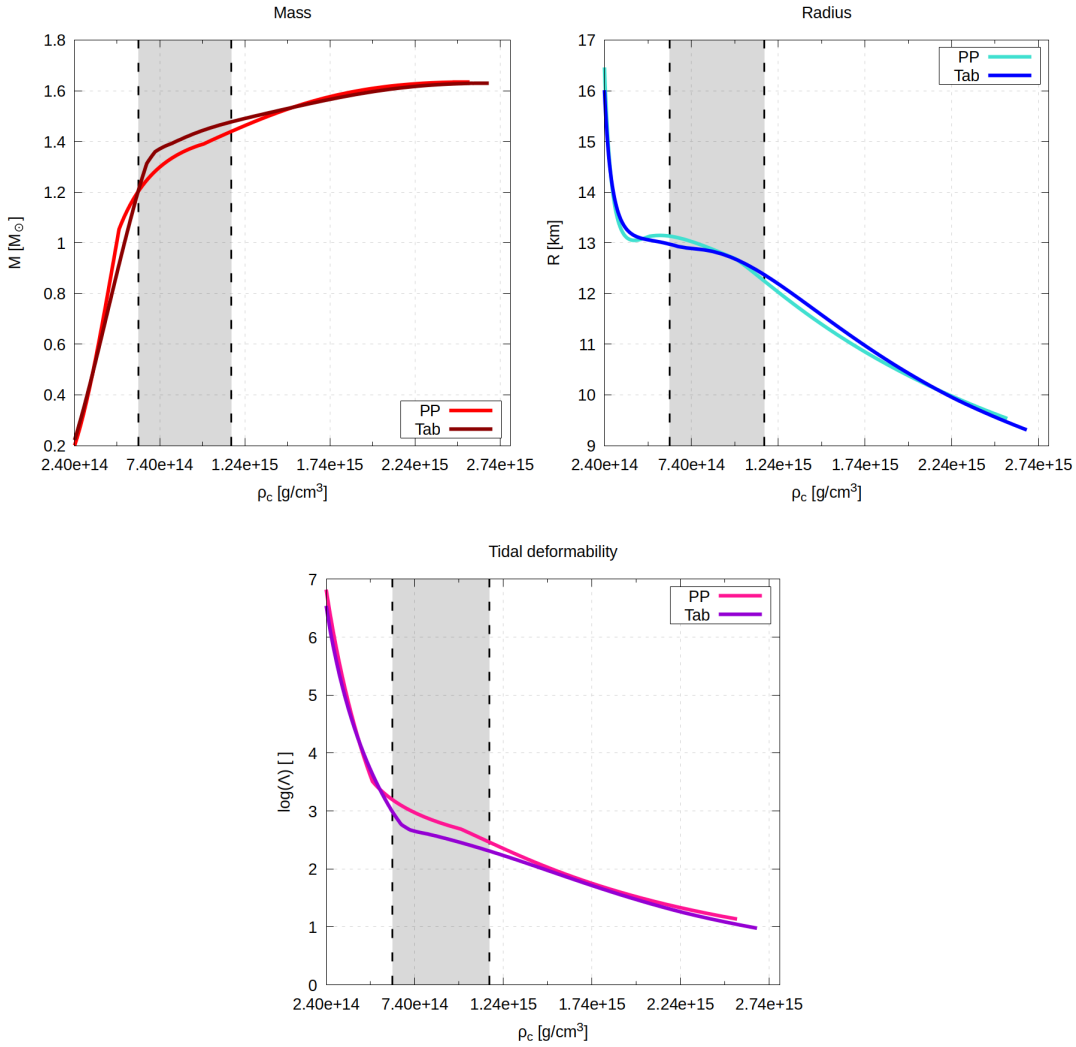

Figure 5.3: Mass, radius and tidal deformability for BGN1H1 EoS using the tabulated and the PP model. Vertical dashed lines mark the start and end of a PT, shadowed.

According to this analysis we conclude that the PTs of an EoS can affect the stellar properties of those stars whose central density is inside the PT, modifying the slope of the mass, radius and tidal deformability curves. In [139] the authors derive the analytical formula for the change of slope in the radius, energy and momentum of inertia (which can translate in changes in mass and tidal deformability) due to PTs at the core of NSs. Furthermore, the presence of PTs can determine the *stability* of the star.

In [138] the authors study the implications of PTs with Gibbs construction in the stability. They find that a PT can lead to NSs completely stable but also generate instabilities. In the cases analyzed before, where all the tabulated EoS present Gibbs constructions in the PTs, we find stable configurations although the slope of the quantities is modified.

In [139] the authors find that a PT with Maxwell construction introduce a unstable branch of NSs. It separates two stable branches representing stars with a core of the two

different phases separated by the PT. To observe this effect described in the literature we use HQC18 EoS [18], one of the EoSs considered for NSs interior in [6]. This model contains two Maxwell PTs and one of them is in the range of central densities for NSs. In figure 5.4 we depict the slightly decreasing mass with central density that separates the two stable branches.

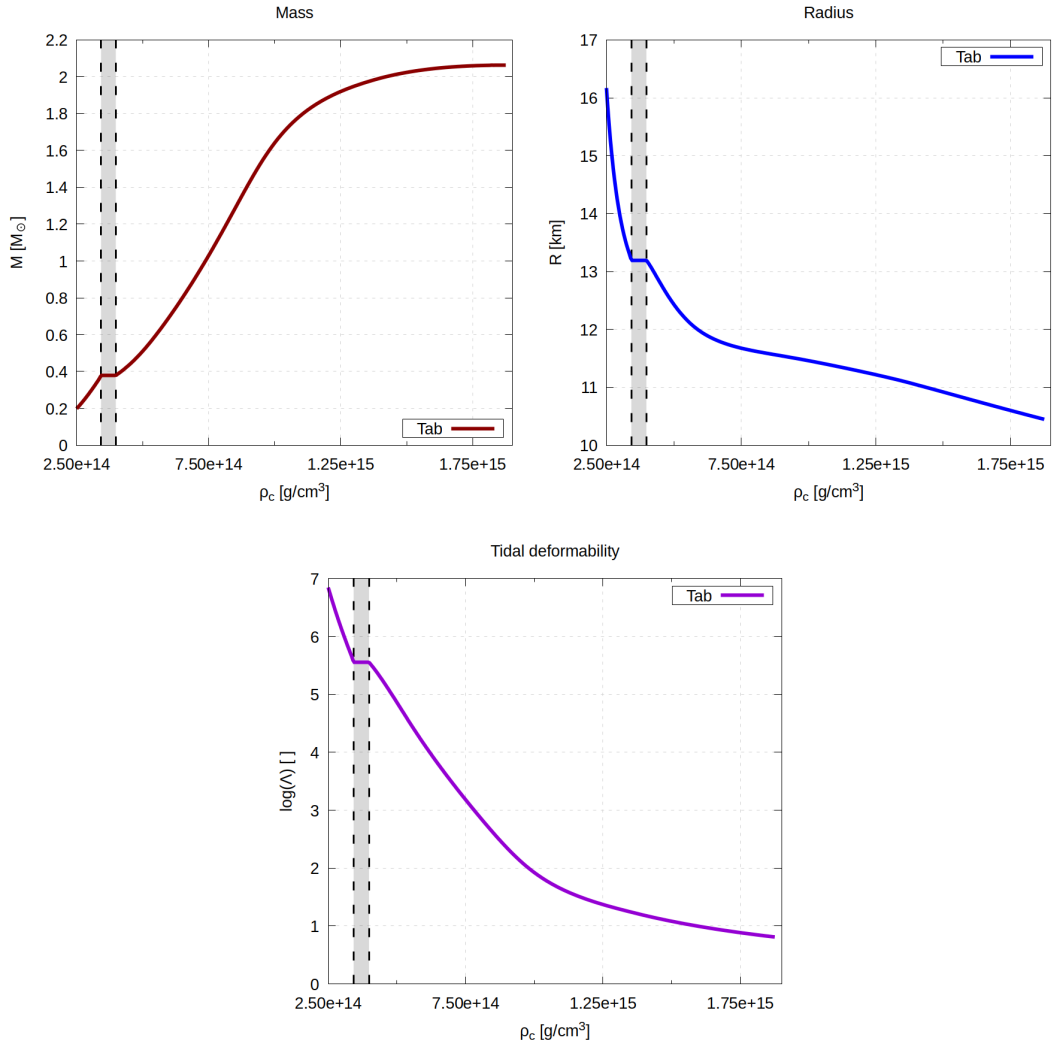

Figure 5.4: Mass, radius and tidal deformability for HQC18 EoS, a tabulated model with two Maxwell PTs. Vertical dashed lines mark the start and end of a PT, shadowed.

On a final analysis of the fidelity of representation of the PP model with respect to the tabulated EoSs, we confront the PP results against the observational constraints on maximum mass ($1.97M_\odot < M_{max} < 2.3M_\odot$) and tidal deformability ($290 < \Lambda_{1.4M_\odot} < 580$) [5, 6, 112]. We identify three PP EoSs that could explain NSs interior according to this criteria: SLy with $M_{max} = 2.05$ and $\Lambda_{1.4M_\odot} = 295.7$, ENG with $M_{max} = 2.24$ and $\Lambda_{1.4M_\odot} = 370.1$ and ALF2 with $M_{max} = 1.98$ and $\Lambda_{1.4M_\odot} = 571.0$. Still, when we compare the same parameters for the corresponding tabulated EoSs we find that although the maximum mass is within the given interval, the tidal deformability is not. From the set of analyzed EoSs none of the tabular models could explain observational data.

Chapter 6

Modeling thermodynamically consistent equations of state

Analytic fits of tabulated EoSs such as the spectral parametrization [69] or the piecewise polytropic (PP) [95] present a fair representation of the pressure throughout neutron stars (NSs) interior. However, the aim for simplicity and efficiency of these models make them unable to capture exceptional thermodynamic behavior in small regions such as phase transitions (PTs). The thermodynamic properties of the EoS affect not only the shape of the pressure but also the hydrodynamic behavior of the fluid (through the convexity of the EoS) and the stellar properties [138, 139]. The influence is noticeable even for thin PTs.

Modeling the pressure of a star along its whole interior requires defining a expression (or several in the piecewise approximations) that captures the general behavior of the quantity. Therefore, particular small regions with different behavior, PTs, cannot be mimicked accurately. PTs should be addressed aside from the global pressure definition to be consistent with the thermodynamic of the tabulated EoSs.

We consider the modeling of PTs and the modeling of the pressure outside them as different tasks. By doing so, we aim to obtain analytic representations of tabulated EoSs that retain their thermodynamic properties.

In this Chapter we present a model for PTs that is calibrated using the tabulated EoS. As it only takes care of the EoS inside these regions, it needs to be inserted in an expression for the pressure that models the rest of the star. Given that the total EoS has to be continuous, our PT model has to conform to the pressure values at the outer extremes of the PT (ρ_L, P_L), (ρ_R, P_R). Therefore, the PT model is sensitive to the analytic EoS that we use for the rest of the star through the values P_L and P_R.

Consequently, we examine two distinct expressions for pressure outside the PTs. On the one hand, we maintain the PP approximation and incorporate our PT model into the appropriate locations. Therefore, the values at the extremes P_L and P_R are given by the corresponding polytropic piece. This approach preserves the good properties of the PP EoS outside the PTs. However, the polytropes of the PP are calibrated to capture the general behavior of the pressure, which may lead to less accuracy in the vicinity of the PT where the pressure behaves differently. This divergence from the tabulated data at P_L and P_R can significantly impede the accuracy of our model, which is calibrated using such data. We name the EoS resulting from inserting our PT model into the PP approximation *thermodynamically consistent piecewise polytropic EoS* (TCPP EoS).

On the other hand, we consider an alternative approach for the general expression of

the pressure. Building upon the idea of the PP model, we create new polytropes that are fitted to the tabulated data *outside* of the PTs. This method enables the polytropes to capture the normal behavior of pressure and avoids being influenced by the altered slope during the PTs. The result is obtaining extremes P_L and P_R that are, in general, closer to the tabulated data in the vicinity of the PT favoring the accuracy of the PT model. The densities where the different polytropic pieces are defined are given by the thermodynamic behavior of the tabulated EoS, hence we name the resulting model *thermodynamically adaptive slope piecewise polytropic EoS* (T-ASPP EoS).

First we formulate a model for PTs depending on the values of P_L and P_R. We subsequently analyze the results considering the TCPP EoS and the T-ASPP EoS. We compare how the different models approximate the stellar properties determined by the tabulated EoSs. We also show some example of the influence on the hydrodynamics of the PTs by comparing the results of the PP model with the TCPP and T-ASPP models.

6.1 Modeling phase transitions

To tackle this problem, the first step is to locate the PTs present in tabulated EoSs. We follow the procedure presented in Section §5.1.2.

Aiming to capture the thermodynamics of the located PTs, instead of relying on the pressure we opt to model a different thermodynamic quantity that displays a more representative behavior along PTs. As we have previously discussed, potential candidates include the adiabatic exponent, the fundamental derivative and the classical sound speed. Our ultimate objective is to obtain an analytic expression for pressure, which would then enable us to derive the internal energy. Therefore, the quantity we model must allow for these expressions, imposing limitations on the magnitudes we may use.

In a cold EoS the entropy is constant and therefore first law of thermodynamics leads to

$$\varepsilon(\rho) = \int \frac{P}{\rho^2} \mathrm{d}\rho,$$

imposing that $P(\rho)/\rho^2$ should have a primitive expression.

We can study the viability of modeling each of the stated thermodynamic quantities from their definitions [80]. They are usually given in terms of the specific volume $V = 1/\rho$ and therefore we perform a change of variable in every definition.

The adiabatic exponent is

$$\gamma = -\frac{V}{P} \left.\frac{\partial P}{\partial V}\right|_s = \frac{\rho}{P} \frac{\partial P}{\partial \rho}.$$

Let $\gamma(\rho)$ be the curve that we obtain modeling this quantity during a PT of a tabulated EoS. Then the expression for the pressure from an initial state (ρ_i, P_i) is

$$P(\rho) = P_i \exp\left(\int_{\rho_i}^{\rho} \frac{\gamma(\rho)}{\rho} \mathrm{d}\rho\right)$$

and the internal energy would involve the integral of $\exp(f(\rho))/\rho^2$, where $f(\rho)$ is a function of the density obtained from the integral above. As this definition of the energy will hardly provide an analytic expression, the adiabatic exponent is not an appropriate quantity to model for our purpose.

The fundamental derivative in terms or the density can be written as

$$\mathcal{G} = 1 + \frac{1}{2}\frac{\rho^2}{\gamma P}\left.\frac{\partial^2 P}{\partial \rho^2}\right|_s = 1 + \frac{P''\rho}{2P'}$$

with the apostrophe denoting derivative with respect to ρ. Integrating the pressure from an initial state (ρ_i, P_i) and letting $G(\rho)$ be the curve we obtain from modeling the fundamental derivative, then

$$P(\rho) = P_i + \int_{\rho_i}^{\rho} P_i' \exp\left(\int_{\rho_i}^{\rho} \frac{2(G(x)-1)}{x}\mathrm{d}x\right)\mathrm{d}\rho.$$

We would need an initial value for the derivative of the pressure, therefore conditioning the slope which is exactly what changes differently during a PT. Also the expression will hardly be integrable, even less the internal energy. Moreover, using the fundamental derivative would require second derivatives of the tabulated EoS. For all these reasons, the fundamental derivative is not an appropriate quantity to model for our goal.

Finally we have the sound speed

$$c_s^2 = \left.\frac{\partial P}{\partial \rho}\right|_s.$$

Let $\mathcal{C}(\rho)$ be the curve we obtain modeling the sound speed from the tabulated EoS. Then from an initial state (ρ_i, P_i) we have

$$P(\rho) = P_i + \int_{\rho_i}^{\rho} \mathcal{C}(t)\mathrm{d}t. \tag{6.1.1}$$

and

$$\varepsilon(\rho) = \varepsilon_i + \int_{\rho_i}^{\rho} \frac{P(t)}{t^2}\mathrm{d}t. \tag{6.1.2}$$

Choosing a curve $\mathcal{C}(\rho)$ that is simple enough, integrals (6.1.1) and (6.1.2) have an analytic solution. We choose to model this thermodynamic quantity.

The sound speed presents a very distinctive behavior along PTs. In these intervals c_s^2 starts decreasing, reaches a minimum and then increases again. This shape could be modeled, for example, with a rotated hyperbola or logarithm. Nevertheless, in order to ensure the integrability of the curve and to make the analytic expression of the EoS simple we propose a polynomial model.

To simplify notation we use $x := \rho$. The model suggested is

$$gn(x) = \sum_{i=0}^{n} a_i \left(\frac{x}{x_m}\right)^i,$$

where we consider $n \in \{2, 3, 4\}$. A linear approximation ($n = 1$) does not allow for the change of monotony during the PT and higher degree ($n > 4$) may introduce unrealistic behavior to the model as we describe further on. The quantity x_m is a scale factor for the density. We set its value to be the density where the minimum of the sound speed is reached along the PT. Finally, a_i are the free parameters of the model.

Pressure must remain a continuous function when we add our model to an expression of the pressure for the rest of the star, here labeled as fit. Given an interval for the PT $[x_L, x_R]$, the pressure is continuous at x_L by taking $\rho_i = x_L$, $P_i = P_L = P_{fit}(x_L)$ in (6.1.1).

The continuity at x_R is imposed by equating $P_{fit}(x_R) = P_{gn}(x_R)$:

$$P_{fit}(x_R) = P_R = P_{gn}(x_R) = P_L + \sum_{i=0}^{n} \frac{a_i}{(i+1)x_m^i}(x_R^{i+1} - x_L^{i+1}).$$

We enforce this condition to our model fixing one of the free parameters, a_0:

$$a_0 = \underbrace{\frac{P_R - P_L}{x_R - x_L}}_{d} - \sum_{i=1}^{n} \frac{a_i}{x_m^i} \underbrace{\frac{x_R^{i+1} - x_L^{i+1}}{(i+1)(x_R - x_L)}}_{\theta_i}.$$

The internal energy is continuous at the left of the interval by taking the initial state $\varepsilon_i = \varepsilon_L = \varepsilon_{fit}(x_L)$. Then it is continuous at the right by taking as internal energy initial value for the next part of the general EoS $\varepsilon_R = \varepsilon_{gn}(x_R)$.

Our model, when including continuity of pressure, has an independent term d given by the extremes of the PT and a constant factor θ_i multiplied by each of the rest free parameters of the model:

$$gn(x) = \sum_{i=1}^{n} \frac{a_i}{x_m^i} \left(x^i - \theta_i\right) + d. \tag{6.1.3}$$

It contains n free parameters. Pressure and internal energy values are obtained straightforwardly

$$P(x) = P_L + \sum_{i=1}^{n} \frac{a_i}{x_m^i} \left(\frac{x^{i+1} - x_L^{i+1}}{i+1} - \theta_i(x - x_L) \right) + d(x - x_L)$$

$$\varepsilon(x) = \varepsilon_L + \sum_{i=1}^{n} \frac{a_i}{i(i+1)x_m^i x} \left(i x_L^{i+1} - (i+1)x_L^i x + x^{i+1} + (i+1)i\theta_i(x \ln(x_L/x) + x - x_L) \right)$$
$$+ d\left(\ln(x/x_L) + \frac{x_L - x}{x} \right) - \frac{P_L(x_L - x)}{x_L x}.$$

Once $gn(x)$ is completely defined assigning a value to its parameters, we have an expression for the EoS.

It is not convenient to introduce n new free parameters for each PT in an EoS model and therefore we determine the a_i values by the features of the PT.

When we localize a PT, we have the density values of its extremes x_L, x_R and the values of the sound speed in them, c_L and c_R respectively. Within the interval we can also find the location of the minimum of the sound speed x_m and its value c_m. We know that in x_L there is a local maximum of the sound speed, as the start of the PT is marked by its change of monotony. At x_m there is a local minimum. We can impose these pairs of values and local extrema to our model for determining the parameters.

We have a total of five conditions (three pair of values, two extrema). We can impose a maximum of n of them to each model at the same time. This gives a set of parametrizations from where we can choose the more appropriate one. Notice, however, that for $n = 2$ our model is a parabola and thus, from the two extrema, it only makes sense to impose the minimum as its vertex. In tables 6.1, 6.2 and 6.3 we gather the labeling of the parametrizations for each of the studied values of n and detail which conditions we impose in each of them.

Given a tabulated EoS and the location of a PT, we calculate all parametrizations for $n = 2, 3, 4$. We remove those that are not causal and thermodynamically consistent. In

Model	Parametrization	Conditions imposed
g2(x)	g2o1	$g2(x_L) = c_L$, $g2(x_m) = c_m$
	g2o2	$g2(x_L) = c_L$, $g2(x_R) = c_R$
	g2o3	$g2(x_m) = c_m$, $g2(x_R) = c_R$
	g2o4	$g2'(x_m) = 0$, $g2(x_L) = c_L$
	g2o5	$g2'(x_m) = 0$, $g2(x_m) = c_m$
	g2o6	$g2'(x_m) = 0$, $g2(x_R) = c_R$

Table 6.1: Possible analytic conditions that determine the parameters of the `g2(x)` PT model.

order to check consistency we verify that the value at the minimum is positive. This is straightforward as the local extrema of the three models can be found analytically. To check causality, we calculate the specific enthalpy using the expressions of pressure and internal energy to evaluate the relativistic sound speed at the maxima and check that is below the light speed in vacuum.

Once we have those models that do not contradict a physically valid EoS, we discard those whose shape contradicts the behavior of the sound speed along a PT. This means that we allow only models with exactly one local extrema that is, indeed, a minimum. This filter of the models is the reason why we do not consider higher order polynomials, as they tend to have more extrema along the PT interval. As a matter of fact, in most of the PTs studied all `g4(x)` models are discarded for this reason.

Model	Parametrization	Conditions imposed
g3(x)	g3o1	$g3(x_L) = c_L$, $g3(x_m) = c_m$, $g3(x_R) = c_R$
	g3o2	$g3'(x_L) = 0$, $g3'(x_m) = 0$, $g3(x_L) = c_L$
	g3o3	$g3'(x_L) = 0$, $g3'(x_m) = 0$, $g3(x_m) = c_m$
	g3o4	$g3'(x_L) = 0$, $g3'(x_m) = 0$, $g3(x_R) = c_R$
	g3o5	$g3'(x_L) = 0$, $g3(x_L) = c_L$, $g3(x_m) = c_m$
	g3o6	$g3'(x_L) = 0$, $g3(x_L) = c_L$, $g3(x_R) = c_R$
	g3o7	$g3'(x_L) = 0$, $g3(x_m) = c_m$, $g3(x_R) = c_R$
	g3o8	$g3'(x_m) = 0$, $g3(x_L) = c_L$, $g3(x_m) = c_m$
	g3o9	$g3'(x_m) = 0$, $g3(x_L) = c_L$, $g3(x_R) = c_R$
	g3o10	$g3'(x_m) = 0$, $g3(x_m) = c_m$, $g3(x_R) = c_R$

Table 6.2: Possible analytic conditions that determine the parameters of the `g3(x)` PT model.

To select the more appropriate model between all remaining alternatives, we evaluate their fitting accuracy calculating the relative least square error of the sound speed. Still, as we are providing an expression for the pressure, it is also crucial for this quantity to closely resemble the data. Hence we also compute the relative error of the pressure.

We determine that the error of a parametrization is the average between the error of

the pressure and the error of the sound speed. Finally we choose the parametrization with smaller error. This approach enables us to select among different fittings for the data without introducing more free parameters into the total EoS model.

Model	Parametrization	Conditions imposed
`g4(x)`	g4o1	$g4(x_L) = c_L$, $g4(x_m) = c_m$, $g4(x_R) = c_R$, $g4'(x_L) = 0$
	g4o2	$g4(x_L) = c_L$, $g4(x_m) = c_m$, $g4(x_R) = c_R$, $g4'(x_m) = 0$
	g4o3	$g4'(x_L) = 0$, $g4'(x_m) = 0$, $g4(x_L) = c_L$, $g4(x_m) = c_m$
	g4o4	$g4'(x_L) = 0$, $g4'(x_m) = 0$, $g4(x_L) = c_L$, $g4(x_R) = c_R$
	g4o5	$g4'(x_L) = 0$, $g4'(x_m) = 0$, $g4(x_m) = c_m$, $g4(x_R) = c_R$

Table 6.3: Possible analytic conditions that determine the parameters of the `g4(x)` PT model.

6.2 Thermodynamically consistent piecewise polytropic EoS

To construct the TCPP EoS we consider that the general expression for the pressure of the star is given by the PP EoS replaced by our polynomial model at the PTs.

We apply our modeling approach to the PTs identified in table 5.2. The selected models and their parameters can be found in tables A.1 and A.3, respectively, in the Appendix. For completeness, we also include in the Appendix the parameters of the studied PP EoSs, in table A.2.

We find that the most preferred model is the parabola, which is consistent with the change of monotony of the sound speed. Additionally, we obtain some higher order models. All of them are causal and thermodynamically consistent and offer a continuous EoS when stitched to the correspondent PP model.

To illustrate the performance of our model we display the main thermodynamic quantities for the tabulated data, the PP and the TCPP EoSs. We show the parabola that models the PT in BGN1H1, figure 6.1, the cubic polynomial for H6, figure 6.2, and the quartic polynomial for ALF1, figure 6.3.

In figure 6.1, depicting BGN1H1 EoS, we can see that the PP EoS has a sound speed lower that the tabulated data at the onset of the PT. Our PT model mimics a smooth descend from this value until reaching the minimum. Still, at the end of the PT it sharply increases beyond both the data and the PP model. This is because the model is parabolic thus it does not have enough free parameters to fit accurately both the minimum and the extremes. On the other hand, the TCPP EoS exhibits a nonconvex region (the fundamental derivative changes sign) similarly to the data. Although the TCPP pressure values deviate further from the data, their shape is more precise.

Figure 6.2, focused on the third PT of H6 EoS, shows a TCPP model which significantly deviates from the data. We impose that our model starts with a decreasing region but in this case the sound speed of the PP model is much lower than the data and the PT model has to remain almost constant. This shows an example of the high sensitivity of our PT model to the pressure value at the extremes. Although the pressure values of the PP EoS are close to the tabulated data in this region, the slope is not accurate with respect to the table. This has a negative impact in the modeling of the PT.

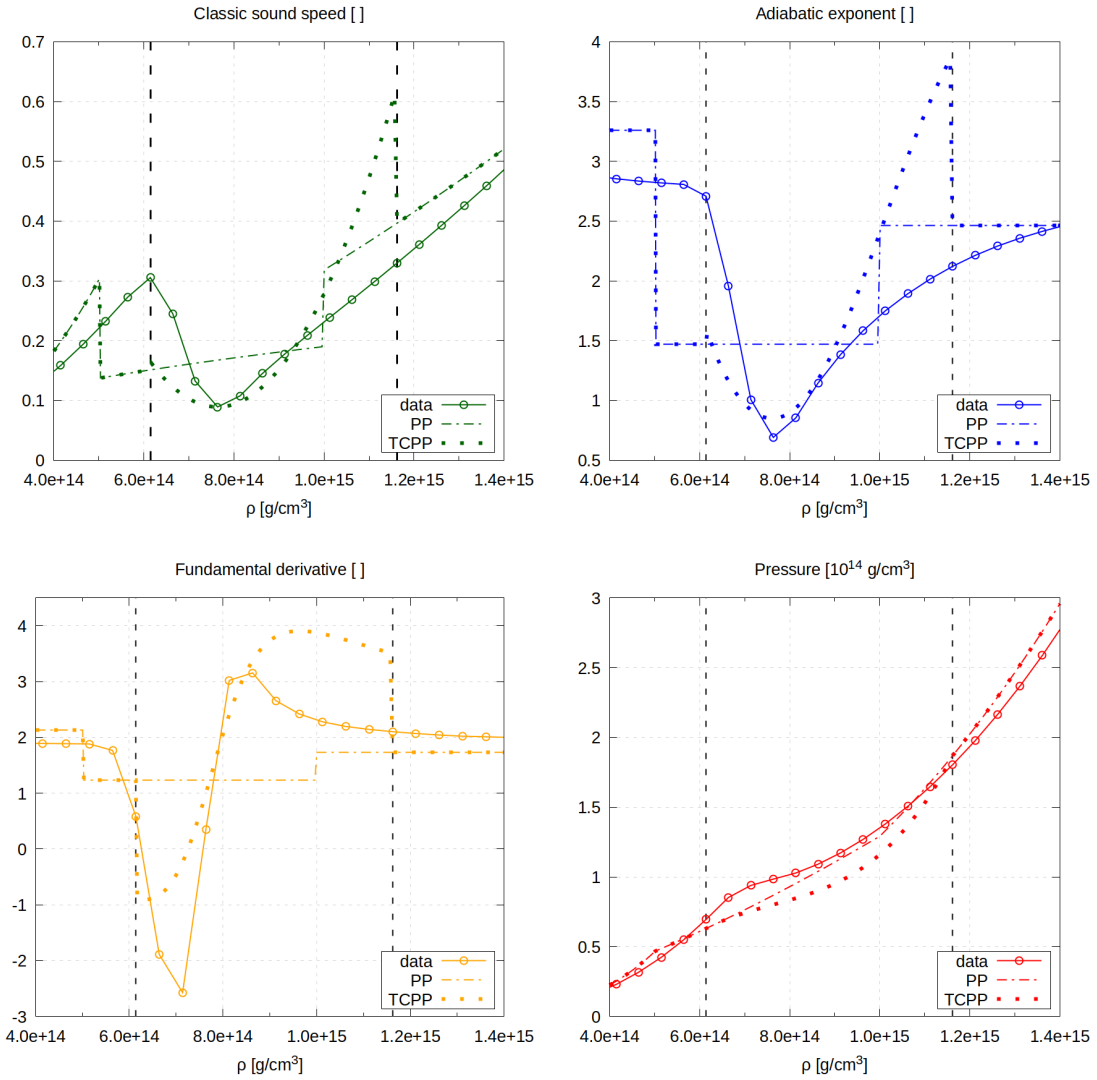

Figure 6.1: Main thermodynamic quantities for BGN1H1 EoS during its PT. Tabulated EoS, PP model and our TCPP model. Vertical dashed lines mark the limits of the PT.

The results for ALF1 EoS are shown in figure 6.3. The TCPP pressure shows better agreement with the data than the PP model. It also captures the nonconvex region. Fourth order polynomials like the one used in the fit of this PT lead to a better agreement with the tabulated EoS due to the higher number of parameters. Nevertheless, they usually have to be discarded because they introduce artificial local extrema along the PT.

6.3 Thermodynamically adaptive slope piecewise polytropic EoS

We follow the idea of the PP model of fitting polytropes with tabulated data for constructing an expression for the pressure outside PTs. Our novel approach is to remove the PT regions and calibrate a polytrope for each interval of data remaining. Therefore, our general fit for the high density region has as many polytropes as PTs plus one.

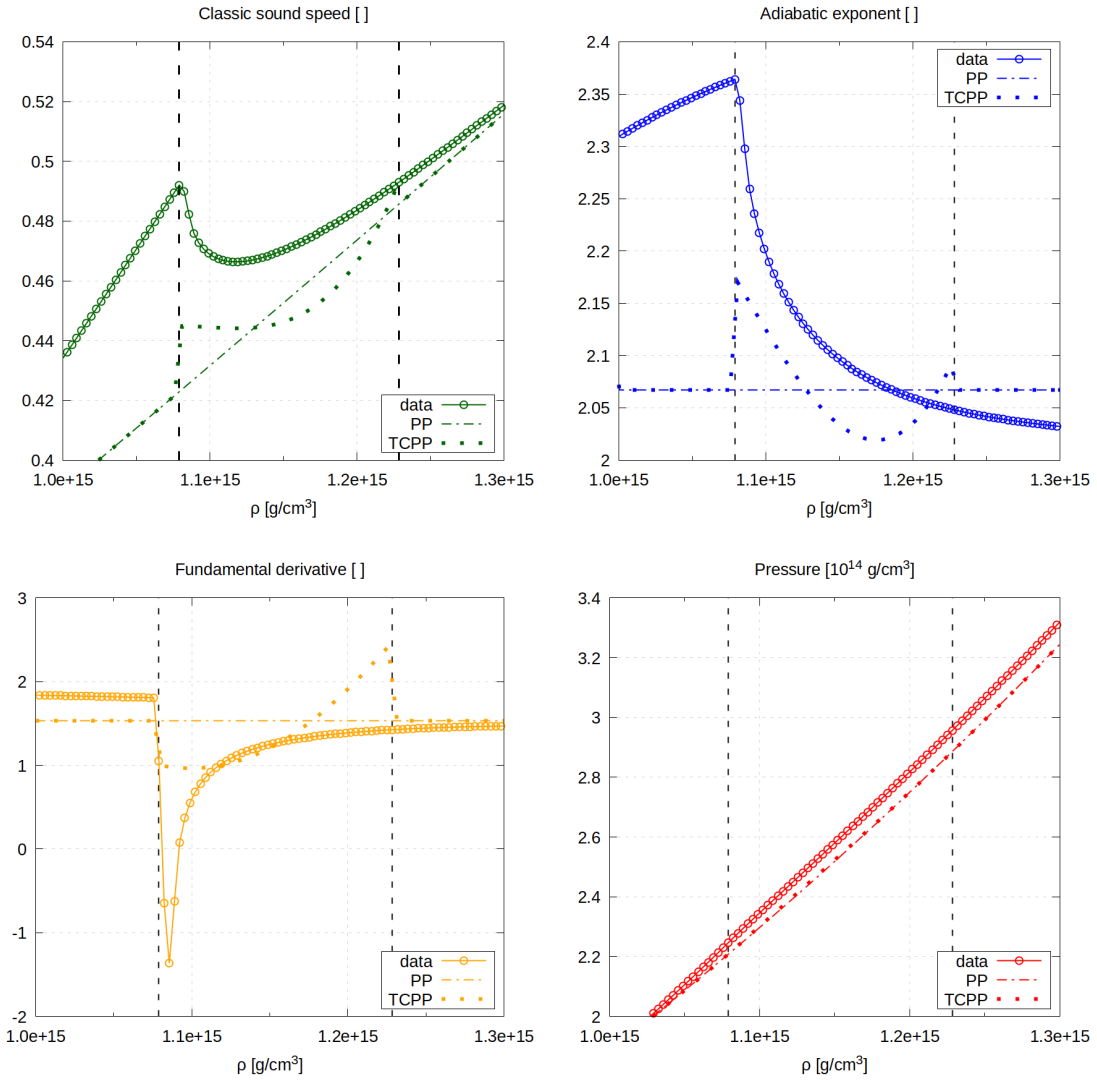

Figure 6.2: Main thermodynamic quantities for H6 EoS during its third PT. Tabulated EoS, PP model and our TCPP EoS. Vertical dashed lines mark the limits of the PT.

We focus on the modeling of the EoSs from Arizona database [3] in order to compare our results with the PP model. As the PTs detected for these EoSs are in the high density region, for our purposes we can maintain the existing crust of four fixed polytropes from the PP model. However, our T-ASPP modeling could be applied to the whole star in order to account for PTs in the crust as those found in the EoSs from CompOSE [1] in table 5.3.

A first polytrope matches the model of the crust at some density ρ_1 and extends up to the start of the first PT of the EoS. To ensure continuity of the pressure, the free parameters of this polytrope $P = \kappa\rho^\Gamma$ are the matching density with the crust last polytrope $P = \kappa_c\rho_c^\Gamma$, ρ_1, and the adiabatic index Γ. The matching density determines $\kappa = \kappa_c\rho_1^{\Gamma_c-\Gamma}$. To fit the relation we minimize the cost function

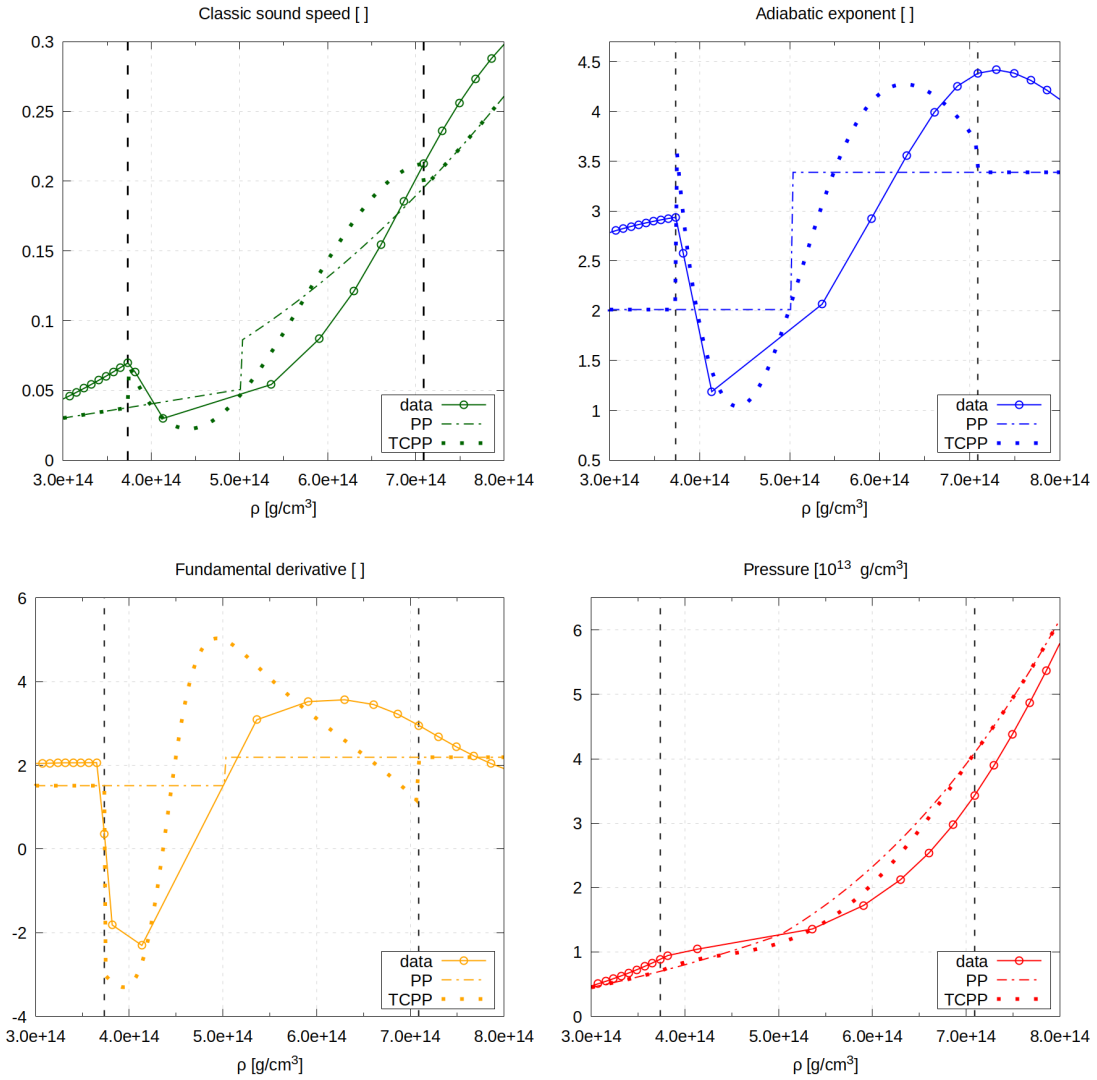

Figure 6.3: Main thermodynamic quantities for ALF1 EoS during its PT. Tabulated EoS, PP model and our TCPP EoS. Vertical dashed lines mark the limits of the PT.

$$S_1 = \sqrt{\frac{1}{m}\sum_{\rho_i>\rho_1}\left(\log(P_i) - \log(\kappa_c \rho_1^{\Gamma_c-\Gamma}) - \Gamma\log(\rho_i)\right)^2}$$

where m is the number of density points above the value ρ_1.

Any polytrope defined in the region after a PT does not have continuity conditions with any other piece and therefore both parameters κ and Γ can be used in the fitting. The cost function minimized is

$$S_2 = \sqrt{\frac{1}{N}\sum_{\rho_i}\left(\log(P_i) - \log(\kappa) - \Gamma\log(\rho_i)\right)^2} \tag{6.3.1}$$

where N is the number of points in the tabulated data.

Given that the high density region of the EoS is adjusted with a number of polytropes equal to the number of PTs plus one, when there are at least two PTs the pressure is fairly

well reconstructed. Nevertheless, in the presence of a single PT, one unique polytrope may not be able to capture correctly the changes of slope of the pressure along the core. We design a procedure to locate significant changes in the slope of pressure within the tabulated data. The method is designed to apply to EoSs with a single PT and it focuses on the region after it.

6.3.1 Locating significant changes of the pressure slope

The pressure in the tabulated data may experiment a significant change of its slope during the higher density region corresponding to the description of the inner core of the NS. When trying to fit the whole core with a single polytrope it captures an average slope of the tabulated points, not being very accurate neither in the outer core or the inner core.

We analyze the sound speed to study the slope of the pressure. We define a *significant change of slope* as a jump discontinuity of the sound speed or a decreasing region that is not a PT. If the sound speed decreases smoothly there is no kink in the adiabatic exponent and therefore the region is not identified as a PT, although it reduces the slope of the pressure. We divide the region after the PT in two different polytropes if we find a significant change of slope in the pressure. Both of the two criteria announced yield a suggestion for the dividing density.

To locate a decreasing region of the sound speed we look for local maxima in the data. To remove oscillatory behavior, we impose that the sound speed decreases for at least two data points after the maximum. If there are more than one maximum, we consider as dividing density suggestion the one at a smaller density.

To locate a jump discontinuity in the sound speed we use the local total variation (LTV) defined in (5.1.1), $TV_j^3(c_s^2)$. We compute this quantity for the whole region after the PT. We look for maxima of the LTV, discarding them as oscillatory behavior if the monotonicity of the LTV changes sign during the three previous or posterior points. We consider a maximum of the LTV relevant if its value is greater that the mean of the LTV during the region plus two times the standard deviation. In a Gaussian distribution this criteria isolates the data outlier from the mean with 95% confidence. We consider that the notion can be extended to our study and the criteria identifies peaks of the LTV that are actually significant jumps in the sound speed. If there are more than one peak obeying this criteria, the dividing density suggestion from this approach is the density value with the larger LTV.

If none of the criteria above yield a dividing density suggestion it means that the pressure behaves smoothly along the core of the NS and it can be well captured by a single polytrope. If just one of the criteria suggests a density, it is taken as the dividing density between two different polytropes for the NS core.

In the case where the two criteria suggest a dividing density, we select the one coming from the LTV of the sound speed. We consider that a jump in the slope may introduce a greater change in the pressure that a smooth region of decreasing sound speed.

When the region after the PT is fitted with two different polytropes, 1 and 2, separated at density ρ_c selected with the method above, then the first polytrope has two free parameters and is fitted optimizing cost S_2 (6.3.1) using densities up to ρ_c. To ensure continuity of the pressure at ρ_c, the second polytrope has a single free parameter, Γ_2, and $\kappa_2 = \kappa_1 \rho_c^{\Gamma_1 - \Gamma_2}$. Therefore the cost function to minimize is

$$S_3 = \sqrt{\frac{1}{N} \sum_{\rho_i > \rho_c} \Big(\log(P_i) - \log(\kappa_1 \rho_c^{\Gamma_1 - \Gamma_2}) - \Gamma_2 \log(\rho_i) \Big)^2}.$$

The dividing densities arising from the extremes of the PT and the study of the sound speed yield this EoS model the name of T-ASPP.

We apply this modeling to the EoSs from Arizona database [3] with PTs located in table 5.2. The parameters of the fitted polytropes (for EoSs with one and more PTs), the selected polynomials for the PTs and the coefficients of the PT models obtained can be found in the Appendix, in tables A.4, A.5 A.6 and A.7 respectively.

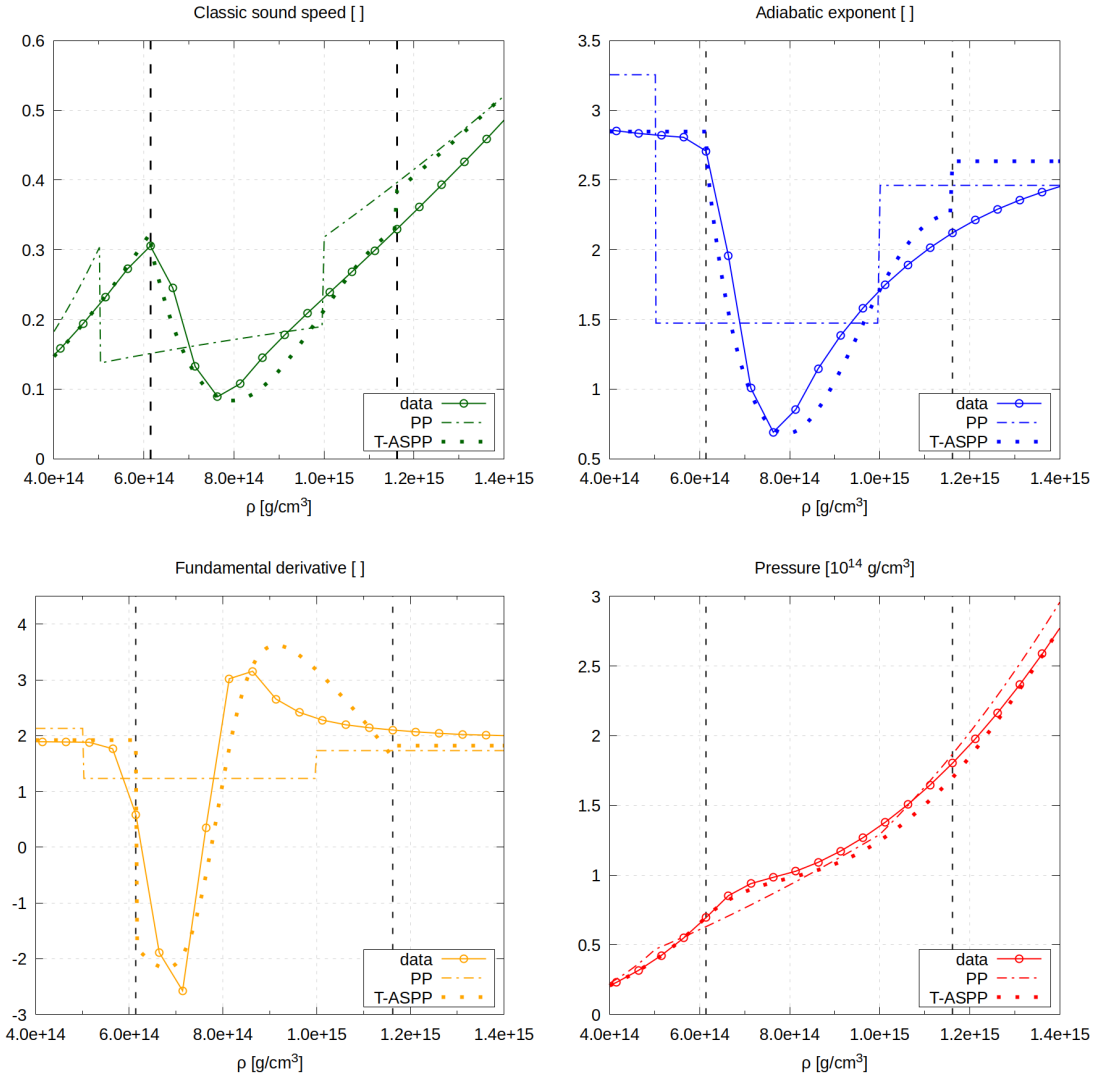

Figure 6.4: Main thermodynamic quantities for BGN1H1 EoS during its PT. Tabulated EoS, PP model and our T-ASPP model. Vertical dashed lines mark the limits of the PT.

To show the performance of the T-ASPP model we present the sound speed, adiabatic exponent, fundamental derivative and pressure compared to the PP model and the tabulated data of BGN1H1, H6 and ALF1 EoSs. This allows a direct comparison with figures 6.1-6.3, which show the results for the TCPP model.

Figure 6.4 shows BGN1H1 EoS. The fit of the pressure of the T-ASPP model follows the pressure data accurately both inside and outside the PT, represented by a fourth order polynomial. All thermodynamic quantities are well captured, including the nonconvex

region. The sound speed presents a roughly noticeable jump in the left extreme of the PT and a much smaller jump at the right than the TCPP model.

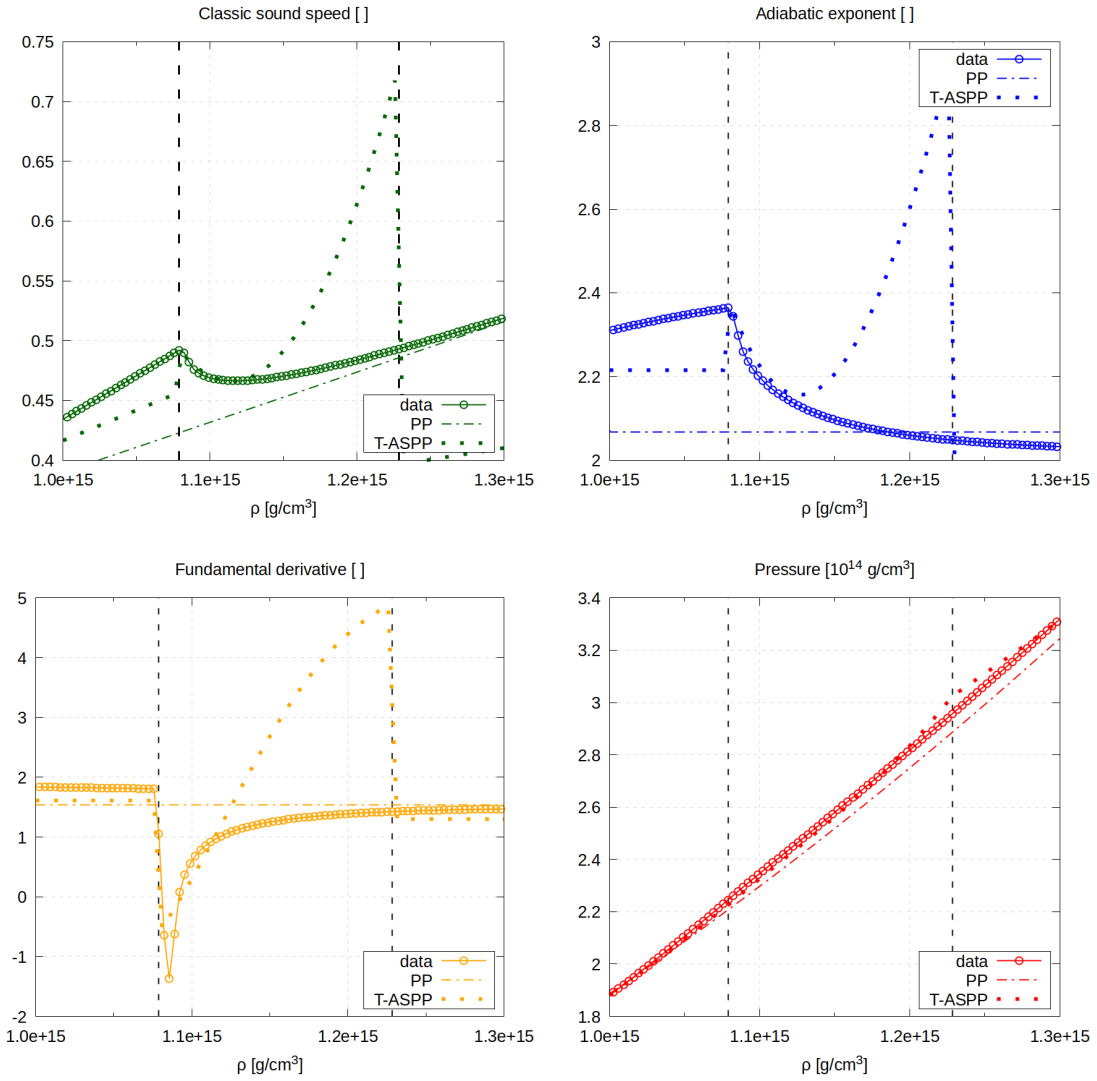

Figure 6.5: Main thermodynamic quantities for H6 EoS during its third PT. Tabulated EoS, PP model and our T-ASPP model. Vertical dashed lines mark the limits of the PT.

In figure 6.5 we depict is the third PT of H6 EoS. As with the TCPP model, this EoS displays how sensitive is our PT model to the pressure values at the extremes. With the T-ASPP model the pressure fit resembles well the data but it departs from the trend at the end of the PT. The polynomial selected in this case is a parabola, that adjust the minimum of the sound speed but increases largely at the end of the PT. This induces a sudden increase of the slope of the pressure that can be noticed in the graphic. Aside from this undesired behavior at the end of the PT, we observe that the new approximation of the EoS outside the PT provides P_L and P_R values which allow the PT model to capture the nonconvex region. Despite the inaccurate fit of the parabola towards the end of the PT, the T-ASPP model captures the thermodynamic properties of the EoS.

Last example, ALF1 EoS in figure 6.6, displays another accurate modeling of the

thermodynamics. The polytrope used for the pressure at the left of the PT follows well the tabulated data, leading to a good representation of the slope. Therefore the transition from the polytrope to the PT model from the left is quite smooth. The polytrope used after the PT resembles the one from the PP, further from the tabulated data and with different slope. Thus the sound speed presents a greater jump at the right extreme of the PT. The change of the pressure at the left with respect to the PP model induces that in this case the PT is represented with a third order polynomial, instead of the fourth degree in the TCPP. Still, the nonconvex region is captured.

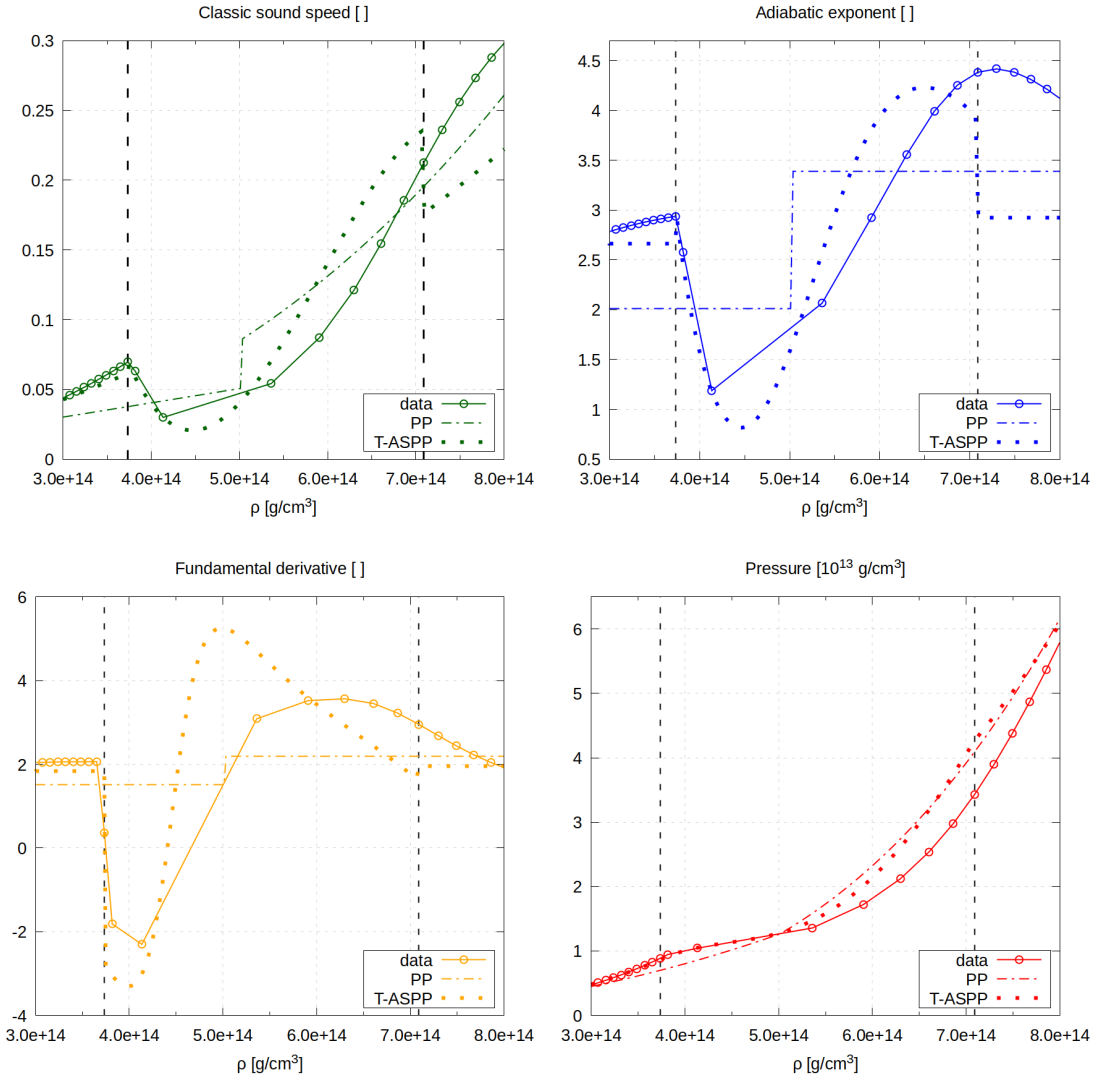

Figure 6.6: Main thermodynamic quantities for ALF1 EoS during its PT. Tabulated EoS, PP model and our T-ASPP model. Vertical dashed lines mark the limits of the PT.

6.4 Comparison of stellar properties

We compute the relative percent difference (RPD) of the stellar properties induced by the different EoS models with respect to the tabulated EoSs to compare the performance in

the representation of NSs.

The sequence of NSs is constructed from the central density of the maximum mass star according to the tabulated EoS. The EoS models are compared down to the central density where the first of them reaches a star of 16km radius.

Results are gathered in table 6.4. The results show that in general no single model is superior in all scenarios. Given an EoS, the smaller error for each quantity may come from different analytic models. Noticeably, on GS2 and ALF2 EoSs the T-ASPP model obtains better results for all stellar properties.

	RPD M			RPD R			RPD Λ		
EoS	PP	TCPP	T-ASPP	PP	TCPP	T-ASPP	PP	TCPP	T-ASPP
PS	1.185	2.508	2.187	3.019	2.617	0.7440	9.143	9.623	8.732
GS1	2.133	5.776	2.481	2.429	2.314	1.298	15.61	24.79	18.66
GS2	2.386	3.568	1.621	2.087	1.961	1.046	16.16	19.33	15.84
BGN1H1	3.888	5.048	2.562	0.856	1.249	1.100	26.80	30.10	36.73
H4	1.217	1.183	1.287	3.268	3.279	3.256	6.056	5.962	6.304
H5	1.520	1.481	2.383	1.918	1.927	2.663	28.10	27.99	26.55
H6	1.474	1.457	1.373	1.883	1.883	1.488	32.748	32.68	33.79
H7	1.447	1.404	1.910	3.007	3.016	3.511	26.24	26.11	25.58
ALF1	6.191	5.732	3.810	2.705	2.617	1.053	34.09	29.62	23.00
ALF2	8.783	9.019	6.815	3.268	3.334	3.298	44.33	45.03	31.289

Table 6.4: RPD of stellar properties with respect to the tabulated EoS for the different EoS models. Colored cells signal the best result for each property and EoS.

In general, the T-ASPP model achieves smaller errors for all quantities in a greater number of EoSs. We highlight the good results obtained for ALF1 and ALF2. For ALF1 the error in mass is 1.62 times smaller with T-ASPP than with PP, the error in radius 2.57 times smaller and the error in tidal deformability 1.48 times smaller. For ALF2, the error in the mass is 1.29 times better with T-ASPP than with PP, the error for the radius is almost the same and the tidal deformability is 1.42 times better with T-ASPP.

We obtain that TCPP model does not improve the error in radius for any EoS, although it does improve slightly some errors in mass and tidal deformability.

In figure 6.7 we draw the information of table 6.4, depicting the RPD for mass, radius and tidal deformability for all EoSs studied with PTs. We show the quantities for the three EoS analytic models. This graphic reveals that the T-ASPP model decreases the general error in mass and tidal deformability, and perform similarly to the PP model for the radius.

The average RPD of mass is around 3.02% for the PP model. TCPP increases to 3.72% while T-ASPP reduces the mean error to 2.64%. For T-ASPP the majority of EoSs have an error around the mean, while the other models present a greater deviation. In the case of the star radius, the error has a more sparse distribution for the three analytic models. Still the PP model presents the greater mean error of 2.44%, followed by the TCPP with 2.42%. The best mean result is again for T-ASPP, with mean RPD for the radius of 1.95%.

The tidal deformability presents significant errors for the three analytic models. While the maximum error for PP and TCPP is around 45%, for T-ASPP is below 40%. TCPP model has the higher mean error of 25.12%. The mean errors for PP, 23.93%, and T-ASPP, 22.65%, are more similar, but again T-ASPP presents the best results.

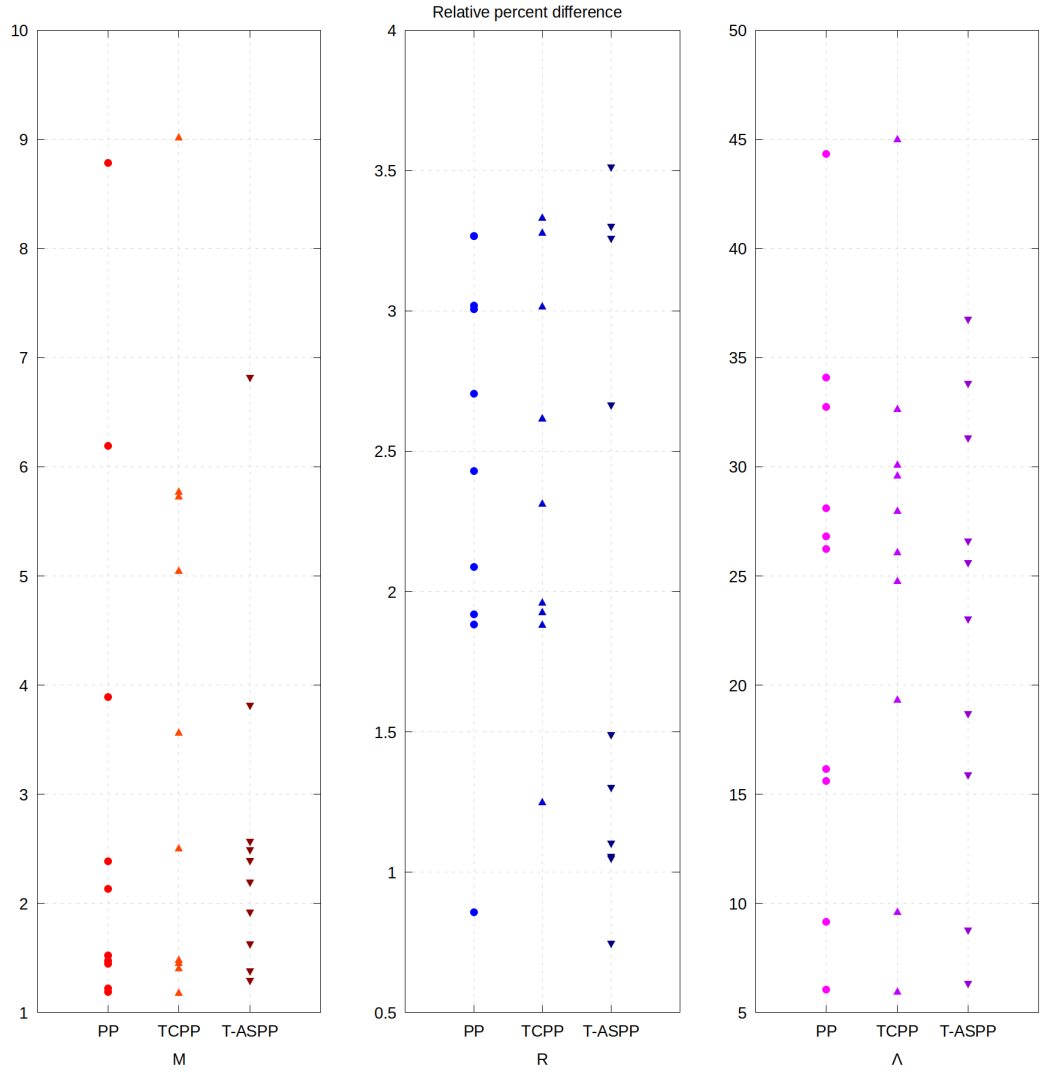

Figure 6.7: Comparison of RPD of mass, radius and tidal deformability for the EoS from [3] with PTs using different EoS analytic models: PP, TCPP and T-ASPP.

In general, we can say that our T-ASPP model improves the representation of the stellar properties of NSs. Although it may contain more free parameters than the PP model, in the case of several PTs within the high density region of the EoS, the analytic expression is equally simple and computationally efficient. It also presents the advantage of a better representation of the thermodynamics, depicting regions of smooth decrease of the sound speed and allowing for nonconvex EoS models.

6.5 Influence in hydrodynamics

With the aim of showcasing the impact of PTs on the fluid hydrodynamic evolution, we use PP, TCPP and T-ASPP models for ALF1 EoS in SRHD. We design two Riemann problems that reveal the impact of an accurate thermodynamics.

We design an analogous to the blast wave problem presented in Chapter 2 to use with cold EoSs. We name it *cold blast wave*. The key difference between the cold blast

wave and traditional blast waves is the density shell. While pressure and velocity values remain constant across contact discontinuities, with a hot EoS $P(\rho, \varepsilon)$ the wave admits an arbitrary jump in density resulting in the characteristic high, thin shell. Using a cold EoS, where the relationship between pressure and density is bijective, means that a constant pressure results in a constant density across the contact discontinuity eliminating the density jump.

The Riemann problems suggested, cold blast wave 1 and 2, are gathered in table 6.5. Notice that the initial value for the density implies the initial value of the pressure. Therefore the initial state of pressure may be different for different modelings of the same EoS. Using the spatial domain $x \in [0, 1]$ with initial discontinuity at $x = 0.5$, we present the solution profile for pressure, density, velocity and fundamental derivative at time $t_f = 0.2$. For the numerical solution we use MFF with PHM reconstruction (see Chapter 4) and divide the domain in 16000 intervals. The graphics are represented in $x \in [0.4, 0.6]$, focused on the waves.

	$\rho_L\,[\mathrm{g/cm^3}]$	v_L	$\rho_R\,[\mathrm{g/cm^3}]$	v_R
Cold blast wave 1	$8{\cdot}10^{13}$	0	$4.3{\cdot}10^{14}$	0
Cold blast wave 2	$3.1{\cdot}10^{14}$	0	$4.45{\cdot}10^{14}$	0

Table 6.5: Riemann problems designed for ALF1 EoS aiming to exemplify the influence of PTs in the hydrodynamics.

Cold blast wave 1 is a Riemann problem where the right initial state is inside the PT of the EoS and the left initial state is at a smaller density outside of it. The change of piece in a piecewise EoS introduces artificial discontinuities in the sound speed that can affect the wave dynamics. Thus it is important to identify the change of pieces that the solution of the problem traverses, allowing to pick out the artificial effects introduced in the dynamics.

For the PP model the problem develops inside the first polytrope of high density matter. Due to the addition of the modeling of the PT, with TCPP the problem traverses the change from the polynomial modeling the PT to the polytrope outside of it. For the T-ASPP there are two changes of definition: from the PT to a polytrope and from this polytrope to the crust.

In figure 6.8 we display the solution of the cold blast wave 1 using PP and TCPP models. The pressure is higher on the right side, causing an expansive wave to move towards the right decreasing both density and pressure. In the case of the PP model, a rarefaction moves to the right. For the TCPP the right initial condition is located in a region of negative fundamental derivative $\mathcal{G}$, leading to a shock wave moving towards the right. Outside of the PT both EoS models coincide, hence the solution profiles are the same after the transition from the polynomial to the polytropic piece. In the solution for the TCPP model we can appreciate a brief constant state after the shock wave moving to the right connecting it to the rarefaction wave. This is due to the jump in the sound speed induced by the change from the polynomial to the polytropic definition.

Figure 6.9 shows the solution for the cold blast wave problem 1 using PP and T-ASPP models. Given that the T-ASPP describes pressure outside the PT differently from the PP the solutions, although similar, do not overlap. The left initial condition is in a $\mathcal{G} < 0$ region for the T-ASPP model, as it was for TCPP. Therefore, the same composite wave formed by a shock and a rarefaction appears. The change of definition from the polynomial of the PT to the polytrope outside it happens at the same density than in the TCPP model

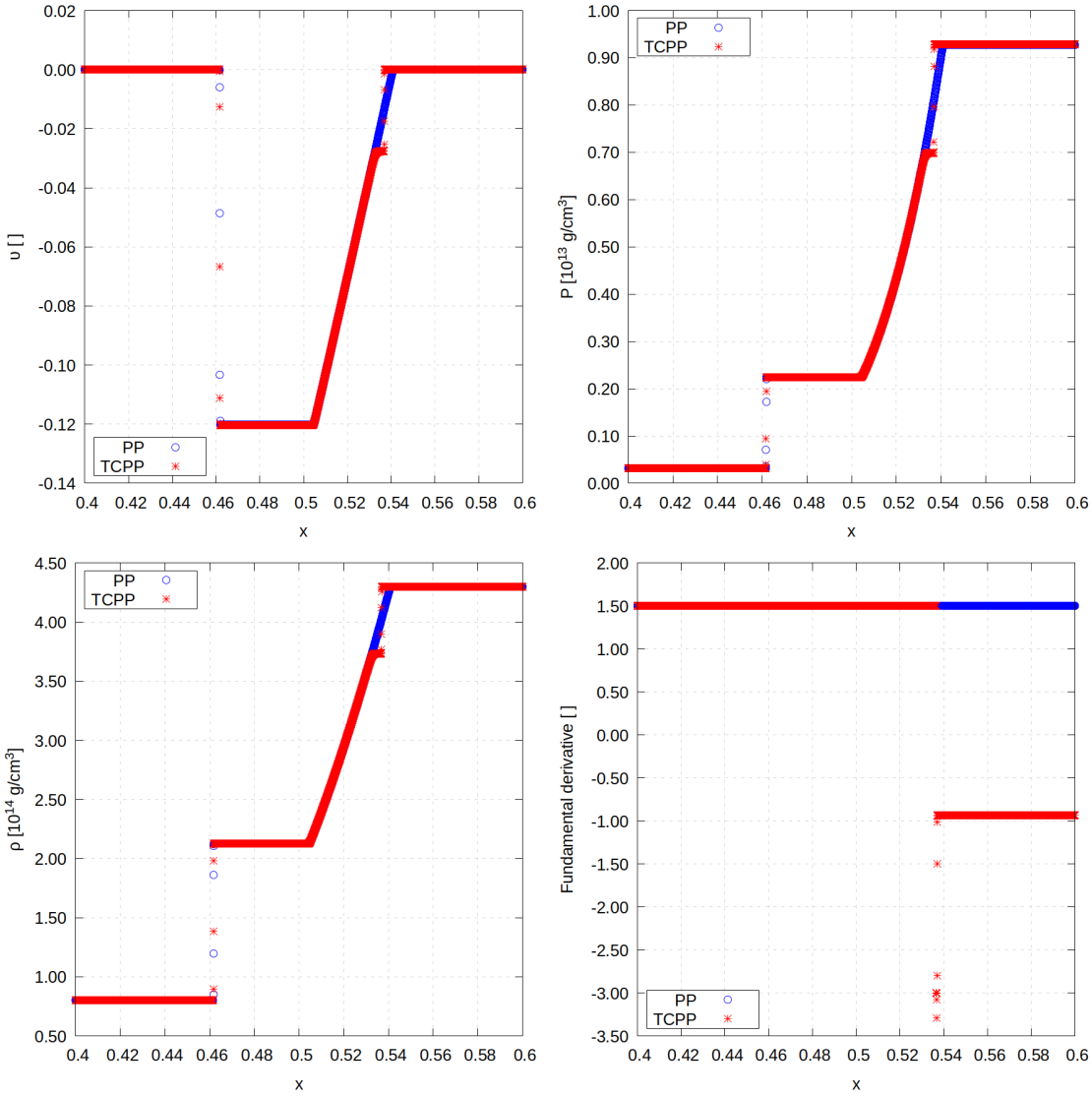

Figure 6.8: Profiles for cold blast wave 1 using ALF1 EoS with PP and TCPP models. Left to right, top to bottom: velocity, pressure, density and fundamental derivative.

but in this case there is no artificial constant state between the shock and the rarefaction. This is because the change of piece is quite smooth in this model as it can be seen in figure 6.6. The change of polytrope between the high density region and the crust of this model occurs during the shock moving to the left, yielding no artificial effects in the dynamics.

The change of pieces can be appreciated clearly in the fundamental derivative, where there are jump discontinuities between the different values.

The solution of the T-ASPP model is a fair representation of the wave dynamics that the tabulated ALF1 EoS would induce.

Cold blast wave 2 problem has the right initial state inside the PT of the EoS. The left initial state is located at a higher density than in the previous cold blast wave and therefore in this case the T-ASPP model presents a single change of piece from the polynomial of the PT to the polytrope outside. For PP and TCPP models, the change of pieces is the same than with the previous cold blast wave.

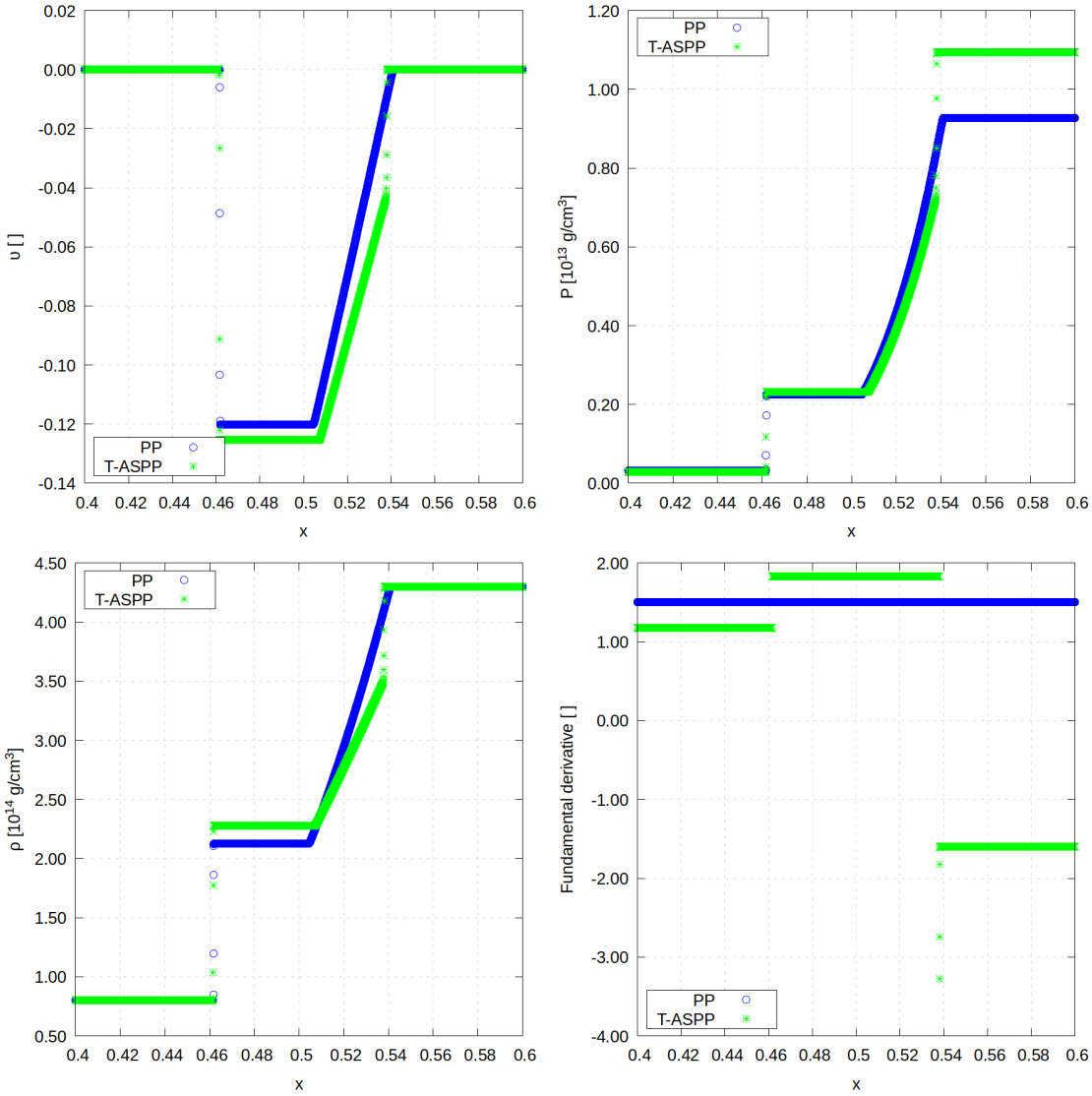

Figure 6.9: Profiles for cold blast wave 1 using ALF1 EoS with PP and T-ASPP models. Left to right, top to bottom: velocity, pressure, density and fundamental derivative.

We present the solution for the cold blast wave 2 using PP and TCPP models in figure 6.10. The PP presents an expansive rarefaction towards the right and a compressive shock to the left. This shock wave is the same that appears for the TCPP model as the left initial condition lies in the polytrope common to both models. The wave to the right in the TCPP model is another shock wave even when the right initial condition is in a region of $\mathcal{G} > 0$. To understand the nature of this wave we refer to the study of nonconvex dynamics performed in Chapter 2.

The right sequence of wave curves associated to this Riemann problem for the TCPP EoS starts with an integral curve since the initial condition lies in a convex region and the pressure has to decrease. This curve encounters a zero of the nonlinearity factor, as we can deduce seeing the change of sign of the fundamental derivative over the solution. Therefore it is terminated and continued with a mixed curve. As the integral curve is short, the mixed curve is soon finished and its jump discontinuity is prolonged by a Hugoniot

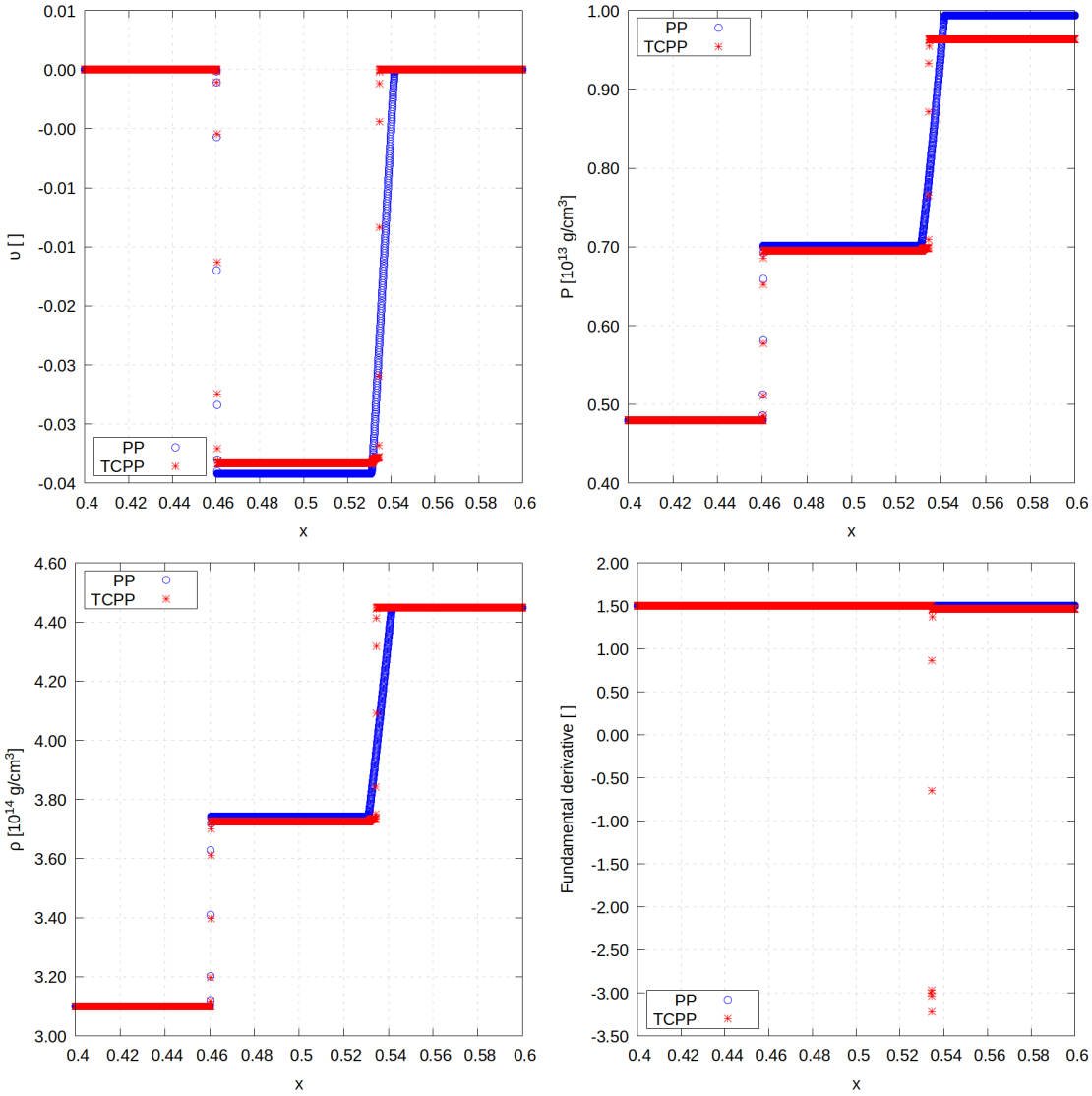

Figure 6.10: Profiles for cold blast wave 2 using ALF1 EoS with PP and TCPP models. Left to right, top to bottom: velocity, pressure, density and fundamental derivative.

curve with origin in the initial state. The associated wave overtakes the previous ones and we observe a shock wave in the solution profile.

The change of piece from the polynomial to the polytrope takes place during the shock and does not modify the wave dynamics.

In figure 6.11 we present the solution for the cold blast wave 2 using PP and T-ASPP models. Following the same reasoning, T-ASPP model yields shock waves both to the left and the right.

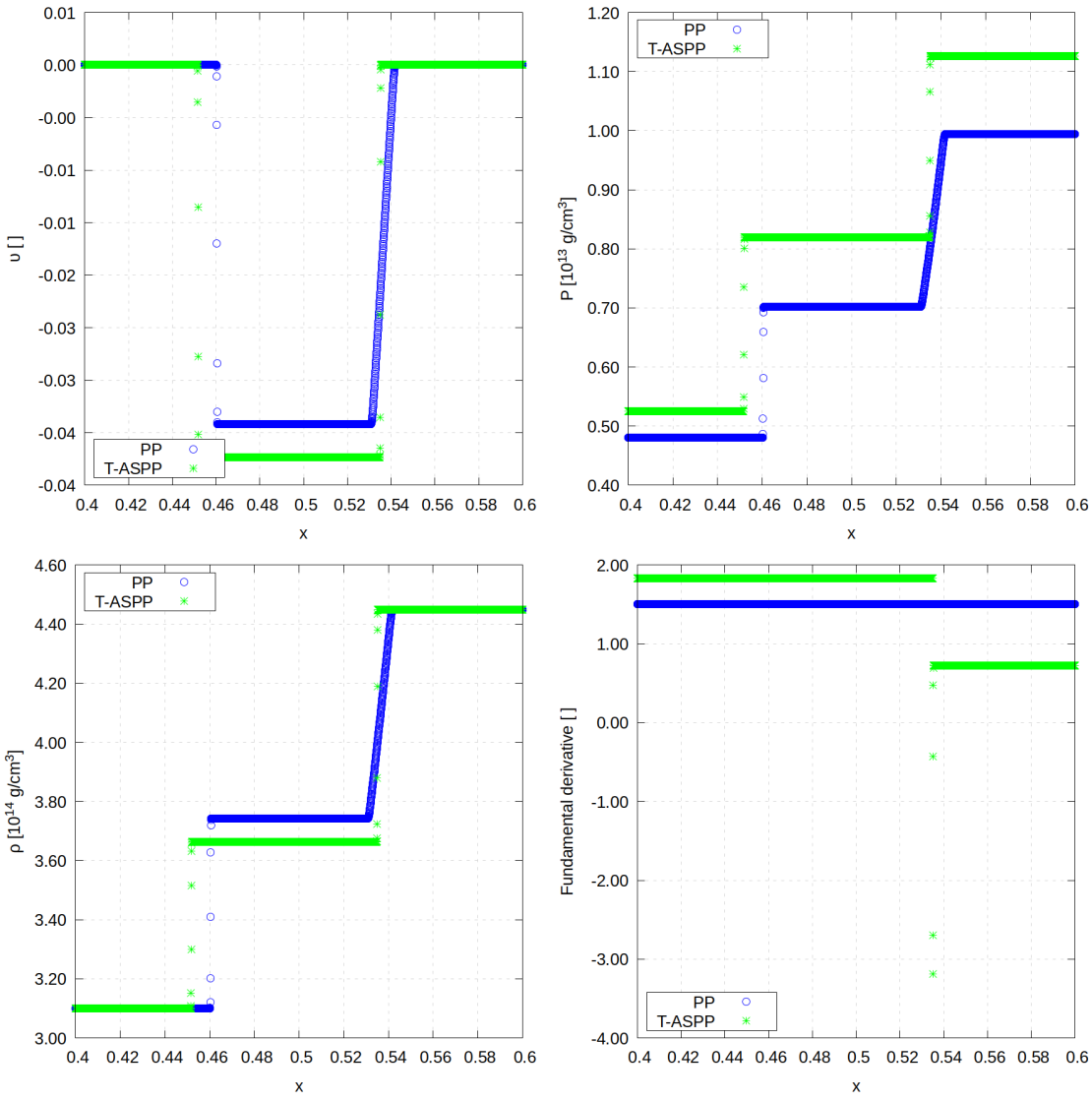

Figure 6.11: Profiles for cold blast wave 2 using ALF1 EoS with PP and T-ASPP models. Left to right, top to bottom: velocity, pressure, density and fundamental derivative.

Chapter 7

Bibliography

[1] CompStar Online Supernovae Equation of State. `https://compose.obspm.fr`. Tables retrieved December 2021.

[2] Einstein toolkit: Open software for relativistic astrophysics. `http://einsteintoolkit.org/`.

[3] Neutron Stars - University of Arizona. `http://xtreme.as.arizona.edu`. Tables retrieved January 2022.

[4] B. P. Abbott et al. Observation of gravitational waves from a binary black hole merger. *Physical Review Letters*, 116(6):061102, 2016.

[5] B. P. Abbott et al. GW170817: Observation of Gravitational Waves from a Binary Neutron Star Inspiral. *Physical Review Letters*, 119:161101, 2017.

[6] B. P. Abbott et al. GW170817: Measurements of Neutron Star Radii and Equation of State. *Physical Review Letters*, 121:161101, 2018.

[7] B. P. Abbott et al. Model comparison from LIGO–Virgo data on GW170817's binary components and consequences for the merger remnant. *Classical and Quantum Gravity*, 37(4):045006, 2020.

[8] B. K. Agrawal, S. Shlomo, and V. Kim Au. Determination of the parameters of a Skyrme type effective interaction using the simulated annealing approach. *Physical Review C*, 72:014310, 2005.

[9] B. K. Agrawal, S. Shlomo, and V. Kim Au. Nuclear matter incompressibility coefficient in relativistic and nonrelativistic microscopic models. *Physical Review C*, 68:031304, 2003.

[10] M. Alford et al. Hybrid Stars that Masquerade as Neutron Stars. *The Astrophysical Journal*, 629(2):969, 2005.

[11] M. A. Aloy et al. GENESIS: A high-resolution code for three-dimensional relativistic hydrodynamics. *The Astrophysical Journal Supplement Series*, 122(1):151, 1999.

[12] M. A. Aloy et al. Neutron star collapse and gravitational waves with a non-convex equation of state. *Monthly Notices of the Royal Astronomical Society*, 484(4):4980–5008, 2019.

[13] A. M. Anile. *Relativistic Fluids and Magneto-fluids: With Applications in Astrophysics and Plasma Physics*. Cambridge Monographs on Mathematical Physics. Cambridge University Press, 1990.

[14] B. M. Argrow. Computational analysis of dense gas shock tube flow. *Springer Verlag*, 6:241–248, 1996.

[15] L. Baiotti. Gravitational waves from neutron star mergers and their relation to the nuclear equation of state. *Progress in Particle and Nuclear Physics*, 109:103714, 2019.

[16] S. Balberg and A. Gal. An effective equation of state for dense matter with strangeness. *Nuclear Physics A*, 625(1-2):435–472, 1997.

[17] A. Bauswein, H-T. Janka, and R. Oechslin. Testing approximations of thermal effects in neutron star merger simulations. *Physical Review D*, 82(8):084043, 2010.

[18] G. Baym et al. From hadrons to quarks in neutron stars: a review. *Reports on Progress in Physics*, 81(5):056902, 2018.

[19] G. Baym, C. Pethick, and P. Sutherland. The Ground State of Matter at High Densities: Equation of State and Stellar Models. *Astronomy & Astrophysics*, 170:299, 1971.

[20] L. Bennour et al. Charge distributions of ^{208}Pb, ^{206}Pb, and ^{205}Tl and the mean-field approximation. *Physical Review C*, 40:2834–2839, 1989.

[21] M. Boyle et al. The SXS Collaboration catalog of binary black hole simulations. *Classical and Quantum Gravity*, 36(19):195006, 2019.

[22] D. Brown et al. Turduckening black holes: An analytical and computational study. *Physical Review D*, 79:044023, 2009.

[23] E. Chabanat. *Interactions effectives pour des conditions extrêmes d'isospin*. PhD thesis, 1995.

[24] E. Chabanat et al. A Skyrme parametrization from subnuclear to neutron star densities. *Nuclear Physics A*, 627(4):710–746, 1997.

[25] G. D'Angelo and P. Bodenheimer. Three-dimensional radiation-hydrodynamics calculations of the envelopes of young planets embedded in protoplanetary disks. *The Astrophysical Journal*, 778(1):77, 2013.

[26] T. Dietrich et al. CoRe database of binary neutron star merger waveforms. *Classical and Quantum Gravity*, 35(24):24LT01, nov 2018.

[27] R. Donat et al. A Flux-split algorithm applied to relativistic flows. *Journal of Computational Physics*, 146:58–81, 1998.

[28] R. Donat and A. Marquina. Capturing Shock Reflections: An Improved Flux Formula. *Journal of Computational Physics*, 125:42–58, 1996.

[29] F. Douchin and P. Haensel. A unified equation of state of dense matter and neutron star structure. *Astronomy & Astrophysics*, 380(1):151–167, 2001.

[30] C. Drischler et al. Limiting masses and radii of neutron stars and their implications. *Physical Review C*, 103(4):045808, 2021.

[31] B. Einfeldt. On Godunov-type methods for gas dynamics. *SIAM Journal on Numerical Analysis*, 25(2):294–318, 1988.

[32] B. Einfeldt et al. On Godunov-type methods near low densities. *Journal of Computational Physics*, 92(2):273–295, 1991.

[33] F. Eulderink and G. Mellema. General relativistic hydrodynamics with a Roe solver. *arXiv preprint astro-ph/9411056*, 1994.

[34] J. A. Font et al. Multidimensional relativistic hydrodynamics: characteristic fields and modern high-resolution shock-capturing schemes. *Astronomy & Astrophysics*, 282:304–314, 1994.

[35] J. A. Font et al. Three-dimensional numerical general relativistic hydrodynamics: Formulations, methods, and code tests. *Physical Review D*, 61:044011, 2000.

[36] B. Giacomazzo and L. Rezzolla. The exact solution of the Riemann problem in relativistic magnetohydrodynamics. *Journal of Fluid Mechanics*, 562:223–259, 2006.

[37] N. K. Glendenning and J. Schaffner-Bielich. First order kaon condensate. *Physical Review C*, 60:025803, 1999.

[38] S. K. Godunov. A difference method for numerical calculation of discontinuous solutions of the equations of hydrodynamics. *Matematicheskii Sbornik (Novaya Seriya)*, 47:271–306, 1959.

[39] A. Guardone and L. Vigevano. Roe Linearization for the van der Waals gas. *Journal of Computational Physics*, 178:50–78, 2002.

[40] P. Haensel, K. P. Levenfish, and D. G. Yakovlev. Adiabatic index of dense matter and damping of neutron star pulsations. *Astronomy & Astrophysics*, 394(1):213–217, 2002.

[41] P. Haensel and B. Pichon. Experimental nuclear masses and the ground state of cold dense matter. *Astronomy & Astrophysics*, 283(1):313–318, 1994.

[42] P. Haensel and A. Y. Potekhin. Analytical representations of unified equations of state of neutron-star matter. *Astronomy & Astrophysics*, 428(1):191–197, 2004.

[43] P Hansel, A. Y. Potekhin, and D. G. Yakovlev. *Neutron Stars 1: Equation of State and Structure*. Astrophysics and Space Science Library, 2007.

[44] B. K. Harrison et al. *Gravitation Theory and Gravitational Collapse*. 1965.

[45] A. Harten et al. Uniformly High Order Accurate Essentially Non-oscillatory Schemes, III. *Journal of Computational Physics*, 131(1):3–47, 1997.

[46] A. Harten, P. D. Lax, and B. van Leer. On upstream differencing and Godunov-type schemes for hyperbolic conservation laws. *SIAM review*, 25(1):35–61, 1983.

[47] A. Harten and S. Osher. Uniformly High-Order Accurate Nonoscillatory Schemes. I. *SIAM Journal on Numerical Analysis*, 24(2):279–309, 1987.

[48] J. Healy et al. The RIT binary black hole simulations catalog. *Classical and Quantum Gravity*, 34(22):224001, 2017.

[49] T. Hinderer. Tidal Love Numbers of Neutron Stars. *The Astrophysical Journal*, 677(2):1216, 2008.

[50] T. Hinderer et al. Tidal deformability of neutron stars with realistic equations of state and their gravitational wave signatures in binary inspiral. *Physical Review D*, 81:123016, 2010.

[51] P. A. Hughes and G. C. Duncan. Simulations of Relativistic Extragalactic Jets. In *American Astronomical Society Meeting Abstracts #184*, volume 184 of *American Astronomical Society Meeting Abstracts*, 1994.

[52] R. A. Hulse and J. H. Taylor. Discovery of a pulsar in a binary system. *The Astrophysical Journal*, 195:L51–L53, 1975.

[53] J. M. Ibáñez et al. On the convexity of relativistic hydrodynamics. *Classical and Quantum gravity*, 30, 2013.

[54] J. M. Ibáñez et al. Anomalous dynamics triggered by a non-convex equation of state in relativistic flows. *Monthly Notices of the Royal Astronomical Society*, 476:1–22, 2018.

[55] G-S. Jiang and C-W. Shu. Efficient implementation of weighted ENO schemes. *Journal of Computational Physics*, 126(1):202–228, 1996.

[56] O. Just, M. Obergaulinger, and H-T. Janka. A new multidimensional, energy-dependent two-moment transport code for neutrino-hydrodynamics. *Monthly Notices of the Royal Astronomical Society*, 453(4):3386–3413, 2015.

[57] R. Kippenhahn, A. Weigert, and A. Weiss. *Stellar structure and evolution*, volume 192. Springer, 1990.

[58] K. Kiuchi et al. Implementation of advanced Riemann solvers in a neutrino-radiation magnetohydrodynamics code in numerical relativity and its application to a binary neutron star merger. *Physical Review D*, 106:124041, 2022.

[59] B. D. Lackey, M. Nayyar, and B. J. Owen. Observational constraints on hyperons in neutron stars. *Physical Review D*, 73:024021, 2006.

[60] L. D. Landau and E. M. Lifshitz. *Fluid Mechanics*. 1987.

[61] L. D. Landau and E. M. Lifshitz. *The classical theory of fields*. 1999.

[62] P. D. Lax. *Hyperbolic Systems of Conservation Laws and the Mathematical Theory of Shock Waves*. CBMS-NSF Regional Conference Series in Applied Mathematics, 1973.

[63] P. D. Lax and B. Wendroff. Systems of conservation laws. *Communications on Pure and Applied Mathematics*, 13:217–237, 1960.

[64] P. G. LeFloch. *Hyperbolic Systems of Conservation Laws : The Theory of Classical and Nonclassical Shock Waves*. Lectures in Mathematics, Birkhauser Verlag AG, 2002.

[65] L. Lehner. Topical review: Numerical relativity: a review. *Classical and Quantum Gravity*, 18, 2001.

[66] R. J. LeVeque. *Numerical methods for conservation laws*. Lectures in Applied Mathematics, Birkhäuser Basel, 1992.

[67] R. J. LeVeque et al. *Computational Methods for Astrophysical Fluid Flow: Saas-Fee Advanced Course 27. Lecture Notes 1997 Swiss Society for Astrophysics and Astronomy*, volume 27. Springer Science & Business Media, 2006.

[68] Y. Li, R. S. Klessen, and M-M. Mac Low. The formation of stellar clusters in turbulent molecular clouds: effects of the equation of state. *The Astrophysical Journal*, 592(2):975, 2003.

[69] L. Lindblom and N. M. Indik. Spectral approach to the relativistic inverse stellar structure problem. *Physical Review D*, 86:084003, 2012.

[70] T. P. Liu. The Riemann problem for general systems of conservation laws. *Journal of Differential Equations*, 18(1):218–234, 1975.

[71] F. Löffler et al. The Einstein Toolkit: a community computational infrastructure for relativistic astrophysics. *Classical and Quantum Gravity*, 29(11):115001, 2012.

[72] A. Marquina. Local piecewise hyperbolic reconstruction of numerical fluxes for nonlinear scalar conservation laws. *SIAM Journal on Scientific Computing*, 15(4):892–915, 1994.

[73] A. Marquina et al. Ultrarelativistic hydrodynamics-High-resolution shock-capturing methods. *Astronomy & Astrophysics*, 258:566–571, 1992.

[74] A. Marquina, S. Serna, and J. M. Ibáñez. Capturing Composite Waves in non-convex special relativistic hydrodynamics. *Journal of Scientific Computing*, 81:2132–2161, 2019.

[75] J. M. Martí and E. Müller. The analytical solution of the Riemann problem in relativistic hydrodynamics. *Journal of Fluid Mechanics*, 258:317–333, 1994.

[76] J. M. Martí and E. Müller. Numerical hydrodynamics in special relativity. *Living Reviews in Relativity*, 6(1):1–100, 2003.

[77] J. M. Martí and E. Müller. Grid-based methods in relativistic hydrodynamics and magnetohydrodynamics. *Living reviews in computational astrophysics*, 1(1):1–182, 2015.

[78] J. M. Martí et al. Morphology and dynamics of highly supersonic relativistic jets. *The Astrophysical Journal*, 448(2):L105, 1995.

[79] J. M. Martí et al. Morphology and dynamics of relativistic jets. *The Astrophysical Journal*, 479(1):151, 1997.

[80] R. Menikoff and B. J. Plohr. The Riemann problem for fluid flow of real materials. *Reviews of Modern Physics*, 61:75–130, 1989.

[81] A. Mignone and G. Bodo. An HLLC Riemann solver for relativistic flows—I. Hydrodynamics. *Monthly Notices of the Royal Astronomical Society*, 364(1):126–136, 2005.

[82] P. Mösta et al. GRHydro: a new open-source general-relativistic magnetohydrodynamics code for the Einstein toolkit. *Classical and Quantum Gravity*, 31(1):015005, 2013.

[83] H. Mueller and B. D. Serot. Relativistic mean-field theory and the high-density nuclear equation of state. *Nuclear Physics A*, 606(3-4):508–537, 1996.

[84] S. Muller and A. Voss. The Riemann Problem for the Euler Equations with Nonconvex and Nonsmooth Equation of State: Construction of Wave Curves. *SIAM Journal Scientific Computing*, 28:651–681, 2006.

[85] M. L. Norman and K. H. A. Winkler. Why Ultrarelativistic Hydrodynamics is Difficult. In *Astrophysical Radiation Hydrodynamics*, pages 449–476. Springer, 1986.

[86] M. Oertel et al. Equations of state for supernovae and compact stars. *Reviews of Modern Physics*, 89(1):015007, 2017.

[87] J. R. Oppenheimer and G. M. Volkoff. On massive neutron cores. *Physical Review*, 55(4):374, 1939.

[88] S. Osher et al. Uniformly high order accurate essentially non-oscillatory schemes, III. *Journal of Computational Physics*, 71(2):231–303, 1987.

[89] V. R. Pandharipande and R. A. Smith. A model neutron solid with pion0 condensate. *Nuclear Physics A*, 237(3):507–532, 1975.

[90] B. Peres, M. Oertel, and J. Novak. Influence of pions and hyperons on stellar black hole formation. *Physical Review D*, 87(4):043006, 2013.

[91] J. A. Pons, J. M. Martí, and E. Müller. The exact solution of the Riemann problem with non-zero tangential velocities in relativistic hydrodynamics. *Journal of Fluid Mechanics*, 422:125–139, 2000.

[92] F. Pretorius. Simulation of binary black hole spacetimes with a harmonic evolution scheme. *Classical and Quantum Gravity*, 23(16):S529, 2006.

[93] J. J. Quirk. A contribution to the great Riemann solver debate. *International Journal for numerical Methods in fluids*, 18:555–574, 1994.

[94] T. Rauscher et al. Nucleosynthesis in massive stars with improved nuclear and stellar physics. *The Astrophysical Journal*, 576(1):323, 2002.

[95] J. S. Read et al. Constraints on a phenomenologically parametrized neutron-star equation of state. *Physical Review D*, 79:124032, 2009.

[96] P. G. Reinhard et al. Shape coexistence and the effective nucleon-nucleon interaction. *Physical Review C*, 60:014316, 1999.

[97] P. G. Reinhard and H. Flocard. Nuclear effective forces and isotope shifts. *Nuclear Physics A*, 584(3):467–488, 1995.

[98] L. Rezzolla and O. Zanotti. *Relativistic hydrodynamics*. Oxford University Press, 2013.

[99] L. Rezzolla, O. Zanotti, and J. A. Pons. An improved exact Riemann solver for multi-dimensional relativistic flows. *Journal of Fluid Mechanics*, 479:199–219, 2003.

[100] M. H. Rice, R. Go. McQueen, and J. M. Walsh. Compression of solids by strong shock waves. In *Solid state physics*, volume 6, pages 1–63. Elsevier, 1958.

[101] B. Riemann. *Über die Fortpflanzung ebener Luftwellen von endlicher Schwingungsweite*, volume 8. Verlag der Dieterichschen Buchhandlung, 1860.

[102] T. Riley et al. A NICER view of the massive pulsar PSR J0740+ 6620 informed by radio timing and XMM-Newton spectroscopy. *The Astrophysical Journal Letters*, 918(2):L27, 2021.

[103] P. L. Roe. Approximate Riemann solvers, parameter vectors, and difference schemes. *Journal of Computational Physics*, 43:357–372, 1981.

[104] N. Roth and D. Kasen. Monte Carlo radiation-hydrodynamics with implicit methods. *The Astrophysical Journal Supplement Series*, 217(1):9, 2015.

[105] V. Schneider et al. New algorithms for ultra-relativistic numerical hydrodynamics. *Journal of Computational Physics*, 105(1):92–107, 1993.

[106] S. Serna. A characteristic-based nonconvex entropy-fix upwind scheme for the ideal magnetohydrodynamic equations. *Journal of Computational Physics*, 228(11):4232–4247, 2009.

[107] S. Serna and A. Marquina. Power ENO methods: a fifth-order accurate Weighted Power ENO method. *Journal of Computational Physics*, 194:632–658, 2004.

[108] S. Serna and A. Marquina. Capturing shock waves in inelastic granular gases. *Journal of Computational Physics*, 209(2):787–795, 2005.

[109] S. Serna and A. Marquina. Capturing blast waves in granular flow. *Computers and Fluids*, 36(8):1364–1372, 2007.

[110] S. Serna and A. Marquina. High order accurate shock capturing schemes for two-component Richtmyer-Meshkov instabilities in compressible magnetohydrodynamics. In *20th AIAA Computational Fluid Dynamics Conference 201*. 2011.

[111] S. Serna and A. Marquina. Anomalous wave structure in magnetized materials described by non-convex equations of state. *Physics of Fluids*, 26, 2014.

[112] M. Shibata et al. Constraint on the maximum mass of neutron stars using GW170817 event. *Physical Review D*, 100:023015, 2019.

[113] M. Shibata and K. Uryū. Simulation of merging binary neutron stars in full general relativity: $\Gamma = 2$ case. *Physical Review D*, 61:064001, 2000.

[114] C-W. Shu and S. Osher. Efficient implementation of essentially non-oscillatory shock-capturing schemes. *Journal of Computational Physics*, 77(2):439–471, 1988.

[115] C-W. Shu and S. Osher. Efficient implementation of essentially non-oscillatory shock-capturing schemes, II. *Journal of Computational Physics*, 83(1):32 – 78, 1989.

[116] J. Smoller. *Shock waves and reaction—diffusion equations*, volume 258. Springer Science and Business Media, 2012.

[117] J. Sollfrank et al. Hydrodynamical description of 200A GeV/c S+ Au collisions: hadron and electromagnetic spectra. *Physical Review C*, 55(1):392, 1997.

[118] M. Spaans and J. Silk. The polytropic equation of state of interstellar gas clouds. *The Astrophysical Journal*, 538(1):115, 2000.

[119] F. D. Swesty. Thermodynamically consistent interpolation for equation of state tables. *Journal of Computational Physics*, 127(1):118–127, 1996.

[120] B. Szilagyi, L. Lindblom, and M. A. Scheel. Simulations of binary black hole mergers using spectral methods. *Physical Review D*, 80(12):124010, 2009.

[121] A. H. Taub. Relativistic Rankine-Hugoniot Equations. *Phys. Rev.*, 74:328–334, 1948.

[122] A. H. Taub. Relativistic fluid mechanics. *Annual review of fluid mechanics*, 10(1):301–332, 1978.

[123] J. H. Taylor and J. M. Weisberg. A new test of general relativity-Gravitational radiation and the binary pulsar PSR 1913+ 16. *The Astrophysical Journal*, 253:908–920, 1982.

[124] P. A. Thompson. *Compressible fluid dynamics*. McGraw-Hill, New Yok, 1972.

[125] P. A. Thompson and K. C. Lambrakis. Negative shock waves. *Journal of Fluid Mechanics*, 60(1):187–208, 1973.

[126] K. S. Thorne. Relativistic shocks: the taub adiabat. *Astrophysical Journal*, 179:897–908, 1973.

[127] K. S. Thorne, J. A. Wheeler, and C. W. Misner. *Gravitation*. Freeman San Francisco, CA, 2000.

[128] R. C. Tolman. Static solutions of Einstein's field equations for spheres of fluid. *Physical Review*, 55(4):364, 1939.

[129] E. F. Toro. *Riemann solvers and numerical methods for fluid dynamics: a practical introduction*. Springer Science and Business Media, 2013.

[130] E. F. Toro, M. Spruce, and W. Speares. Restoration of the contact surface in the HLL-Riemann solver. *Shock waves*, 4:25–34, 1994.

[131] S. Typel, M. Oertel, and T. Klähn. CompOSE CompStar online supernova equations of state harmonising the concert of nuclear physics and astrophysics compose. obspm. fr. *Physics of Particles and Nuclei*, 46:633–664, 2015.

[132] B. Van Leer. Towards the ultimate conservative difference scheme. V. A second-order sequel to Godunov's method. *Journal of Computational Physics*, 32(1):101–136, 1979.

[133] L. R. Weih, E. R. Most, and L. Rezzolla. Optimal Neutron-star Mass Ranges to Constrain the Equation of State of Nuclear Matter with Electromagnetic and Gravitational-wave Observations. *The Astrophysical Journal*, 881(1):73, 2019.

[134] B. Wendroff. The Riemann problem for materials with nonconvex equations of state I: Isentropic flow. *Journal of Mathematical Analysis and Applications*, 38(2):454–466, 1972.

[135] B. Wendroff. The Riemann problem for materials with nonconvex equations of state II: General Flow. *Journal of Mathematical Analysis and Applications*, 38(3):640–658, 1972.

[136] K. Wu and H. Tang. High-order accurate physical-constraints-preserving finite difference weno schemes for special relativistic hydrodynamics. *Journal of Computational Physics*, 298:539–564, 2015.

[137] K. Wu and H. Tang. Physical-constraint-preserving central discontinuous galerkin methods for special relativistic hydrodynamics with a general equation of state. *The Astrophysical Journal Supplement Series*, 228(1):3, 2016.

[138] J. L. Zdunik et al. Phase transitions in rotating neutron stars cores: back bending, stability, corequakes, and pulsar timing. *Astronomy & Astrophysics*, 450(2):747–758, 2006.

[139] J. L. Zdunik, P. Haensel, and R. Schaeffer. Phase transitions in stellar cores. II-Equilibrium configurations in general relativity. *Astronomy & Astrophysics*, 172:95–110, 1987.

[140] Ya. B. Zeldovich and I. D. Novikov. *Relativistic astrophysics. Vol.1: Stars and relativity.* 1971.

Appendix A

Additional tables

EoS	PT1	PT2	PT3	PT4
PS	g2o6			
GS1	g2o6			
GS2	g2o6			
BGN1H1	g2o5			
H4	g2o6	g2o2	g2o6	g3o2
H5	g2o6	g2o4	g2o6	
H6	g2o6	g2o2	g3o4	
H7	g2o6	g3o2	g2o6	
ALF1	g4o1			
ALF2	g2o6			

Table A.1: Type of polynomial model obtained for each of the PTs located in table 5.2 using TCPP model.

EoS	$\log(P_1)$	Γ_1	Γ_2	Γ_3
PS	34.671	2.216	1.640	2.365
GS1	34.504	2.350	1.267	2.421
GS2	34.642	2.519	1.571	2.314
BGN1H1	34.623	3.258	1.472	2.464
H4	34.669	2.909	2.246	2.144
H5	34.609	2.793	1.974	1.915
H6	34.593	2.637	2.121	2.064
H7	34.559	2.621	2.048	2.006
ALF1	34.055	2.013	3.389	2.033
ALF2	34.616	4.070	2.411	1.890

Table A.2: Parameters of the PP EoSs used in the construction of the TCPP model, extracted from [95]. Notice that P_1, the pressure where the high density region meets the fit for the crust, is in dyne/cm^2.

PT	a_1	a_2	a_3	a_4
PS	-0.2999434	0.1499717	0	0
GS1	-0.1992662	0.09963312	0	0
GS2	-0.7030000	0.3515000	0	0
BGN1H1	-3.949183	1.974592	0	0
H4 (PT1)	-3.311180	1.655590	0	0
H4 (PT2)	-10.36376	5.114054	0	0
H4 (PT3)	-41.58576	20.79288	0	0
H4 (PT4)	344.9046	-352.4198	119.9783	0
H5 (PT1)	-1.558999	0.794997	0	0
H5 (PT2)	-5.171105	2.585552	0	0
H5 (PT3)	-24.32069	12.16035	0	0
H6 (PT1)	-1.197840	0.5989198	0	0
H6 (PT2)	-1.292044	0.6332808	0	0
H6 (PT3)	97.41861	-99.21711	3.367187	0
H7 (PT1)	-1.494551	0.7472754	0	0
H7 (PT2)	364.9504	-368.5709	124.0638	0
H7 (PT3)	-70.27469	35.13734	0	0
ALF1	-9.996823	8.486970	-2.731144	0.2484120
ALF2	-0.5362804	0.2681402	0	0

Table A.3: Parameters obtained for the model of each of the PTs with TCPP model. The terms θ_i, d and x_m of equation (6.1.3) can be obtained from the given location of the PT and the evaluation of the PP EoS.

	Polytrope 1		Polytrope 2		Polytrope 3	
EoS	ρ_1	Γ	κ	Γ	ρ_c	Γ
PS	5.408342e+13	2.700651	1.678417e-19	2.201028		
GS1	7.245427e+13	2.627418	3.029894e-21	2.297987	1.987850e15	2.700192
GS2	6.909353e+13	2.736653	1.898658e-19	2.193692		
BGN1H1	9.991575e+13	2.847990	3.671349e-26	2.632914		
ALF1	1.390908e+14	2.663749	1.515736e-30	2.925772	1.423560e15	1.493853
ALF2	2.132768e+14	4.466608	2.875044e-20	2.260870	1.156867e15	1.736335

Table A.4: Parameters of the polytropes fitted for T-ASPP model in the case of a single PT. Parameter ρ_1 is the density where the high density fit meets the crust. The presence of a third polytrope and its dividing density ρ_c are determined from the behavior of the sound speed.

	Polytrope 1		Polytrope 2		Polytrope 3		Polytrope 4		Polytrope 5	
EoS	ρ_1	Γ	κ	Γ	κ	Γ	κ	Γ	κ	Γ
H4	8.857179e13	2.904905	3.674223e-21	2.322651	1.082695e-19	2.223440	7.678047e-18	2.100814	4.686073e-13	1.785478
H5	7.403334e+13	2.666776	1.776434e-16	2.000432	2.422123e-15	1.924059	8.959896e-15	1.886911		
H6	7.564155+13	2.699506	6.498099e-20	2.231733	1.141858e-19	2.214444	1.569845e-10	1.609401		
H7	6.505443e+13	2.530689	4.778496e-17	2.036248	9.280893e-17	2.016653	3.575624e-16	1.978326		

Table A.5: Parameters of the polytropes fitted for T-ASPP model in the case of several PTs. Parameter ρ_1 is the density where the high density fit meets the crust.

EoS	PT1	PT2	PT3	PT4
PS	g2o5			
GS1	g2o6			
GS2	g2o6			
BGN1H1	g4o2			
H4	g2o6	g2o6	g2o1	g4o2
H5	g4o5	g2o6	g4o1	
H6	g2o6	g2o6	g2o1	
H7	g2o6	g2o6	g2o5	
ALF1	g3o1			
ALF2	g2o6			

Table A.6: Type of polynomial model obtained for each of the PTs located in table 5.2 using T-ASPP model.

PT	a_1	a_2	a_3	a_4
PS	-0.291327	0.145664	0	0
GS1	-0.216637	0.108318	0	0
GS2	-1.017213	0.508607	0	0
BGN1H1	-23.53632	21.61414	-7.821805	0.876630
H4 (PT1)	-3.264435	1.632217	0	0
H4 (PT2)	-19.41081	9.705403	0	0
H4 (PT3)	-148.8775	74.58862	0	0
H4 (PT4)	-234.6205	227.1035	-79.04511	4.247607
H5 (PT1)	-3.8317865	3.359718	-1.257225	0.221007
H5 (PT2)	-12.85180	6.425898	0	0
H5 (PT3)	8248.275	-8235.706	2687.375	40.25310
H6 (PT1)	-1.942309	0.971154	0	0
H6 (PT2)	-9.298705	4.649353	0	0
H6 (PT3)	-50.87276	25.53068	0	0
H7 (PT1)	-1.880712	0.940356	0	0
H7 (PT2)	-33.41581	16.70790	0	0
H7 (PT3)	-1369.555	684.7774	0	0
ALF1	-7.368422	5.477297	-1.275412	0
ALF2	-0.337758	0.168879	0	0

Table A.7: Parameters obtained for the model of each of the PTs with T-ASPP model. The terms θ_i, d and x_m of equation (6.1.3) can be obtained from the given location of the PT and the evaluation of the polytropic pieces provided.